9-20-2018 2:30 PM

Coupling Scanning Electrochemical Microscopy and 3D Modelling to Probe Membrane Permeability of Human Bladder Cancer (T24) Cells

Fraser Filice
The University of Western Ontario

Supervisor
Dr. Zhifeng Ding
The University of Western Ontario

Graduate Program in Chemistry
A thesis submitted in partial fulfillment of the requirements for the degree in Doctor of Philosophy
© Fraser Filice 2018

Follow this and additional works at: https://ir.lib.uwo.ca/etd

Part of the Analytical Chemistry Commons, and the Physical Chemistry Commons

Abstract

Scanning electrochemical microscopy (SECM) scans a biased ultramicroelectrode (≤ 25 µm) probe over a sample to characterize topography, physical properties and chemical reactivity. In this dissertation, SECM was used to investigate the metal-induced changes in membrane response of single live human bladder cancer cells (T24). SECM imaging was coupled to 3D finite element method (FEM) simulations which were the first of their kind, providing advanced quantification of sample traits under conditions not previously usable.

The effects of Cd^{2+} on T24 cell membrane permeability were examined. Experimental depth-scan imaging was coupled with full 3D FEM simulations, eliminating many limitations of previous 2D-axially symmetric models. Hundreds of probe approach curves (PACs) can now be extracted from depth-images and theoretically fit to quantify membrane permeability at any location across the cell surface (Chapter 2).

SECM was utilized to examine the membrane response of T24 cells following exposure to toxic dichromate (Cr(VI)). Two electrochemical mediators were examined, the membrane permeable ferrocenemethanol ($FcCH_2OH$) and impermeable ferrocenecarboxylate ($FcCOO^-$). Cr(VI) induced permeability change was observed with both mediators and compared (Chapter 3). Chronic Cr(VI) induced cell stress, was then examined. Similar permeability curve shape was observed, with shifts in response time based on concentration of Cr(VI) stressor (Chapter 4).

Trace essential metals such as Cr(III) are essential in low concentrations but toxic in high concentration. Membrane-response was investigated by SECM, using both $FcCH_2OH$ and $FcCOO^-$ redox mediators. Theoretical SECM depth-scans were produced using 3D FEM simulations, and used to quantify cell membrane permeability (Chapter 5).

Complex close-proximity cell clusters were experimentally imaged by SECM 3D scanning mode. Tailored 3D model geometries were created, generating complimentary theoretical maps of the experimental cell clusters. The simulations were capable of providing a strong

theoretical fit to the experimental results. Limits of cell proximity for SECM characterization were determined based on the probe size (Chapter 6).

Nanoscale SECM imaging of single live cells were performed using a laser-pulled 130 nm radius Pt disk electrode. A tailored 3D model was created, from which cell topography was accurately characterized using membrane-impermeable $Ru(NH_3)_6{}^{3+}$, and cell membrane permeability was quantified with $FcCH_2OH$ (Chapter 7).

Keywords

Co-Authorship Statement

This thesis includes material from five published manuscripts that are presented in Chapters 1, 2, 3, 4 and 7. Also included in this thesis is material from two manuscripts prepared for submission, which are presented in Chapters 5 and 6. All manuscripts were finalized and submitted by ZD.

The manuscript presented in Chapter 1 was published and co-authored by F.P. Filice and Z. Ding (*Analyst,* **2018,** DOI: 10.1039/C8AN01490F). Literary reviews and writing of the manuscript were performed by FPF. Editing was performed by FPF and ZD.

The manuscript presented in Chapter 2 was published and co-authored by, F.P. Filice, M.S.M. Li, J. D. Henderson and Z. Ding (*Anal. Chim. Acta* **2016**, *908*, 85-94.). All of the experiments were completed by FPF and JDH (50% each). COMSOL simulations were completed by FPF. FPF wrote and revised the manuscript, which was edited by FPF, MSML, JDH and ZD.

The manuscript presented in Chapter 3 was published and co-authored by J. D. Henderson, F.P. Filice, M.S.M. Li and Z. Ding (*Chemelectrochem* **2017**, *4*, 856-863.). $FcCH_2OH$ experiments were performed by JDH (80%) and FPF (20%). FcCOOH experiments were performed by FPF. COMSOL simulations were completed by FPF. MTT cellular viability assays were performed by FPF and MSML. FPF and JDH wrote and revised the manuscript, which was edited by FPF, MSML, JDH and ZD.

The manuscript presented in Chapter 4 was published and co-authored by F.P. Filice, M.S.M. Li, J. M Wong and Z. Ding (*Journal of Bioinorganic Chemistry* **2018**, *182*, 222-229.). All of the experiments were completed by FPF and JMW. COMSOL simulations were completed by FPF. MTT cellular viability assays were performed by FPF and JMW. FPF wrote and revised the manuscript, which was edited by FPF and ZD.

The manuscript presented in Chapter 5 was co-authored by F.P. Filice, J. D. Henderson, M.S.M. Li and Z. Ding (**2018,** *Submitted*). $FcCH_2OH$ experiments were performed by JDH (80%) and FPF (20%). FcCOOH experiments were performed by FPF. COMSOL simulations were completed by FPF. MTT cellular viability assays were performed by FPF

and MSML. FPF wrote and revised the manuscript, which was edited by FPF, MSML, JDH and ZD.

The manuscript presented in Chapter 6 was co-authored by F.P. Filice, M.S.M. Li, J. M Wong and Z. Ding (**2018,** *Submitted*). All of the experiments
were completed by MSML, FPF and JMW. COMSOL simulations were completed by FPF. MSML was responsible for the fabrication and optimization of the 4.4 μm UME. FPF wrote and revised the manuscript, which was edited by FPF and ZD.

The manuscript presented in Chapter 7 was published and co-authored by F.P. Filice, M.S.M. Li and Z. Ding (*Adv. Theory Simulations,* **2018,** DOI: 10.1002/adts.201800124). All of the experiments and COMSOL simulations were completed by FPF. MSML fabricated and optimized the nanoelectrode. FPF wrote and revised the manuscript, which was edited by FPF and ZD.

Part of the content in the future works of Chapter 8 was published and co-authored by F.P. Filice and Z. Ding (*Analyst,* **2018,** DOI: 10.1039/C8AN01490F). Literary reviews and writing of the manuscript were performed by FPF. Editing was performed by FPF and ZD.

Acknowledgments

I would like to first and foremost thank Dr. Zhifeng Ding for all of his support and guidance throughout my PhD and undergraduate studies at Western University. I am grateful for the many opportunities Dr. Ding has provided to me over the years, to train on cutting-edge instrumentation and experience a broad range of interesting techniques. I know without him I wouldn't be the scientist I am today. I am thankful to have been part of his research group.

I would like to thank all Ding group members, past and present, for being great coworkers and great friends. I must thank Dr. Michelle S. M. Li, Jeffrey D. Henderson, Jonathan R. Adsetts, Jonathan M. Wong and Lina Yao, with whom I have worked closely on the SECM project. I must also give special thanks to Daniel Vaccarello, Amy Tapley, Matthew Turnbull, and Mahdi Hesari for all their help throughout my PhD.

I greatly appreciate all of the work the staff of the Chemistry Department, especially those in the Electronic Shop, who have spent many hours fixing the Ding Lab electrode puller and other instruments throughout the duration of my studies. I must thank Aneta Borecki for her knowledge of cell culture and cellular viability assays, Dr. Todd Simpson for his assistance characterizing electrodes at Western's Nanofabrication Facility, and Dr. Kristin Chadwick (The London Regional Flow Cytometry Facility) for her knowledge and guidance on flow cytometry experiments. In addition, I must thank Drs. Janine Mauzeroll and Laurence Danis at McGill University for their mentoring in the fabrication of laser-pulled nanoelectrodes.

I would also like to thank Dr. Martin J. Stillman for giving me the unique opportunity to help organize, run, and present at the 6th Georgian Bay International Conference on Bioinorganic Chemistry (CanBIC) in Parry Sound, Ontario. This event was a lot of fun and an excellent experience.

Finally, I must give special thanks to my parents, Patrick Filice and Mary Pat Filice, as well as my sister, Lauren Filice. Thank you for being a great family and always supporting me. I know I could not have done this without you.

Table of Contents

List of Figures

List of Appendices

List of Abbreviations

Abbreviation	Definition
A	Amperes (Amps)
a	Radius of electrode
Abs	Absorbance
AFM	Atomic force microscopy
BSA	Bovine serum albumin
C_B	Concentration in the solution domain
C_C	Concentration in the cell interior
CE	Counter/auxiliary electrode
CV	Cyclic voltammetry or cyclic voltammogram
CVD	Chemical vapor deposition
D	Diffusion coefficient (m^2/s)
d	Tip-to-sample distance
DAG-lactone	Diacylglycerol-lactone
DMSO	Dimethyl sulfoxide
DNA	Deoxyribonucleic acid
ECL	Electrochemiluminescence
EDTA	Ethylenediaminetetraacetic acid
F	Faraday constant (96,485 C/mol)
FBS	Fetal bovine serum
$FcCH_2OH$	Ferrocenemethanol (FcMeOH)
$FcCOO^-$	Ferrocenecarboxylate anion
$FcCOO^{2-}$	Ferrocenecarboxylate di-anion
FcCOOH	Ferrocenecarboxylic acid
$Fc(COO)_2^{2-}$	1,'1-ferrocene dicarboxylate anion
$Fc(COOH)_2$	1,'1-ferrocene dicarboxylic acid
FEA	Finite elemental analysis (finite elemental method)
FEM	Finite elemental method (finite elemental analysis)
FIB	Focused ion beam
GOx	Glucose oxidase

GSH	Glutathione
HeLa	Human cervical cancer cells
i	current (A)
i_∞	Steady state (bulk) current
i_{ss}	Steady state current
I_T	Normalized current
KCl	Potassium chloride
L	Normalized distance
LMWCr	Low-molecular-weight chromium-binding substance
LOx	Lactate oxidase
MAPK	Mitogen-activated protein kinase
MTT	3-(4,5-dimethylthiazol-2-yl)-2,5-diphenyltetrazolium bromide
N	Number of individual cell measurements
n	Number of electrodes transferred in the redox reaction
O	Oxidized species
PAC	Probe approach curve
PBS	Phosphate buffered saline
P	Membrane permeability coefficient
R	Reduced species
RE	Reference electrode
RG	The ratio of the glass sheathing radius to the conductive wire radius
RNS	Reactive nitrogen species
ROS	Reactive oxygen species
$Ru(NH_3)_6^{3+}$	Hexaaminetruthenium(III) cation
$Ru(NH_3)_6Cl_3$	Hexaamineruthenium trichloride
SDS	Sodium dodecyl sulfate
SECM	Scanning electrochemical microscopy
SEM	Scanning electron microscopy
SICM	Scanning ion conductance microscope
SNOM	Scanning near-field optical microscopy
SPM	Scanning probe microscopy
T24 cells	Human bladder cancer cells

TyR   Tyrosinase biomarker

UME   Ultramicroelectrode

WE   Working electrode

Chapter 1

1   Introduction

Single live cell analysis methods provide information on the characteristics of idividual cells, yielding not only bulk population averages but also their heterogeneity. Scanning electrochemical microscopy (SECM) offers single live cell analysis through non-invasive, high-resolution, mapping of electrochemical measurment in or around the cell sample of interest. Membrane permeability and rate of membrane species transport can be quantified by SECM. Cell response to external stressors can be monitored and modelled, and will be explored in greater detail for the metals Cd, Cr(VI) and Cr(III) in this thesis. Quantification of many traits of the sample under study are commonly performed through the use of Finite Element Method (FEM) simulations. However, typical FEM models are over-simplified and restricted to a 2D axially symmetric geometry. Advancements in FEM models for SECM analysis to single live cells will be discussed in greater detail in this thesis, including 3D modelling, sample mapping, complex sample geometries and dual mediator characterization. SECM is also able to offer nanoscale mapping and low concentration detection, providing a powerful bioanalytical tool for live cell studies. Nanoscale imaging of a single live cell with laser-pulled electrodes and the subsequent quantification of topography and membrane permeability will be explored in this thesis as well.

1.1   Background of Scanning Electrochemical Microscopy

Numerous analytical tools have been developed for the analysis of live cells and their functions. However, the majority of these focus on analyzing the bulk cell population. While allowing for rapid characterization, these techniques are often incapable of

detecting the heterogeneity of the cells under study and giving chemical reactivity information. Single cell techniques facilitate to meet the research demands on an individual basis. Among those, scanning electrochemical microscopy (SECM) has shown great research interest in recent years.

In fact, SECM is a powerful non-invasive analytical technique of the scanning probe microscopy family.[1-3] This technique utilizes a small diameter (≤ 25 µm) electrochemical probe to image a region of space with extreme precision. Faradaic current is recorded with electrode position to reconstruct detailed maps of topography and sample reactivity. SECM utilizes an electrochemically active redox species, either introduced into the system or intrinsic to the sample under study. The electrochemical mediator is either oxidized or reduced at the electrode tip in a diffusion-controlled process yielding steady state current.

The SECM concept was introduced in 1986 by Engstrom et al.,[4] and showed great promise as a new electroanalytical technique. Early SECM development and experimentation was performed by Bard et al. beginning in 1989, which laid the groundwork for its application to a diverse range of research fields.[5-6] SECM has since been employed in a vast number of applications,[7] including but not limited to kinetic studies,[8-9] surface and interface studies,[10-12] and microstructure fabrication.[13-14] SECM has also found applications as a bioanalytical tool for cellular imaging,[15-24] membrane transport,[16, 25-31] neurotransmitter release,[32-33] multidrug resistance studies,[17-18] reactive oxygen species (ROS) and reactive nitrogen species (RNS) mapping,[23, 34-39] and cellular redox processes.[21, 31, 40-44]

SECM has been employed in combination with other complimentary bioanalytical tools. These include as SECM-AFM,[45] SECM-NSOM,[46-47] SECM-SICM,[48] SECM-Raman imaging,[49] SECM-Fluorescence microscopy,[50] SECM-Microfluidic systems,[51] and many more. SECM is also commonly used in compliment with finite element method (FEM) simulations to quantify physical characteristics of the sample under study.[52-55]

The focus of this chapter will be on biological applications of SECM for the study of single live cells. Cell-related SECM progresses such as instrumentation, reactive oxygen and nitrogen species, membrane transport, heavy metal stress, finite element simulations and nanoscale images will be highlighted. For a survey of the general applications of SECM, please see the 2016 review "Scanning Electrochemical Microscopy: A Comprehensive Review of Experimental Parameters from 1989 to 2015" by the Mauzeroll group at McGill University.[7]

1.2 SECM Principles
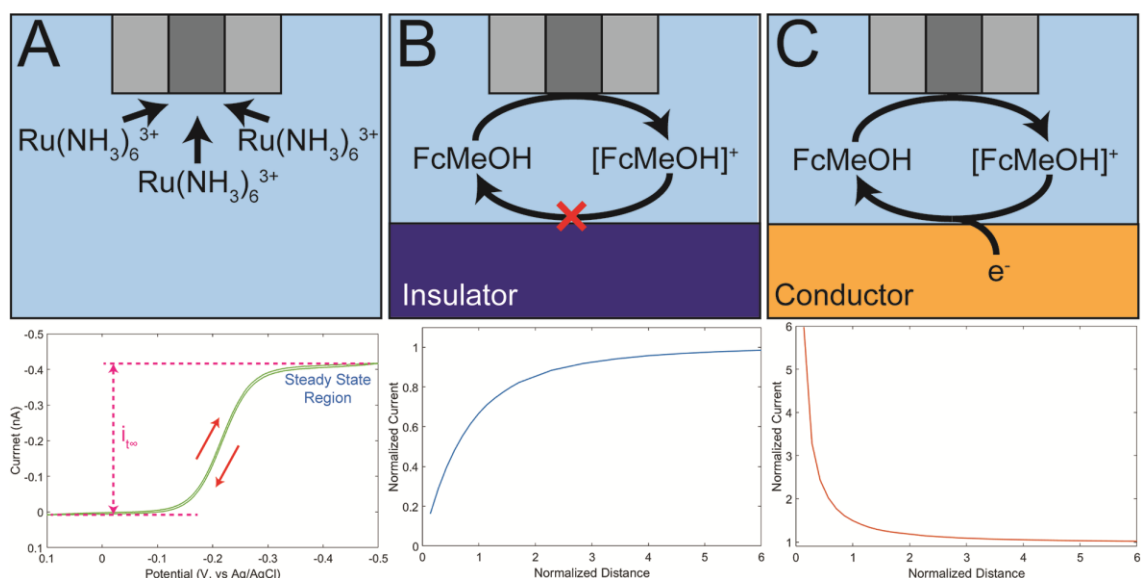
Figure 1.1 – (A) Hemispherical diffusion of a redox mediator $Ru(NH_3)_6^{3+}$ toward a UME tip that results in a steady-state CV in bulk solution. (B) Hindered diffusion by insulating substrate, when a biased UME approaches an insulator (negative feedback). (C) Electrochemical recycling at a conductive substrate, generating a positive feedback probe approach curve.

SECM resolution relies on the precise positioning of UMEs (≤ 25 µm) or even smaller nanoelectrode probes. Electrodes of UME size or smaller are capable of providing a diffusion limited steady state redox current.[3, 56] The resistive drops in potential are negligible as the current is commonly very small (nA to fA range).[2, 7] Figure 1.1A shows a cyclic voltammogram (CV) of 10 mM $Ru(NH_3)_6^{3+}$ collected with a 320 nm diameter Pt

electrode. When a sufficient potential is applied, a 1 electron transfer reaction occurs at the electrode tip at a constant rate, dictated by the rate of diffusion in the system. Figure 1.1B shows a normalized electrode probe approach to an insulating substrate. The adjacent insulating substrate hinders the diffusion toward the electrode tip, causing a decrease in current (negative feedback). However, if a PAC to a conductive substrate is performed (Figure 1.1C), the electrochemical regeneration of the mediating species can occur at the conductor surface. This causes recycling of the mediator between the two surfaces, which increases with closer proximity causing an increase in current (positive feedback).

1.3 Analytical and Instrumental Methodology
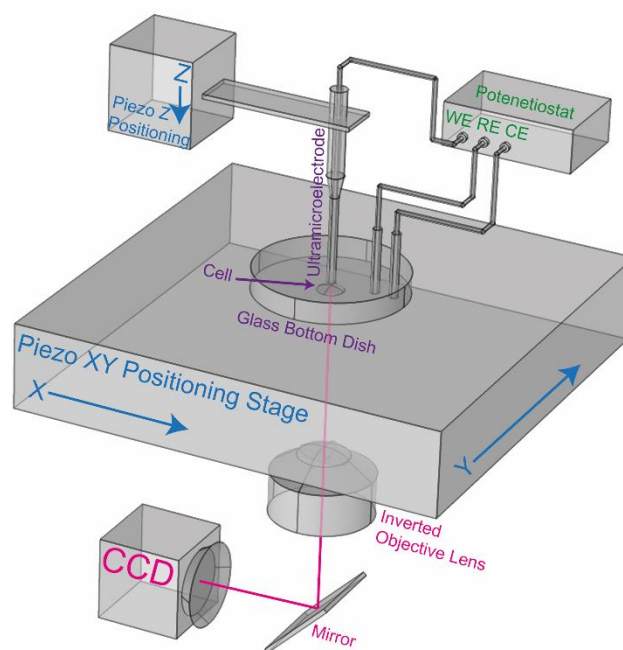
Figure 1.2 - Typical setup for a bio-SECM: The sample is mounted on a stage below the ultramicroelectrode probe. The UME tip to sample position is controlled by an XYZ positioning system. The electrochemical cell can consist of a 2 or 3 electrode system (WE, CE/RE or WE, CE, RE respectively). An inverted objective microscope is often used for electrode positioning and optical imaging. Data output from the potentiostat, positioning system, and camera are logged simultaneously by a computer.

A typical SECM is composed of a low current electrochemical potentiostat, a high-resolution positioning system, and a small diameter SECM probe (Figure 1.2). SECMs now often include an optical imaging system to aid in cell and electrode positioning and relocation.[19] The electrochemical system is normally a low current potentiostat. Current response is dependant on probe size and the concentration of species being monitored. As a result, the requirements for the selected potentiostat can range from low nanoamps (nA), down to femtoamps (fA). Lower current systems are also susceptible to electrical noise from external sources. It is important to consider instrument grounding and isolation, instrument shielding (faraday cage), the quality of shielded analog cabling, and physical isolation for vibration.

Accurate movement of the electrode tip relative to the cell is essential. These positioning systems are commonly piezoelectric positioners, or high accuracy stepper motors. Many early designs of SECM positioning systems utilized open loop positioning systems, which rely on logging the number of steps and a known step size to determine electrode position. These systems, while incredibly accurate, are susceptible to minor drift in electrode position dependant on the tolerance specification for each step. Over the course of long duration scans, the accumulation of drift from each individual step can cause significant deviation. Closed loop positioning systems are now utilized as common practice, providing a solution to this problem, by using active monitoring of the positioning.[34, 57] This active sensing of position is coupled to a feedback loop, where compensation for probe drift is applied.

The SECM probe is arguably the most important part of the instrument. SECM resolution is directly dependant on the size of the electrochemical probe. Various methods of SECM electrode fabrication have been developed including encasing a metal or other conductor in glass,[58] laser pulling both metal and glass,[59-60] chemical vapor deposition (CVD), pyrolytic carbon deporition,[61] and many more specialized electrodes.[54, 62] Electrodes can also be modified in a molecule-specific coating to create specialized sensors.[63]

A close relative to the SECM imaging method, is the Scanning Ion Conductance Microscope (SICM).[64] SICM imaging utilizes an electrolyte filled nanopipette in place of

an SECM disk electrode. Where the resolution of an SECM comes from the critical radius of the UME disk, SICM yields a similar result through the radius of the nanopipette tip. SICM probes are often gravity-pulled or laser-pulled from glass capillaries and filled with electrolyte when performing the experiment.

1.4 SECM Scanning Methods
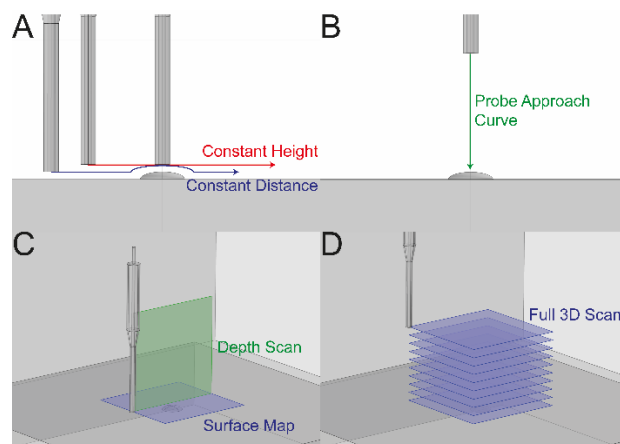
Figure 1.3 - (A) Horizontal 1D scanning methods for SECM imaging of a sample (B) 1D electrode tip movement in z direction to yield probe approach curve (C) Common 2D scanning methods across a cell (D) Full 3D scanning method over a cell

Various imaging modes for SECM probe movement exist. Simple 1D line scans such as the constant height scan in Figure 1.3A fix the height of the electrode and scan horizontally across the sample. Constant distance imaging, however, moves the probe up and down as it passes over the substrate, in an attempt to keep the tip-to-cell distance constant.[23, 65] Various methods have been used to control SECM tip-to-cell distance including SECM-AFM systems,[45, 66] shear force,[67-68] impedance,[23, 65] faradaic current,[69] and ion current.[48, 70] Each of these methods provides its own advantages and disadvantages. Both the constant height and the many forms of constant distance scans provide excellent information of topography and variation in surface reactivity. Another simple 1D scan is the probe approach curve (PAC, Figure 1.3B), where the electrode is moved linearly toward the substrate providing detailed information about a specific point on the sample. PACs provide excellent tip-to-substrate information, and more detailed

reactivity information at a specific location. As a result, PACs are more commonly employed for the detection of membrane permeability, or surface emission/consumption of species.

2D scanning modes such as depth scanning[37] and surface mapping have the advantage of providing information on a much larger region over the cell (Figure 1.3C). They are commonly composed of hundreds of constant height, constant distance, or PACs at fixed distances from each-other. Depth scan mode operates in the x-z or y-z plane over a sample, where surface maps are generally taken as a x-y map over the cell. A full 3D map over a cell provides information on a volume of space, which is composed of numerous surface maps and depth scans with a fixed spacing (Figure 1.3D). This provides a significant amount of data, and the ability to extract any needed scan in post processing. This scanning method does, however, come at the expense of long experiment run times.

SECM hopping mode can be performed as a 2D or 3D imaging method.[71] When scanned in 2D, the electrode is moved in a similar plane to depth scanning mode. However, the order in which the two axes are scanned changes. Depth scanning performs a single horizontal line scan above the sample (x or y axis) before moving the electrode one step down (z axis) and repeating the line scan. In hopping mode, a single PAC is performed (z axis) to the sample until a predefined feedback is detected at the probe tip. The electrode is then repositioned horizontally (x or y axis) before the PAC scan is repeated. Similarly, when performed as a 3D scan, a 2D array of PACs is performed over a sample, imaging a volume of space over the sample surface.

In 2010, the Schuhmann group reported the 4D shearforce-based constant distance mode.[67] Using 4D shearforce, multiple constant distance surface images are obtained above the sample. The tip-to-sample distance is determined by the probe shearforce, and the tip is retracted to the desired distance.[67] This generates a comprehensive 4D data set of electrode tip current and shearforce in a volume of space over the sample.

High precision electrochemical characterization of live cells by SECM can often carry significant costs. However low-cost solutions to SECM imaging are viable for basic uses.

In 2017 it was shown that a SECM could be built from low-cost consumer-available parts and 3D printing for $100 (USD, UME probe not included).[72] The low-cost SECM instrument utilized an Arduino UNO microcontroller for position control, signal generation for the potentiostat, and data logging. The potentiostat was custom built and included a summing amplifier, potential control circuitry, and a transimpedance amplifier (Figure 1.4). Off the shelf stepper controllers and NEMA 17 stepper motors were utilized with 500 μm per revolution threaded rods. This provides a 2.5 μm step size for the positioning system. The SECM body was assembled from custom fabricated 3D printed parts. The software was created in Sketch, and incorporated multiple scanning techniques, including line scans and hopping mode. The author has provided models for the 3D printable parts (.stl files), Arduino sketch, bill of materials, and detailed instructions, free of charge in their manuscript Support Information (SI). This provides an excellent low-cost option for individuals and schools interested in SECM based sample analysis.
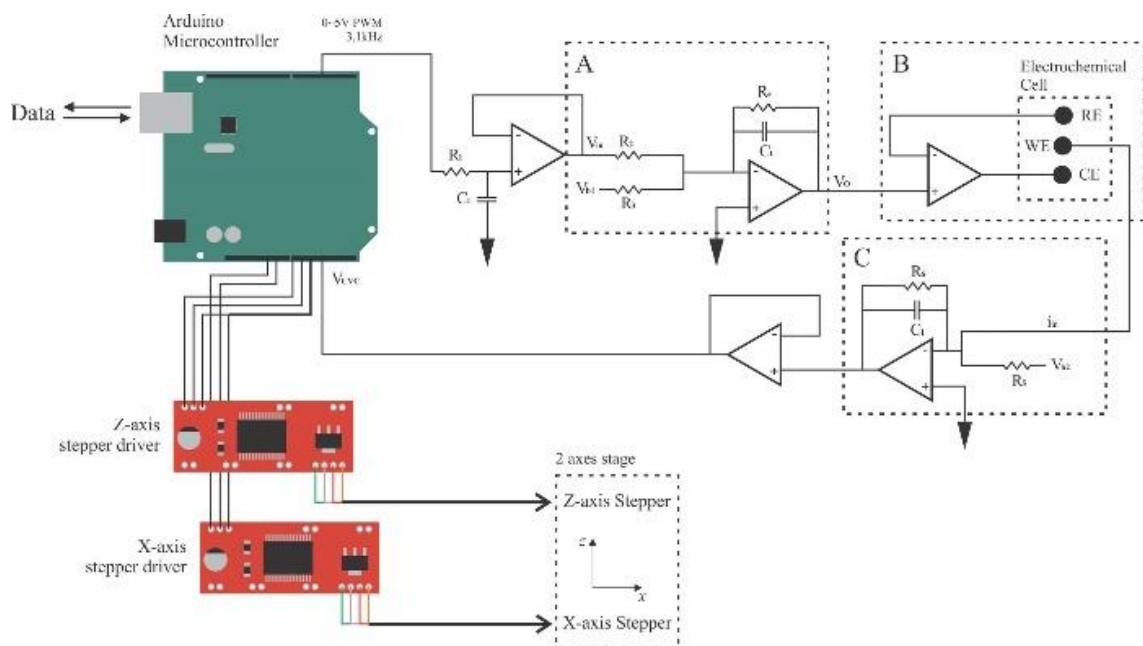
Figure 1.4 - Diagram of electronic components of the EC-SPM setup showing the microcontroller board, custom built potentiostat, and "off-the-shelf" stepper controller boards. Highlighted in the potentiostat circuit diagram are (A) the summing amplifier, (B) potential control circuit and electrochemical cell and (C) transimpedance amplifier. Reprinted (adapted) with permission from (Meloni, G. N., 3D Printed and Microcontrolled: The One Hundred Dollars Scanning Electrochemical Microscope. Anal. Chem. 2017, 89 (17), 8643-8649.). Copyright (2017) American Chemical Society. [72]

1.5   Applications of SECM
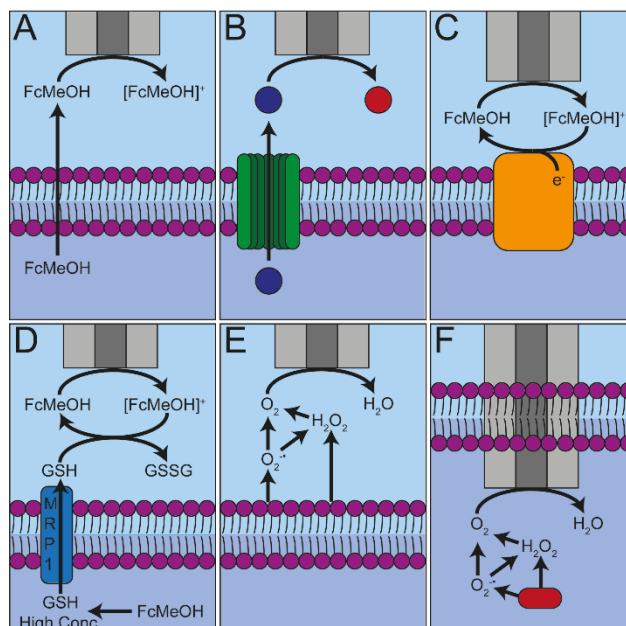
Figure 1.5 – Illustrative SECM applications to live cells. (A) Membrane permeability. (B) Ion channel flux detection. (C) Mediator regeneration at embedded proteins. (D) Mediator regeneration by flux of species from the cell. (E) Extracellular ROS detection. (F) Intracellular ROS detection.

SECM has shown numerous applications to live cells. This section serves as a survey of some of the recent advances in the field of live cell imaging by SECM, incorporating many different techniques and forms of detection. A graphical summary of many of the common applications of SECM is provided in Figure 1.5. This figure includes the detection of membrane permeability performed by monitoring the flux of mediator through the phospholipid membrane (Figure 1.5A). A similar technique involves the rate of flux of species from ion channels, which can be monitored by positioning the electrode over the ion channels (Figure 1.5B). If a sufficiently small electrode is used this can be done over individual ion channels showing hotspots of reactivity. Electrochemically active membrane-embedded proteins can participate in the reaction at the UME either by regenerating mediator species, or through direct reaction with the electrode (Figure 1.5C). The efflux or uptake of chemical species from the cell can also be detected indirectly

through the regeneration of an electrochemical mediating species (Figure 1.5D). A good example of this process is the regeneration of $FcCH_2OH$ from $[FcCH_2OH]^+$ caused by the antioxidant glutathione (GSH). Another common application of SECM is the detection and monitoring of ROS species, either extracellular (Figure 1.5E) or intracellular (Figure 1.5F). Many of these methods of detection will be discussed further in the following chapter subsections.

1.5.1 Reactive Oxygen Species and Reactive Nitrogen Species Detection

Oxidative stress is an area of significant interest,[73] as it is an important marker for carcinogenic cell behavior,[74] in cell signalling and inflammatory response,[75] and has been linked to long-term genetic damage.[76] Excessive concentrations of ROS or RNS can overwhelm a cell's antioxidant defenses, triggering apoptosis.[77] Due to the electrochemical reactivity of both ROS and RNS species, a label-free method of characterization of cell oxidative species production is possible with SECM. This technique provides a non-invasive, highly localized method for performing live cell analysis, allowing for species detection and mapping in the region of interest.[78] Significant success has been seen using this method to map inflammatory ROS production in the extracellular space over live cells.[23, 37, 39] Combination SECM-fluorescence microscopy techniques have also been developed to simultaneously monitor extracellular and intracellular ROS.[50]

SECM has also shown promise for use directly monitoring intracellular ROS species. Examination of intracellular ROS can be performed utilizing small scale (<300 nm diameter) electrodes. Mirkin et al. showed the characterization of internal cell ROS and RNS species using 20, 150, and 300 nm Pt Black electrodes.[79] Production rates of $O_2^{\bullet-}$ and $NO^{\bullet}$ were monitored in two metastatic breast cancer cell lines (MDA-MB-231, and MDA-MB-468) as well as control human breast epithelial cells (MCF-10A). Probe approach curves where tip insertion into the cell interior was examined with all studied electrode sizes. ROS and RNS production was also induced in healthy MCF-10A cells through the introduction of diacylglycerol-lactone (DAG-lactone), increasing the

activation of protein kinase C. Following cell treatment with DAG-lactone and DMSO, no measurable ROS/RNS oxidation was detected for the first 25 min of study (Figure 1.6B). Following this initial period, multiple sharp bursts of oxidative stress were observed electrochemically in the cell interior. This observation is in agreement with previous studies that show DAG-lactone induced PKC activation of 25 min.[80]
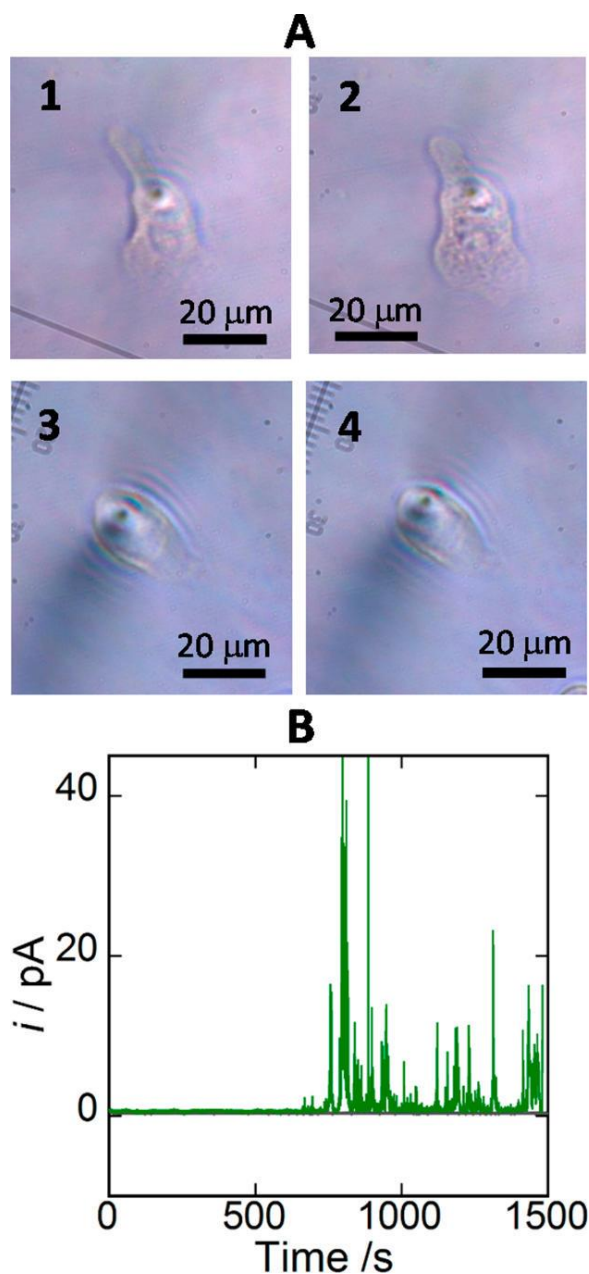
Figure 1.6 - Oxidative stress detection in an MCF-10A cell treated with DAG-lactone. (A) Optical images of two immobilized MCF-10A cells in PBS before (1,3) and 30 min after adding DAG-lactone dissolved in DMSO (2) or an equal volume of DMSO (0.1% v/v) (4). (B) Current recordings at the 40 nm platinized tip inside an MCF-10A cell treated with DAG-lactone (green curve) or with DMSO (black curve). ET = 850 mV. Reprinted (adapted) with permission from (Li, Y.; Hu, K.; Yu, Y.; Rotenberg, S. A.; Amatore, C.; Mirkin, M. V., Direct Electrochemical

Measurements of Reactive Oxygen and Nitrogen Species in Nontransformed and Metastatic Human Breast Cells. J. Am. Chem. Soc. 2017, 139 (37), 13055-13062.). Copyright (2017) American Chemical Society.[79]

1.5.2   Cell Membrane Transport

SECM provides highly localized characterization of electrochemical processes. By positioning an electrode in close proximity to a cell membrane, the transport of electrochemically active biological molecules can be quantified.[52, 81-82] External nontoxic electrochemical mediators can also be added to characterize physical properties of a cell if no intrinsic redox source is present. This can allow for the detection of cell emissions, uptake of resources, and general membrane permeability (Figure 1.7). Imaging can be performed over ion channels,[29, 83] pores,[34, 84] or even used to measure the flux of molecules across the cell membrane.[52, 85]
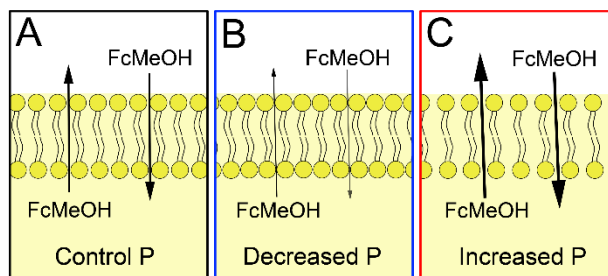
Figure 1.7 - Simplistic representation of (A) control, (B) decreased, and (C) increased membrane permeability to FcCH$_2$OH via passive diffusion.[86]

Membrane permeability is often characterized on live cells by introducing an electrochemical mediator with partial permeability to the cell membrane.[20, 52, 87] Alternatively a mediator that is generally excluded from the cell can be used to determine severe damage to the live cell and operate as a good indicator for cell viability. In 2016, Li et al. showed the membrane permeability characterization of T24 live cells, stressed with Cd^{2+}, with various redox mediators.[88] Hydrophilic redox mediators such as ferrocene carboxylate (FcCOO$^−$), 1,1'-ferrocene dicarboxylate (Fc(COO)$_2{}^{2-}$) and hexaamineruthenium(III) (Ru(NH$_3$)$_6{}^{3+}$) were examined by SECM depth scanning mode

(Figure 1.8A-C). PACs were extracted from these depth scans and membrane permeability was quantified through the aid of membrane permeability FEA simulations (Figure 1.8D-F). The charged nature of these redox mediators normally makes them impermeable to the cell membrane. However, when exposed to sufficient Cd^{2+} (4.4 mM for 1 hr) permeability was induced in the cells exposed to $FcCOO^-$ and $Fc(COO)_2^{2-}$ (Figure 1.8G and H respectively). This concentration also corresponded to the beginning of a decrease in cell population viability, monitored by MTT assay. This indicates significant damage to the cell membrane or nonspecific diffusion channels permitting mediator flux. $Ru(NH_3)_6^{3+}$ was found to show an increase in membrane permeability much earlier, at concentrations as low as 2 mM Cd^{2+} (Figure 1.8I). A time-dependant examination of the hydrophobic mediator ferrocenemethanol ($FcCH_2OH$) was also performed, which is partially permeable to the cell membrane. This mediator showed an initial decrease in membrane permeability between Cd^{2+} injection (25 μM) and 2 hr exposure. Membrane permeability reached a minimum at this time, where it was 1/5 the value observed before injection. Following this, the membrane was observed to increase to double the permeability (4 hr) observed before injection and plateaued at this value (6 hr total study time).
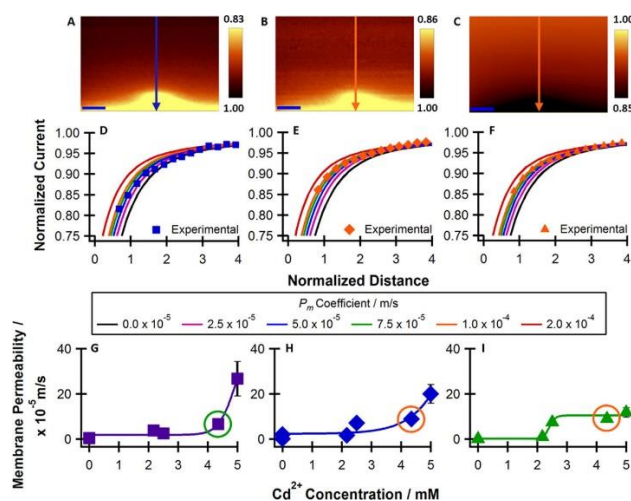
Figure 1.8 - SECM depth scan images of T24 cells treated with 4.4 mM Cd^{2+} for 1 h detecting using: (A) $FcCOO^-$, (B) $Fc(COO)_2^{2-}$ and (C) $Ru(NH_3)_6^{3+}$. The scale bar in each image represents 10 μm. The arrows in (A)−(C) indicate where the cross

section was taken to extract the PACs (D)−(F), respectively. Experimental PACs were overlaid onto simulated curves to quantify membrane permeability. Trends of the average membrane permeability after acute Cd^{2+} concentrations (G)−(I). Reprinted (adapted) with permission from (Li, M. S. M.; Filice, F. P.; Henderson, J. D.; Ding, Z., Probing Cd^{2+}-Stressed Live Cell Membrane Permeability with Various Redox Mediators in Scanning Electrochemical Microscopy. J. Phys. Chem. C 2016, 120 (11), 6094-6103.). Copyright (2016) American Chemical Society. [88]

In 2016, Bondarenko et al. investigated the effects of fixation and induced permeabilization on cells (Figure 1.9A).[89] Fixation is a process that halts biological activity in a cell, while preserving cell proteins, carbohydrates, and other structures by cross linking proteins inside the cell.[89] Cell topography scans (using SECM and AFM) showed an increase in cell height following fixation. Constant height SECM scans with a 25 μm UME were taken over a variety of different cell lines. Cells were patterned into clusters using a polyimide mask, and variation in cell concentration as well as UME scan speed were examined. Investigation of cell clusters using a $FcCH_2OH$ (hydrophobic) electrochemical mediator showed significant change in the current profile dependant on UME tip speed (Figure 1.9B). Scans taken over fixed cells (formaldehyde) showed less drastic change in current profile and a simplified electrochemical signal (Figure 1.9C). UME tip speed had a less significant effect on fixed cells as well. The SECM signal was not drastically affected by the permeabilization (Triton x-100) of the cells (Figure 1.9D). The use of the hydrophilic mediator FcCOOH, showed significant current decrease over both living and fixed cells, and was minimally affected by scan rate (Figure 1.9E and F). Permeabilized cells had a significant decrease in current feedback, similar to that seen with $FcCH_2OH$ (Figure 1.9G). The proteins bovine serum albumin (BSA) and the intracellular melanoma biomarker tyrosinase (TyR) both contain electrochemically active amino acids. These proteins were examined in several cell lines by SECM and immunoassay staining.
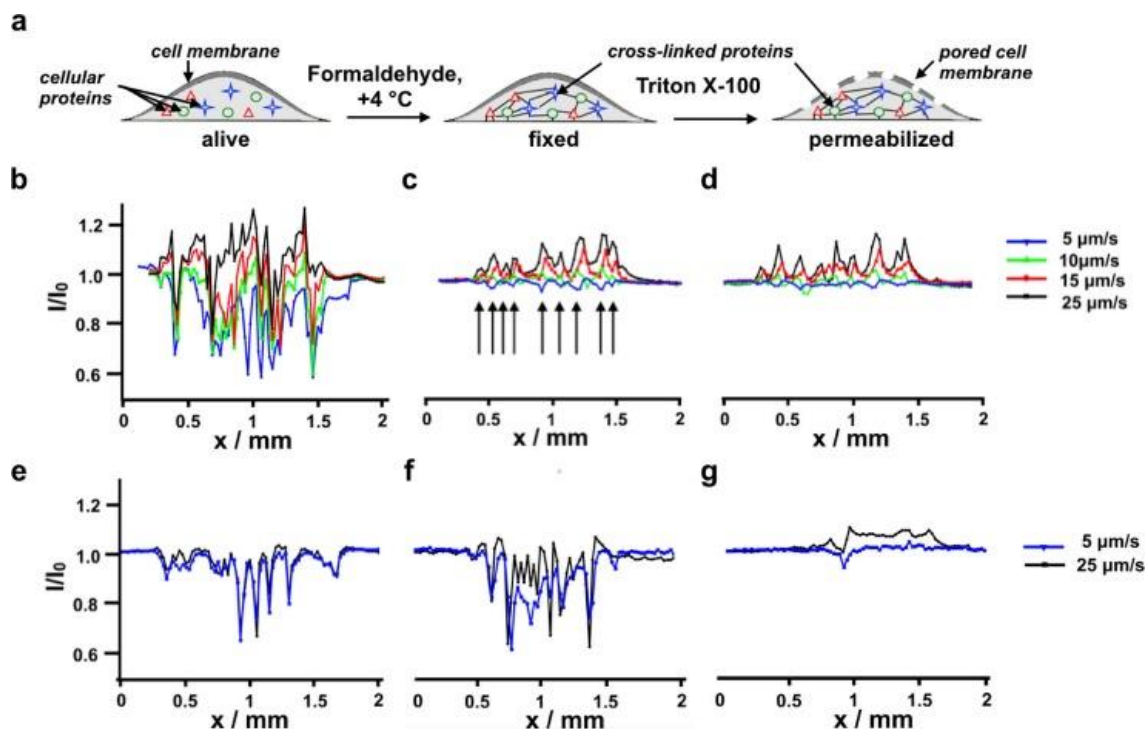
Figure 1.9 - Schematic representation of alive, fixed, and permeabilized cell (a). Influence of the UME translation speed on the SECM response (normalized current) provided by alive (b and e), fixed (c and f), and permeabilized (d and g) adherent WM-115 melanoma cells in the presence of noncharged (FcCH$_2$OH, b−d) and charged (FcCOOH, e−g) redox mediators. Reprinted (adapted) with permission from (Bondarenko, A.; Lin, T. E.; Stupar, P.; Lesch, A.; Cortes-Salazar, F.; Girault, H. H.; Pick, H., Fixation and Permeabilization Approaches for Scanning Electrochemical Microscopy of Living Cells. Anal. Chem. 2016, 88 (23), 11436-11443.). Copyright (2016) American Chemical Society. [89]

In 2017, Soldà et al. showed glucose uptake by single live cells using custom biosensor probes.[90] Biosensor materials included the enzymes glucose oxidase (GOx) or lactate oxidase (LOx), which are sensitive to the presence of glucose and lactate, respectively. Various forms of application were investigated for the fabrication of biosensor electrodes, including cross-linking, electropolymerization, and adsorption by physical and electrostatic interactions. For all biosensors, sensitivity increased with coating thickness up to a maximum of 20 μm in thickness onto 10 μm Pt UMEs. It was also determined that

the electropolymerization methodology produced probes with ~4 times the spatial resolution of the other techniques. This is due to the biosensor material being spatially confined on the Pt disk, while other methods spread across the glass sheathing of the UME in addition to the Pt. Once optimized, these biosensor electrodes were applied to the imaging of MCF10A human breast epithelial cells by SECM (Figure 1.10A). 2D images of these cells were acquired, showing current decrease over the surfaces of the live cells, corresponding to the metabolic consumption of glucose by the cell (Figure 1.10B). SECM voltage switching[91] was employed to compare the topographic and electrochemical response of the glucose to the topography only using $Ru(NH_3)_6{}^{3+}$ as an electrochemical mediator (Figure 1.10C). The average glucose uptake was determined to be 17 ± 3 μM using this method.
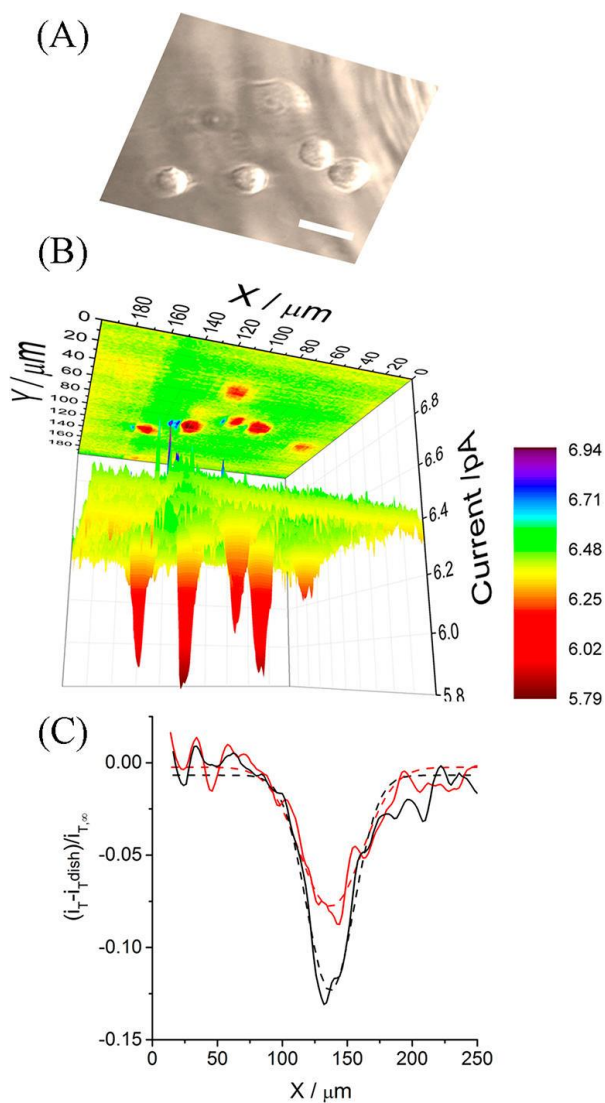
Figure 1.10 - (A) Optical image of the scanned MCF10A cells. Scale bar: 30 µm. (B) Representative SECM image of glucose uptake of several MCF10A cells. SECM experiments were carried out in constant height mode using an electropolymerized 10 µm Pt GOx-UME biosensors in PBS buffer containing 0.1 mM glucose, 10 µM insulin, and 2.5% horse serum. Scan speed 15 µm/s. E = +0.65 V vs Ag/AgCl, 3 M KCl. Comparison between the two profiles: black line contains both functional and topographical contribution, while red line corresponds only to the topographical contribution. The currents were normalized by the respective steady-state bulk current values and subtracted by the normalized currents on the Petri dish. The measurements were performed with the same electropolymerized 10 µm Pt GOx-

based UME biosensors in PBS buffer containing of glucose 0.1 mM, insulin 10 μM, and 500 μM of $[Ru(NH_3)_6]^{3+}$.[Solda, A.; Valenti, G.; Marcaccio, M.; Giorgio, M.; Pelicci, P. G.; Paolucci, F.; Rapino, S., Glucose and Lactate Miniaturized Biosensors for SECM-Based High-Spatial Resolution Analysis: A Comparative Study. ACS Sens. 2017, 2 (9), 1310-1318.] - Published by The Royal Society of Chemistry.[90]

In 2017 Polcari et al. showed the HeLa and HeLa-R MRP1 activity via SECM.[92] Cells were cultured on custom-patterned Zeonor cell culture substrates. Oxygen plasma was used to treat the patterned spots. This promotes attachment, proliferation, and growth of HeLa cells. Optimization of oxygen plasma spot size was performed using 10, 12, 15, 30 and 50 μm spots. Cells cultured with 10-15 μm spots had a globular morphology and unstable attachment. 30 μm spots allowed the cells to adhere with a more triangular shape. A spot size of 50 μm exhibited typical morphology of the HeLa cell line and no detected increase in stress. A dual redox mediator methodology was used, employing both $FcCH_2OH$ and Ruhex mediators. The $FcCH_2OH$ traveled into the cells, inducing an increase in glutathione (GSH) release from HeLa cells from the MRP1 pumps embedded in the membrane. RuHex, however, does not interact with expelled GSH, providing information on topography only. Using a combination of the $FcCH_2OH$ and Ruhex images, as well as an extracted map of normalized tip-to substrate distance, it was possible to deconvolute the heterogeneous rate constant profile (k). The k scan profile provides an indication of the MRP1 functional activity in the imaged cell. The anticancer drug doxorubicin was used to treat HeLa and HeLa-R cells, at 0.05 μM and 0.10 μM (1/10 and 1/5 of the LD_{50}, respectively). Constant height SECM images of these cells were taken, and the k map was calculated (Figure 1.11). Cells were also characterized by western blotting and flow cytometry, allowing for the quantification of the MRP1 expression factor in each of these studied cell populations. HeLa-R populations were observed to have 6.7× the expression of MRP1 relative to HeLa populations. However, a correlation between expression factor and activity was not found.
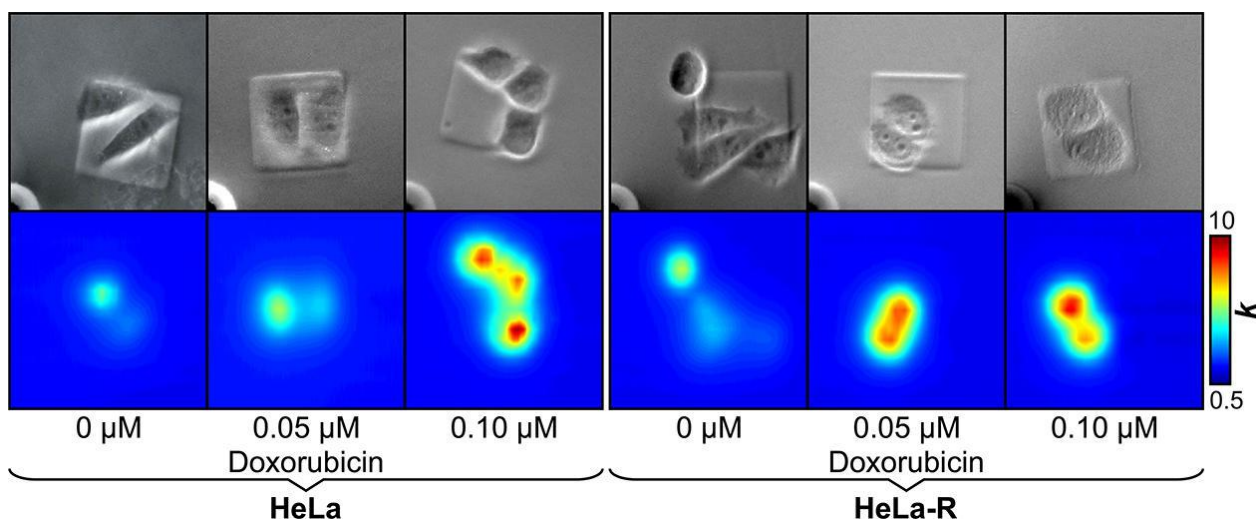
Figure 1.11 - MRP1 functional activity of six different cell populations obtained through a doxorubicin drug challenge. Top panel: Optical micrographs of the cell populations during SECM imaging. Bottom panel: Extracted apparent heterogeneous rate constant profile. A single scale is used for all populations to visualize differences in contrast. Values are presented as 10^{-3} cm s^{-1}. (Imaging conditions: a = 3.5 µm; v =10 µm s^{-1}). Reprinted (adapted) with permission from (Polcari, D.; Hernandez-Castro, J. A.; Li, K.; Geissler, M.; Mauzeroll, J., Determination of the Relationship between Expression and Functional Activity of Multidrug Resistance-Associated Protein 1 using Scanning Electrochemical Microscopy. Anal. Chem. 2017, 89 (17), 8988-8994.). Copyright (2017) American Chemical Society. [92]

1.5.3   Heavy Metal Exposure

Many heavy metals are common in nature or are readily used in industrial processes. Some heavy metals are necessary for humans in trace quantities but toxic at high concentration, while many are strictly toxic if consumed. Heavy metal toxicity has been shown to induce stress in live cells, and in high enough quantities activate apoptotic and necrotic pathways.[93-94] They have been shown to affect membrane fluidity through oxidative damage and lipid peroxidation.[95-96] Changes in membrane permeability induced by oxidative stress is detectable by SECM, making it an excellent tool for localized

analysis of membrane damage.[20, 52] SECM provides a non-destructive, non-invasive method of cell analysis. When applied to the imaging and characterization of live cells, this technique provides a method of repeated rapid characterization of the cell sample. As a result, SECM can be used to image the same cell repeatedly and provide time-dependant analysis of cell homeostasis.

1.5.4   Imaging Live Cells in the Nanoscale

SECM resolution is directly dependant on the size of the electrochemical probe. As a result, there has been a push to fabricate smaller probes since the inception of the technique. A recent review by Bard et al. in Chemical Communications (2018) provides an excellent examination of general SECM techniques and applications at the nanometer scale.[97] This section will focus more exclusively on SECM applications towards single live cell analysis. Note that nanoscale probes are commonly used to electrochemically analyze intracellular processes, due to the less invasive nature of their small size.[31, 35]

Nanoscale imaging comes with many technical challenges. Smaller scale electrodes require positioning closer to the sample of interest to detect electrochemical feedback. As a result, variation in sample height, and sample tilt play a much larger role at smaller scale. Depth-based scanning techniques are a common way to avoid this limitation, however, do not guarantee that collision with the substrate can be avoided. Many combination methods such as 4D shearforce,[67] hopping mode,[71] SECM-SICM,[48] and SECM-AFM[45] show thier strengths when imaging nanoscale. Soft probes have also been fabricated which can be scanned across the sample surface without causing significant damage or stress to the sample or probe.[98-99] Voltage switching methods have been explored for live cell study at the nano scale, allowing for the simultaneous aquisition of SECM data with multiple electrochemically active mediators.[91]

In 2017 Takahashi et al. showed effective use of combination SECM-SICM electrode probes to image single 3T3-L1 fixed cells (Figure 1.12A).[100] Dual conductor SECM-SICM electrode probes were created in-house using a CO_2 laser puller and pyrolytic

carbon deposition method.[48] This fabrication method allows for nanoscale electrodes with small RGs (a=278 nm, RG= 1.1). The SECM probe is used with a FcCH$_2$OH electrochemical mediator to determine the membrane flux of the 3T3-L1 cells (Figure 1.12B). The simultaneous SICM scan is used to determine cell topography (Figure 1.12C). Comparison of the SECM and SICM scans show sites of heterogeneous current response across the cell surface (labelled as white arrows on the images). The first derivative of the topography image was also calculated providing a 2D plot of slope to characterize surface roughness (Figure 1.12D). Regions with a steep vertical slope are observed at the positions of heterogeneous current feedback, indicating a difference in current-distance responses between SECM and SICM based on geometry. The SECM-SICM method was also applied to imaging regions of the cell where intracellular lipid droplets were present. The presence of these lipid droplets yielded no significant difference in the faradaic current when comparing cells with and without the droplets. This indicates that the lipid droplets were not close to the membrane surface but were deeper inside the cell.
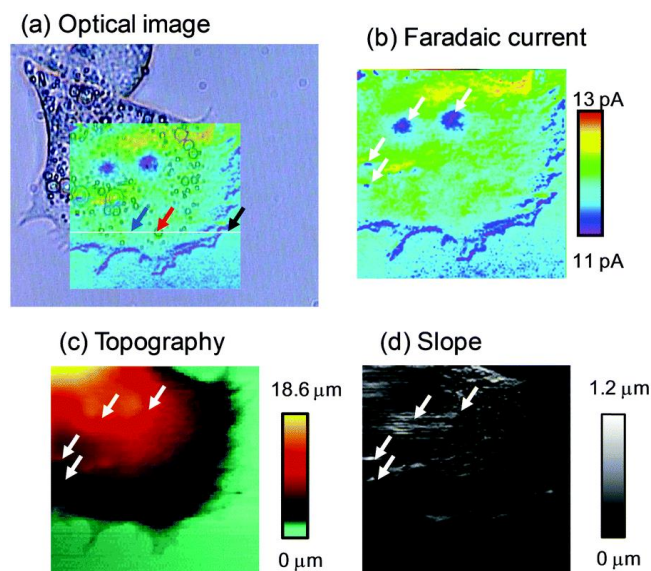
Figure 1.12 - (a) Optical image and SECM–SICM, (b) faradaic current, (c) topography, and (d) slope images of adipocyte in 0.5 mM FcCH$_2$OH + PBS. The SECM electrode radius is 117 nm with RG = 1.1. The SECM and SICM electrodes were held at 500 and 200 mV vs. Ag/AgCl, respectively. Hopping amplitude was 3.0

mm. The surface area of the captured images was 80 mm × 80 mm. [Takahashi, Y.; Ida, H.; Matsumae, Y.; Komaki, H.; Zhou, Y.; Kumatani, A.; Kanzaki, M.; Shiku, H.; Matsue, T., 3D electrochemical and ion current imaging using scanning electrochemical-scanning ion conductance microscopy. Phys. Chem. Chem. Phys. 2017, 19 (39), 26728-26733.] - Published by the PCCP Owner Societies. [100]

In 2018, Shen et al. showed SECM imaging of neurotransmission at the synaptic cleft between living *Aplysia* neurons.[101] Imaging within the synaptic cleft has been difficult in the past due to its extremely small size (300 nm × <100 nm). A 30 nm diameter nanoITES pipette electrode was used to selectively image acetylcholine release. The direct measurement of acetylcholine in the synaptic cleft reduces the dilution of the neurotransmitter, as it diffuses away from the site of release into the extracellular medium. This increases the performance of the low concentration electrochemical measurement. Synaptic neurotransmitter release was composed of singlet, doublet and multiplet profiles (Figure 1.13A-C). The singlet profile was observed 50% of the time with lower frequency, for doublet and multiplet. The frequency of synaptic acetylcholine release was consistent with measured norepinephrine release (measured by carbon nanofiber electrode). The average number of acetylcholine molecules released for the doublet was double that observed for the singlet. Quantitative analysis of the amperometric peak half widths and number of molecules suggests the release of multiple vesicles, or partial release of a single vesicle (Figure 1.13D and E).
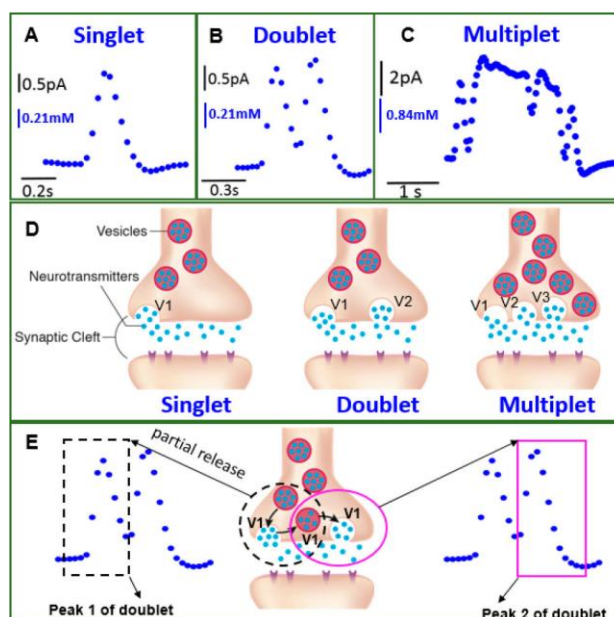
Figure 1.13 - Single synaptic cholinergic neurotransmission measured in situ. (A−C) Current−time trace (amperometry) representing synaptic transmitter concentration and release dynamics simultaneously, where diverse cholinergic concentration dynamics were observed consisted of singlet (panel A), doublet (panel B) and multiplet (panel C). Single current (concentration) maxima occur during singlet release (50% occurrence frequency out of 16 events total); a second current maximum occurs before the first current peak decreases to the base value for the doublet events (∼30% occurrence frequency); multiple concentration peaks (more than two) were observed for multiplet with lower occurrence frequency (∼20%). **(D)** Proposed mechanism on variation in synaptic transmitter release dynamics. Neurotransmitter is released into the synaptic cleft from a single vesicle (Left). Neurotransmitter is released into the synaptic cleft from two vesicles, V1 and V2, simultaneously (Middle) or multiple vesicles simultaneously, which are going through either different stages of exocytosis as shown here, or similar stages of exocytosis (Right). **(E)** An alternative mechanism is possible for explaining doublets and multiplets based on the phenomenon of partial release. A vesicle goes through partial release twice, generating a doublet (Middle); the two individual peaks (Peak 1 and Peak 2) correspond to each partial release event. Reprinted (adapted) with

permission from (Shen, M.; Qu, Z.; DesLaurier, J.; Welle, T. M.; Sweedler, J. V.; Chen, R., Single Synaptic Observation of Cholinergic Neurotransmission on Living Neurons: Concentration and Dynamics. J. Am. Chem. Soc. 2018, 140 (25), 7764-7768.). Copyright (2018) American Chemical Society. [101]

In 2017, Page et al. characterized the uptake of $[Ru(NH_3)_6]^{3+}$ by live *Zea mays* root hair cells using SECM-SICM.[70] SECM-SICM dual electrode probes were custom fabricated with a total probe diameter of 500 nm, composed of a SICM nanopipette and pyrolytically deposited carbon SECM electrode. The SICM nanopipette was filled with a 10 mM $[Ru(NH_3)_6]^{3+}$ (RuHex) solution, with no RuHex in bulk solution. This provided a localized source of RuHex, which was electrochemically reduced at the carbon electrode tip. The concentration at the nanopipette orifice was 2 mM. The SICM electrode measures resistance between itself and an Ag/AgCl electrode in bulk solution providing topographic information and does not react with the RuHex. This imaging methodology was validated experimentally on root cells as well as simulated using the FEM method. A single *Zea mays* root hair cell was imaged at two locations, the cell tip and body (Figure A). Variation in cell height was observed at the two locations on the cell (Figure B). Monitoring the uptake of RuHex by the live cell shows faster uptake at the root hair tip, with uptake rates of 0.27 ± 0.05 cm s^{-1} for the cell tip and 0.22 ± 0.05 cm s^{-1} for the cell body being observed (Figure C and D).
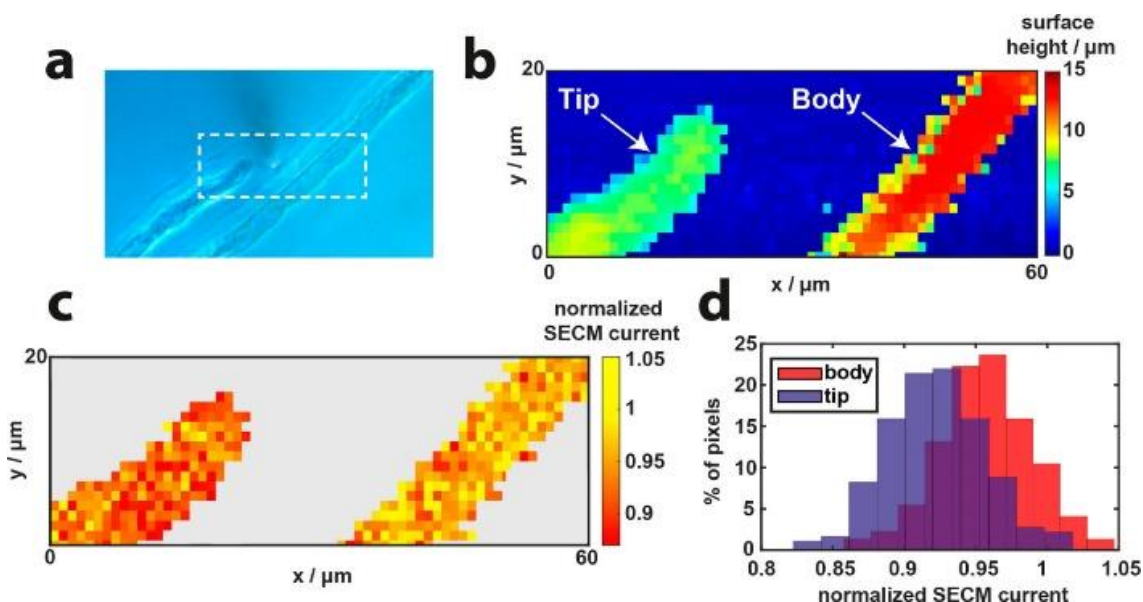
Figure 1.14 - SICM-SECM topographical and [Ru(NH$_3$)$_6$]$^{3+}$ uptake mapping of two regions of a single *Zea mays* root hair cell. (a) Optical image of the scanned root hair cell; scan area denoted by the dashed rectangle. (b) Substrate topography extracted from the z-position at the point of closest approach from the SICM channel. (c) Normalized SECM current map showing a clear difference in uptake between the root hair cell body (higher current, lower uptake) and the root hair cell tip (lower current, higher uptake). "Normalized current" is the ratio of the [Ru(NH$_3$)$_6$]$^{3+}$ reduction current at the point of closest approach to the same reduction current in bulk. (d) Histograms of the normalized SECM current across the two different regions of the root hair cell, "tip" and "body" (see part b). Reprinted (adapted) with permission from (Page, A.; Kang, M.; Armitstead, A.; Perry, D.; Unwin, P. R., Quantitative Visualization of Molecular Delivery and Uptake at Living Cells with Self-Referencing Scanning Ion Conductance Microscopy-Scanning Electrochemical Microscopy. Anal. Chem. 2017, 89 (5), 3021-3028.). Copyright (2017) American Chemical Society.[70]

1.6 Scope of Dissertation

The scope of this dissertation focuses on the investigation of cell membrane response to toxic heavy metals in T24 human bladder cancer cells. This investigation is performed using SECM coupled with FEM simulations.

Chapter 2 focuses on the effects of Cd^{2+} on single live T24 cell membrane permeability. The experimental depth scan imaging of the single live cells was coupled with, full 3D finite element method (FEM) simulations for the first time. This allowed for the extraction and fitting of experimental PACs at any location across the cell surface to quantify cell membrane permeability. Previous 2D axially symmetric models were limited to symmetric samples and PAC generation directly over the cell center. As a result, these previous models failed to take advantage of the large data sets provided by the numerous multidimensional experimental scanning methods, such as depth scan. Creation and validation of a full 3D model for SECM analysis of single live cell membrane permeability was explored in this chapter. Cells were incubated with different concentrations of Cd^{2+}, and the resulting membrane permeability change was determined.

In Chapter 3, SECM and 3D FEM simulations were utilized to examine the membrane response of T24 cells following exposure to toxic dichromate (Cr (VI)). Two electrochemical mediators were examined in this chapter, the membrane permeable $FcCH_2OH$ and the membrane impermeable $FcCOO^-$. With $FcCH_2OH$ as the SECM mediator, Cr (VI) exposure was observed to induce three distinct concentration dependant membrane permeability regions. Performing the same membrane permeability characterization with the impermeable $FcCOO^-$ mediator, incubation with high concentrations of Cr (VI) induced permeability for the charged $FcCOO^-$ to the cell membrane. The study in this chapter was also coupled with a MTT cell viability assay with a related trend to the membrane permeability response with $FcCH_2OH$ as the SECM mediator. Quantification of membrane permeability incorporated a simulation model geometry with a more accurate cell geometry. Optimizations were also made to the solution domain geometry and a symmetry plane was incorporated to reduce resource demand and compute times.

In Chapter 4, Cr (VI) induced cell stress with lower chronic concentrations was examined for longer durations. Three Cr (VI) concentrations (2, 5 and 10 µM) were examined, yielding similar response curve shapes over the study period. The time required to observe the membrane permeability response was shifted in a concentration-dependant fashion with higher concentrations of Cr (VI) exhibiting much faster response. The 2 and 5 µM tests spanned 5 days of incubation, after which SECM analysis was no longer possible due to significant population decrease, where the 10 µM sample reached this state following only 3 days of incubation. MTT viability studies were performed, providing complimentary analysis of overall health and wellness of the cell populations under study. A resistance to the external $K_2Cr_2O_7$ stressor was observed after 1 day of incubation. However, cells exhibited a strong drop in viability following 2-3 days incubation.

In Chapter 5, the membrane response of single live cells to the trace essential heavy metal Cr (III) was successfully interrogated using both $FcCH_2OH$ and $FcCOO^-$ as SECM mediators. Full 3D FEM simulations were computed to allow for the quantification of cell membrane permeability by SECM. Using the 3D model of the cell system, full SECM depth scans were simulated. The simulated and experimentally acquired depth scan images allow for the extraction of electrode PACs at any location across the cell, for rapid membrane permeability quantification. With the membrane permeable $FcCH_2OH$, incubation three distinct trends were observed in membrane response. The $FcCOO^-$ mediator was initially impermeable, but similarly exhibited strong increases in membrane permeability when subjected to 7500 µM $CrCl_3$ for 1 hr. This study was also coupled with a MTT cell viability test, which showed a gradual decrease in cell viability once 500 µM of Cd (III) was exceeded.

In Chapter 6, the analysis of complex systems of cell clusters in close proximity was carried out by means of SECM image stack 3D scanning mode with 10 µm and 4.4 µm diameter UMEs. Tailored 3D model geometries were created to allow for the simulation of these cell maps. Full 3D mapping was performed using the simulation model to compliment the 3D dataset acquired experimentally. Experimental surface maps of pairs

of double cells were acquired with both 10 μm and 4.4 μm UMEs, and them modelled to generate complimentary theoretical maps. The simulations with tailored full 3D models were capable of providing a strong theoretical fit to the experimental results when the geometry of both adjacent cells was considered. Probe size-dependant limits of cell proximity for SECM characterization were theoretically determined using this model.

Chapter 7 describes the nanoscale SECM imaging of a single live cell, with a laser-pulled quartz sheathed electrode having a 130 nm radius Pt disk. A single live cell was imaged using the membrane impermeable $Ru(NH_3)_6^{3+}$, and membrane permeable $FcCH_2OH$ mediators in rapid succession. Replicating accurate sample geometry in the theoretical model becomes much more important as electrode size decreases. Cell topography was accurately characterized, and a tailored 3D model of the single live cell was created. Using this model, membrane permeability quantification was performed.

Finally, Chapter 8 provides a summary of the collective work, as well as discussing future works to be considered.

1.7   References

1. Bard, A. J.; Faulkner, L. R., *Electrochemical Methods: Fundamentals and Applications, 2nd Edition*. 2 ed.; John Wiley & Sons, Inc.: 2001, p 864.
2. Bard, A. J.; Mirkin, M. V., *Scanning Electrochemical Microscopy*. 2 ed.; CRC Press: 2012, p 670.
3. Zoski, C. G., Review—Advances in Scanning Electrochemical Microscopy (Secm). *J. Electrochem. Soc.* **2015,** *163* (4), H3088-H3100.
4. Engstrom, R. C.; Weber, M.; Wunder, D. J.; Burgess, R.; Winquist, S., Measurements within the Diffusion Layer Using a Microelectrode Probe. *Anal. Chem.* **2002,** *58* (4), 844-848.
5. Bard, A. J.; Denuault, G.; Lee, C.; Mandler, D.; Wipf, D. O., Scanning Electrochemical Microscopy - a New Technique for the Characterization and Modification of Surfaces. *Acc. Chem. Res.* **2002,** *23* (11), 357-363.
6. Bard, A. J.; Fan, F. R. F.; Kwak, J.; Lev, O., Scanning Electrochemical Microscopy. Introduction and Principles. *Anal. Chem.* **2002,** *61* (2), 132-138.
7. Polcari, D.; Dauphin-Ducharme, P.; Mauzeroll, J., Scanning Electrochemical Microscopy: A Comprehensive Review of Experimental Parameters from 1989 to 2015. *Chem. Rev.* **2016,** *116* (22), 13234-13278.
8. Ding, Z.; Quinn, B. M.; Bard, A. J., Kinetics of Heterogeneous Electron Transfer at Liquid/Liquid Interfaces as Studied by Secm. *J. Phys. Chem. B* **2001,** *105* (27), 6367-6374.

9. Wittstock, G.; Burchardt, M.; Pust, S. E.; Shen, Y.; Zhao, C., Scanning Electrochemical Microscopy for Direct Imaging of Reaction Rates. *Angew. Chem. Int. Ed. Engl.* **2007,** *46* (10), 1584-617.

10. Nowierski, C.; Noël, J. J.; Shoesmith, D. W.; Ding, Z., Correlating Surface Microstructures with Reactivity on Commercially Pure Zirconium Using Scanning Electrochemical Microscopy and Scanning Electron Microscopy. *Electrochem. Commun.* **2009,** *11* (6), 1234-1236.

11. Yin, Y.; Niu, L.; Lu, M.; Guo, W.; Chen, S., In Situ Characterization of Localized Corrosion of Stainless Steel by Scanning Electrochemical Microscope. *Appl. Surf. Sci.* **2009,** *255* (22), 9193-9199.

12. Combellas, C.; Fuchs, A.; Kanoufi, F., Scanning Electrochemical Microscopy with a Band Microelectrode: Theory and Application. *Anal. Chem.* **2004,** *76* (13), 3612-8.

13. Tang, J.; Zheng, J.-J.; Yu, Y.-T.; Chen, l.; Zhang, N.; Tian, Z., Selective Etching of Zno Films on an Ito Substrate Using a Scanning Electrochemical Microscope. *Electrochim. Acta* **2012,** *83*, 247-252.

14. Eifert, A.; Mizaikoff, B.; Kranz, C., Advanced Fabrication Process for Combined Atomic Force-Scanning Electrochemical Microscopy (Afm-Secm) Probes. *Micron* **2015,** *68*, 27-35.

15. Amemiya, S.; Guo, J.; Xiong, H.; Gross, D. A., Biological Applications of Scanning Electrochemical Microscopy: Chemical Imaging of Single Living Cells and Beyond. *Anal. Bioanal. Chem.* **2006,** *386* (3), 458-71.

16. Li, M. S.; Filice, F. P.; Ding, Z., A Time Course Study of Cadmium Effect on Membrane Permeability of Single Human Bladder Cancer Cells Using Scanning Electrochemical Microscopy. *J. Inorg. Biochem.* **2014,** *136*, 177-83.

17. Kuss, S.; Polcari, D.; Geissler, M.; Brassard, D.; Mauzeroll, J., Assessment of Multidrug Resistance on Cell Coculture Patterns Using Scanning Electrochemical Microscopy. *Proc. Nat. Acad. Sci. U.S.A.* **2013,** *110* (23), 9249-54.

18. Kuss, S.; Cornut, R.; Beaulieu, I.; Mezour, M. A.; Annabi, B.; Mauzeroll, J., Assessing Multidrug Resistance Protein 1-Mediated Function in Cancer Cell Multidrug Resistance by Scanning Electrochemical Microscopy and Flow Cytometry. *Bioelectrochemistry* **2011,** *82* (1), 29-37.

19. Beaulieu, I.; Kuss, S.; Mauzeroll, J.; Geissler, M., Biological Scanning Electrochemical Microscopy and Its Application to Live Cell Studies. *Anal. Chem.* **2011,** *83* (5), 1485-92.

20. Koley, D.; Bard, A. J., Triton X-100 Concentration Effects on Membrane Permeability of a Single Hela Cell by Scanning Electrochemical Microscopy (Secm). *Proc. Nat. Acad. Sci. U.S.A.* **2010,** *107* (39), 16783-7.

21. Liu, B.; Rotenberg, S. A.; Mirkin, M. V., Scanning Electrochemical Microscopy of Living Cells: Different Redox Activities of Nonmetastatic and Metastatic Human Breast Cells. *Proc. Nat. Acad. Sci. U.S.A.* **2000,** *97* (18), 9855-60.

22. Bard, A. J.; Li, X.; Zhan, W., Chemically Imaging Living Cells by Scanning Electrochemical Microscopy. *Biosens. Bioelectron.* **2006,** *22* (4), 461-72.

23. Zhao, X.; Diakowski, P. M.; Ding, Z., Deconvoluting Topography and Spatial Physiological Activity of Live Macrophage Cells by Scanning Electrochemical Microscopy in Constant-Distance Mode. *Anal. Chem.* **2010,** *82* (20), 8371-3.

24. Lee, C.; Kwak, J.; Bard, A. J., Application of Scanning Electrochemical Microscopy to Biological Samples. *Proc. Nat. Acad. Sci. U.S.A.* **1990,** *87* (5), 1740-3.

25. Nioradze, N.; Kim, J.; Amemiya, S., Quasi-Steady-State Voltammetry of Rapid Electron Transfer Reactions at the Macroscopic Substrate of the Scanning Electrochemical Microscope. *Anal. Chem.* **2011,** *83* (3), 828-35.

26. Cannan, S.; Cervera, J.; Steliaros, R. J.; Bitziou, E.; Whitworth, A. L.; Unwin, P. R., Scanning Electrochemical Microscopy (Secm) Studies of Catalytic Ec' Processes: Theory and Experiment for Feedback, Generation/Collection and Imaging Measurements. *Phys. Chem. Chem. Phys.* **2011,** *13* (12), 5403-12.

27. Matrab, T.; Hauquier, F.; Combellas, C.; Kanoufi, F., Scanning Electrochemical [Corrected] Microscopy Investigation of Molecular Transport [Corrected]within Polymer Brushes. *Chemphyschem* **2010,** *11* (3), 670-82.

28. Koley, D.; Bard, A. J., Inhibition of the Mrp1-Mediated Transport of the Menadione-Glutathione Conjugate (Thiodione) in Hela Cells as Studied by Secm. *Proc. Nat. Acad. Sci. U.S.A.* **2012,** *109* (29), 11522-7.

29. Kim, J.; Izadyar, A.; Shen, M.; Ishimatsu, R.; Amemiya, S., Ion Permeability of the Nuclear Pore Complex and Ion-Induced Macromolecular Permeation as Studied by Scanning Electrochemical and Fluorescence Microscopy. *Anal. Chem.* **2014,** *86* (4), 2090-8.

30. Bergner, S.; Wegener, J.; Matysik, F. M., Simultaneous Imaging and Chemical Attack of a Single Living Cell within a Confluent Cell Monolayer by Means of Scanning Electrochemical Microscopy. *Anal. Chem.* **2011,** *83* (1), 169-74.

31. Sun, P.; Laforge, F. O.; Abeyweera, T. P.; Rotenberg, S. A.; Carpino, J.; Mirkin, M. V., Nanoelectrochemistry of Mammalian Cells. *Proc. Nat. Acad. Sci. U.S.A.* **2008,** *105* (2), 443-8.

32. Liebetrau, J. M.; Miller, H. M.; Baur, J. E.; Takacs, S. A.; Anupunpisit, V.; Garris, P. A.; Wipf, D. O., Scanning Electrochemical Microscopy of Model Neurons: Imaging and Real-Time Detection of Morphological Changes. *Anal. Chem.* **2003,** *75* (3), 563-571.

33. Kurulugama, R. T.; Wipf, D. O.; Takacs, S. A.; Pongmayteegul, S.; Garris, P. A.; Baur, J. E., Scanning Electrochemical Microscopy of Model Neurons: Constant Distance Imaging. *Anal. Chem.* **2005,** *77* (4), 1111-7.

34. Zhu, R.; Macfie, S. M.; Ding, Z., Cadmium-Induced Plant Stress Investigated by Scanning Electrochemical Microscopy. *J. Exp. Bot.* **2005,** *56* (421), 2831-8.

35. Wang, Y.; Noel, J. M.; Velmurugan, J.; Nogala, W.; Mirkin, M. V.; Lu, C.; Guille Collignon, M.; Lemaitre, F.; Amatore, C., Nanoelectrodes for Determination of Reactive Oxygen and Nitrogen Species inside Murine Macrophages. *Proc. Nat. Acad. Sci. U.S.A.* **2012,** *109* (29), 11534-9.

36. Zhao, X.; Petersen, N. O.; Ding, Z., Comparison Study of Live Cells by Atomic Force Microscopy, Confocal Microscopy, and Scanning Electrochemical Microscopy. *Can. J. Chem.* **2007,** *85* (3), 175-183.

37.   Zhang, M. M.; Long, Y. T.; Ding, Z., Cisplatin Effects on Evolution of Reactive Oxygen Species from Single Human Bladder Cancer Cells Investigated by Scanning Electrochemical Microscopy. *J. Inorg. Biochem.* **2012,** *108*, 115-22.

38.   Zhao, X.; Zhang, M.; Long, Y.; Ding, Z., Redox Reactions of Reactive Oxygen Species in Aqueous Solutions as the Probe for Scanning Electrochemical Microscopy of Single Live T24 Cells. *Can. J. Chem.* **2010,** *88* (6), 569-576.

39.   Zhao, X.; Lam, S.; Jass, J.; Ding, Z., Scanning Electrochemical Microscopy of Single Human Urinary Bladder Cells Using Reactive Oxygen Species as Probe of Inflammatory Response. *Electrochem. Commun.* **2010,** *12* (6), 773-776.

40.   Zhan, D.; Li, X.; Nepomnyashchii, A. B.; Alpuche-Aviles, M. A.; Fan, F.-R. F.; Bard, A. J., Characterization of Ag+ Toxicity on Living Fibroblast Cells by the Ferrocenemethanol and Oxygen Response with the Scanning Electrochemical Microscope. *J. Electroanal. Chem.* **2013,** *688*, 61-68.

41.   Li, X.; Bard, A. J., Scanning Electrochemical Microscopy of Hela Cells – Effects of Ferrocene Methanol and Silver Ion. *J. Electroanal. Chem.* **2009,** *628* (1-2), 35-42.

42.   Cai, C.; Liu, B.; Mirkin, M. V.; Frank, H. A.; Rusling, J. F., Scanning Electrochemical Microscopy of Living Cells. 3.Rhodobactersphaeroides. *Anal. Chem.* **2002,** *74* (1), 114-119.

43.   Feng, W.; Rotenberg, S. A.; Mirkin, M. V., Scanning Electrochemical Microscopy of Living Cells. 5. Imaging of Fields of Normal and Metastatic Human Breast Cells. *Anal. Chem.* **2003,** *75* (16), 4148-54.

44.   Liu, B.; Cheng, W.; Rotenberg, S. A.; Mirkin, M. V., Scanning Electrochemical Microscopy of Living Cells. *J. Electroanal. Chem.* **2001,** *500* (1-2), 590-597.

45.   Casero, E.; Vazquez, L.; Parra-Alfambra, A. M.; Lorenzo, E., Afm, Secm and Qcm as Useful Analytical Tools in the Characterization of Enzyme-Based Bioanalytical Platforms. *Analyst* **2010,** *135* (8), 1878-903.

46.   Zu, Y. B.; Ding, Z. F.; Zhou, J. F.; Lee, Y. M.; Bard, A. J., Scanning Optical Microscopy with an Electrogenerated Chemiluminescent Light Source at a Nanometer Tip. *Anal. Chem.* **2001,** *73* (10), 2153-2156.

47.   Lee, Y.; Ding, Z.; Bard, A. J., Combined Scanning Electrochemical/Optical Microscopy with Shear Force and Current Feedback. *Anal. Chem.* **2002,** *74* (15), 3634-43.

48.   Takahashi, Y.; Shevchuk, A. I.; Novak, P.; Zhang, Y.; Ebejer, N.; Macpherson, J. V.; Unwin, P. R.; Pollard, A. J.; Roy, D.; Clifford, C. A.; Shiku, H.; Matsue, T.; Klenerman, D.; Korchev, Y. E., Multifunctional Nanoprobes for Nanoscale Chemical Imaging and Localized Chemical Delivery at Surfaces and Interfaces. *Angew. Chem. Int. Ed. Engl.* **2011,** *50* (41), 9638-42.

49.   Schorr, N. B.; Jiang, A. G.; Rodriguez-Lopez, J., Probing Graphene Interfacial Reactivity Via Simultaneous and Colocalized Raman-Scanning Electrochemical Microscopy Imaging and Interrogation. *Anal. Chem.* **2018,** *90* (13), 7848-7854.

50.   Salamifar, S. E.; Lai, R. Y., Use of Combined Scanning Electrochemical and Fluorescence Microscopy for Detection of Reactive Oxygen Species in Prostate Cancer Cells. *Anal. Chem.* **2013,** *85* (20), 9417-21.

51. Momotenko, D.; Cortes-Salazar, F.; Lesch, A.; Wittstock, G.; Girault, H. H., Microfluidic Push-Pull Probe for Scanning Electrochemical Microscopy. *Anal. Chem.* **2011,** *83* (13), 5275-82.

52. Guo, J.; Amemiya, S., Permeability of the Nuclear Envelope at Isolated Xenopus Oocyte Nuclei Studied by Scanning Electrochemical Microscopy. *Anal. Chem.* **2005,** *77* (7), 2147-56.

53. Filice, F. P.; Li, M. S.; Henderson, J. D.; Ding, Z., Mapping Cd(2)(+)-Induced Membrane Permeability Changes of Single Live Cells by Means of Scanning Electrochemical Microscopy. *Anal. Chim. Acta* **2016,** *908*, 85-94.

54. Lee, Y.; Amemiya, S.; Bard, A. J., Scanning Electrochemical Microscopy. 41. Theory and Characterization of Ring Electrodes. *Anal. Chem.* **2001,** *73* (10), 2261-7.

55. Sklyar, O.; Kueng, A.; Kranz, C.; Mizaikoff, B.; Lugstein, A.; Bertagnolli, E.; Wittstock, G., Numerical Simulation of Scanning Electrochemical Microscopy Experiments with Frame-Shaped Integrated Atomic Force Microscopy--Secm Probes Using the Boundary Element Method. *Anal. Chem.* **2005,** *77* (3), 764-71.

56. Amemiya, S.; Bard, A. J.; Fan, F. R. F.; Mirkin, M. V.; Unwin, P. R., Scanning Electrochemical Microscopy. In *Annu. Rev. Anal. Chem.*, 2008; Vol. 1, pp 95-131.

57. Zhu, R.; Ding, Z., Enhancing Image Quality of Scanning Electrochemical Microscopy by Improved Probe Fabrication and Displacement. *Can. J. Chem.* **2005,** *83* (10), 1779-1791.

58. Wei, C.; Bard, A. J., Scanning Electrochemical Microscopy Xxix . In Situ Monitoring of Thickness Changes of Thin Films on Electrodes *J. Electrochem. Soc.* **1995,** *142* (8), 2523-2527.

59. Danis, L.; Polcari, D.; Kwan, A.; Gateman, S. M.; Mauzeroll, J., Fabrication of Carbon, Gold, Platinum, Silver, and Mercury Ultramicroelectrodes with Controlled Geometry. *Anal. Chem.* **2015,** *87* (5), 2565-9.

60. Actis, P.; Tokar, S.; Clausmeyer, J.; Babakinejad, B.; Mikhaleva, S.; Cornut, R.; Takahashi, Y.; Lopez Cordoba, A.; Novak, P.; Shevchuck, A. I.; Dougan, J. A.; Kazarian, S. G.; Gorelkin, P. V.; Erofeev, A. S.; Yaminsky, I. V.; Unwin, P. R.; Schuhmann, W.; Klenerman, D.; Rusakov, D. A.; Sviderskaya, E. V.; Korchev, Y. E., Electrochemical Nanoprobes for Single-Cell Analysis. *ACS Nano* **2014,** *8* (1), 875-84.

61. McKelvey, K.; Nadappuram, B. P.; Actis, P.; Takahashi, Y.; Korchev, Y. E.; Matsue, T.; Robinson, C.; Unwin, P. R., Fabrication, Characterization, and Functionalization of Dual Carbon Electrodes as Probes for Scanning Electrochemical Microscopy (Secm). *Anal. Chem.* **2013,** *85* (15), 7519-26.

62. Danis, L.; Snowden, M. E.; Tefashe, U. M.; Heinemann, C. N.; Mauzeroll, J., Development of Nano-Disc Electrodes for Application as Shear Force Sensitive Electrochemical Probes. *Electrochim. Acta* **2014,** *136*, 121-129.

63. Polcari, D.; Kwan, A.; Van Horn, M. R.; Danis, L.; Pollegioni, L.; Ruthazer, E. S.; Mauzeroll, J., Disk-Shaped Amperometric Enzymatic Biosensor for in Vivo Detection of D-Serine. *Anal. Chem.* **2014,** *86* (7), 3501-7.

64. Page, A.; Perry, D.; Unwin, P. R., Multifunctional Scanning Ion Conductance Microscopy. *Proc. Math. Phys. Eng. Sci.* **2017,** *473* (2200), 20160889.

65. Diakowski, P. M.; Ding, Z. F., Interrogation of Living Cells Using Alternating Current Scanning Electrochemical Microscopy (Ac-Secm). *Phys. Chem. Chem. Phys.* **2007,** *9* (45), 5966-5974.

66. Macpherson, J. V.; Unwin, P. R.; Hillier, A. C.; Bard, A. J., In-Situ Imaging of Ionic Crystal Dissolution Using an Integrated Electrochemical/Afm Probe. *J. Am. Chem. Soc.* **1996,** *118* (27), 6445-6452.

67. Nebel, M.; Eckhard, K.; Erichsen, T.; Schulte, A.; Schuhmann, W., 4d Shearforce-Based Constant-Distance Mode Scanning Electrochemical Microscopy. *Anal. Chem.* **2010,** *82* (18), 7842-8.

68. Hengstenberg, A.; Blochl, A.; Dietzel, I. D.; Schuhmann, W., Spatially Resolved Detection of Neurotransmitter Secretion from Individual Cells by Means of Scanning Electrochemical Microscopy. *Angew. Chem. Int. Ed. Engl.* **2001,** *40* (5), 905-908.

69. Fan, F. R.; Bard, A. J., Imaging of Biological Macromolecules on Mica in Humid Air by Scanning Electrochemical Microscopy. *Proc. Nat. Acad. Sci. U.S.A.* **1999,** *96* (25), 14222-7.

70. Page, A.; Kang, M.; Armitstead, A.; Perry, D.; Unwin, P. R., Quantitative Visualization of Molecular Delivery and Uptake at Living Cells with Self-Referencing Scanning Ion Conductance Microscopy-Scanning Electrochemical Microscopy. *Anal. Chem.* **2017,** *89* (5), 3021-3028.

71. Lazenby, R. A.; McKelvey, K.; Unwin, P. R., Hopping Intermittent Contact-Scanning Electrochemical Microscopy (Hic-Secm): Visualizing Interfacial Reactions and Fluxes from Surfaces to Bulk Solution. *Anal. Chem.* **2013,** *85* (5), 2937-44.

72. Meloni, G. N., 3d Printed and Microcontrolled: The One Hundred Dollars Scanning Electrochemical Microscope. *Anal. Chem.* **2017,** *89* (17), 8643-8649.

73. Di Meo, S.; Reed, T. T.; Venditti, P.; Victor, V. M., Role of Ros and Rns Sources in Physiological and Pathological Conditions. *Oxid. Med. Cell Longev.* **2016,** *2016*, 1245049.

74. Waris, G.; Ahsan, H., Reactive Oxygen Species: Role in the Development of Cancer and Various Chronic Conditions. *J. Carcinog.* **2006,** *5*, 14.

75. Thannickal, V. J.; Fanburg, B. L., Reactive Oxygen Species in Cell Signaling. *Am. J. Physiol. Lung Cell Mol. Physiol.* **2000,** *279* (6), L1005-28.

76. Valko, M.; Izakovic, M.; Mazur, M.; Rhodes, C. J.; Telser, J., Role of Oxygen Radicals in DNA Damage and Cancer Incidence. *Mol. Cell. Biochem.* **2004,** *266* (1-2), 37-56.

77. Valencia, A.; Moran, J., Reactive Oxygen Species Induce Different Cell Death Mechanisms in Cultured Neurons. *Free Radic. Biol. Med.* **2004,** *36* (9), 1112-25.

78. Amatore, C.; Arbault, S.; Bouton, C.; Coffi, K.; Drapier, J. C.; Ghandour, H.; Tong, Y., Monitoring in Real Time with a Microelectrode the Release of Reactive Oxygen and Nitrogen Species by a Single Macrophage Stimulated by Its Membrane Mechanical Depolarization. *Chembiochem* **2006,** *7* (4), 653-61.

79. Li, Y.; Hu, K.; Yu, Y.; Rotenberg, S. A.; Amatore, C.; Mirkin, M. V., Direct Electrochemical Measurements of Reactive Oxygen and Nitrogen Species in Nontransformed and Metastatic Human Breast Cells. *J. Am. Chem. Soc.* **2017,** *139* (37), 13055-13062.

80. Steinberg, S. F., Structural Basis of Protein Kinase C Isoform Function. *Physiol. Rev.* **2008,** *88* (4), 1341-78.

81. Yasukawa, T.; Kondo, Y.; Uchida, I.; Matsue, T., Imaging of Cellular Activity of Single Cultured Cells by Scanning Electrochemical Microscopy. *Chem. Lett.* **1998,** *27* (8), 767-768.

82. Yasukawa, T.; Uchida, I.; Matsue, T., Permeation of Redox Species through a Cell Membrane of a Single, Living Algal Protoplast Studied by Microamperometry. *BBA - Biomembranes* **1998,** *1369* (1), 152-158.

83. Kim, J.; Izadyar, A.; Nioradze, N.; Amemiya, S., Nanoscale Mechanism of Molecular Transport through the Nuclear Pore Complex as Studied by Scanning Electrochemical Microscopy. *J. Am. Chem. Soc.* **2013,** *135* (6), 2321-9.

84. Tsionsky, M.; Cardon, Z. G.; Bard, A. J.; Jackson, R. B., Photosynthetic Electron Transport in Single Guard Cells as Measured by Scanning Electrochemical Microscopy. *Plant Physiol.* **1997,** *113* (3), 895-901.

85. Chen, Z.; Xie, S.; Shen, L.; Du, Y.; He, S.; Li, Q.; Liang, Z.; Meng, X.; Li, B.; Xu, X.; Ma, H.; Huang, Y.; Shao, Y., Investigation of the Interactions between Silver Nanoparticles and Hela Cells by Scanning Electrochemical Microscopy. *Analyst* **2008,** *133* (9), 1221-8.

86. Henderson, J. D.; Filice, F. P.; Li, M. S. M.; Ding, Z., Tracking Live Cell Response to Cadmium (Ii) Concentrations by Scanning Electrochemical Microscopy. *J. Inorg. Biochem.* **2016,** *158*, 92-98.

87. Zhang, M. N.; Ding, Z.; Long, Y. T., Sensing Cisplatin-Induced Permeation of Single Live Human Bladder Cancer Cells by Scanning Electrochemical Microscopy. *Analyst* **2015,** *140* (17), 6054-60.

88. Li, M. S. M.; Filice, F. P.; Henderson, J. D.; Ding, Z., Probing Cd2+-Stressed Live Cell Membrane Permeability with Various Redox Mediators in Scanning Electrochemical Microscopy. *J. Phys. Chem. C* **2016,** *120* (11), 6094-6103.

89. Bondarenko, A.; Lin, T. E.; Stupar, P.; Lesch, A.; Cortes-Salazar, F.; Girault, H. H.; Pick, H., Fixation and Permeabilization Approaches for Scanning Electrochemical Microscopy of Living Cells. *Anal. Chem.* **2016,** *88* (23), 11436-11443.

90. Solda, A.; Valenti, G.; Marcaccio, M.; Giorgio, M.; Pelicci, P. G.; Paolucci, F.; Rapino, S., Glucose and Lactate Miniaturized Biosensors for Secm-Based High-Spatial Resolution Analysis: A Comparative Study. *ACS Sens.* **2017,** *2* (9), 1310-1318.

91. Takahashi, Y.; Shevchuk, A. I.; Novak, P.; Babakinejad, B.; Macpherson, J.; Unwin, P. R.; Shiku, H.; Gorelik, J.; Klenerman, D.; Korchev, Y. E.; Matsue, T., Topographical and Electrochemical Nanoscale Imaging of Living Cells Using Voltage-Switching Mode Scanning Electrochemical Microscopy. *Proc. Nat. Acad. Sci. U.S.A.* **2012,** *109* (29), 11540-5.

92. Polcari, D.; Hernandez-Castro, J. A.; Li, K.; Geissler, M.; Mauzeroll, J., Determination of the Relationship between Expression and Functional Activity of Multidrug Resistance-Associated Protein 1 Using Scanning Electrochemical Microscopy. *Anal. Chem.* **2017,** *89* (17), 8988-8994.

93. Hartwig, A., Metal Interaction with Redox Regulation: An Integrating Concept in Metal Carcinogenesis? *Free Radic. Biol. Med.* **2013,** *55*, 63-72.

94. Jomova, K.; Valko, M., Advances in Metal-Induced Oxidative Stress and Human Disease. *Toxicol.* **2011,** *283* (2-3), 65-87.

95. Garcia, J. J.; Martinez-Ballarin, E.; Millan-Plano, S.; Allue, J. L.; Albendea, C.; Fuentes, L.; Escanero, J. F., Effects of Trace Elements on Membrane Fluidity. *J. Trace Elem. Med. Biol.* **2005,** *19* (1), 19-22.

96. Van der Paal, J.; Neyts, E. C.; Verlackt, C. C. W.; Bogaerts, A., Effect of Lipid Peroxidation on Membrane Permeability of Cancer and Normal Cells Subjected to Oxidative Stress. *Chem. Sci.* **2016,** *7* (1), 489-498.

97. Kai, T.; Zoski, C. G.; Bard, A. J., Scanning Electrochemical Microscopy at the Nanometer Level. *Chem. Commun. (Camb.)* **2018,** *54* (16), 1934-1947.

98. Cortes-Salazar, F.; Trauble, M.; Li, F.; Busnel, J. M.; Gassner, A. L.; Hojeij, M.; Wittstock, G.; Girault, H. H., Soft Stylus Probes for Scanning Electrochemical Microscopy. *Anal. Chem.* **2009,** *81* (16), 6889-96.

99. Cortes-Salazar, F.; Momotenko, D.; Lesch, A.; Wittstock, G.; Girault, H. H., Soft Microelectrode Linear Array for Scanning Electrochemical Microscopy. *Anal. Chem.* **2010,** *82* (24), 10037-44.

100. Takahashi, Y.; Ida, H.; Matsumae, Y.; Komaki, H.; Zhou, Y.; Kumatani, A.; Kanzaki, M.; Shiku, H.; Matsue, T., 3d Electrochemical and Ion Current Imaging Using Scanning Electrochemical-Scanning Ion Conductance Microscopy. *Phys. Chem. Chem. Phys.* **2017,** *19* (39), 26728-26733.

101. Shen, M.; Qu, Z.; DesLaurier, J.; Welle, T. M.; Sweedler, J. V.; Chen, R., Single Synaptic Observation of Cholinergic Neurotransmission on Living Neurons: Concentration and Dynamics. *J. Am. Chem. Soc.* **2018,** *140* (25), 7764-7768.

Chapter 2

2   Mapping Cd^{2+}-induced Membrane Permeability Changes of Single Live Cells by Means of Scanning Electrochemical Microscopy

Scanning Electrochemical Microscopy (SECM) is a powerful, noninvasive, analytical methodology which can be used to investigate live cell membrane permeability. Depth scan SECM imaging allowed for the generation of 2D current maps of live cells relative to electrode position in the x-z or y-z plane. Depending on resolution, one depth scan image can contain hundreds of probe approach curves (PACs). Individual PACs were obtained by simply extracting vertical cross-sections from the 2D image. These experimental PACs were overlain onto theoretically generated PACs simulated at specific geometry conditions. Simulations were generated using 3D models in COMSOL Multiphysics to determine the cell membrane permeability coefficients at different locations on the surface of the cells. Common in literature, theoretical PACs are generated using a 2D axially symmetric geometry. This saves on both compute time and memory utilization. However, due to symmetry limitations of the model, only one experimental PAC right above the cell can be matched with simulated PAC data. Full 3D models in this article were developed for the SECM system of live cells, allowing all experimental PACs over the entire cell to become usable. Cd^{2+}-induced membrane permeability changes of single human bladder (T24) cells were investigated at several positions above the cell, displaced from the central axis. The experimental T24 cells under study were incubated with Cd^{2+} in varying concentrations. It is experimentally observed that 50 and 100 μM Cd^{2+} caused a decrease in membrane permeability, which was uniform across all locations over the cell regardless of Cd^{2+} concentration. The Cd^{2+} was found to have detrimental effects on the cell, with cells shrinking in size and volume,

and the membrane permeability decreasing. A mapping technique for the analysis of the cell membrane permeability under the Cd^{2+} stress is realized by the methodology presented.

2.1   Introduction

Scanning electrochemical microscopy (SECM) is a powerful non-invasive analytical method in the Scanning Probe Microscopy (SPM) family.[1-3] SECM operates by moving a biased ultramicroelectrode (UME) (25 µm diameter electrode or smaller) over a substrate with extreme precision.[1, 4-5] The UME tip and substrate are submerged in an electrolyte solution containing a redox agent. An electrochemical current is monitored with reference to the UME-substrate position, which is affected by topographical changes and electrochemical characteristics of the substrate as the electrode sweeps in the vicinity of the sample surface.[1-2, 4-6] Receiving significant early development by Bard et al. since 1989,[4] SECM has since been employed for chemical kinetics studies, chemical imaging, potential distributions, and microfabrications.[7-9] Recent developments towards biological applications have been pursued,[10-16] such as electron transfer kinetics and molecular transport,[17-19] neurotransmitter releases,[20-22] reactive oxygen and nitrogen species release,[23-30] and the assessment of drug resistance on biological cells.[29, 31-32] SECM offers great opportunities to study physiological processes at the cell membrane in real-time, and to investigate cellular properties such as membrane permeability.[33-35] As the probe makes no contact with the cells, these physiological processes remain unchanged, assuming that the selected redox mediator itself has no effect on the cell's homeostasis.[33] This is advantageous over common methods of live cell monitoring, such as continuous time-lapse fluorescence experiments, which suffer from photo-bleaching that potentially alters cell homeostasis.[36-38]

The UME is biased at a potential generating a steady state current in a redox active solution, as the electrochemically driven reaction progresses. Upon approach to a substrate, diffusion of unreacted mediator species from the bulk solution towards the electrode tip is hindered (Figure 2.1). This reduces the rate of reaction at the electrode tip, and consequently the reaction draws less current. In cases such as an approach to some

substrates (conductors, for instance) spent mediator can be regenerated, causing an increase in current.[2]
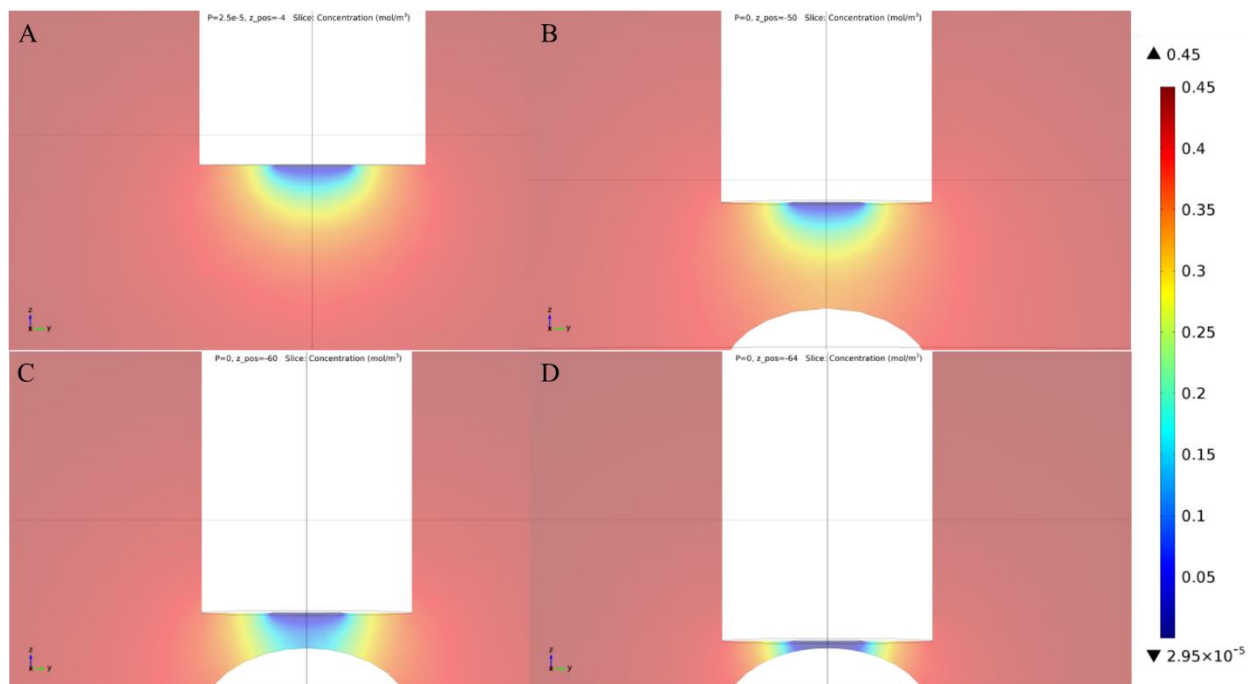
Figure 2.1 - (A) Theoretically generated (finite element method) steady state concentration map of a 10 μm RG3 electrode in bulk solution. (B) Electrode on approach to ideal insulating ellipsoid cell substrate at 15 μm from cell surface. (C) Electrode on approach to ideal insulating ellipsoid cell substrate at 5 μm from cell surface. (D) Electrode on approach to ideal insulating ellipsoid cell substrate at 1 μm from cell surface.

Traditionally, acquiring SECM probe approach curves (PACs) involves a biased UME approaching the sample at a single point vertically.[20, 33-34] To characterize a single sample at different locations, multiple approaches would be required, which is both time consuming and difficult. By completing multiple approaches, there is also an increased risk of crashing the electrode into the sample or substrate, due to the possible height variations of the substrate surface. An electrode crash can be damaging to the sample or the electrode itself. In the Ding research group, a different method of SECM analysis, called depth scan imaging, has been previously developed.[29, 35, 39-40] The depth scan mode

passes the UME in x-axis or y-axis direction performing a horizontal line scan at that constant height. The electrode is then lowered in the z-axis by a preset depth distance and another line scan is carried out. This action is repeated until the desired depth is reached. The repeated horizontal sampling at various approaching heights to the sample produces a two-dimensional image of the current feedback in the x-z or y-z plane in real-time. The depth scan imaging method allows the distance to the sample to be more easily gauged during the scan, removing the limitation of conventional SECM approach methods. One depth image can also provide hundreds of PACs, limited by the user-defined image width and resolution. By simply selecting vertical cross-sections from the image, experimental PAC data can be extracted, producing a plot of current vs. the distance to the substrate. Note that the Schuhmann group developed a 4D shearforce-based constant-distance mode,[41] where multiple constant-distance images can be obtained above the sample topography, a comprehensive 4D data set containing the SECM tip current response as a function of x-, y-, and z-position of the SECM tip. Different types of 3D plots such as depth scan images can be extracted from these 4D raw data, while the method employed by the Ding Lab generates a depth image experimentally.

Extracted experimental PACs are then compared to simulated PACs to obtain quantitative analysis of sample traits, such as the reaction kinetic and physical properties.[5-6, 18] Conventionally, simulations of this system are completed using a 2D axially symmetric model geometry in finite element analysis software, such as COMSOL Multiphysics. At the time of computation, the 2D model is duplicated in a radial fashion about the axis of symmetry creating a pseudo three-dimensional (3D) model for computation. This symmetric model design saves a great deal of computational time and system resources. However, the requirement that a model be symmetric is a severe limitation. The PACs to a substrate of non-uniform geometry produced in each SECM depth scan image are not all usable for comparison to the conventional theoretical PACs. Only the PAC directly above the center of the symmetric sample can be matched with simulated PAC data. By expanding to a 3D model, off-axis PAC analysis of single live cells becomes possible, as seen in my very recent development of a full 3D simulation model for SECM of an interdigitated array of gold electrodes.[39]

The use of 3D models for characterization of SECM data can allow for even broader use of SECM than what was possible before. The primary issue with performing 3D simulations previously has been the heavy demand on system resources. Long compute times, large amounts of memory, and heavy CPU utilization have previously required powerful computers to execute. The simulation geometry, meshing and physics have been optimized to allow for such simulations to be computed in reasonable time using consumer-grade hardware.

With SECM, monitoring cell membrane permeability is commonly achieved by comparing experimental results to simulated PACs of known permeability coefficients.[34] The shape of a PAC is dependent on the ability of a mediator to pass through the membrane. At close proximity of the UME to the cell, diffusion is limited similar to an approach towards an ideal insulating substrate. As the UME approaches the membrane, the flux of the redox mediator across the membrane is detected as an additional faradaic current. The redox mediator used in this study is ferrocenemethanol, which is commonly employed for biological electrochemistry as it is non-toxic to many cells lines.[25, 31, 35, 42] Ferrocenemethanol is able to diffuse across the cell membrane to the cell interior, and back out. As the electrode approaches closer to the cell membrane, more rapid flux of ferrocenemethanol occurs through the cell membrane toward the electrode tip. The rate of flux across the membrane is dependent on the membrane permeability coefficient. This enables matching of experimental and simulated PACs for quantification of membrane permeability. Recently, the Ding Lab reported that membrane permeability of live human bladder cancer (T24) cells can be altered using the addition of Cd^{2+} into solution.[35] It was observed that increasing Cd^{2+} concentrations lead to quicker changes in membrane permeability and morphological changes, such as spreading and flattening of the T24 cells.

Cd^{2+} cytotoxicity in humans can arise from contaminated drinking water and foods, cigarettes, and through occupational hazards.[43] Once in the body, Cd^{2+} can accumulate within several organs, such as the kidneys and liver.[44-46] The half-life of Cd^{2+} within the body has been reported to be between 10 and 30 years, allowing for bioaccumulation to

occur.[43, 47] Once in the body, Cd^{2+} can cause a wide range of issues, from organ damage to bone diseases and carcinogenesis. Due to its cytotoxic nature, and the bioaccumulation which may occur within the body, research in both understanding the biological pathways affected by Cd^{2+} and treatment measures have been studied.[47-49] Studies in multiple cell lines have shown that Cd^{2+} alters various biological pathways (ex. Mitogen-activated protein kinase) by disrupting the desired homeostatic protein levels.[48-50] A common side effect in these Cd^{2+} cytotoxicity studies is the increased production of reactive oxygen species.[48-51] Elevation of Cd^{2+} levels can lead to increased oxidative stress within the cell, which may lead to the overwhelming of the anti-oxidant defense system, and thus a link between diseases and carcinogenesis has been identified.[43, 52] The presence of Cd^{2+} has also been linked to higher protein levels, such as nuclear transcription factors, NF-κβ, AP-1 and p53.[49, 53] As well, Cd^{2+} has been shown to induce cellular death by either the apoptotic or necrotic mechanisms.[43, 48, 54-55]

Herein, for the first time, the 3D modeling of an SECM approach to a single live cell membrane will be reported, which proves very useful in conjunction with SECM depth scan imaging. 3D simulations can generate multiple PACs at any location over the sample to match any experimental PACs, providing further insight into the mapping of membrane permeability across a single live cell.

2.2   Experimental

2.2.1   Materials

Ferrocenemethanol ($FcCH_2OH$) (97%), potassium chloride (KCl) (99%), and cadmium chloride (anhydrous grade) ($CdCl_2$) were purchased from Sigma-Aldrich (Mississauga, ON). A stock solution of 0.9 mM $FcCH_2OH$ with 0.1 M KCl as a supporting electrolyte, was prepared in deionized water (18.2 MΩ MilliQ water, Millipore, Etobicoke, ON). For the SECM depth scan study, the live cells were cultured in Petri dishes (P50-G-0-30-F, MatTek Corporation, Ashland, MA). The stock solution of 1 M $CdCl_2$ was prepared in the deionized water. For incubation experiments, $CdCl_2$ stock solutions were syringe-filtered through sterile 0.2 μm Supor® Membrane (PALL Life Sciences, Mississauga,

ON) and added to the cell sample Petri dishes inside a laminar flow hood. For live cell SECM experiments, 2 mL of 0.9 mM stock solution was diluted to 0.45 mM with phosphate buffered saline (PBS, pH 7.4) and carried out at 37.0 ± 0.2 °C.

2.2.2 Electrode Fabrication

Electrodes were fabricated as reported elsewhere.[27, 35, 56-57] Briefly, borosilicate glass capillary tubes (o.d.: 2.00 mm, i.d.: 1.16 mm, length: 10.00 cm, Sutter Instruments, Novato, CA) were pulled and sealed with a micropipette puller (PP-83, Narishige, Japan). 10 µm electrodes were created by inserting a 10 µm Pt wire (Goodfellow Metals, Cambridge, UK) into a heat-sealed and pulled borosilicate capillary. The capillary was placed under internal vacuum and heated to form tight glass sheathing around the Pt wire. The sealed glass tube was then manually polished on a custom made polishing wheel with alumina polishing pads (3.0, 0.3, and 0.05 µm, Buehler, Whitby, ON) to expose the Pt wire at the tip of the glass electrode. Electrodes are characterized by the ratio of insulating glass sheath radius to conductive Pt wire radius (RG) (Eq. 2.1).

$$RG = \frac{total\ radius\ of\ electrode}{radius\ Pt\ Wire} \qquad [2.1]$$

The electrode RG was polished to approximately 3.[56] Characterization of the electrode's RG is important for generation of theoretical PACs to ensure close agreement with experimentally obtained PACs, as variation in electrode RG affects the curve shape obtained.[56] An example of the RG effect on the PAC shape can be found in Figure 2.2. Electrode tips were examined during the polishing process using an optical microscope and tested for functionality using cyclic voltammetry (CV).
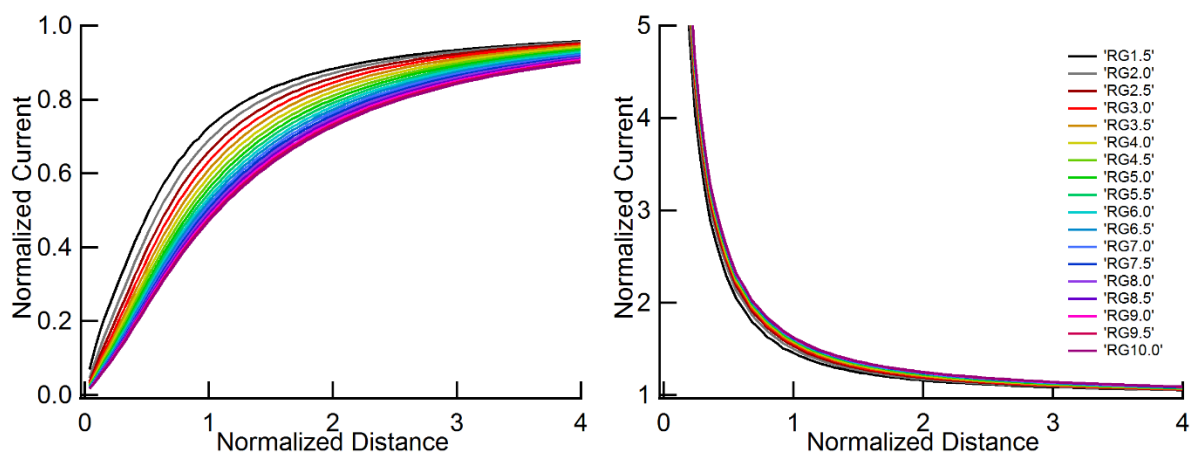
Figure 2.2 - Theoretically generated PACs with various RG values for approach to a flat ideal insulating substrate (left), and an ideal conducting substrate (right).

2.2.3   Instrumentation

SECM experiments were conducted on a modified Alpha-SNOM (WITec, Ulm, Germany) with a home-made UME holder in place of a primary lens above the sample.[25, 35] Optical images of the samples were taken from the inverted objective lens (50× lens, N.A. 0.55, W.D. 10.1 mm, Nikon, Japan) and camera positioned below the sample. Positioning of the sample and electrode were performed by the Alpha-SNOM piezoelectric xy-stage and z-axis with 1 nm precision. All electrochemical experimentation was performed using an Electrochemical Analyzer (CHI 800B, CH Instruments, Austin, TX) with a CHI 200 Picoamp Booster to reduce noise. A Ag/AgCl wire suspended from the UME holder into solution was used as a combined reference and counter electrode. The signal was transported to a data acquisition channel of the Alpha-SNOM microscope.

2.2.4   Cell Culture

Human bladder carcinoma cells, T24 cells (ATCC® HTB-4™) were purchased from American Type Culture Collection (ATCC, Manassas, VA). These cells were incubated in McCoy's 5a medium with the addition of 10 % fetal bovine serum (FBS). T24 cells were cultured in uncoated T25 flasks (Becton Dickinson, Franklin Lakes, NJ). When

cells reached 80-100% confluency the media was decanted, and cells were washed with PBS solution. 0.05% trypsin with 0.006% EDTA was then used to release cells from the inner surface of the flask. T24 cells were incubated at 37 °C with 5 % CO_2 (Sanyo, Japan). All live cell experiments were performed within a small passage window (P45 – P48). McCoy's 5a medium (modified) was purchased from ATCC, while all other culture solutions and sera were purchased from Invitrogen (Burlington, ON).

For SECM live cell experiments, cells were plated on glass bottom Petri dishes the day before use. Incubation of cells with $CdCl_2$ was performed by adding the desired concentrations of $CdCl_2$ to the samples and incubating them for 1 h prior to the SECM experiment. Cells were removed from the incubator and the medium drawn from the dish. The cells were then washed 3× or more with PBS prior to SECM analysis. Once ready for SECM, the PBS was exchanged with 0.45 mM FeMeOH with 0.05 M KCl in PBS.

2.2.5   SECM Experiments

SECM of live T24 cells was performed by securing a Petri dish containing the cells on the heated 2D scanning stage (Bioscience Tools, San Diego, CA) of the microscope. The stage was set to a temperature of 37.0 ± 0.2 °C to mimic human body temperature. The electrochemical analyzer was set to produce a constant voltage corresponding to the oxidation plateau of the electrochemical mediator (0.300 V for $[FcCH_2OH]^+$ production, determined by CV). The electrode was then lowered into solution using the microscope z axis until it was in close proximity to the cells. The optical objective lens was calibrated to be centered on the position of the electrode tip. This allowed for visual tracking of both the electrode tip and the sample for analysis by SECM. The scan width and depth can be set in the WITec software, as well as the integration time and resolution of the scan image.

For the live cell study, each scan had 128×128 pixels, with a scan scale of 60 µm (width) vs. 80 µm (depth) and an acquisition time of 0.01 s for each pixel. To optimize the electrode distance, depth scans were performed above the sample. The electrode height was gradually lowered until feedback was seen. Care had to be taken to ensure

contact with the sample did not occur. Once the electrode height had been optimized the microscope was zeroed at this position. This makde it easy to return to this height if the electrode had to be raised at any point during the experiment.

2.2.6   The Simulation Workstation Computer

COMSOL Multiphysics (version 4.4) software was used for all simulations. A custom-built workstation computer for COMSOL simulations was assembled using an Intel Core I7 4930K (6-core, 12-thread), and 32 GB Kingston HyperX Fury Black memory on the LGA2011 platform. A Mushkin Chronos Sandforce 480 GB SSD was also added to increase swap speeds for large simulations and to reduce load and save times for commonly used models. All parts used in the construction of the workstation are consumer available, "gaming grade" hardware. Parts were selected, acquired and assembled in-house with optimization for COMSOL simulations prioritized. Ubuntu Linux 14.04.1 LTS was installed as a reliable platform for running simulations.

2.3 Theory and Simulations

2.3.1   Simulation Methodology

The experimental physical dimensions were reflected in simulation geometry (Figure 2.3A). An ellipsoid with a height of 10 µm and a diameter of 30 µm was used as a cell on a flat glass Petri dish. The electrode was defined as a Pt disk with a diameter of 10 µm and an RG of 3 (Figure 2.3B). The electrode z and x positions were parameterized in the program code that allows for parametric movement of the electrode position, automating the approach to the substrate.

A bulk solution concentration of $FcCH_2OH$ was set at 0.45 mM to match the solution used in the physical experiment. At the UME with a biased potential of 0.300 V, the oxidation of $FcCH_2OH$ to $[FcCH_2OH]^+$ is a one electron process, Eq. 2.2, and is controlled by diffusion. Diffusion of $FcCH_2OH$ in bulk solution and the cell interior followed Fick's second law as expressed by Eqs. 2.3 and 2.4, respectively:

$$FcMeOH \rightarrow [FcMeOH]^+ + e^- \quad [2.2]$$

$$\frac{\partial c_B}{\partial t} = D \left(\frac{\partial^2 c_B}{\partial x^2} + \frac{\partial^2 c_B}{\partial y^2} + \frac{\partial^2 c_B}{\partial z^2} \right) \qquad [2.3]$$

$$\frac{\partial c_C}{\partial t} = D \left(\frac{\partial^2 c_C}{\partial x^2} + \frac{\partial^2 c_C}{\partial y^2} + \frac{\partial^2 c_C}{\partial z^2} \right) \qquad [2.4]$$

where c_B and c_C represent the FcCH$_2$OH concentration in the two domains and D is the diffusion coefficient for FcCH$_2$OH set at 7.6×10^{-10} m^2/s.[1, 33, 58] Please note that conventional 2D axially symmetric modeling follows diffusion equations described elsewhere,[57] and is illustrated in Figure 2.3**Error! Reference source not found.**C and D.
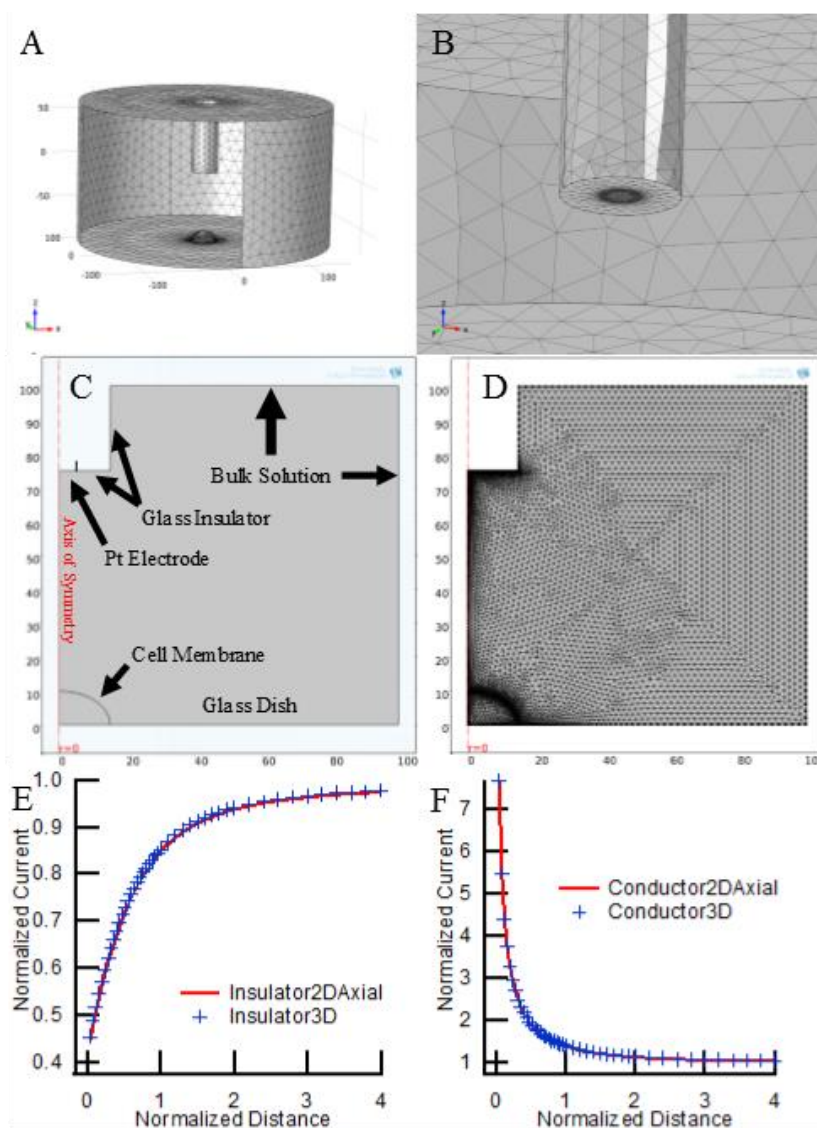
Figure 2.3 - (A) Meshed 3D COMSOL model geometry of SECM approach to a T24 Cell. (B) Zoomed-in meshed 3D SECM probe. (C)2D axially symmetric COMSOL model geometry of SECM approach to the T24 Cell with labelled boundary conditions. (D) Meshed 2D SECM model with axial symmetry. (E) Comparison of SECM PACs to an 3D insulating membrane in 2D axial symetry and 3D models. (F) Comparison of SECM PACs to a conductor membrane in 2D axial symetry and 3D models.

2.3.2   Verification of 3D modeling

The boundary at the cell membrane was temporarily configured to act as an ideal insulator (no flux boundary), or an ideal conductor (regenerating $FcCH_2OH$ in solution at initial concentration). In both cases, boundaries interfacing with bulk solution were set to generate a concentration matching the initial $FcCH_2OH$ bulk concentration. The bulk solution concentration simulates diffusion from bulk towards the system under study, where a theoretical infinite supply of new $FcCH_2OH$ exists. For the other boundaries, the glass dish and glass electrode sheathing were set as no-flux boundaries to simulate the insulating characteristics of these substrates. The Pt disk of the electrode tip was set to remove $FcCH_2OH$ from solution, generating an ideal concentration of 0 M at the electrode tip. The model geometry was finely meshed using a tetrahedral mesh with a maximum element size of 15 µm (**Error! Reference source not found.** A). To yield higher quality results, the meshing of the model was further refined at the electrode tip boundary and the cell membrane boundary to 0.1 µm (**Error! Reference source not found.** A and B). The element growth rate was defined at 1.4 ensuring a smooth gradual transition between element sizes, and the curvature factor was defined as 0.5 for meshing around rounded boundary surfaces. The meshing had an error of less than 5.0×10^{-3} with only 4 iterations (Figure 2.4A). The convergence plots for the segregated groups simulated (cell exterior and cell interior) can be found in Figure 2.4B.
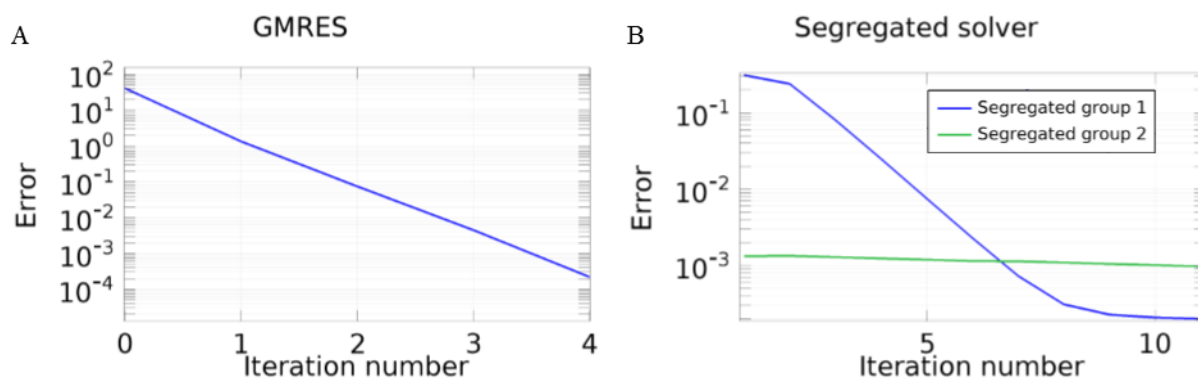
Figure 2.4 - (A) Meshing convergence plot for single data point. (B) Convergence plot for the two segregated groups within the simulation model. Segregated group 1 includes the concentration simulation within the bulk solution. Segregated group 2 includes simulation within the cell.

A post-processing surface integration was performed on the resulting simulation concentration map data to calculate the current over the circular electrode tip surface. For a PAC, the tip currents corresponding to more than 100 tip-to-substrate distances, d, were calculated following Eq. 2.5:[39]

$$i = nFD \int_0^A \left[\frac{\partial c}{\partial z}\right]_z da \quad [2.5]$$

In this formula, A is the surface area of the UME disk, n the number of electrons (1) transferred in the FcCH$_2$OH oxidation half reaction, F the Faraday's constant (96,485 C/mol), and D the diffusion coefficient for FcCH$_2$OH. The resulting tip current was normalized with respect to the limiting current at the disk electrode with a distance far away from the substrate, i_∞ (taken at a normalized distance of 13 from the cell surface), yielding:

$$I_T = \frac{i}{i_\infty} \qquad [2.6]$$

A PAC was obtained by plotting the normalized tip current (Eq 2.6) versus the normalized tip-to-substrate distance (d/r where r is the Pt electrode radius). The PACs to the insulator and conductor are plotted in Figure 2.3E and F (blue crosses), respectively.

Using the same electrode geometry, a CV was also simulated, which agreed very well with that obtained experimentally (Figure 2.5).
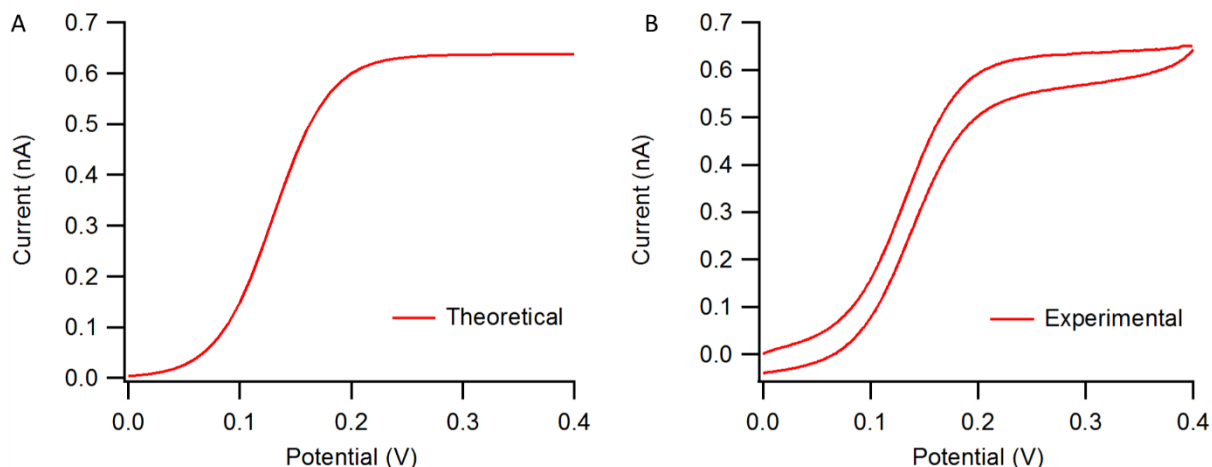
Figure 2.5 - (A) Theoretically generated cyclic voltammogram (CV) for a 10 μm electrode with an RG of 3, and a FcCH₂OH concentration of 0.43 mM. (B) Experimentally acquired CV in the FcCH₂OH solution. The theoretical CV was found to have a steady-state current of 0.636 nA, while the experimental one to be 0.630 nA. There is close agreement between the experimentally acquired and simulated current values.

2D axially symmetric modeling (**Error! Reference source not found.** C and D) with the same geometry as the above 3D was used to generate PACs to the same insulator and conductor. The model is functionally rotated about the axis of symmetry to generate a pseudo-3D model of the system under study, **Error! Reference source not found.**C [59]. The two PACs (red solid) obtained from this approach are then superposed to those generated using the above 3D model. The 3D PACs can be seen overlap very well with those created through the 2D axially symmetric method (**Error! Reference source not found.** E and F). Verification of PACs to a flat conductor or insulator substrate was carried out using 3D modeling with various RG values. Two sets of PACs to a flat conductor and insulator substrates with RG values of 10 and 1.5 are demonstrated in Figure 2.6. They overlap very well with the simulated curves by Shao and Mirkin using a 2D model [60]. Because of the great demand on the computer resource, meshing for 3D

simulations was not as fine as for 2D simulations. However, convergence plots were monitored to ensure meshing error was minimized.
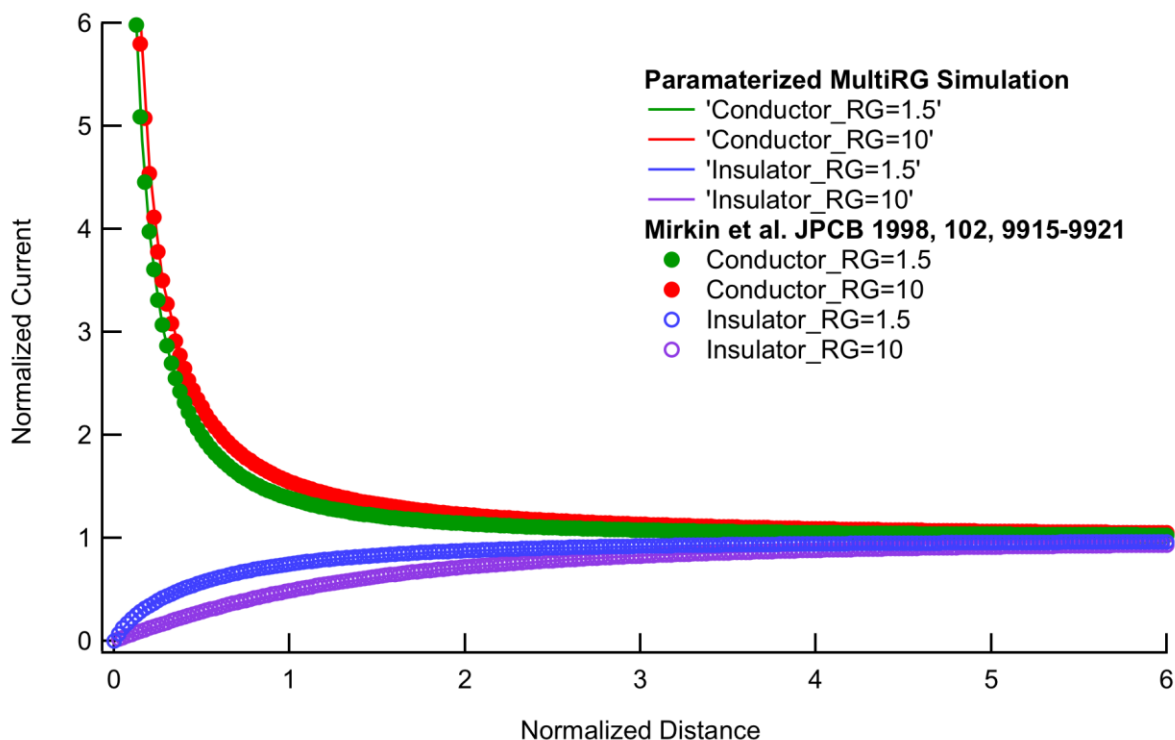
Figure 2.6 - Simulated PACs to a flat conductor and insulator substrates with RG values of 10 and 1.5, which overlap very well with the simulated curves by Mirkin et al [60]

Experimental PACs are similarly normalized to the bulk solution current value taken from the steady state region of a PAC. Experimental PACs are then overlaid on top of the simulated theoretical PACs. Theoretical curves are simulated with an absolute distance from the substrate designed into the model geometry. Experimental PACs are matched to these curves to determine the tip to substrate distance of the closest point in the approach. Experimental PACs in this report each represent an individual SECM experiment performed on one T24 cell. Each membrane permeability coefficient reported here represents an average ± standard deviation where the number of cells is between 6 and 12 unless otherwise stated.

2.3.3   Live Cell Membrane Permeability

The geometry for the permeability simulations was configured the same as that of the insulator/conductor geometry detailed above. The interior of the ellipsoid cell represents its own domain separate from the solution domain, with its own physics and concentration settings (Eq. 2.4). Both the bulk and cell domains were also set to have the same diffusion coefficient for $FcCH_2OH$. A flux boundary was set across the cell membrane separating these two domains. The flux across the membrane was controlled by the permeability, Eqs. 2.7 and 2.8:

$$influx_{cell} = P * (c_B - c_C) \quad [2.7]$$

$$influx_{bulk} = P * (c_C - c_B) \quad [2.8]$$

In addition to the above parametric electrode-to-substrate distance movement, membrane permeability can also be varied through the parameterization of the permeability coefficient (P). This allows for an automated parametric sweep of various permeability coefficients to yield a set of PACs.
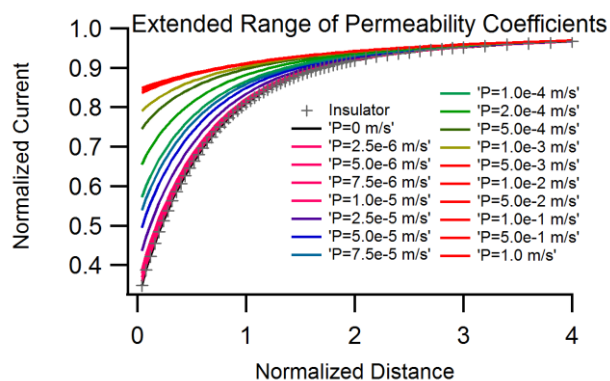
Figure 2.7 - Probe approach curves (PACs) to a live cell with a large range of simulated permeability coefficients, simulated with the electrode centered over the cell.

The two domains are both subjected to a two-step simulation process as elegantly demonstrated by Koley and Bard [34]. The first study step is a time-dependent fixed geometry simulation. The cell was provided with a 600 s soak time to allow the exterior and interior $FcCH_2OH$ concentrations to equilibrate. The initial $FcCH_2OH$ concentration was set as 0.45 mM (bulk solution), and 0.0 mM inside the cell. The fixed geometry characteristic ensured the model geometry is not affected by the parametric sweep conditions keeping the electrode position fixed. During this step, the electrode was turned off by setting the Pt tip as a no flux boundary. The solution of this first step was stored by COMSOL to be used as an initial model for the second study step.

The second study step used a stationary phase. The electrode tip was turned on by generating a concentration of 0 M at the Pt disk. The parameterized electrode z and x positions allowed for the automated movement of the electrode tip, while the parameterized permeability coefficient allowed for the automated configuration of membrane permeability. As a result, numerous PACs can be generated from a single simulation, limited only by PC workstation memory and compute power. All the other boundary conditions remain the same.

A broad range of permeability coefficients between 0.0 and 1.0 m/s were explored and compared (Figure 2.7). The permeability coefficient of P=0.0 m/s overlapped with the curve of an ideal insulator, for further model verification. An effective range of permeability coefficients was found for experimental PAC permeability characterization between 2.5×10^{-5} and 1.0×10^{-3} m/s: these are the two detection limits. Above 1.0×10^{-3} or below 2.5×10^{-5} m/s, the PACs became similar to each other and difficult to differentiate. As a result, it was far more difficult to match experimental PACs in these permeability ranges.

It is important to note that the defined simulation model did not account for forced convection occurring at the electrode tip by the motion of the electrode [61]. Each individual electrode position was simulated as an independent simulation. It is assumed that the influences of forced convection were minimal at the electrode scan rate used experimentally.

2.4   Results and Discussion

2.4.1   Mapping Cell Membrane Permeability

Using the 3D model, I proceeded to demonstrate the potential for use in biological SECM studies. Specifically, a series of theoretical PACs were simulated using various membrane permeability coefficients at different positions above the elliptical cell. Morphology of single T24 cells was monitored using an inverted optical microscope (Figure 2.8A). SECM depth images were then taken (Figure 2.8B). PACs were extracted from the depth image at the cell center, ½ cell radius, and the edge of the cell for comparison to theoretical PACs by simply drawing the vertical cross-section lines in the WITec software suite (Figure 2.8C). A PAC was also extracted at 2× cell radius, adjacent to the cell (Figure 2.8C). This was performed to determine if there was a strong influence from an adjacent cell.
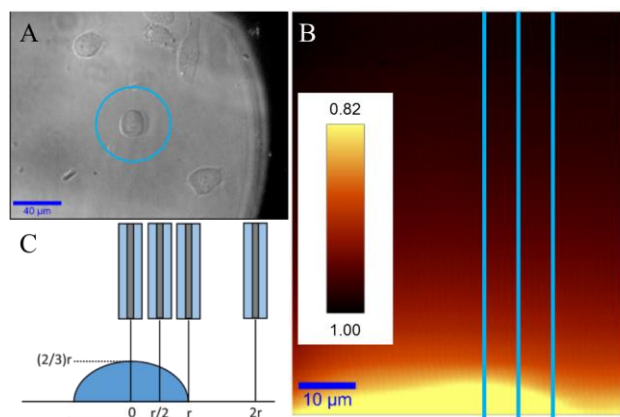
Figure 2.8 - (A) Optical image of a T24 cell under study. (B) A typical SECM depth mode image of a Cell with cross sections labelled. (C) Graphical representation of 4 cross section locations and normalized measurements of an average cell.

2.4.2   Membrane Permeability Quantification for Cells Incubated with Different Cd^{2+} Concentrations

Three different Cd^{2+} concentrations of 0, 50 and 100 μM were utilized for incubation with T24 cells for 1 hr. Single live cells after incubation were located optically and the SECM probe was positioned above the cells using the inverted microscope. Depth images

were obtained following the procedure as described in the experimental section. Figure 2.9 demonstrates typical depth images of these single cells under study. Vertical cross-sections of the SECM depth scan image were taken to yield multiple PACs to the cell center (green) which can be characterized through traditional 2D-axial simulation methods. The blue cross sections were taken at ½ cell radius, and the edge of the cell, as well as the point of 2× cell radius. These cross-sections cannot be characterized using a symmetrical model geometry, and therefore require the use of the new 3D simulation methods. The extracted experimental PACs were overlaid onto the set of theoretical PACs simulated at the same geometric position relative to the cell center, Figure 2.10. The shape of the experimental PAC changed with the location of each cross-section, becoming less pronounced the further the electrode moved from the cell's highest point. It is evident that the simulated PACs follow the same tendency (Figure 2.10). The observed trend can be partially attributed to the greater distance from the substrate at asymmetric (off-axis) positions. Due to geometry restrictions, an experimental approach made to sites other than the highest point of the cell cannot be made to the same distance without crashing the electrode into those elevated parts of the cell. Another major contributor to the weaker signal is the steep angle of the substrate away from parallel to the electrode tip. This occurs more significantly at off-axis positions above the curved cell membrane further from the cell's central axis. The angled sample provides less restricted access to the electrode tip, allowing for more $FcCH_2OH$ diffusion to the SECM probe and to be oxidized at this location.
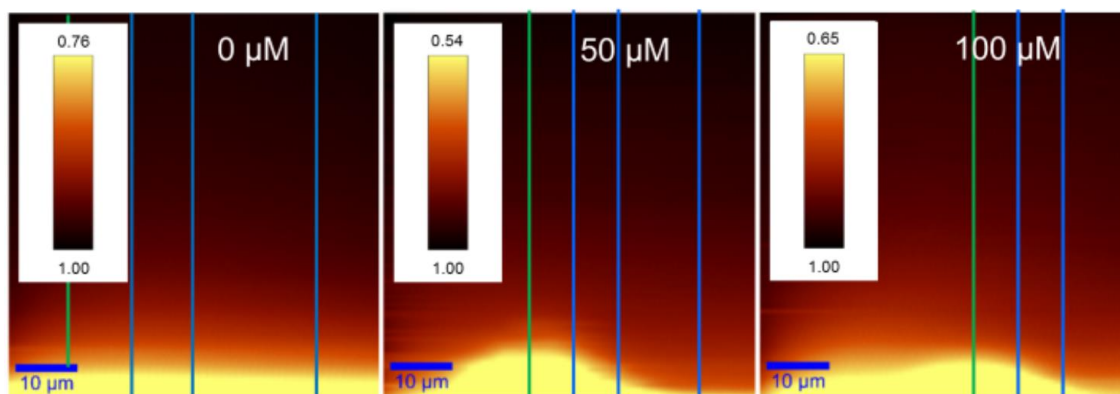
Figure 2.9 - Typical SECM depth images of single T24 cells after incubation with 0, 50 and 100 μM Cd²⁺, respectively. With labelled cross section PAC extractions. Green cross section represents cell highest point extraction which can be characterized using traditional 2D-Axial simulations, where blue represent cross sections requiring off axis 3D simulation.

For control (no Cd^{2+} administered) T24 cells, at the cell's highest point (x = 0) a permeability coefficient of $7.2 \times 10^{-5} \pm 2.5 \times 10^{-5}$ m/s was present. At the half radius position (x = r/2) the cell membrane permeability coefficient was $7.1 \times 10^{-5} \pm 1.0 \times 10^{-5}$ m/s. The permeability coefficient at the cell edge (x = r) was found to be $7.9 \times 10^{-5} \pm 3.0 \times 10^{-5}$ m/s. All three locations over the cell have a relatively consistent permeability coefficient around 7.4×10^{-5} m/s, Figure 2.10A, B and C (light blue circles).

The Cd^{2+} concentrations of 50 and 100 μM in the incubation medium decreased the cell membrane permeability (blue and purple circles in Figure 2.10A, B and C). The higher the concentration of Cd^{2+} used, the lower the membrane permeability became within the same 1 h exposure duration. The Cd^{2+} containing concentrations, 50 μM Cd^{2+}, had caused a membrane permeability coefficient decrease to $5.0 \times 10^{-5} \pm 2.2 \times 10^{-5}$ m/s at x = 0, $4.6 \times 10^{-5} \pm 1.0 \times 10^{-5}$ m/s at x = r/2, and $5.0 \times 10^{-5} \pm 1.6 \times 10^{-5}$ m/s at x = r. All 3 locations over the cell maintain a membrane permeability coefficient surrounding 4.9×10^{-5} m/s. The cells incubated with 100 μM Cd^{2+} had further reduced membrane permeability coefficients of $2.5 \times 10^{-5} \pm 1.8 \times 10^{-5}$ m/s at x=0, $2.8 \times 10^{-5} \pm 1.9 \times 10^{-5}$ m/s at x = r/2, and $2.5 \times 10^{-5} \pm 1.1 \times 10^{-5}$ m/s at x = r. The 3 observed locations maintained a

membrane permeability coefficient averaging 2.6×10^{-5} m/s. The lower permeability values seen at higher Cd^{2+} concentrations have high standard deviations relative to their averages. This is due to the permeability values of the PACs being low compared to the statistical variation. For example, the 100 µM Cd^{2+} permeability average taken at x = r, was calculated using 11 individual cell PACs fit between 5.0×10^{-5} and the 0.0×10^{-5} m/s.

Incubation with higher Cd^{2+} concentrations within the examined concentration range led to lower membrane permeability. This decrease in permeability suggests that the cell membrane is contracting, preventing the flux of $FcCH_2OH$ across the membrane. This results in the decrease in faradic current. A more partial negative feedback or PAC was observed with respect to the control T24 cell. However, once a high enough concentration of Cd^{2+} is used (250 µM, data not shown), the cell membrane no longer contracts and begins to relax. This results in a higher flux of $FcCH_2OH$ to cross the cell membrane, suggesting that too much Cd^{2+} results in the relaxation of the cell membrane.[62] Increasing the flux of $FcCH_2OH$ across the membrane, will allow for an increased in faradaic current to be detected. As a result, the PACs will become more partially positive in feedback. This observation is consistent to a previously published study by the Ding Lab of high cadmium concentration injection studies using SECM.[35]

While increasing concentrations of Cd^{2+} (50 and 100 µM) in the incubation medium induced changes in membrane permeability, similar to the control, a constant membrane permeability at all locations was determined for each cell incubated with the two Cd concentrations (Figure 2.10A, B and C). The cross-sections taken at each position over the cell, with each Cd^{2+} incubation concentration surveyed, maintained the same permeability coefficient uniformly over the cell surface.

The observation of uniform membrane permeability across the entire surface of the cell was determined using an electrode with a 5 µm radius. This electrode size provides good cell definition and a strong current signal for SECM. However, the electrode size is large relative to the average cell diameter of 30 µm. This could be providing an average membrane permeability of smaller domains of varying permeability. Through the use of

SECM with smaller electrodes, coupled with 3D modeling, further analysis into the membrane permeability characteristics of single live cells is anticipated.
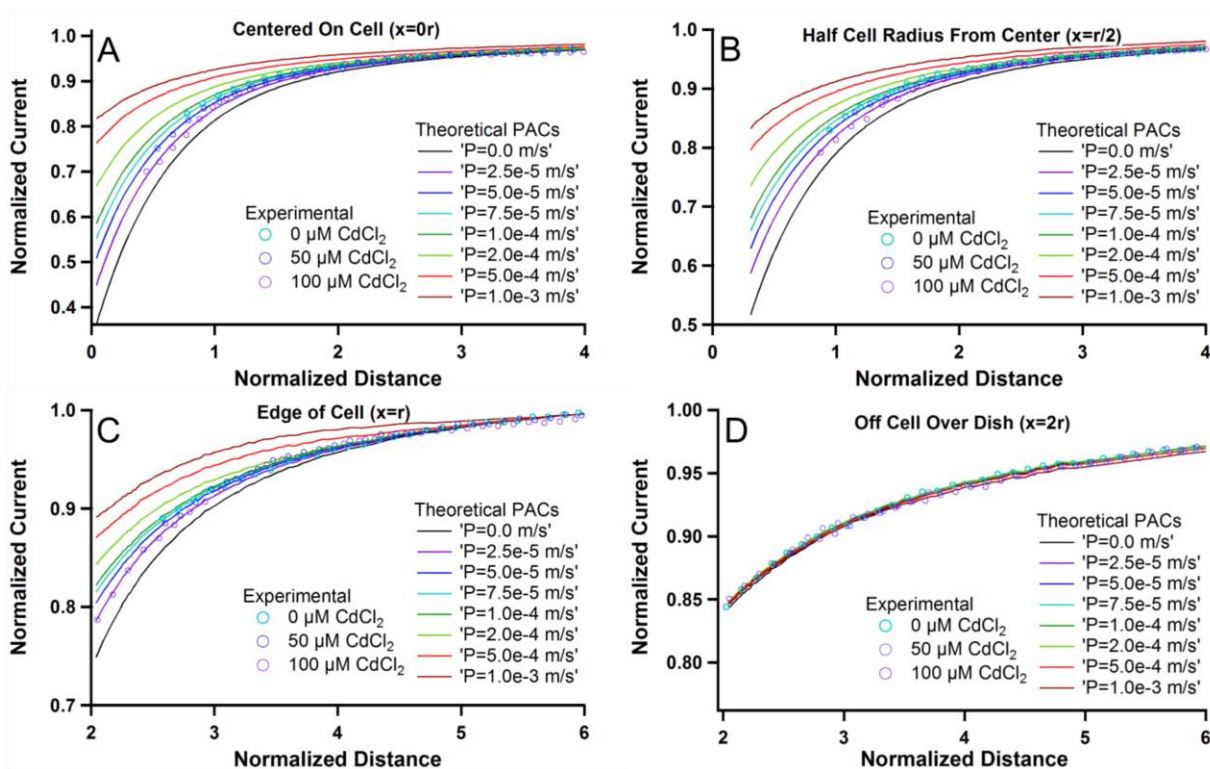
Figure 2.10 - (A) Extracted experimental PACs along the symmetrical axis to single live cells incubated with 0, 50 and 100 μM Cd^{2+}, overlayed with a set of simulated PACs. (B) Simulated and extracted experimental PACs to single live cells at half cell radius, which were incubated with 0, 50 and 100 μM Cd^{2+}, respectively. (C) Simulated and extracted experimental PACs to single live cells at full cell radius, which were incubated with 0, 50 or 100 μM Cd^{2+}, respectively. (D) Simulated and Experimental PACs to Petri dish at 2× cell radius and the nearest cells were incubated with 0, 50 and 100 μM Cd^{2+}, respectively.

The experimental and simulated PACs sampled at the off-cell (2r) location were largely indistinguishable from each other, yielding the same cell membrane permeability. The contribution of the adjacent cell was too weak at the surveyed location to yield a sufficient response. All the simulated PACs with various membrane permeability coefficients were not distinguishable from one another (Figure 2.10D). The theoretical

PACs for the approach above the glass dish (insulator) with the cell adjacent to the site yielded curves that were overlapped well with experimental PACs (Figure 2.10D). As a result, all simulated curves overlap one another into a similar shape regardless of membrane permeability coefficient.

2.4.3   Cell Membrane Permeability Change Mechanism
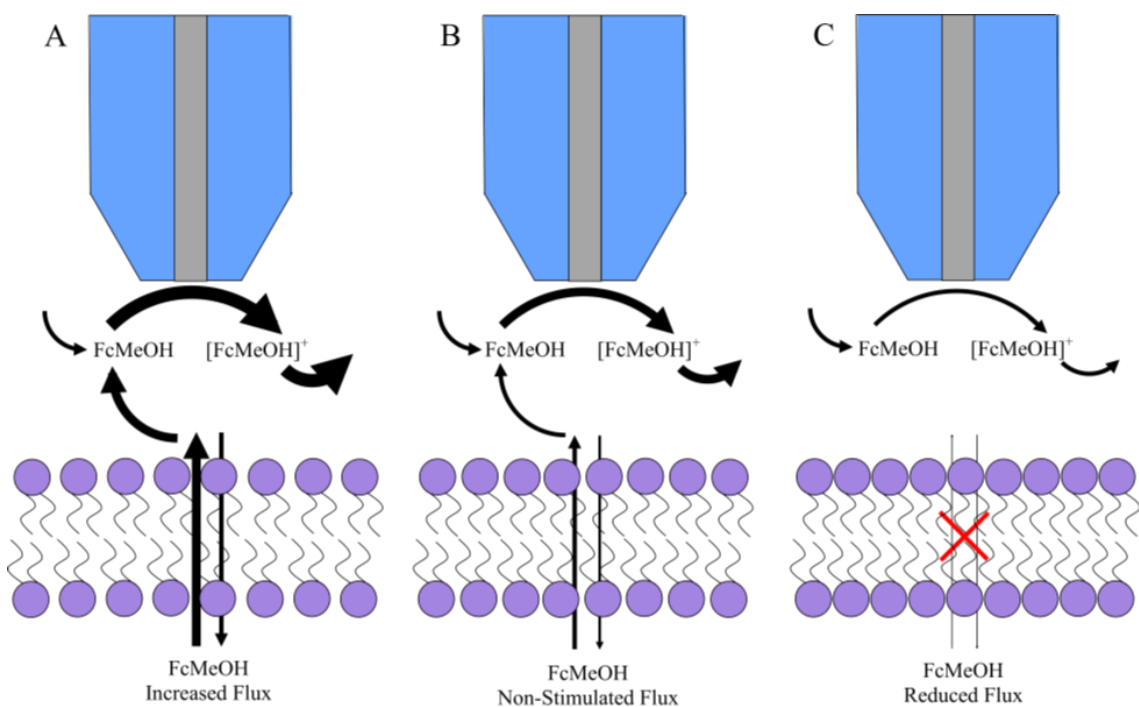
Figure 2.11 - Schematic for SECM probe approach experiments toward cell membranes with increased FcCH₂OH flux (A), non-stimulated FcCH₂OH flux (B) and decreased FcCH₂OH flux (C).

The injection of large Cd^{2+} concentrations into the cell-containing experimental solution in previous work performed in the Ding Lab[35] is similar to acute and lethal exposures for live cells. Whereas the incubation of T24 cells with diluted Cd^{2+} concentrations in this research shows similarities to the low chronic exposure in our modern society, which is a real challenge for population health in the 21st century. A prominent example is the occurrence of Itai-Itai disease for the people living in the Jinzu river area (Japan) in the

1950s, as a result of Cd^{2+} cytotoxicity due to the ore mining processes contaminating the river water.[46] For humans, an increase in urinary excretion of Cd^{2+} is associated with an accumulation of Cd^{2+} in the renal cortex,[46] making bladder cells an ideal organ to study Cd^{2+} cytotoxicity. Since we have previously correlated a trend between Cd^{2+}-stressed T24 cells and membrane permeability,[35, 62] we are confident that Cd^{2+} treatment results in free Cd^{2+} entering the cells, possibly through ion channels and solute carriers.[46] It is very likely that Cd^{2+} is disrupting homeostatic levels, resulting in oxidative damage and possibly cellular death pathways, such as apoptosis.[43, 48, 63]

After Cd^{2+} stress, the cells were observed to be shrinking in size and volume. However, while extracting the PACs at the 3 locations over the cell, we found that the membrane permeability remained relatively constant. Membrane permeability can be used to assess the membrane integrity of cells, such as dye exclusion viability studies, where an impermeable dye can permeate into the cell only when membrane integrity is lost.[43, 64-65] Maintaining membrane permeability throughout the cell (x = 0r, r/2, r, 2r) indicates plasma membrane integrity remains constant. Increased $FcCH_2OH$ flux as illustrated by Figure 2.11A relative to the non-stimulated flux (Figure 2.11B) was not seen at the explored concentrations. In contrast, a decreased $FcCH_2OH$ flux was observed as demonstrated in Figure 2.11C and therefore a decrease in membrane permeability was shown.

2.5   Conclusions

The development of a 3D simulation model for SECM analysis along with the SECM depth imaging allows for mapping membrane permeability of single live cells. Here for the first time we were able to extract permeability coefficients at any positions over the cell. It is expected that adjacent cells with a distance more than 2× cell radius will not interfere the determination of cell membrane permeability coefficients. The Cd^{2+} that has entered a cell might activate cell apoptosis. Initial signs of this include cells shrinking in size and volume, and a decrease in the membrane permeability. While the membrane permeability of $FcCH_2OH$ with a 5 µm radius electrode was consistent across the T24 cells, this scenario is not necessary the case for all cellular studies. Smaller SECM probes

will enhance the image resolution and reveal membrane characteristics above organelles or smaller cell structures. 3D simulation models presented here are robust and can become greatly advantageous in single live cell studies.

2.6 References

1. Bard, A. J.; Faulkner, L. R., *Electrochemical Methods: Fundamentals and Applications, 2nd Edition*. 2 ed.; John Wiley & Sons, Inc.: 2001, p 864.
2. Bard, A. J.; Mirkin, M. V., *Scanning Electrochemical Microscopy*. 2 ed.; CRC Press: 2012, p 670.
3. Zoski, C. G., Review—Advances in Scanning Electrochemical Microscopy (Secm). *J. Electrochem. Soc.* **2015,** *163* (4), H3088-H3100.
4. Bard, A. J.; Fan, F. R. F.; Kwak, J.; Lev, O., Scanning Electrochemical Microscopy. Introduction and Principles. *Anal. Chem.* **2002,** *61* (2), 132-138.
5. Mirkin, M. V.; Nogala, W.; Velmurugan, J.; Wang, Y., Scanning Electrochemical Microscopy in the 21st Century. Update 1: Five Years After. *Phys. Chem. Chem. Phys.* **2011,** *13* (48), 21196-212.
6. Sun, P.; Mirkin, M. V., Kinetics of Electron-Transfer Reactions at Nanoelectrodes. *Anal. Chem.* **2006,** *78* (18), 6526-34.
7. Lin, C. W.; Fan, F. R. F.; Bard, A. J., High Resolution Photoelectrochemical Etching of N-Gaas with the Scanning Electrochemical and Tunneling Microscope. *J. Electrochem. Soc.* **1987,** *134* (4), 1038-1039.
8. Craston, D. H.; Lin, C. W.; Bard, A. J., High Resolution Deposition of Silver in Nafion Films with the Scanning Tunneling Microscope. *J. Electrochem. Soc.* **1988,** *135* (3), 785-786.
9. Noel, J. M.; Latus, A.; Lagrost, C.; Volanschi, E.; Hapiot, P., Evidence for Oh Radical Production During Electrocatalysis of Oxygen Reduction on Pt Surfaces: Consequences and Application. *J. Am. Chem. Soc.* **2012,** *134* (5), 2835-41.
10. Zhao, C.; Wittstock, G., An Secm Detection Scheme with Improved Sensitivity and Lateral Resolution: Detection of Galactosidase Activity with Signal Amplification by Glucose Dehydrogenase. *Angew. Chem. Int. Ed. Engl.* **2004,** *43* (32), 4170-2.
11. Schulte, A.; Schuhmann, W., Single-Cell Microelectrochemistry. *Angew. Chem. Int. Ed. Engl.* **2007,** *46* (46), 8760-77.
12. Zhan, D.; Fan, F. R.; Bard, A. J., The Kv Channel Blocker 4-Aminopyridine Enhances Ag+ Uptake: A Scanning Electrochemical Microscopy Study of Single Living Cells. *Proc. Nat. Acad. Sci. U.S.A.* **2008,** *105* (34), 12118-22.
13. Schulte, A.; Nebel, M.; Schuhmann, W., Scanning Electrochemical Microscopy in Neuroscience. In *Annu. Rev. Anal. Chem.*, Yeung, E. S.; Zare, R. N., Eds. 2010; Vol. 3, pp 299-318.
14. Beaulieu, I.; Kuss, S.; Mauzeroll, J.; Geissler, M., Biological Scanning Electrochemical Microscopy and Its Application to Live Cell Studies. *Anal. Chem.* **2011,** *83* (5), 1485-92.

15.   Wu, Z. Q.; Jia, W. Z.; Wang, K.; Xu, J. J.; Chen, H. Y.; Xia, X. H., Exploration of Two-Enzyme Coupled Catalysis System Using Scanning Electrochemical Microscopy. *Anal. Chem.* **2012,** *84* (24), 10586-92.

16.   Abucayon, E.; Ke, N.; Cornut, R.; Patelunas, A.; Miller, D.; Nishiguchi, M. K.; Zoski, C. G., Investigating Catalase Activity through Hydrogen Peroxide Decomposition by Bacteria Biofilms in Real Time Using Scanning Electrochemical Microscopy. *Anal. Chem.* **2014,** *86* (1), 498-505.

17.   Nioradze, N.; Kim, J.; Amemiya, S., Quasi-Steady-State Voltammetry of Rapid Electron Transfer Reactions at the Macroscopic Substrate of the Scanning Electrochemical Microscope. *Anal. Chem.* **2011,** *83* (3), 828-35.

18.   Matrab, T.; Hauquier, F.; Combellas, C.; Kanoufi, F., Scanning Electrochemical [Corrected] Microscopy Investigation of Molecular Transport [Corrected]within Polymer Brushes. *Chemphyschem* **2010,** *11* (3), 670-82.

19.   Cannan, S.; Cervera, J.; Steliaros, R. J.; Bitziou, E.; Whitworth, A. L.; Unwin, P. R., Scanning Electrochemical Microscopy (Secm) Studies of Catalytic Ec' Processes: Theory and Experiment for Feedback, Generation/Collection and Imaging Measurements. *Phys. Chem. Chem. Phys.* **2011,** *13* (12), 5403-12.

20.   Liebetrau, J. M.; Miller, H. M.; Baur, J. E.; Takacs, S. A.; Anupunpisit, V.; Garris, P. A.; Wipf, D. O., Scanning Electrochemical Microscopy of Model Neurons: Imaging and Real-Time Detection of Morphological Changes. *Anal. Chem.* **2003,** *75* (3), 563-571.

21.   Kurulugama, R. T.; Wipf, D. O.; Takacs, S. A.; Pongmayteegul, S.; Garris, P. A.; Baur, J. E., Scanning Electrochemical Microscopy of Model Neurons: Constant Distance Imaging. *Anal. Chem.* **2005,** *77* (4), 1111-7.

22.   Takahashi, Y.; Shevchuk, A. I.; Novak, P.; Babakinejad, B.; Macpherson, J.; Unwin, P. R.; Shiku, H.; Gorelik, J.; Klenerman, D.; Korchev, Y. E.; Matsue, T., Topographical and Electrochemical Nanoscale Imaging of Living Cells Using Voltage-Switching Mode Scanning Electrochemical Microscopy. *Proc. Nat. Acad. Sci. U.S.A.* **2012,** *109* (29), 11540-5.

23.   Zhu, R.; Macfie, S. M.; Ding, Z., Cadmium-Induced Plant Stress Investigated by Scanning Electrochemical Microscopy. *J. Exp. Bot.* **2005,** *56* (421), 2831-8.

24.   Amatore, C.; Arbault, S.; Bouton, C.; Coffi, K.; Drapier, J. C.; Ghandour, H.; Tong, Y., Monitoring in Real Time with a Microelectrode the Release of Reactive Oxygen and Nitrogen Species by a Single Macrophage Stimulated by Its Membrane Mechanical Depolarization. *Chembiochem* **2006,** *7* (4), 653-61.

25.   Zhao, X.; Petersen, N. O.; Ding, Z., Comparison Study of Live Cells by Atomic Force Microscopy, Confocal Microscopy, and Scanning Electrochemical Microscopy. *Can. J. Chem.* **2007,** *85* (3), 175-183.

26.   Amatore, C.; Arbault, S.; Bouton, C.; Drapier, J. C.; Ghandour, H.; Koh, A. C., Real-Time Amperometric Analysis of Reactive Oxygen and Nitrogen Species Released by Single Immunostimulated Macrophages. *Chembiochem* **2008,** *9* (9), 1472-80.

27.   Zhao, X.; Diakowski, P. M.; Ding, Z., Deconvoluting Topography and Spatial Physiological Activity of Live Macrophage Cells by Scanning Electrochemical Microscopy in Constant-Distance Mode. *Anal. Chem.* **2010,** *82* (20), 8371-3.

28. Wang, Y.; Noel, J. M.; Velmurugan, J.; Nogala, W.; Mirkin, M. V.; Lu, C.; Guille Collignon, M.; Lemaitre, F.; Amatore, C., Nanoelectrodes for Determination of Reactive Oxygen and Nitrogen Species inside Murine Macrophages. *Proc. Nat. Acad. Sci. U.S.A.* **2012,** *109* (29), 11534-9.

29. Zhang, M. M.; Long, Y. T.; Ding, Z., Cisplatin Effects on Evolution of Reactive Oxygen Species from Single Human Bladder Cancer Cells Investigated by Scanning Electrochemical Microscopy. *J. Inorg. Biochem.* **2012,** *108*, 115-22.

30. Salamifar, S. E.; Lai, R. Y., Use of Combined Scanning Electrochemical and Fluorescence Microscopy for Detection of Reactive Oxygen Species in Prostate Cancer Cells. *Anal. Chem.* **2013,** *85* (20), 9417-21.

31. Kuss, S.; Cornut, R.; Beaulieu, I.; Mezour, M. A.; Annabi, B.; Mauzeroll, J., Assessing Multidrug Resistance Protein 1-Mediated Function in Cancer Cell Multidrug Resistance by Scanning Electrochemical Microscopy and Flow Cytometry. *Bioelectrochemistry* **2011,** *82* (1), 29-37.

32. Kuss, S.; Polcari, D.; Geissler, M.; Brassard, D.; Mauzeroll, J., Assessment of Multidrug Resistance on Cell Coculture Patterns Using Scanning Electrochemical Microscopy. *Proc. Nat. Acad. Sci. U.S.A.* **2013,** *110* (23), 9249-54.

33. Guo, J.; Amemiya, S., Permeability of the Nuclear Envelope at Isolated Xenopus Oocyte Nuclei Studied by Scanning Electrochemical Microscopy. *Anal. Chem.* **2005,** *77* (7), 2147-56.

34. Koley, D.; Bard, A. J., Triton X-100 Concentration Effects on Membrane Permeability of a Single Hela Cell by Scanning Electrochemical Microscopy (Secm). *Proc. Nat. Acad. Sci. U.S.A* **2010,** *107* (39), 16783-7.

35. Li, M. S.; Filice, F. P.; Ding, Z., A Time Course Study of Cadmium Effect on Membrane Permeability of Single Human Bladder Cancer Cells Using Scanning Electrochemical Microscopy. *J. Inorg. Biochem.* **2014,** *136*, 177-83.

36. Lippincott-Schwartz, J.; Patterson, G. H., Development and Use of Fluorescent Protein Markers in Living Cells. *Science* **2003,** *300* (5616), 87-91.

37. Stephens, D. J.; Allan, V. J., Light Microscopy Techniques for Live Cell Imaging. *Science* **2003,** *300* (5616), 82-6.

38. Coutu, D. L.; Schroeder, T., Probing Cellular Processes by Long-Term Live Imaging--Historic Problems and Current Solutions. *J. Cell Sci.* **2013,** *126* (Pt 17), 3805-15.

39. Filice, F. P.; Li, M. S. M.; Henderson, J. D.; Ding, Z., Three-Dimensional Electrochemical Functionality of an Interdigitated Array Electrode by Scanning Electrochemical Microscopy. *J. Phys. Chem. C* **2015,** *119* (37), 21473-21482.

40. Zhang, M. N.; Ding, Z.; Long, Y. T., Sensing Cisplatin-Induced Permeation of Single Live Human Bladder Cancer Cells by Scanning Electrochemical Microscopy. *Analyst* **2015,** *140* (17), 6054-60.

41. Nebel, M.; Erichsen, T.; Schuhmann, W., Constant-Distance Mode Secm as a Tool to Visualize Local Electrocatalytic Activity of Oxygen Reduction Catalysts. *Beilstein J. Nanotechnol.* **2014,** *5*, 141-51.

42. Yasukawa, T.; Uchida, I.; Matsue, T., Permeation of Redox Species through a Cell Membrane of a Single, Living Algal Protoplast Studied by Microamperometry. *BBA - Biomembranes* **1998,** *1369* (1), 152-158.

43. Lopez, E.; Figueroa, S.; Oset-Gasque, M. J.; Gonzalez, M. P., Apoptosis and Necrosis: Two Distinct Events Induced by Cadmium in Cortical Neurons in Culture. *Br. J. Pharmacol.* **2003,** *138* (5), 901-11.

44. Moulis, J. M.; Thevenod, F., New Perspectives in Cadmium Toxicity: An Introduction. *Biometals* **2010,** *23* (5), 763-8.

45. Thevenod, F.; Lee, W. K., Cadmium and Cellular Signaling Cascades: Interactions between Cell Death and Survival Pathways. *Arch. Toxicol.* **2013,** *87* (10), 1743-86.

46. Thevenod, F.; Lee, W.-K., Toxicology of Cadmium and Its Damage to Mammalian Organs. In *Cadmium: From Toxicity to Essentiality*, Sigel, A.; Sigel, H.; Sigel, R. K. O., Eds. 2013; Vol. 11, pp 415-490.

47. Chen, D. J.; Xu, Y. M.; Du, J. Y.; Huang, D. Y.; Lau, A. T., Cadmium Induces Cytotoxicity in Human Bronchial Epithelial Cells through Upregulation of Eif5a1 and Nf-Kappab. *Biochem. Biophys. Res. Commun.* **2014,** *445* (1), 95-9.

48. Chen, L.; Liu, L.; Huang, S., Cadmium Activates the Mitogen-Activated Protein Kinase (Mapk) Pathway Via Induction of Reactive Oxygen Species and Inhibition of Protein Phosphatases 2a and 5. *Free Radic. Biol. Med.* **2008,** *45* (7), 1035-44.

49. Hartwig, A., Metal Interaction with Redox Regulation: An Integrating Concept in Metal Carcinogenesis? *Free Radic. Biol. Med.* **2013,** *55*, 63-72.

50. Pelicano, H.; Carney, D.; Huang, P., Ros Stress in Cancer Cells and Therapeutic Implications. *Drug Resist. Updat.* **2004,** *7* (2), 97-110.

51. Chen, L.; Liu, L.; Yin, J.; Luo, Y.; Huang, S., Hydrogen Peroxide-Induced Neuronal Apoptosis Is Associated with Inhibition of Protein Phosphatase 2a and 5, Leading to Activation of Mapk Pathway. *Int. J. Biochem. Cell Biol.* **2009,** *41* (6), 1284-95.

52. Chuang, S. M.; Wang, I. C.; Yang, J. L., Roles of Jnk, P38 and Erk Mitogen-Activated Protein Kinases in the Growth Inhibition and Apoptosis Induced by Cadmium. *Carcinogenesis* **2000,** *21* (7), 1423-32.

53. Leonard, S. S.; Harris, G. K.; Shi, X., Metal-Induced Oxidative Stress and Signal Transduction. *Free Radic. Biol. Med.* **2004,** *37* (12), 1921-42.

54. Shi, H.; Hudson, L. G.; Liu, K. J., Oxidative Stress and Apoptosis in Metal Ion-Induced Carcinogenesis. *Free Radic. Biol. Med.* **2004,** *37* (5), 582-93.

55. Lopez, E.; Arce, C.; Oset-Gasque, M. J.; Canadas, S.; Gonzalez, M. P., Cadmium Induces Reactive Oxygen Species Generation and Lipid Peroxidation in Cortical Neurons in Culture. *Free Radic. Biol. Med.* **2006,** *40* (6), 940-51.

56. Zhu, R.; Ding, Z., Enhancing Image Quality of Scanning Electrochemical Microscopy by Improved Probe Fabrication and Displacement. *Can. J. Chem.* **2005,** *83* (10), 1779-1791.

57. Zhu, R.; Macfie, S. M.; Ding, Z., Effects of Cadmium on Photosynthetic Oxygen Evolution from Single Stomata in Brassica Juncea (L.) Czern. *Langmuir* **2008,** *24* (24), 14261-8.

58. Miao, W.; Ding, Z.; Bard, A. J., Solution Viscosity Effects on the Heterogeneous Electron Transfer Kinetics of Ferrocenemethanol in Dimethyl Sulfoxide−Water Mixtures. *J. Phys. Chem. B* **2002,** *106* (6), 1392-1398.

59. Sklyar, O.; Wittstock, G., Numerical Simulations of Complex Nonsymmetrical 3d Systems for Scanning Electrochemical Microscopy Using the Boundary Element Method. *J. Phys. Chem. B* **2002,** *106* (30), 7499-7508.

60. Shao, Y.; Mirkin, M. V., Probing Ion Transfer at the Liquid/Liquid Interface by Scanning Electrochemical Microscopy (Secm). *J. Phys. Chem. B* **1998,** *102* (49), 9915-9921.

61. Kuss, S.; Trinh, D.; Danis, L.; Mauzeroll, J., High-Speed Scanning Electrochemical Microscopy Method for Substrate Kinetic Determination: Method and Theory. *Anal. Chem.* **2015,** *87* (16), 8096-101.

62. Henderson, J. D.; Filice, F. P.; Li, M. S. M.; Ding, Z., Tracking Live Cell Response to Cadmium (Ii) Concentrations by Scanning Electrochemical Microscopy. *J. Inorg. Biochem.* **2016,** *158*, 92-98.

63. Chen, L.; Xu, B.; Liu, L.; Luo, Y.; Zhou, H.; Chen, W.; Shen, T.; Han, X.; Kontos, C. D.; Huang, S., Cadmium Induction of Reactive Oxygen Species Activates the Mtor Pathway, Leading to Neuronal Cell Death. *Free Radic. Biol. Med.* **2011,** *50* (5), 624-32.

64. Sridhar, A.; de Boer, H. L.; van den Berg, A.; Le Gac, S., Microstamped Petri Dishes for Scanning Electrochemical Microscopy Analysis of Arrays of Microtissues. *PLoS One* **2014,** *9* (4), e93618.

65. McNeil, P. L.; Steinhardt, R. A., Plasma Membrane Disruption: Repair, Prevention, Adaptation. *Annu. Rev. Cell Dev. Biol.* **2003,** *19*, 697-731.

Chapter 3

3 Tracking Live Cell Response to Hexavalent Chromium Toxicity by Scanning Electrochemical Microscopy

This study explores the effects of Cr (VI) on live-cell response. Human bladder cancer (T24) cells are incubated with varying concentrations of Cr(VI) and cell membrane permeability is monitored by using membrane-permeable and -impermeable redox mediators, ferrocenemethanol and ferrocenecarboxylic acid, respectively (see picture). Change in membrane permeability correlates with changes in cell viability.

The effects of exposure to toxic heavy metals, such as chromium, are of interest in scientific research, owing to the association with oxidative stress, cytotoxicity, and carcinogenicity. This study aims to explore the effects of Cr (VI) on live-cell responses. Herein, scanning electrochemical microscopy (SECM) is employed by using depth scan imaging and feedback mode to monitor the membrane permeability of single live human bladder cancer (T24) cells following 1 h incubations with Cr (VI) stimuli. By using membrane-permeable and -impermeable redox mediators, ferrocenemethanol and ferrocenecarboxylic acid, respectively, SECM depth scans yield both electrochemical and topographic information. This provides insights into the relative changes in membrane homeostasis with increased exposure to Cr (VI). Here, SECM has shown great power in determining membrane response to Cr (VI) exposure. Dependent on the level of exposure, transition between three distinct trends was observed. At low incubation concentrations of Cr (VI), the cell membrane permeability coefficients were relatively unaffected. With moderate increases in Cr (VI) concentrations, membrane permeability coefficients of the incubated cells were observed to decrease. Finally, with the higher incubation concentrations, membrane permeability coefficients were found to increase toward values similar to control cells. The Cr (VI) toxicity was further investigated by

means of a MTT cell viability study, which exhibited a similar decreasing trend to the cell membrane permeability. These findings further demonstrate the strength of SECM as a bioanalytical technique for monitoring cellular homeostasis.

3.1   Introduction

Due to the increasing environmental concentrations of heavy metals,[1-2] research efforts have focused on the biological effects of their exposure. In the case of chromium (Cr), the resulting oxidative stress, cytotoxicity, and carcinogenicity associated with many Cr-containing complexes have been extensively studied.[1, 3-7] Chromium is most commonly found in the stable hexavalent or trivalent oxidation states, Cr (VI) and Cr (III), respectively. Exposure to Cr (VI) occurs mainly through anthropogenic sources, due to its heavy use in chrome plating, welding, and leather tanning processes.[1] The heavy use of Cr in industrial processes has resulted in the environmental contamination of groundwater and soil.[1, 8] In addition, non-occupational sources of exposure commonly include housewares, automobile emissions and cigarette smoke.

Regarded as the most toxic of the commonly occurring oxidation states, Cr (VI) has no essential biological role. Instead it leads to detrimental health effects caused by two main mechanisms: the introduction of genomic instability and the generation of reactive oxygen species (ROS) and reactive nitrogen species (RNS).[7, 9] Cr (VI) species readily enter cells through non-specific phosphate/sulfate transporters, later undergoing an intracellular reduction to Cr (III).[3, 10] The reactive intermediates formed during this reduction process (Cr (V), Cr (IV), and Cr (III)) have been observed to react with DNA forming a variety of DNA-adducts.[1] This process results in high genomic instability in cells following Cr (VI) exposure.[1] In addition, exposure to Cr (VI) has been associated with increased ROS concentrations.[9] ROS have an important role in cell signaling and other biological processes. Disruptions in homeostatic levels of ROS can affect many essential processes, such as cell proliferation, DNA damage and anti-inflammatory responses.[9] Elevated levels of ROS have also been associated with oxidative damage to cellular structures by lipid peroxidation as well as oxidative DNA damage and strand breaks.[9, 11-12] Defense mechanisms in place to combat oxidative stress, such as the

enzyme superoxide dismutase and the antioxidant molecule glutathione, may become overwhelmed with high levels of exposure.[9]

Warranted by increases in environmental pollution largely focused on water contamination, a number of studies have examined the effects of Cr toxicity on marine life.[2, 6, 13-14] In mammals exposed to Cr (VI), like with other heavy metals, accumulation and adverse health effects have been observed in the kidney, liver, and lungs.[7, 15-16] Monitoring levels of exposure, commonly done through urine content, has been reported to demonstrate a substantial half-life of ~10 years.[16] Due to Cr (VI)'s ability to cause biological damage and its long half-life required to exit the body through the urinary tract, my current study has focused on the bladder as a model system. By using a human urinary bladder cancer (T24) cell line, I aim to investigate the effects of Cr toxicity on membrane homeostasis.

Previous studies focusing on the effects of Cr toxicity on cellular processes have relied heavily on conventional fluorescence microscopy techniques. Fluorescent techniques used to monitor dynamic cellular processes are limited in that they require special precautions in order to avoid light-induced ROS production, possibly leading to cellular damage.[17-18] This requires careful selection of dyes (or tags) whose excitation is of long, low energy wavelength light. However, these specialized fluorescent dyes are often expensive or may require a costly synthesis. In addition, these fluorescent techniques are often destructive, and samples must be discarded following measurement. Scanning electrochemical microscopy (SECM) has advantages in the study of live cells as cellular homeostasis remains unchanged given an appropriate non-toxic mediator is selected. The non-destructive, non-invasive nature of SECM as a method of monitoring dynamic cellular processes allows for the measurement of living unaltered biological samples. By operating SECM in depth scan mode, topographic information is provided in addition to electrochemical activity details collected characterizing cellular process.

SECM is a powerful scanning probe microscopy technique which benefitted greatly from the seminal work accomplished by Bard et al. since 1989.[19-20] This technique is used to monitor the electrochemical behavior of a sample based on the generation/regeneration of

the mediating species at a working electrode, commonly an ultramicroelectrode (UME) or nanoelectrode. In its applications to live cells, by operating in feedback mode, dynamic cellular processes can be observed by monitoring relative changes in faradaic current. As the UME approaches the cellular membrane, a current drop is commonly observed as the membrane hinders diffusion to the electrode tip (negative feedback). SECM can use this phenomenon in conjunction with a membrane permeable electrochemical mediator, to characterize and monitor membrane permeability of the cell. Approach to a more permeable membrane will exhibit a much smaller decrease in current, as the mediator is able to move through the cell interior and replenish mediator at the electrode tip. The UME tip current relative to distance from the membrane is commonly reported as a probe approach curve (PAC). Coupled with finite elemental analysis simulations of the electrochemical system, a quantitative cell membrane permeability can be obtained. Both electrochemical mediators used to determine membrane permeability in this study (ferrocenemethanol and ferrocenecarboxylic acid) have been shown to have no detrimental effects on the studied cell line over the experimental timeframe.[21-22]

The practice of SECM is not limited to biological samples, as it has been employed in a vast number of applications[23] including but not limited to kinetic studies,[24] surface and interface studies,[25-26] microstructure fabrication,[27-28] as well as the mentioned biological applications such as cellular imaging,[29-30] membrane transport,[31-34] multidrug resistance,[35-36] ROS and RNS mapping,[30, 37-40] and cellular redox processes.[41-47]

Herein, I examine the effects associated with exposure to potassium dichromate ($K_2Cr_2O_7$) on cell membrane permeability and cellular viability. SECM can provide localized membrane permeability study of single live cells making it a powerful bioanalytical tool.

3.2 Experimental Section

3.2.1   Materials

$FcCH_2OH$ (97%), FcCOOH (97%), potassium chloride (KCl, 99%), and $K_2Cr_2O_7$ (99%) were purchased from Sigma-Aldrich Canada and used without further purification.

SECM mediator solutions containing 0.9 mM $FcCH_2OH$ with 0.1 M KCl were prepared in deionized water (18.2 MΩ.cm, MilliQ water, Millipore, Etobicoke, ON), while 0.5 mM $FcCOO^-$ stock solutions were prepared in 1× phosphate buffered saline (PBS, Life Technologies, Burlington, ON). Stock solutions of 0.25 M $K_2Cr_2O_7$ were prepared using autoclaved deionized water (18.2 MΩ.cm, MilliQ water, Etobicoke, ON) and syringe-filtered through sterile 0.2 μm Supor® Membrane (PALL Life Sciences, Mississauga, ON). 3-(4,5-dimethylthiazol-2-yl)-2,5-diphenyltetrazolium bromide (MTT) was acquired from R&D Systems Inc. (Minneapolis, MN) in the TACS® MTT Cell Proliferation Assay Kit. Spectroscopic grade dimethyl sulfoxide (DMSO) was used to dissolve the formazan crystals (Caledon Laboratory Ltd, Georgetown, ON).

3.2.2 Cell Preparation

Human bladder cancer cells (T24 cells (HTB-4™)) were acquired from American Type Culture Collection (ATCC, Manassas, VA, USA) and maintained according to ATCC protocol. These cells were incubated in McCoy's 5a medium (ATCC, Manassas, VA, USA), modified with 10% fetal bovine serum (Invitrogen, Burlington, ON). For SECM live cell experiments, T24 cells were aliquoted directly onto glass bottom Petri dishes (P50G-0-30-F, MatTek Corporation, Ashland, MA, USA). An hour prior to SECM testing, $K_2Cr_2O_7$ (stock solution) was injected into the growth medium in the desired concentrations for $K_2Cr_2O_7$ testing. The growth medium was then decanted and the cells were washed twice with 1× PBS prior to replacement with the mediator solution for SECM experiments.

3.2.3 Cellular Viability

Cellular viability following 1 hr exposure to $K_2Cr_2O_7$ was tracked using the MTT assay.[48] The MTT tetrazolium dye (yellow) is capable of moving into cells and is reduced in healthy cells to produce formazan crystals (purple). These crystals can be dissolved and detected using a spectrophotometer.

Briefly, 2×10^4 T24 cells were plated onto Corning Scientific Costar™ 96-well polystrol flat bottom plates and grown for 24 hr. The medium was then replaced with fresh

medium containing varying concentrations of $K_2Cr_2O_7$. Sodium dodecyl sulfate was used as a positive control for the assay at 0.05, 0.10, 0.15, and 0.20 mg/mL. Wells containing no cells (blank wells) were also prepared to allow for the removal of background medium effects and treated following the full MTT protocol.

Following $K_2Cr_2O_7$ treatment (1 hr), the growth medium was replaced with 100 µL of fresh medium (absent of phenol red) and 10 µL of the MTT reagent. Following incubation for 6 hr, the MTT solution was removed and replaced with 50 µL of spectroscopic grade DMSO to dissolve the formazan crystals. The absorbance (Abs) at 540 nm was read by a M1000 PRO plate reader (Tecan, Switzerland) following 1 s of shaking at 2 mm amp and 654 rpm. The effects of FcCOOH and FcCH$_2$OH have been investigated elsewhere and determined to be non-toxic during these experimental conditions.[22]

3.2.4   SECM Instrumentation and Experimental Procedure

A detailed description of the SECM instrumentation and experimental procedures can be found in Chapter 2 section 2.2.5.[49] Briefly, SECM experiments were carried out using an Alpha-SNOM (WITec, Ulm, Germany) outfitted with a specially fabricated UME and a micro-incubator Petri dish mount (Bioscience Tools, San Diego, California, USA). The inverted objective lens (50×, N.A. 0.55, W.D. 10.1 mm, Nikon, Japan) located below the cells, assisted in the positioning and optical imaging of both the UME and cells. High resolution UME manipulation was achieved through the WITec piezoelectric servo controller. Electrochemical instrumentation consisted of a CH Instruments Electrochemical Analyzer (CHI800B, Austin, TX) and CHI200 Picoamp Booster to reduce signal noise. A simple two-electrode set-up was used with the working electrode defined as the UME and the reference/counter couple as a Ag/AgCl electrode. All potentials reported in this report are vs. Ag/AgCl.

Before each experiment, cyclic voltammetry (CV) was used to test for steady-state performance of the UME probe. The Petri dish containing the $K_2Cr_2O_7$-treated cells (30-40% confluency) was then secured to the heating stage mount maintained at 37.0 ± 0.2

˚C. Each Petri dish was analyzed for a maximum duration of 60 min. Identified through CV, a biased UME tip potential of 0.3 V for $FcCH_2OH$ and 0.4 V for $FcCOO^-$ was used to obtain their steady state current. SECM analysis of all samples was performed at a maximum UME tip speed of 21.4 µm/s, to limit the effects of forced convection and maintain steady state current.[50] SECM was performed on the desired cells using the depth scan imaging. Depth scan analyzes a 2D region of space by moving the electrode in the x-z plane and produces real time probe-to-cell distance information. This allows the prevention of collisions and the acquisition of hundreds of PACs per single scan. Manipulation of depth scan parameters, such as x and z movement distance, and image resolution, was made possible through the WITec software.

3.2.5   Simulation
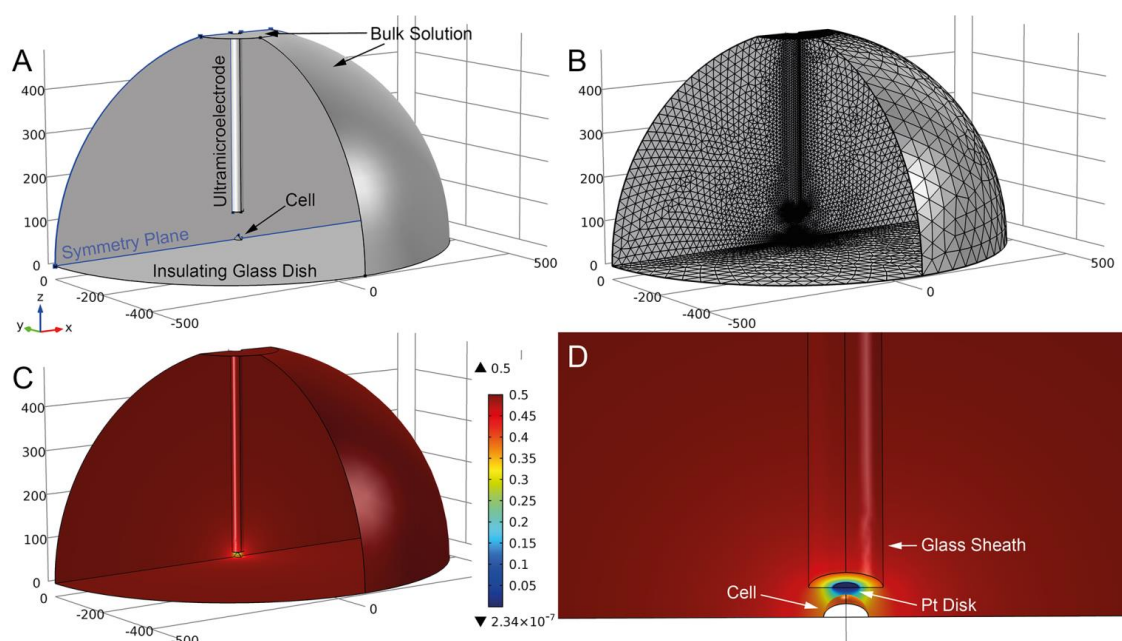
Figure 3.1 - (A) 3D model of the SECM approach to an isolated cell with key features, boundaries, and domains labeled. (B) Meshed 3D model. (C) Surface concentration map of the bulk solution domain following computation. (D) Zoomed in and labelled view of the surface concentration map displayed in C, focusing on the electrode tip in close proximity to the cell membrane.

Theoretical PACs were obtained using COMSOL Multiphysics (v5.2). A 3D model of the experimental SECM setup was generated, with a symmetry plane through the center of the UME and cell (Figure 3.1A). Dimensions of the electrode were specified to recreate the physical model of the UME (10 µm Pt diameter, RG3). Cells were surveyed optically to determine the average T24 cell size (86 cells). The long axis of the cell has an average diameter of 26.33 ± 0.62 µm, while the shorter axis was determined to be 18.23 ± 0.39 µm. The average cell height was determined previously to be 8.7 ± 3.3 µm.[22] Therefore, the model cell was represented as a quarter 3-dimensional ellipsoid with radii y = 13.5 µm, x = 9.0 µm, and z = 8.0 µm.

The COMSOL model geometry was then meshed using a free tetrahedral mesh. The size of the mesh is directly related to the accuracy of the finite element analysis simulation (Figure 3.1B). Therefore, areas where the concentration change is the most significant (i.e. the UME Pt surface and the cell membrane) were meshed much finer than bulk solution.

Two independent domains were identified for the bulk solution (C_B) and the cell's interior (C_C), which were provided concentrations matching the initial conditions ($C_B = 0.45$ mM $FcCH_2OH$ or $C_B = 0.50$ mM $FcCOOH$; $C_C = 0$ M $FcCH_2OH$ or $FcCOOH$).

For the mediators, $FcCH_2OH$ and $FcCOOH$, a one-electron oxidation reaction will occur under adequate potential bias. This is recreated in the simulation by defining a mediator concentration of zero at the biased Pt surface. Since the oxidation of the mediator is a diffusion-controlled process, its concentration at the UME tip can be described by Fick's second law of diffusion (Eqs. 3.1 and 3.2).

$$\frac{\partial C_B(x,y,z)}{\partial t} = D \left(\frac{\partial^2 C_B(x,y,z)}{\partial x^2} + \frac{\partial^2 C_B(x,y,z)}{\partial y^2} + \frac{\partial^2 C_B(x,y,z)}{\partial z^2} \right) \text{ [3.1]}$$

$$\frac{\partial C_C(x,y,z)}{\partial t} = D \left(\frac{\partial^2 C_C(x,y,z)}{\partial x^2} + \frac{\partial^2 C_C(x,y,z)}{\partial y^2} + \frac{\partial^2 C_C(x,y,z)}{\partial z^2} \right) \text{ [3.2]}$$

Defining the cell membrane as a flux boundary (Eqs. 3.3 and 3.4) allowed for the two domain concentrations to approach equilibrium during the time study step (discussed

later) while a constant supply of mediator was provided by the bulk solution boundaries (see Figure 3.1). The flux across the membrane boundary is dependent on a permeability coefficient (P) and the concentration difference.

$$f_{in} = P(C_B - C_C) \quad [3.3]$$

$$f_{out} = P(C_C - C_B) \quad [3.4]$$

Each cell membrane permeability simulation consists of two individual study steps carried out in sequence: a time-dependent study step and a stationary phase study step. The time-dependent study step was conducted over a 10 min simulated timeframe. During this study step, the Pt electrode surface was defined as a no-flux boundary, simulating the unbiased or 'turned off' state. This allows the mediator concentrations in C_B and C_C to approach equilibrium (Eqs. 3.3 and 3.4). The concentration profile generated by the time-dependent study step was saved by COMSOL and carried forward as an initial condition in the stationary phase simulation. In this step the UME was biased or 'turned on' and approached toward the cell membrane. While lowering the parameterized electrode toward the cell, COMSOL generated concentration maps for each defined electrode height (Figure 3.1 C and D).

Parameterizing the model definitions, electrode height (z-axis) and permeability coefficient, allows for the automated simulation of a single SECM depth scan experiment. These nested parameters allowed for the simulated depth scans, each with a different permeability coefficient, generating a complete set of PACs within a single simulation run.

Concentration information at the electrode tip was obtained by integrating the flux to the Pt surface at each simulated electrode position. As displayed in Eq. 3.5, the current (i) measured depends on the concentration gradient ($\partial C_B / \partial z$), the number of electrons transferred (n) and the disk radius (a).

$$i = 2\pi n D F \int_0^a r \left[\frac{\partial C_B(r,z,t)}{\partial z} \right] dr \quad [3.5]$$

The other constants considered are the Faraday constant (F = 96,485 C/mol) and the diffusion coefficient of the species (D). The diffusion coefficient for $FcCH_2OH$ in both domains was set to 7.6×10^{-10} m^2/s and 5.7×10^{-10} m^2/s for $FcCOOH$.[21, 51-52]

Theoretical and experimental PACs were normalized and plotted together to allow quantification of membrane permeability coefficients. By convention, current is normalized to the current observed at a theoretically infinite distance (normalized distance to sample ≥ 10). The distance is normalized to the UME critical radius used experimentally (5 μm).

3.3   Results and Discussion

3.3.1   Quantification of Membrane Permeability

By examining SECM depth scan images of $K_2Cr_2O_7$-treated T24 cells (Figure 3.2), changes in cellular topography can be monitored. In these SECM images, it can be seen that when the UME was far from the cell (several tip radii away), the detected tip current remained typical of the steady state, diffusion-controlled current (black). However, as the UME approached the cell, the cell's topography began to influence the electrochemical current (yellow, Figure 3.2). The cell effectively limited the diffusion of the redox species to the UME tip.

For cells incubated with 0 (control) and 1000 μM $K_2Cr_2O_7$ (Figure 3.2 A and C), cells displayed relatively flat topography. While for cells treated with 100 μM $K_2Cr_2O_7$, the topographic coverage decreased relative to control cells (became more rounded). This can be best visualized by extracting the horizontal line scan above the cell and the dish (Figure 3.2). These observations were consistent with their respective optical images (see Optical Observations Section 3.3.5).

Vertical cross-section lines extracted from the depth scan images (black arrows, Figure 3.2A-C) provided the unnormalized experimental PACs. Once normalized, these PACs can be quantified through successful overlay against the theoretical set of permeability curves. Experimental PACs were extracted to the tallest (or largest) point of the cell's

electrochemical feedback to provide higher accuracy in its quantification (smaller tip-to-sample distance). Additionally, since the membrane permeability of cells was previously demonstrated to be consistent across the entire cell using a 10 µm Pt UME (RG3),[49] PACs extracted with slight deviations from the cell center exhibit negligible deviation in PAC shape due to geometry.
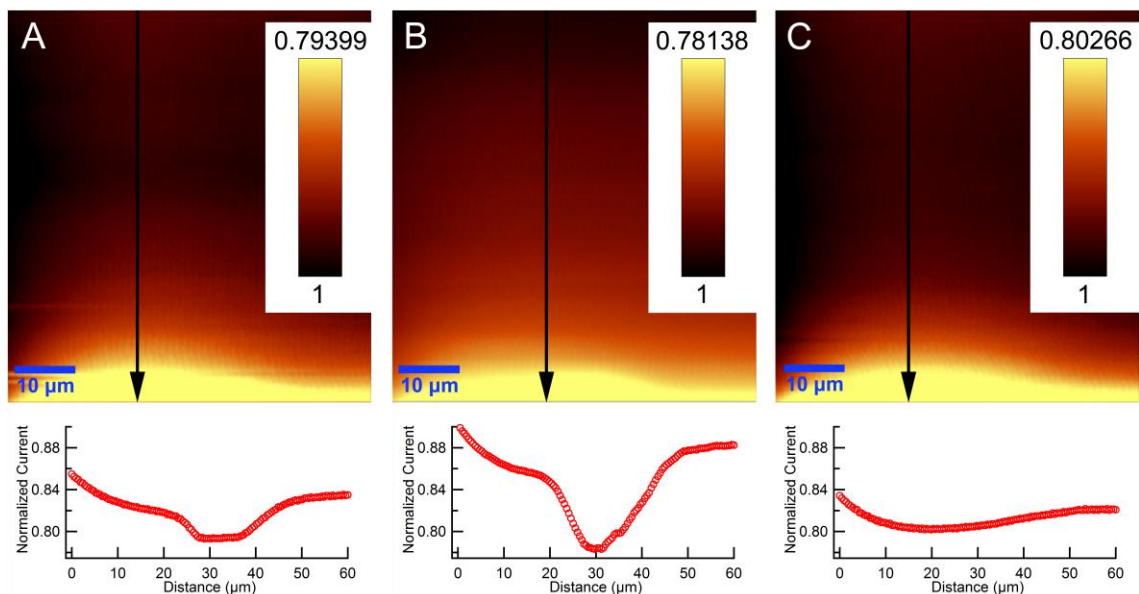
Figure 3.2 - Typical depth scan images of T24 cells incubated with 0, 100, and 1000 µM K$_2$Cr$_2$O$_7$ (A–C), respectively for 1 hr. The blue scale bar in the SECM images represents 10 µm. The black arrows overlaying depth scan images display vertical cross-sections used to extract permeability information. The inset current scale bars display the normalized current of extracted PAC. A horizontal cross section of each cell is provided at a normalized distance of 0.7 from the cell surface. These SECM images were collected using a 10 µm Pt UME with an RG of 3.

3.3.2   Ferrocenemethanol (FcCH$_2$OH) Serving as the Mediator

FcCH$_2$OH is partially permeable to the cell membrane under normal control conditions (81 ± 17 µm/s, Figure 3.3). FcCH$_2$OH strikes a delicate balance between hydrophobicity and hydrophilicity. It is hydrophobic enough to enter the interior of the cell membrane without being repelled, but hydrophilic enough to not be trapped in the hydrophobic

interior of the membrane. Overall, the membrane response of $K_2Cr_2O_7$-treated T24 cells was minimal when incubated with low concentrations of $K_2Cr_2O_7$ (< 50 µM, Figure 3.3A). It is suspected that the membrane stability within this concentration range indicates that the cellular defense mechanisms are able to sufficiently manage the toxic effects of $K_2Cr_2O_7$ within the 1 hr treatment period. These cells also displayed no obvious morphological changes when compared to the control cells.

As the concentrations of the administered $K_2Cr_2O_7$ increased (50-500 µM), the membrane permeability decreased in two distinct steps (Figure 3.3B). The initial decrease (50-100 µM) lowered the average permeability coefficient to 50 µm/s. The second decrease (250-500 µM) matched an average permeability coefficient of 25 µm/s. These changes in membrane permeability (lowering) suggest that the cellular defense systems are working to counteract the $K_2Cr_2O_7$-treatment.

Another explanation is that a decrease in the cell's surface area is causing a decrease in phospholipid spacing. With a closely packed phospholipid bilayer, passive diffusion of FcCH$_2$OH will become increasingly difficult. Membranes with closely packed hydrophilic heads will prevent the flux of the relatively hydrophobic mediator, FcCH$_2$OH. Together, the morphological observations (Figure 3.2) and the membrane permeability response findings (Figure 3.3) support this possible explanation. However, the decrease in permeability is likely caused by some complexity of mechanisms.
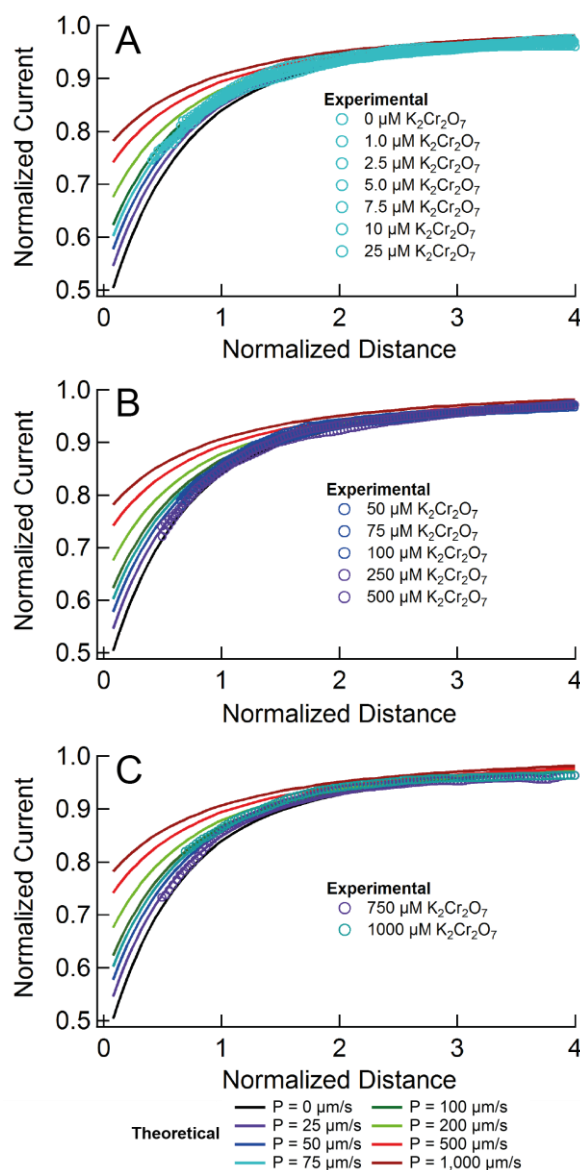
Figure 3.3 - Overlap of experimental PACs with the theoretical ones with definite permeability coefficients, displaying regions of (A) stable, (B) decreasing, and (C) increasing membrane permeability following 1 hr of $K_2Cr_2O_7$ incubation.

At the highest examined concentrations (500-1000 μM $K_2Cr_2O_7$), the membrane permeability increased in two increments (Figure 3.3C). The first increase occurred at 750 μM treatment and matched the simulated permeability coefficient of 50 μm/s. This was followed by a second increase found at the 1000 μM $K_2Cr_2O_7$-treatment, which matched the control cell's permeability coefficient of 75 μm/s.

It is possible that the increase in membrane permeability is due to the overwhelming of the antioxidant defense systems of the cells, since it is well known that the intracellular reduction of Cr (VI) to Cr (III) leads to increased ROS generation.[7, 9] Increased ROS can lead to changes in cellular structure by the disruption of cell signaling pathways, lipid peroxidation, and DNA damage.[1, 3, 9] In particular, lipid peroxidation has been demonstrated to drastically change membrane characteristics by increasing the number polar functional group within the internal membrane region.[11-12] Increased internal membrane polarity will result in decreased membrane fluidity with respect to hydrophobic species, such as $FcCH_2OH$, due to increasing difference in polarity.

Another possible contributing factor to increased membrane permeability is that the increased oxidative stress and DNA damage may lead to cell death via apoptosis or necrosis. Apoptosis has been reported to occur in a number of mammalian cell lines following exposure to Cr (VI).[3, 7] It may also be possible that excessive membrane damage via lipid peroxidation is resulting in a loss of membrane integrity and perhaps cellular death by necrosis. However, as part of the experimental design, the Petri dishes were thoroughly rinsed following metal exposure, likely detaching and removing dying or dead cells. As a result, my current study focuses on the membrane trend of remaining living cells. It is possible that the cellular anti-oxidant systems, such as superoxide dismutase, catalase, and glutathione peroxidase, inadequately deal with the resulting elevated levels of ROS, likely impacting cellular function.

3.3.3 Ferrocenecarboxylic Acid (FcCOO⁻) Serving as the Mediator

Since $FcCOO^-$ is more hydrophilic than $FcCH_2OH$, and is charged in nature, it is unable to cross the cell membrane. Therefore, using $FcCOO^-$ as the redox mediator in bio-SECM allows for a more detailed imaging of the cell's topography under control conditions, as it is largely independent of the effects of membrane permeability. It can also serve as an indicator for significant disruptions in cell membrane performance. Figure 3.3 displays representative PAC curves, for exposure to various $K_2Cr_2O_7$ concentrations in the presence of $FcCOO^-$.

Following 1 hr $K_2Cr_2O_7$ treatment of concentrations less than 500 μM (0, 10, 50, and 250 μM), no detectable changes in permeability were observed (0 m/s, Figure 3.4A). In such cases, the mediator was impermeable to the phospholipid bilayer. At the higher concentrations of this range (50 and 250 μM), a decrease in permeability coefficient was found while using $FcCH_2OH$; however, the detection of such a change is not possible with $FcCOO^-$ (since P = 0 m/s). It is for this reason $FcCOO^-$ is suitable only for detection of significant damage to membrane integrity, and cell topography studies. Membrane stability, as discussed previously, is a result of the cellular defense systems remaining capable of compensating for any increases in ROS from Cr (VI) exposure.

At higher concentrations of treatment (500–1000 μM), an increasing trend in permeability was observed (Figure 3.4B). This trend was similar to that of the $FcCH_2OH$ study. When incubated with 500 μM $K_2Cr_2O_7$, the membrane permeability coefficient increased to 25 μm/s. Treatment of the T24 cells with 750 μM $K_2Cr_2O_7$ increased the membrane permeability coefficient to 200 μm/s. The highest concentration sample (incubated at 1000 μM $K_2Cr_2O_7$) had a membrane permeability coefficient of 500 μm/s. This shows a trend of membrane permeability gradually increasing with increased Cr (VI) concentration. The cause of the permeability increase is attributed to the overwhelming of anti-oxidant defense systems, a rise in levels of ROS and subsequent lipid peroxidation.
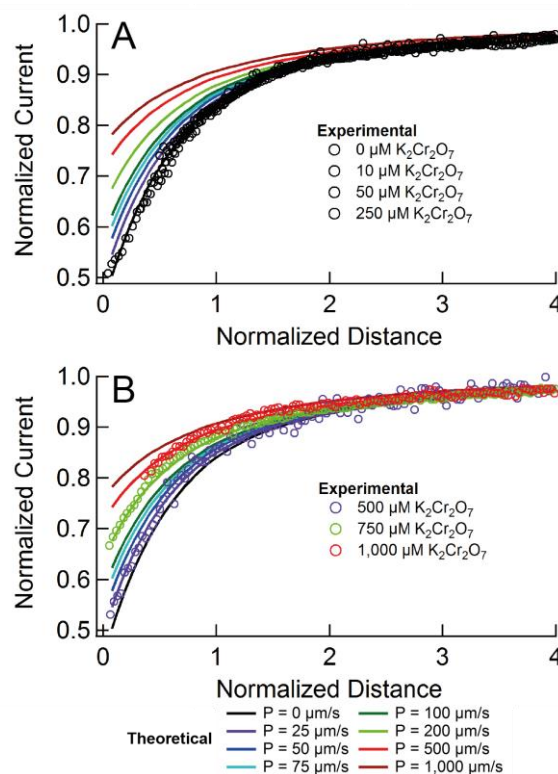
Figure 3.4 - Overlap of experimental PACs with the theoretical ones with definite permeability coefficients, displaying regions of (A) stable and (B) increasing membrane permeability following 1 hr of $K_2Cr_2O_7$ incubation.

3.3.4   Trends in Permeability Coefficient Change

A complete set of membrane permeability data was obtained for each incubation concentration to provide an average membrane permeability coefficient (N > 4 cells). The calculated average permeability coefficients for $K_2Cr_2O_7$ using both the partially permeable $FcCH_2OH$ and impermeable $FcCOO^-$ mediators were plotted against their respective incubation concentrations (Figure 3.5). To clearly visualize the membrane response trend, a logarithmic scale was used to sufficiently space the incubation concentrations along the x-axis.

The trend in permeability coefficient change determined for incubations with $K_2Cr_2O_7$ was found to agree with those discussed previously (Figure 3.3 and Figure 3.4). Figure 3.5A displays the three distinct regions of membrane response using $FcCH_2OH$ as the

redox mediator. A relatively stable region (~75 µm/s) was observed for incubations below 50 µM incubations with $K_2Cr_2O_7$ (region a). Incubations of 50–500 µM $K_2Cr_2O_7$ resulted in the loss of membrane stability and a region of decreasing permeability coefficient was observed (region b). Beyond 500 µM incubations (750, 1000 µM) the permeability coefficient returned to a permeability coefficient similar to control status (region c).

Similarly, when the membrane permeability of $K_2Cr_2O_7$-treated T24 cells were investigated using $FcCOO^-$ as the redox mediator (Figure 3.5B). Stability was observed (0 m/s, region a) across all concentrations occupied by regions a and b in the $FcCH_2OH$ trend. This trend was expected, as the $FcCOO^-$ is both charged and hydrophilic, making it impermeable to a healthy cell membrane. While $FcCH_2OH$ may exhibit a decrease in permeability, the membrane permeability to $FcCOO^-$ cannot succeed lower than 0 m/s. The 500 µM $K_2Cr_2O_7$ concentration appears to be a turning point for 1 hr incubations of T24 cells with $K_2Cr_2O_7$. The permeability of the $FcCOO^-$ increased following this concentration (up to 400 µm/s, region c), similar to that observed with $FcCH_2OH$.
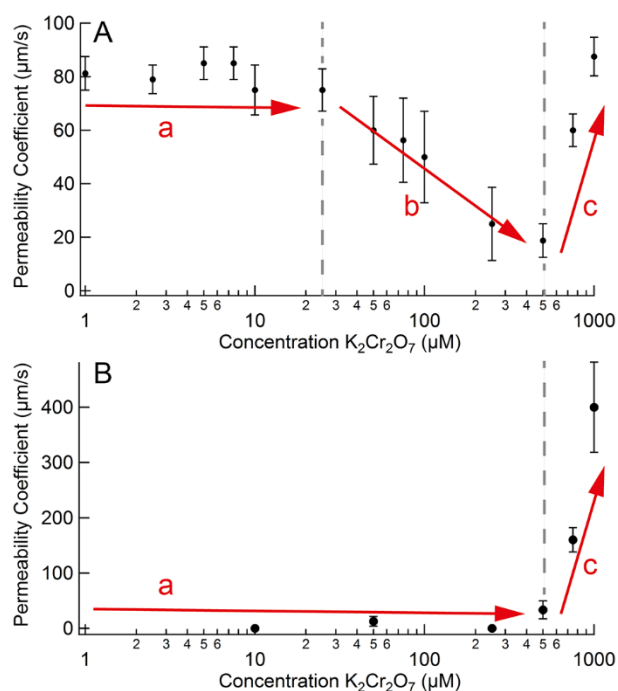
Figure 3.5 - Graphical representation of the membrane permeability change vs K₂Cr₂O₇ incubation concentration, acquired with (A) FcCH₂OH and (B) FcCOOH mediators. Three regions of (a) stable, (b) decreasing, and (c) increasing permeability coefficients are labeled and separated by the grey dashed lines.

3.3.5   Optical Observations

Using the inverted optical microscope integrated into the SECM set-up, single cells were located and imaged at different incubation concentrations of $K_2Cr_2O_7$, while in the presence of FcCH₂OH and FcCOO⁻. The two mediators showed no visible effect on the cells and therefore further discussion focuses on the impact of Cr (VI) exposure. Optical observations made on typical control cells revealed distinct cellular features (Figure 3.6A). The morphology of the control T24 cells provided a benchmark for comparison to the $K_2Cr_2O_7$-treated cell samples. On average, as incubation concentrations reached 100 μM $K_2Cr_2O_7$ (Figure 3.6B), the visible features on the cells receded in comparison to the control cells. Cells were observed to become more rounded with exposure. As incubation concentrations continued to increase, the features seen in control cells were found to return. This is clearly demonstrated in the optical image of average cells incubated with

1000 μM $K_2Cr_2O_7$ (Figure 3.6C). The incubation of T24 cells with higher concentrations of $K_2Cr_2O_7$ yielded decreased populations (confluency) of healthy cells. Since viability was affected, it is assumed that a greater number of unhealthy cells that were loosely bound to the Petri dish were removed during the washing process (see Chapter 3.2.4 SECM Instrumentation and Experimental Procedure).

On average, control cells were found to exhibit several features and were spread over a large area of the Petri dish. Following incubations at intermediate concentrations, the average cell shape was observed to become more rounded by both optical and depth scan observations. The featureless optical images and a decrease in membrane coverage suggest the contraction of cellular membrane morphology. Exceeding intermediate concentrations caused the average T24 cell to return to a status similar to that of the control cells.[53]
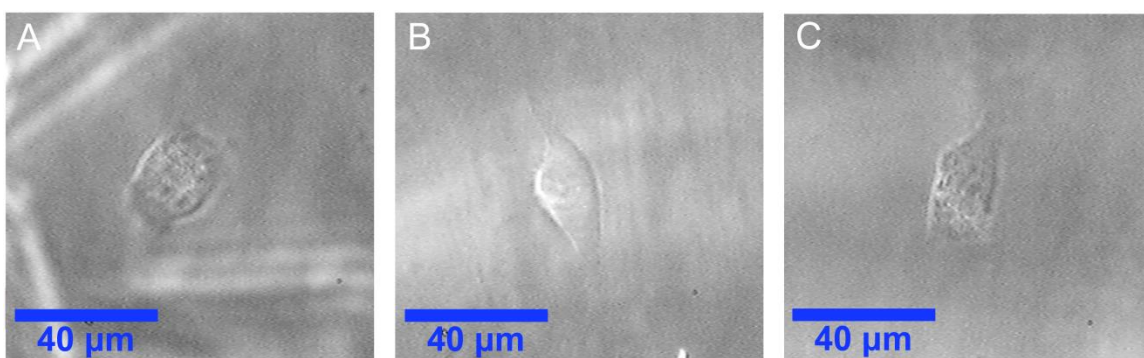
Figure 3.6 - Typical (A-C) optical images of T24 cells incubated with 0, 100, and 1000 μM $K_2Cr_2O_7$, respectively. The scale bar in the images represent 40 μm. These were taken from the same SECM scans shown in Figure 3.2.

3.3.6   MTT Cell Viability Study of T24 Cells Incubated with $K_2Cr_2O_7$ for 1hr

Since membrane permeability was affected by the additions of $K_2Cr_2O_7$ stressor, it was important to assess the viability of the cells. The use of a well-established method of cell viability analysis, such as the MTT cell viability assay,[54] provided a large scale determination of overall health and wellness of the T24 samples (Figure 3.7). The healthy

population of cells exposed to various concentrations of heavy metal stressor for 1 hr, were compared to the healthy population of an untreated sample from the same culture over the same timeframe (Eq. 3.6).

$$cell\ viability\ (\%) = \left(\frac{A_{sample} - A_{blank}}{A_{control} - A_{blank}}\right) 100\% \qquad [3.6]$$

Low concentrations of $K_2Cr_2O_7$ were observed to have little effect on cell viability. Concentrations below 10 µM were found to be within the error bars of the untreated control and each other, over the course of the 1 hr incubation. As $K_2Cr_2O_7$ concentration increased past 10 µM, a gradual decrease in cell viability was observed. This confirms that a relationship between $K_2Cr_2O_7$-treatment and cellular death exists in the T24 cell line. Similar to this cellular viability trend, the SECM-determined membrane permeability to FcCH$_2$OH indicated significant change following treatment with 25 µM $K_2Cr_2O_7$ (Figure 3.5A). The effects of the Cr (VI) stressor can be observed using both experimental methods at the same concentration range. This indicates that the disruptions in membrane permeability may be related to the internal disruption in cell homeostasis, as observed by MTT cell viability assay. If internal processes are influenced by the presence of the Cr (VI), whether by ROS production or some other means, the effects of this stressor are apparent on the membrane integrity of the cells.
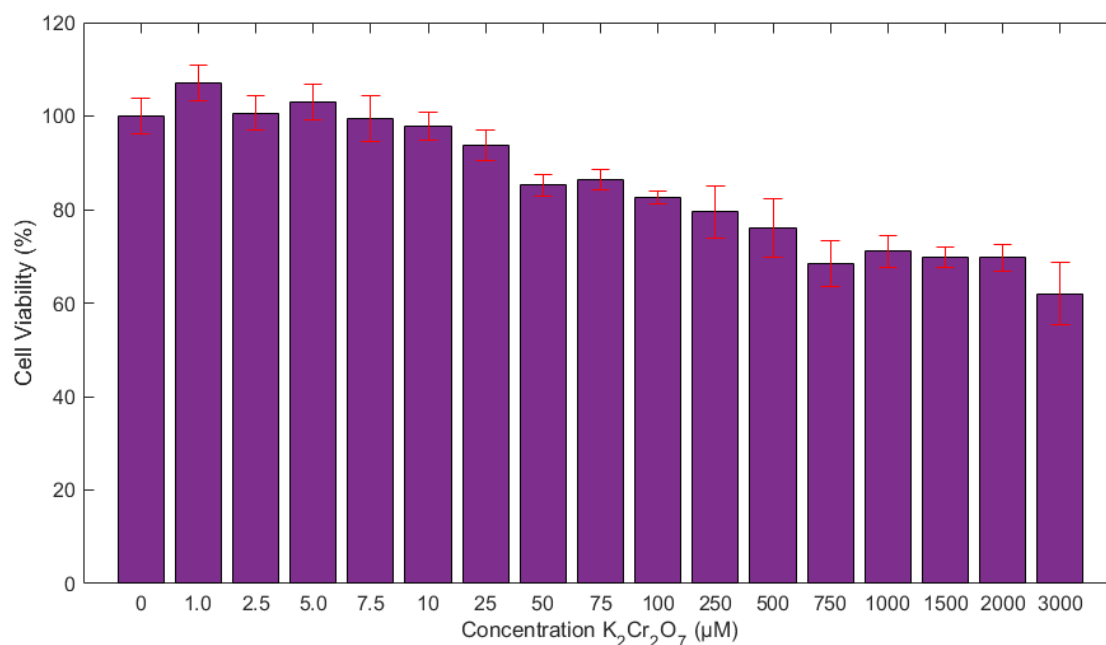
Figure 3.7 - Cell viability of T24 cells treated with a wide range of concentrations of K₂Cr₂O₇ for 1 hr, between 0 µM and 3000 µM. Cell viability measured by MTT cell assay. Represented as Mean ± Standard Error of 4 separate experiments (4-8 replications per experiment).

3.4 Conclusions

By use of SECM, a powerful non-invasive technique for monitoring live cells, the membrane response of T24 cells following exposure to Cr (VI) was successfully reported here. Through comparison of experimental data with theoretical PACs, relative changes in membrane permeability coefficients were determined.

Using FcCH₂OH as the SECM mediator, Cr (VI) exposure lead to the discovery of three distinct concentration-induced membrane permeability regions. With low Cr (VI) dosages (0-50 µM), membrane permeability coefficients were found to be relatively stable, displaying little change compared to control cells. Exceeding low level exposure (50-500 µM), the permeability coefficients decreased. Ultimately with higher (acute) exposure (500-1000 µM), the permeability coefficients increased and returned to values similar to that of control cells. These results agree well with another study in which the T24 cells

were treated with Cd (II) as the toxic metal.[49] However, the response triggered by both Cr (VI) and Cd (II) was found to differ in the concentrations required to initiate each permeability region. These results confirmed that Cr (VI) is less toxic than Cd (II).

The occurrence of significant membrane damage was confirmed using FcCOO⁻ as the SECM mediator. FcCOO⁻ is initially impermeable to the cell membrane and becomes permeable only with significant membrane integrity loss. The MTT cell viability assay confirmed a relationship between cellular death and Cr (VI) exposure. This current study indicates SECM may prove useful in exploring the membrane response in cells to various stimuli. This bioanalytical method is by no means limited to T24 cells and can be applied to other biological systems, such as other cell lines or tissues.

3.5   References

1.   O'Brien, T. J.; Ceryak, S.; Patierno, S. R., Complexities of Chromium Carcinogenesis: Role of Cellular Response, Repair and Recovery Mechanisms. *Mutat. Res.* **2003,** *533* (1-2), 3-36.
2.   Chen, T.; Zhou, Z.; Xu, S.; Wang, H.; Lu, W., Adsorption Behavior Comparison of Trivalent and Hexavalent Chromium on Biochar Derived from Municipal Sludge. *Bioresour. Technol.* **2015,** *190*, 388-94.
3.   Bagchi, D.; Bagchi, M.; Stohs, S. J., Chromium (Vi)-Induced Oxidative Stress, Apoptotic Cell Death and Modulation of P53 Tumor Suppressor Gene. *Mol. Cell. Biochem.* **2001,** *222* (1-2), 149-58.
4.   Catelas, I.; Petit, A.; Vali, H.; Fragiskatos, C.; Meilleur, R.; Zukor, D. J.; Antoniou, J.; Huk, O. L., Quantitative Analysis of Macrophage Apoptosis Vs. Necrosis Induced by Cobalt and Chromium Ions in Vitro. *Biomaterials* **2005,** *26* (15), 2441-53.
5.   Fang, Z.; Zhao, M.; Zhen, H.; Chen, L.; Shi, P.; Huang, Z., Genotoxicity of Tri- and Hexavalent Chromium Compounds in Vivo and Their Modes of Action on DNA Damage in Vitro. *PLoS One* **2014,** *9* (8), e103194.
6.   Kovacik, J.; Babula, P.; Hedbavny, J.; Krystofova, O.; Provaznik, I., Physiology and Methodology of Chromium Toxicity Using Alga Scenedesmus Quadricauda as Model Object. *Chemosphere* **2015,** *120*, 23-30.
7.   Wang, X. F.; Xing, M. L.; Shen, Y.; Zhu, X.; Xu, L. H., Oral Administration of Cr(Vi) Induced Oxidative Stress, DNA Damage and Apoptotic Cell Death in Mice. *Toxicol.* **2006,** *228* (1), 16-23.
8.   Mohmand, J.; Eqani, S. A.; Fasola, M.; Alamdar, A.; Mustafa, I.; Ali, N.; Liu, L.; Peng, S.; Shen, H., Human Exposure to Toxic Metals Via Contaminated Dust: Bio-Accumulation Trends and Their Potential Risk Estimation. *Chemosphere* **2015,** *132*, 142-51.

9. Hartwig, A., Metal Interaction with Redox Regulation: An Integrating Concept in Metal Carcinogenesis? *Free Radic. Biol. Med.* **2013,** *55*, 63-72.

10. Kalahasthi, R. B.; Rao, R. H.; Murthy, R. B.; Kumar, M. K., Effect of Chromium(Vi) on the Status of Plasma Lipid Peroxidation and Erythrocyte Antioxidant Enzymes in Chromium Plating Workers. *Chem. Biol. Interact.* **2006,** *164* (3), 192-9.

11. Cordeiro, R. M., Reactive Oxygen Species at Phospholipid Bilayers: Distribution, Mobility and Permeation. *Biochim. Biophys. Acta* **2014,** *1838* (1 Pt B), 438-44.

12. Wong-Ekkabut, J.; Xu, Z.; Triampo, W.; Tang, I. M.; Tieleman, D. P.; Monticelli, L., Effect of Lipid Peroxidation on the Properties of Lipid Bilayers: A Molecular Dynamics Study. *Biophys. J.* **2007,** *93* (12), 4225-36.

13. Hutchinson, T. H.; Williams, T. D.; Eales, G. J., Toxicity of Cadmium, Hexavalent Chromium and Copper to Marine Fish Larvae (Cyprinodon Variegatus) and Copepods (Tisbe Battagliai). *Mar. Environ. Res.* **1994,** *38* (4), 275-290.

14. Gikas, P.; Romanos, P., Effects of Tri-Valent (Cr(Iii)) and Hexa-Valent (Cr(Vi)) Chromium on the Growth of Activated Sludge. *J. Hazard. Mater.* **2006,** *133* (1-3), 212-7.

15. Petersen, R.; Thomsen, J. F.; Jorgensen, N. K.; Mikkelsen, S., Half Life of Chromium in Serum and Urine in a Former Plasma Cutter of Stainless Steel. *Occup. Environ. Med.* **2000,** *57* (2), 140-2.

16. Setyaningsih, Y.; Husodo, A. H.; Astuti, I., Detection of Urinary 8-Hydroxydeoxyguanosine (8-Ohdg) Levels as a Biomarker of Oxidative DNA Damage among Home Industry Workers Exposed to Chromium. *Procedia Environ. Sci.* **2015,** *23*, 290-296.

17. Wright, A.; Bubb, W. A.; Hawkins, C. L.; Davies, M. J., Singlet Oxygen–Mediated Protein Oxidation: Evidence for the Formation of Reactive Side Chain Peroxides on Tyrosine Residues. *Photochem. Photobiol.* **2002,** *76* (1), 35-46.

18. Dixit, R.; Cyr, R., Cell Damage and Reactive Oxygen Species Production Induced by Fuorescence Microscopy: Effect on Mitosis and Guidelines for Non-Invasive Fuorescence Microscopy. *Plant J.* **2003,** *36*, 280-290.

19. Bard, A. J.; Denuault, G.; Lee, C.; Mandler, D.; Wipf, D. O., Scanning Electrochemical Microscopy - a New Technique for the Characterization and Modification of Surfaces. *Acc. Chem. Res.* **2002,** *23* (11), 357-363.

20. Bard, A. J.; Fan, F. R. F.; Kwak, J.; Lev, O., Scanning Electrochemical Microscopy. Introduction and Principles. *Anal. Chem.* **2002,** *61* (2), 132-138.

21. Li, M. S. M.; Filice, F. P.; Henderson, J. D.; Ding, Z., Probing Cd2+-Stressed Live Cell Membrane Permeability with Various Redox Mediators in Scanning Electrochemical Microscopy. *J. Phys. Chem. C* **2016,** *120* (11), 6094-6103.

22. Li, M. S. M.; Filice, F. P.; Ding, Z., Determining Live Cell Topography by Scanning Electrochemical Microscopy. *J. Electroanal. Chem.* **2016,** *779*, 176-186.

23. Polcari, D.; Dauphin-Ducharme, P.; Mauzeroll, J., Scanning Electrochemical Microscopy: A Comprehensive Review of Experimental Parameters from 1989 to 2015. *Chem. Rev.* **2016,** *116* (22), 13234-13278.

24. Ding, Z.; Quinn, B. M.; Bard, A. J., Kinetics of Heterogeneous Electron Transfer at Liquid/Liquid Interfaces as Studied by Secm. *J. Phys. Chem. B* **2001,** *105* (27), 6367-6374.

25. Nowierski, C.; Noël, J. J.; Shoesmith, D. W.; Ding, Z., Correlating Surface Microstructures with Reactivity on Commercially Pure Zirconium Using Scanning Electrochemical Microscopy and Scanning Electron Microscopy. *Electrochem. Commun.* **2009,** *11* (6), 1234-1236.

26. Yin, Y.; Niu, L.; Lu, M.; Guo, W.; Chen, S., In Situ Characterization of Localized Corrosion of Stainless Steel by Scanning Electrochemical Microscope. *Appl. Surf. Sci.* **2009,** *255* (22), 9193-9199.

27. Tang, J.; Zheng, J.-J.; Yu, Y.-T.; Chen, l.; Zhang, N.; Tian, Z., Selective Etching of Zno Films on an Ito Substrate Using a Scanning Electrochemical Microscope. *Electrochim. Acta* **2012,** *83*, 247-252.

28. Eifert, A.; Mizaikoff, B.; Kranz, C., Advanced Fabrication Process for Combined Atomic Force-Scanning Electrochemical Microscopy (Afm-Secm) Probes. *Micron* **2015,** *68*, 27-35.

29. Bard, A. J.; Li, X.; Zhan, W., Chemically Imaging Living Cells by Scanning Electrochemical Microscopy. *Biosens. Bioelectron.* **2006,** *22* (4), 461-72.

30. Zhao, X.; Diakowski, P. M.; Ding, Z., Deconvoluting Topography and Spatial Physiological Activity of Live Macrophage Cells by Scanning Electrochemical Microscopy in Constant-Distance Mode. *Anal. Chem.* **2010,** *82* (20), 8371-3.

31. Huang, C.; Liu, C.; Loo, J.; Stakenborg, T.; Lagae, L., Single Cell Viability Observation in Cell Dielectrophoretic Trapping on a Microchip. *Appl. Phys. Lett.* **2014,** *104* (1), 013703.

32. Koley, D.; Bard, A. J., Inhibition of the Mrp1-Mediated Transport of the Menadione-Glutathione Conjugate (Thiodione) in Hela Cells as Studied by Secm. *Proc. Nat. Acad. Sci. U.S.A.* **2012,** *109* (29), 11522-7.

33. Kim, J.; Izadyar, A.; Shen, M.; Ishimatsu, R.; Amemiya, S., Ion Permeability of the Nuclear Pore Complex and Ion-Induced Macromolecular Permeation as Studied by Scanning Electrochemical and Fluorescence Microscopy. *Anal. Chem.* **2014,** *86* (4), 2090-8.

34. Bergner, S.; Wegener, J.; Matysik, F.-M., Monitoring Passive Transport of Redox Mediators across a Confluent Cell Monolayer with Single-Cell Resolution by Means of Scanning Electrochemical Microscopy. *Anal. Methods* **2012,** *4* (3), 623-629.

35. Kuss, S.; Cornut, R.; Beaulieu, I.; Mezour, M. A.; Annabi, B.; Mauzeroll, J., Assessing Multidrug Resistance Protein 1-Mediated Function in Cancer Cell Multidrug Resistance by Scanning Electrochemical Microscopy and Flow Cytometry. *Bioelectrochemistry* **2011,** *82* (1), 29-37.

36. Kuss, S.; Polcari, D.; Geissler, M.; Brassard, D.; Mauzeroll, J., Assessment of Multidrug Resistance on Cell Coculture Patterns Using Scanning Electrochemical Microscopy. *Proc. Nat. Acad. Sci. U.S.A.* **2013,** *110* (23), 9249-54.

37.   Zhao, X.; Zhang, M.; Long, Y.; Ding, Z., Redox Reactions of Reactive Oxygen Species in Aqueous Solutions as the Probe for Scanning Electrochemical Microscopy of Single Live T24 Cells. *Can. J. Chem.* **2010,** *88* (6), 569-576.

38.   Zhang, M. M.; Long, Y. T.; Ding, Z., Cisplatin Effects on Evolution of Reactive Oxygen Species from Single Human Bladder Cancer Cells Investigated by Scanning Electrochemical Microscopy. *J. Inorg. Biochem.* **2012,** *108*, 115-22.

39.   Zhao, X.; Lam, S.; Jass, J.; Ding, Z., Scanning Electrochemical Microscopy of Single Human Urinary Bladder Cells Using Reactive Oxygen Species as Probe of Inflammatory Response. *Electrochem. Commun.* **2010,** *12* (6), 773-776.

40.   Zhao, X.; Petersen, N. O.; Ding, Z., Comparison Study of Live Cells by Atomic Force Microscopy, Confocal Microscopy, and Scanning Electrochemical Microscopy. *Can. J. Chem.* **2007,** *85* (3), 175-183.

41.   Zhan, D.; Li, X.; Nepomnyashchii, A. B.; Alpuche-Aviles, M. A.; Fan, F.-R. F.; Bard, A. J., Characterization of Ag+ Toxicity on Living Fibroblast Cells by the Ferrocenemethanol and Oxygen Response with the Scanning Electrochemical Microscope. *J. Electroanal. Chem.* **2013,** *688*, 61-68.

42.   Li, X.; Bard, A. J., Scanning Electrochemical Microscopy of Hela Cells – Effects of Ferrocene Methanol and Silver Ion. *J. Electroanal. Chem.* **2009,** *628* (1-2), 35-42.

43.   Sun, P.; Laforge, F. O.; Abeyweera, T. P.; Rotenberg, S. A.; Carpino, J.; Mirkin, M. V., Nanoelectrochemistry of Mammalian Cells. *Proc. Nat. Acad. Sci. U.S.A.* **2008,** *105* (2), 443-8.

44.   Cai, C.; Liu, B.; Mirkin, M. V.; Frank, H. A.; Rusling, J. F., Scanning Electrochemical Microscopy of Living Cells. 3.Rhodobactersphaeroides. *Anal. Chem.* **2002,** *74* (1), 114-119.

45.   Feng, W.; Rotenberg, S. A.; Mirkin, M. V., Scanning Electrochemical Microscopy of Living Cells. 5. Imaging of Fields of Normal and Metastatic Human Breast Cells. *Anal. Chem.* **2003,** *75* (16), 4148-54.

46.   Liu, B.; Cheng, W.; Rotenberg, S. A.; Mirkin, M. V., Scanning Electrochemical Microscopy of Living Cells. *J. Electroanal. Chem.* **2001,** *500* (1-2), 590-597.

47.   Liu, B.; Rotenberg, S. A.; Mirkin, M. V., Scanning Electrochemical Microscopy of Living Cells: Different Redox Activities of Nonmetastatic and Metastatic Human Breast Cells. *Proc. Nat. Acad. Sci. U.S.A.* **2000,** *97* (18), 9855-60.

48.   Mosmann, T., Rapid Colorimetric Assay for Cellular Growth and Survival: Application to Proliferation and Cytotoxicity Assays. *J. Immunol. Methods* **1983,** *65* (1-2), 55-63.

49.   Filice, F. P.; Li, M. S.; Henderson, J. D.; Ding, Z., Mapping Cd(2)(+)-Induced Membrane Permeability Changes of Single Live Cells by Means of Scanning Electrochemical Microscopy. *Anal. Chim. Acta* **2016,** *908*, 85-94.

50.   Kuss, S.; Trinh, D.; Danis, L.; Mauzeroll, J., High-Speed Scanning Electrochemical Microscopy Method for Substrate Kinetic Determination: Method and Theory. *Anal. Chem.* **2015,** *87* (16), 8096-101.

51.   Guo, J.; Amemiya, S., Permeability of the Nuclear Envelope at Isolated Xenopus Oocyte Nuclei Studied by Scanning Electrochemical Microscopy. *Anal. Chem.* **2005,** *77* (7), 2147-56.

52.   Miao, W.; Ding, Z.; Bard, A. J., Solution Viscosity Effects on the Heterogeneous Electron Transfer Kinetics of Ferrocenemethanol in Dimethyl Sulfoxide–Water Mixtures. *J. Phys. Chem. B* **2002,** *106* (6), 1392-1398.

53.   Henderson, J. D.; Filice, F. P.; Li, M. S. M.; Ding, Z., Tracking Live Cell Response to Cadmium (Ii) Concentrations by Scanning Electrochemical Microscopy. *J. Inorg. Biochem.* **2016,** *158*, 92-98.

54.   Soleimani, A.; Moustafa, M. M. A. R.; Borecki, A.; Gillies, E. R., A Comparison of Covalent and Noncovalent Strategies for Paclitaxel Release Using Poly(Ester Amide) Graft Copolymer Micelles. *Can. J. Chem.* **2015,** *93* (4), 399-405.

Chapter 4

4 The Effects of Chronic Exposure to Hexavalent Chromium on Single Live Cells Interrogated by Scanning Electrochemical Microscopy

Chromium is a useful heavy metal which has been employed in numerous industrial and home applications. However, there are several known health risks associated with its uses. Cr (VI) is a toxic heavy metal which serves no essential biological role in humans. It has been associated with oxidative stress, cytotoxicity, and carcinogenicity. Contamination of groundwater or soil due to improper handling lead to long term environmental damage. This study explores the effects of long duration chronic exposure to Cr (VI) on live human cells. Herein, scanning electrochemical microscopy (SECM) depth scan imaging was employed to monitor the membrane permeability of single live human bladder cancer (T24) cells following incubation with various Cr (VI) concentration stimuli. SECM was used to provide insights into the long duration effects on membrane homeostasis of individual cells exposed to constant levels of Cr (VI). Further investigation of total population viability was performed by MTT assay. Dependent on the exposure time, transition between three distinct trends was observed. At short incubation times ($\leq$1-3 hr) with low concentrations of Cr (VI) (0-10 μM), membrane permeability was largely unaffected. As time increased a decrease in membrane permeability coefficient was observed, reaching a minimum at 3-6 hr. Following this a dramatic increase in membrane permeability was observed as cell viability decreased. Higher concentrations were also found to accelerate the timeframe at which these trends occurred. These findings further demonstrate the strength of SECM as a bioanalytical technique for monitoring cellular homeostasis.

4.1 Introduction

Chromium is an important industrial element, used in leather tanning, chrome plating, steel manufacture, welding, production of pigments and dyes, as well as ore and petroleum refining processes.[1] Chromium is most commonly found in its stable metallic, hexavalent or trivalent oxidation states, Cr(0), Cr (VI) and Cr (III), respectively. The heavy use of Cr in industry processes has resulted in the environmental contamination of groundwater and soil in many locations, with a long environmental half-life.[1-2] Non-industrial sources also exist for Cr exposure, including housewares, automobile emissions and cigarette smoke. Increased environmental concentrations of heavy metals, including Cr,[1, 3] have led to research efforts focusing on the biological effects of their exposure. In the case of Cr, the resulting oxidative stress, cytotoxicity, and carcinogenicity associated with many Cr-containing complexes have been extensively studied.[1, 4-8]

Cr (VI) serves no essential biological role in humans. Cr (VI) is classified as a known group I carcinogen by the International Agency for Research on Cancer (IARC).[9-10] Cr(VI) also has numerous short-term detrimental effects, such as the generation of reactive oxygen species (ROS) and reactive nitrogen species (RNS).[8, 11] It is also capable of inhibiting antioxidant enzymes, and binding antioxidant defense systems such as glutathione (GSH), leading to greater oxidative stress.[11-12] Cr (VI) can readily enter cells through non-specific phosphate/sulfate transporters, where it may undergo reduction to Cr (III), with reactive intermediates formed during this reduction process (Cr (V), and Cr (IV)).[4, 13] High genomic instability in cells is generally observed following Cr (VI) exposure, due to heavy metal induced protein, and DNA damage.[1]

ROS play an important role in cell signaling, as well as other biological processes. Disruptions in homeostatic levels of ROS can affect many essential cell processes, such as cell proliferation and anti-inflammatory responses.[11] Elevated levels of ROS have also been associated with oxidative damage to cellular and nuclear membranes, as well as damage to the endoplasmic reticulum and other key structures by lipid peroxidation as well as oxidative DNA damage and strand breaks.[11-12, 14-15]

Cr (VI) commonly bioaccumulates in the kidney, liver, and lungs of mammals, leading to adverse health effects in these tissues, as well as related tissues.[8, 16-17] Monitoring of exposure to Cr is commonly done through urine content, for which a substantial half-life of 10 years in the body has been reported.[17] Due to Cr (VI)'s ability to cause various forms of biological damage, as well as its long half-life in the body, my current study has focused on the long duration exposure of bladder cells as a model system. By using a human urinary bladder cancer (T24) cell line, I aim to investigate the effects of Cr toxicity on membrane homeostasis. T24 cells have a doubling time of 18-19 h, allowing the study of chronic potassium dichromate ($K_2Cr_2O_7$) over multiple generations of cell division.

Analysis of cell membrane transport can be performed through a number of possible methods but scanning electrochemical microscopy (SECM) provides some unique advantages for study of individual live cells. SECM allows for the non-destructive, non-invasive study of single live cells, given an appropriate, non-toxic mediator is selected. SECM makes no direct contact with the cell, and can be performed under homeostatic conditions. This permits the continuous monitoring of dynamic cellular processes of living unaltered biological samples.

SECM is a powerful scanning probe microscopy (SPM) technique. SECM benefitted greatly from the seminal work accomplished by Bard et al. since 1989.[18-19] SECM has been employed in a vast number of applications[20] including but not limited to kinetic studies,[21] surface and interface studies,[22-23] microstructure fabrication,[24-25] as well as the mentioned biological applications such as cellular imaging,[26-27] membrane transport,[28-31] multidrug resistance,[32-33] ROS and RNS mapping,[27, 34-37] and cellular redox processes.[38-44]

SECM commonly utilizes an ultramicroelectrode (UME) or nanoelectrode as the working electrode. This technique is used to monitor the electrochemical generation/regeneration of the mediating species, which can either be added or native to the sample under study. By operating SECM in depth scan mode, topographic information is provided in addition to electrochemical activity. In its applications to live cells, the SECM is operated in feedback mode, allowing dynamic cellular processes to be observed through relative

changes in faradaic current at the UME probe. As the UME approaches the cellular membrane, a current drop is commonly observed as the membrane hinders diffusion to the electrode tip (negative feedback). SECM utilizes this phenomenon to determine surface topography. However, with the use of a membrane-permeable electrochemical mediator, membrane permeability of the cell can be characterized. Finite element analysis simulations of the electrochemical system can be used in conjunction with this experimental technique, to provide quantitative analysis of cell membrane permeability. Approach to a more permeable membrane exhibits a much smaller decrease in current, as the mediator is able to move through the cell interior and replenish unreacted mediator at the electrode tip. The UME tip current relative to distance from the membrane is commonly reported as a probe approach curve (PAC). The electrochemical mediator used to determine membrane permeability in this study, ferrocenemethanol, has been shown to have no detrimental effects on the studied cell line over the experimental timeframe.[36, 39, 45-46]

I previously reported on the $K_2Cr_2O_7$ induced membrane permeability change in T24 cells when incubated with a wide concentration range.[47] Exposure to the $K_2Cr_2O_7$ stressor was carried out over a 1 h incubation period. This study provided insight into the immediate effects of acute exposure to $K_2Cr_2O_7$. Low concentrations ≤25 µM for 1 h incubation had no appreciable effect on membrane permeability. Exceeding these concentrations, a decrease in membrane permeability was observed, as well as a decrease in cellular viability. At concentrations exceeding 500 µM, membrane permeability sharply increased. This increase also included normally impermeable charged mediators (ferrocenecarboxylic acid).

This short (1 h) incubation time, however, does not provide information on the long-term effects of $K_2Cr_2O_7$. By examining lower concentrations (0-10 µM), where negligible effect was previously observed, and extending the incubation time, the effects of $K_2Cr_2O_7$ will be further illustrated, on single live cells. Herein, the effects associated with long duration chronic exposure to low concentrations of $K_2Cr_2O_7$ on cell membrane permeability and cellular viability by SECM will be examined. SECM as a powerful

bioanalytical tool will be shown to provide localized membrane permeability study of single live cells.

4.2 Experimental Section

4.2.1 Materials

FcCH$_2$OH (97%), potassium chloride (KCl, 99%), and K$_2$Cr$_2$O$_7$ (99%) were purchased from Sigma-Aldrich Canada and used without further purification. Stock SECM mediator solution was prepared using 0.9 mM FcCH$_2$OH, dissolved in 1× phosphate buffered saline (PBS, Life Technologies, Burlington, ON). Stock solutions of 0.25 M K$_2$Cr$_2$O$_7$ were prepared using autoclaved deionized water (18.2 MΩ.cm, MilliQ water, Etobicoke, ON) and syringe-filtered through sterile 0.2 μm Supor$^®$ Membrane (PALL Life Sciences, Mississauga, ON). 3-(4,5-dimethylthiazol-2-yl)-2,5-diphenyltetrazolium bromide (MTT) was acquired from R&D Systems Inc. (Minneapolis, MN) as part of the TACS® MTT Cell Proliferation Assay Kit. Spectroscopic grade dimethyl sulfoxide (DMSO) was used to dissolve the formazan crystals (Caledon Laboratory Ltd., Georgetown, ON).

4.2.2 Cell Preparation

Human bladder cancer cells (T24 cells (HTB-4™)) were acquired from American Type Culture Collection (ATCC, Manassas, VA, USA) and maintained according to ATCC protocol. Cells were cultured in McCoy's 5a medium (ATCC, Manassas, VA, USA), modified with 10% fetal bovine serum (Invitrogen, Burlington, ON). T24 cells were grown in a humidified incubator at 37 °C and 5 % CO$_2$ (Sanyo, Japan). Care was taken to ensure all experimentation occurred within a small passage number range (P47-P55). For SECM live cell experiments, T24 cells were aliquoted directly onto glass-bottom Petri dishes (P50G-0-30-F, MatTek Corporation, Ashland, MA, USA). K$_2$Cr$_2$O$_7$ (stock solution) was injected into the growth medium, simulating the presence of the external stressor in the cells immediate environment, in the desired concentrations for K$_2$Cr$_2$O$_7$ testing. The cells were then incubated for the desired timeframe. Prior to analysis via SECM, the growth medium was decanted, and the cells were washed twice with 1× PBS.

The medium was then replaced with the FcCH$_2$OH mediator solution for SECM experiments.

4.2.3   Cell Viability

MTT tetrazolium dye (yellow) is capable of moving into cells and is reduced in healthy cells to produce formazan crystals (purple). These crystals can be dissolved and detected using a spectrophotometer. Cellular viability tests were performed using the MTT assay procedure following 1, 2, 3, and 5 days exposure to K$_2$Cr$_2$O$_7$.[48] Briefly, about 20,000 T24 cells (Determined with a haemocytometer) were plated onto Corning Scientific Costar™ 96-well polystyrol flat bottom plates and allowed to incubate for 24 h. K$_2$Cr$_2$O$_7$ was then administered to the cell sample along with fresh medium. Sodium dodecyl sulfate (SDS) was used as a positive control for the assay at 0.05, 0.10, 0.15, and 0.20 mg/mL. Wells containing no cells (blank wells) were also prepared to allow for the removal of background medium effects and treated by the full MTT protocol.

Following incubation with K$_2$Cr$_2$O$_7$ for the desired duration, the growth medium was replaced with 100 µL of fresh medium (absent of phenol red) and 10 µL of the MTT reagent. The sample was incubated for an additional 6 hr allowing the formazan crystals to form. The MTT solution was then removed and the formazan crystals were dissolved with 50 µL of spectroscopic grade DMSO. The absorbance (Abs) at 540 nm was read by a M1000 PRO plate reader (Tecan, Switzerland) following 1 s of shaking at 2 mm amplitude and 654 rpm. The effects FcCH$_2$OH have been investigated elsewhere and determined to be non-toxic during these experimental conditions.[46]

4.2.4   SECM Instrumentation and Experimental Procedure

A detailed description of the SECM instrumentation and experimental procedures can be found in Chapter 2 section 2.2.5.[49] Briefly, SECM experiments were carried out using a modified Alpha-SNOM (WITec, Ulm, Germany). The SNOM has been outfitted with a custom fabricated UME mount in place of a conventional upright objective lens, and a micro-incubator Petri dish mount (Bioscience Tools, San Diego, California, USA). The inverted objective lens (50×, N.A. 0.55, W.D. 10.1 mm, Nikon, Japan) was used to assist

in the positioning of the UME over live cells of interest, as well as provide optical imaging of the cells under study. High resolution UME positioning was achieved through the WITec piezoelectric positioning system. Electrochemical instrumentation consisted of a CH Instruments Electrochemical Analyzer (CHI800B, Austin, TX) and CHI200 Picoamp Booster to enhance the low current signal observed with small electrodes and dilute solutions while limiting signal noise. A simple two-electrode set-up was used with the UME as the working electrode, and a Ag/AgCl wire as the reference/counter electrode. All potentials reported in this report are vs Ag/AgCl. Before each experiment, cyclic voltammetry (CV) was used to test for steady-state performance of the UME probe and solution. The Petri dish containing the $K_2Cr_2O_7$-treated cells (30-40% confluency) was then secured to the heating stage mount maintained at 37.0 ± 0.2 ˚C. Each Petri dish was analyzed for a maximum duration of 60 min. A biased UME tip potential of 0.3 V (identified through CV) was applied to obtain steady state current with the $FcCH_2OH$ electrochemical mediator. SECM analysis of all samples was performed at a maximum UME tip speed of 21.5 µm/s, to limit the effects of forced convection and maintain steady state current.[50] The SECM depth scan imaging method was utilized on the desired cells. Depth scan analyzes a 2D region of space above the sample, imaging in the x-z plane. Depth scan imaging produces real time probe-to-cell distance information and assists in preventing an electrode collision with the sample. Depth scan also allows for the acquisition of hundreds of PACs per single scan. Manipulation of depth scan parameters, such as x and z movement distance, and image resolution, was made possible through the WITec software.

4.2.5   Simulation
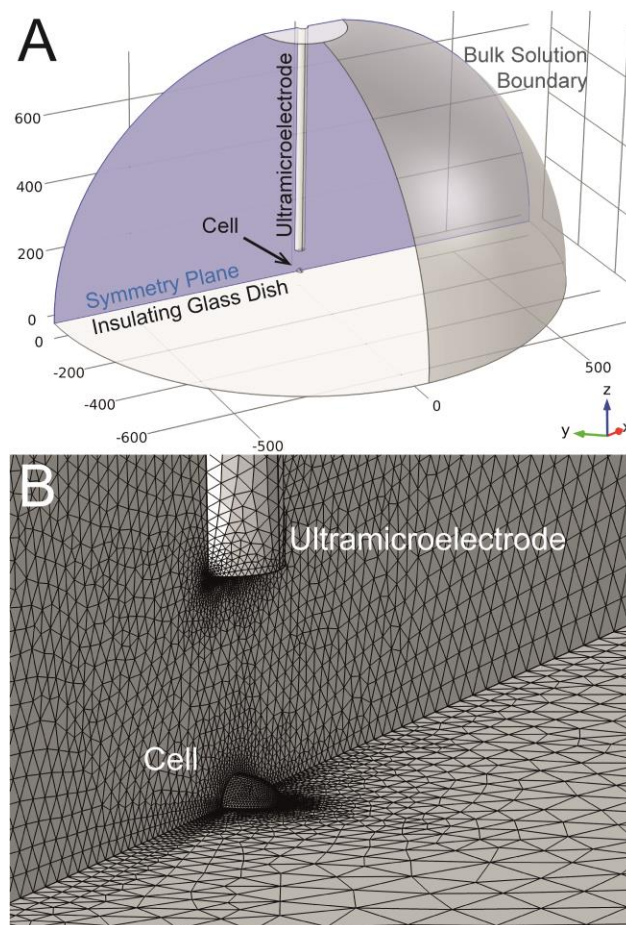
Figure 4.1 - (A) 3D model of the SECM approach to an isolated cell with key features, boundaries, and domains labeled. (B) Zoomed in and labelled view of the Meshed 3D model, focusing on the electrode tip in close proximity to the cell membrane.

Theoretical PACs were generated using COMSOL Multiphysics software (v5.2). A 3D model with a symmetry plane was created to simulate the same physical geometry as the SECM experiments. The symmetry plane bisected the UME and cell, along both of their centers (Figure 4.1A). The electrode geometry was defined to recreate the physical characteristics of the UME utilized for the experimental analysis (10 µm Pt diameter, RG3). Cells were surveyed optically and measured to determine the average T24 cell size (94 cells). The long axis of the cell has an average diameter of 27.9 ± 0.6 µm, while the

shorter axis was determined to be 17.6 ± 0.3 µm. The average cell height was determined previously to be 8.7 ± 3.3 µm.[46] Therefore, a quarter 3D ellipsoid was used to represent the cell geometry with radii y = 14.0 µm, x = 9.0 µm, and z = 8.0 µm. The model is defined as two separate domains, each with their own geometry and physics. The cell interior and solution domains each maintain their own concentration of mediator (C_C, and C_B respectively). The initial states of these domain concentrations were specified as C_B = 0.9 mM $FcCH_2OH$ and C_C = 0 M $FcCH_2OH$. In the solution domain, the bulk solution boundaries were defined as being 150× the Pt UME radius away from the cell (750 µm away). These boundaries were defined to regenerate the same concentration as the initial solution (0.9 mM), simulating a theoretical infinite volume of solution extending beyond the model. The rate of solution transport is governed by the diffusion coefficient for the model (D), and Fick's second law of diffusion (Eqs. 4.1 and 4.2). The diffusion coefficient for $FcCH_2OH$ in both domains was set to 7.6×10^{-10} m^2/s.[45, 51-52]

$$\frac{\partial C_B(x,y,z)}{\partial t} = D \left(\frac{\partial^2 C_B(x,y,z)}{\partial x^2} + \frac{\partial^2 C_B(x,y,z)}{\partial y^2} + \frac{\partial^2 C_B(x,y,z)}{\partial z^2} \right) \text{ [4.1]}$$

$$\frac{\partial C_C(x,y,z)}{\partial t} = D \left(\frac{\partial^2 C_C(x,y,z)}{\partial x^2} + \frac{\partial^2 C_C(x,y,z)}{\partial y^2} + \frac{\partial^2 C_C(x,y,z)}{\partial z^2} \right) \text{ [4.2]}$$

For the $FcCH_2OH$ mediator, a diffusion limited one-electron oxidation reaction will occur under adequate potential bias. This is recreated in the simulation by defining a mediator concentration of zero at the biased Pt surface. The cell membrane is defined as a flux boundary (Eqs. 4.3 and 4.4), allowing for the transport across the membrane boundary, between the two defined domains (cell and solution). The flux across the membrane boundary is dependent on a permeability coefficient (P) and the simulated concentration difference across the membrane boundary.

$$f_{in} = P(C_B - C_C) \quad \text{[4.3]}$$

$$f_{out} = P(C_C - C_B) \quad \text{[4.4]}$$

The COMSOL model geometry was then meshed using a free tetrahedral mesh. The meshing element size is directly related to the accuracy of the finite element analysis

simulation (Figure 4.1B). Therefore, in regions of the model where the concentration change is the most significant (ex. the UME Pt surface and the cell membrane), the meshing element size was further reduced.

Each cell membrane permeability simulation consisted of two individual study steps carried out in sequence. First a time-dependent study step was performed over a simulated 10 min equilibration period, where the electrode boundary was turned off (no flux boundary setting). The mass transport of the $FcCH_2OH$ species was calculated over time, governed by the physics conditions specified above. The final concentration profile generated during this equilibration was saved and used as the initial concentration distribution for the second study step. The second step was a stationary phase study step (steady state). In this step, the UME is biased or 'turned on,' and the SECM probe was approached toward the cell membrane. Each electrode position was simulated as a separate simulation, parameterized using the parametric sweep function of COMSOL. Membrane permeability coefficient was also parameterized, with both parametric instruction sets nested, allowing for the simulation of multiple physical conditions within the same model. Each individual simulation maintains a full concentration map for the defined electrode position and physics conditions.

Concentration information at the electrode tip was obtained by integrating the flux to the Pt surface at each simulated electrode position (Eq. 4.5).

$$i = 2\pi n D F \int_0^a r \left[\frac{\partial C_B(r,z,t)}{\partial z} \right] dr \qquad [4.5]$$

The current (i) measured depends on the concentration gradient ($\partial C_B / \partial z$), the number of electrons transferred (n) and the UME disk radius (a). The other constants considered are the Faraday constant ($F = 96,485$ C/mol) and the diffusion coefficient of the species (D).

Theoretical and experimental PACs were normalized and plotted together to allow quantification of membrane permeability coefficients. The distance was normalized to the UME critical radius used experimentally (5 μm). Current was normalized to that observed in bulk solution (theoretically infinite distance from substrate, ≥ 10). Theoretical PACs

were simulated with an absolute distance to substrate, and maintain the same curve shape as the experimentally acquired PACs with the same physical geometry. As a result, fitting of theoretical and experimental PACs can be used to accurately characterize UME tip to sample distance and substrate topography.

4.3   Results and Discussion

4.3.1   Quantification of Trends in Membrane Permeability Coefficient Changes by SECM

The SECM depth scan moves the UME probe over the cell under study (Figure 4.2A) and generates a 2D current map of this solution region. SECM depth scan imaging was used to study the T24 cells treated with various concentrations of $K_2Cr_2O_7$ over time. Vertical cross-sections can be utilized to extract probe approach curves (PACs) from the depth scan images (Figure 4.2B). Once normalized, these PACs can be overlaid against a set of theoretically generated PAC curves, allowing for quantification of membrane permeability and distance to substrate (Figure 4.2C). Experimental PACs to the middle of the cell's central mass were extracted. PACs at this location yield the smallest tip-to-sample distance, as they are extracted above the tallest point on the cell's surface. The membrane permeability of cells was previously demonstrated to be consistent across the entire cell using a 10 µm Pt UME with a RG value of 3.[49] It was also shown that minor deviations from cell center have minimal effect on the characterization of cell membrane permeability. PACs extracted with slight deviations from the center of the cell did not affect its membrane permeability coefficient. However, PAC extraction at significant deviation from cell center requires dedicated location-specific simulations to quantify.
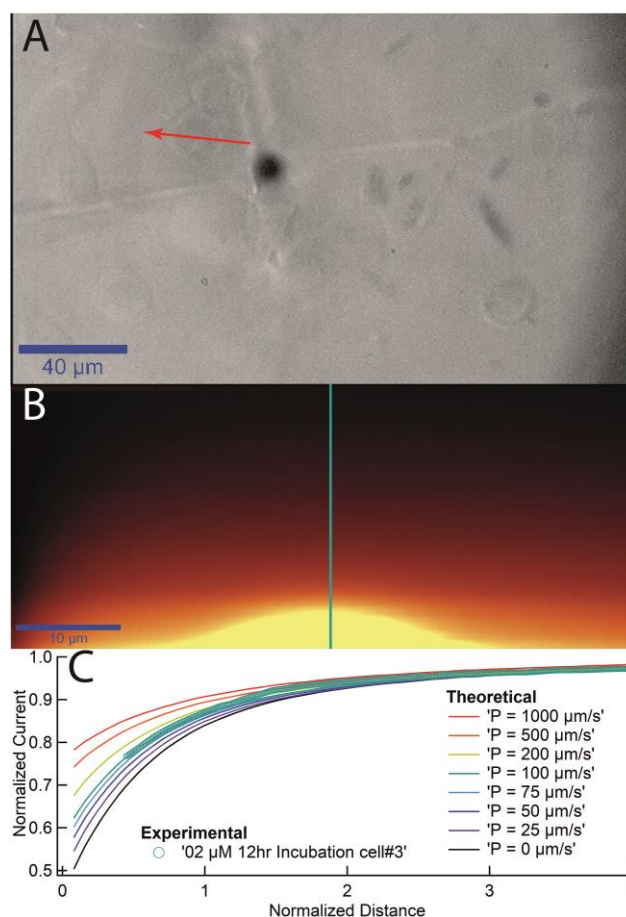
Figure 4.2 - (A) Optical image of T24 cell sample following 12 hr incubation with 2 μM K$_2$Cr$_2$O$_7$. UME path and direction of travelling are labelled in red. (B) 2D depth scan image with PAC cross section labelled in teal. (C) Extracted PAC fit to theoretical curves.

The electrochemical mediator FcCH$_2$OH is partially permeable to the cell membrane under normal control conditions. FcCH$_2$OH is hydrophilic enough to be used in the aqueous cell interior and exterior, but lyophilic enough to exist in the hydrophobic interior of the phospholipid membrane, although not to the degree where it would remain trapped inside. This allows it to pass through the cell membrane without being repelled. Analysis of control cell membrane permeability, with no K$_2$Cr$_2$O$_7$ added, over a range of incubation times yielded a membrane permeability of 81 ± 17 μm/s (Figure 4.3A), which is consistent with values previously reported.[47, 49]
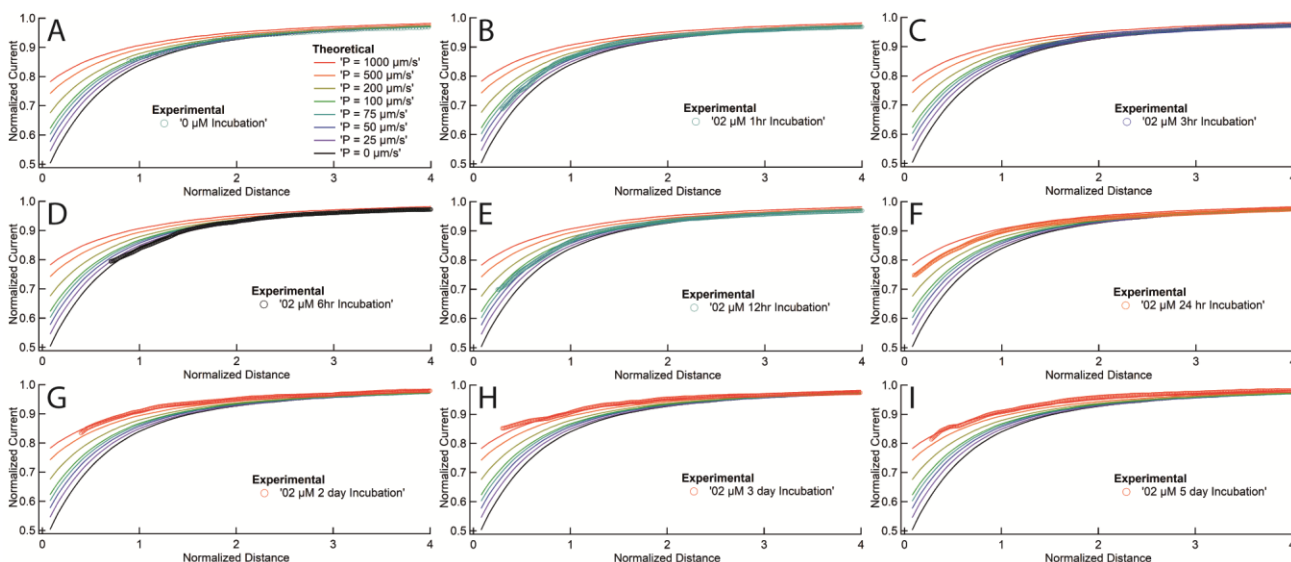
Figure 4.3 - Overlap of experimental PACs with theoretical PACs simulated at known distance to substrate, and permeability coefficient. Time-lapse PACs after incubations with 2 μM K₂Cr₂O₇ are displayed for (A) Control untreated conditions, (B) 1 hr incubation, (C) 3 hr, (D) 6 hr, (E) 12 hr, (F) 24 hr, (G) 2 day, (H) 3 day, and (I) 5 day.

By subjecting the T24 cell samples to low doses of $K_2Cr_2O_7$ for various time periods, the membrane permeability was observed to change. Incubation with 2 μM of $K_2Cr_2O_7$ for 1 hr showed nearly no change in the average membrane permeability at 81 ± 34 μm/s (Figure 4.3B), but a definite increase in the overall variation in permeability was observed. This minimal change in membrane permeability at this concentration is consistent with a previous study performed using short duration exposure.[47] However, once the incubation time was increased to 3 hr, the membrane permeability was observed to drop to 45 ± 20 μm/s (Figure 4.3C). This trend continued as the incubation time was further increased to 6 hr, where a significant drop to 5 ± 3 μm/s (Figure 4.3D) was observed. Extending the incubation time to 12 hr, however, the opposite effect is seen with a relaxation in the cell membrane permeability to 50 ± 16 μm/s (Figure 4.3E).

Incubation of T24 cells for a full day with 2 μM $K_2Cr_2O_7$ yielded a rapid increase in membrane permeability, up to 358 ± 70 μm/s (Figure 4.3F). Two days incubation at the

same concentration further increased the membrane permeability to 840 ± 143 µm/s (Figure 4.3G). By the third day, membrane permeability had increased to 916 ± 76 µm/s (Figure 4.3H). And extending the study to 5 days showed a membrane permeability, of 889 ± 69 µm/s (Figure 4.3I). It should be noted that after 5 days of incubation with 2 µM $K_2Cr_2O_7$, significant die off of the viable population for SECM analysis was observed.
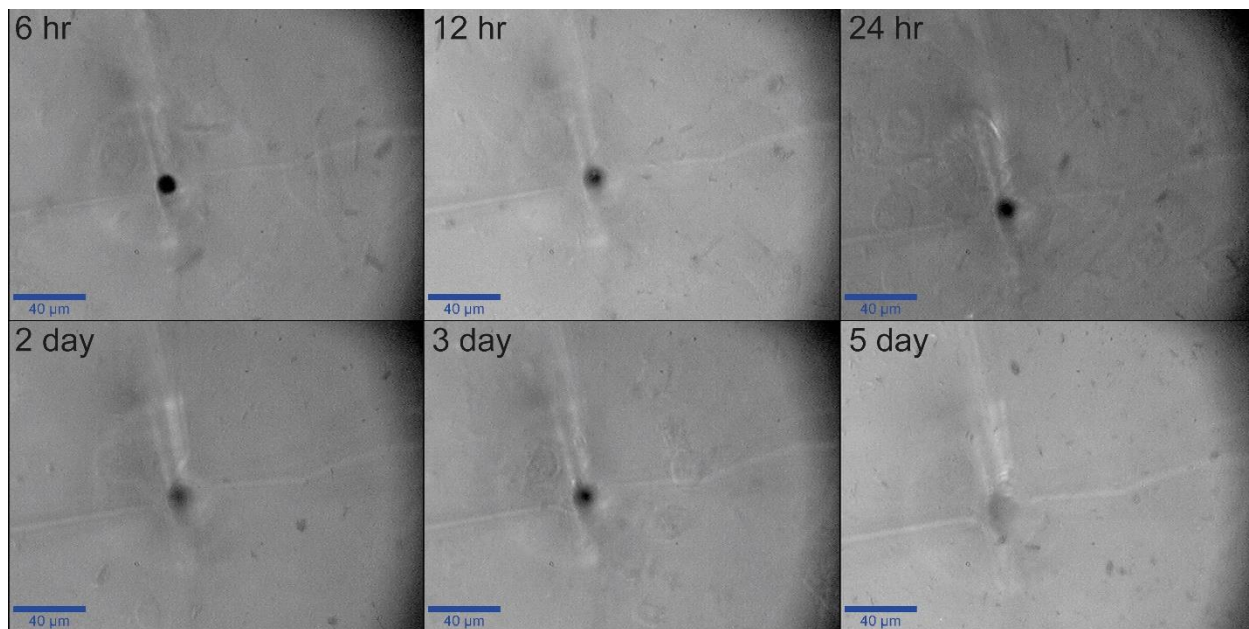
Figure 4.4 - Optical images of T24 live cell samples following exposure to 2 µM $K_2Cr_2O_7$ for 6 hr, 12 hr, 24 hr, 2 days, 3 days and 5 days.

The overall trend produced through the incubation of the T24 cells with 2 µM $K_2Cr_2O_7$ is displayed in Figure 4.5A. Individual data points in Figure 4.5 were calculated as the average of 5-16 individual cell membrane permeability values (average 7.5) ± standard error. This figure illustrates the initial decrease in membrane permeability between 1 and 6 h, and then the rapid rise in membrane permeability as the incubation time exceeded 6 h. This rapid rise in membrane permeability is a likely indicator that the cells internal antioxidant defense systems can no longer cope with the presence of the $K_2Cr_2O_7$. It is well known that the intracellular reduction of Cr (VI) to Cr (III) leads to increased ROS generation.[8, 11] Both Cr (III) and Cr (VI) are capable of generating ROS, although the increased permeability of Cr (VI) to the cell membrane makes it more environmentally

hazardous.[4, 13] Increased oxidative stress is known to disrupt cell signaling pathways, as well as induce lipid peroxidation, protein and DNA damage, as well initiate cell apoptosis.[1, 4, 11-12] In particular, lipid peroxidation drastically changes membrane characteristics, increasing the number polar functional group within the internal membrane region or affecting the packing efficiency of the phospholipids.[14-15] Increased internal membrane polarity will result in decreased membrane permeability with respect to hydrophobic species, such as $FcCH_2OH$, due to increasing difference in polarity, while less efficient packing can increase the membrane fluidity.
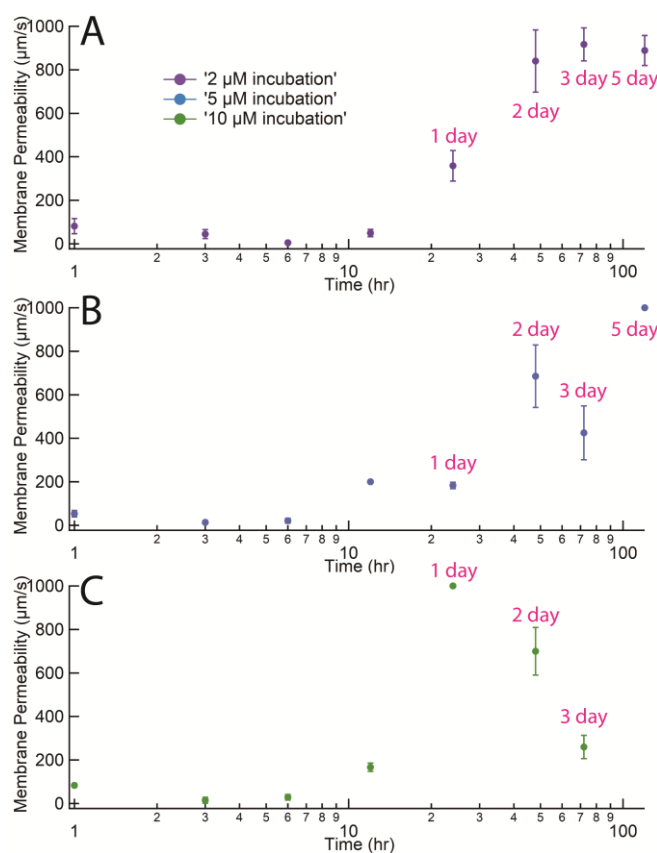
Figure 4.5 - Graphical representation of the time-lapse membrane permeability change vs $K_2Cr_2O_7$ incubation concentration, acquired following incubations with $K_2Cr_2O_7$ at concentrations of (A) 2 μM, (B) 5 μM, and (C) 10 μM.

Another possible contributing factor to increased membrane permeability is the initiation of apoptotic cell death pathway, or necrosis, due to increased oxidative stress and DNA

damage. $K_2Cr_2O_7$ has been reported to initiate cell apoptosis in a number of mammalian cell lines.[4, 8] Necrosis is also a method of cellular death, which includes unregulated digestion of cell components, including the loss of membrane integrity. Necrosis can be initiated by oxidative stress or lipid peroxidation, among other sources. The SECM experimental design incorporated low velocity, but thorough rinsing of the Petri dishes under study following metal exposure, in preparation for SECM analysis. Poorly adhered cells and cell debris were commonly removed from the cell sample by the rinsing process. This process might remove dying or dead cells and debris, incapable of remaining adhered to the Petri dish surface. As a result, my current SECM study likely focuses on the membrane permeability trend of remaining living cells.

For this study, low doses of $K_2Cr_2O_7$ were selected for long duration incubation of the T24 cells. All three dosages selected (2, 5, and 10 µM), were observed to yield minimal membrane permeability change in a previous study performed on short duration exposure, performed over a 1 h incubation period.[47] Cells incubated with 2 µM of $K_2Cr_2O_7$ discussed above, had an average membrane permeability of 81 ± 34 µm/s (Figure 4.5A). 5 µM had a slightly lower membrane permeability than observed earlier, at 54 ± 15 µm/s (Figure 4.5B). And finally 10 µM was found to conform strongly to the previous study with 83 ± 8 µm/s (Figure 4.5C). This minimal change in membrane permeability at these lower concentrations is consistent with the previous study.

Extending the incubation time past 1 h, the 5 and 10 µM dosage of $K_2Cr_2O_7$ were found to induce a similar trend to that observed in the 2 µM incubation but occurred at an earlier time (Figure 4.5). These two concentrations reached their permeability minimum at 3 h with 14 ± 7 µm/s for 5 µM and 15 ± 13 µm/s for 10 µM. The two concentrations maintain similar membrane permeability up to 12 h with the 5 µM dosage cells displaying 200 ± 0 µm/s and 10 µM showing 167 ± 19 µm/s. Following this timeframe, the induced membrane permeability of the two concentrations began to deviate from each other. The 5 µM continued its gradual rise to its maximum observed permeability at 5 days, where it exceeded 1000 µm/s, while the 10 µM reaches its maximum after 24 h by also exceeding 1000 µm/s. The 10 µM, however, over the following 2 days exhibited a

gradual decrease in permeability, with 700 ± 110 µm/s on day 2 and 260 ± 53 µm/s on day 3. Similar to that observed with the 2 µM incubation, significant die-off of the cell population was observed in the sample at 5 days for 5 µM $K_2Cr_2O_7$ sample, and at 3 days for 10 µM.

4.3.2   MTT Cell Viability Study of T24 Cells Incubated with $K_2Cr_2O_7$

The addition of small doses of toxic $K_2Cr_2O_7$ to T24 cells caused dramatic time-lapse change in the live cell membrane permeability. Cellular viability studies can provide insight into the bulk health and wellness of the cell population when exposed to the external stressor, $K_2Cr_2O_7$. MTT is a well-established method of cell viability analysis which can be used to indicate the total viable population of the cell sample [53]. A healthy cell sample was split into multiple smaller samples, which were in turn exposed to various concentrations of heavy metal stressor. The samples which received the dosages of $K_2Cr_2O_7$ were compared to the healthy population of an untreated sample from the same culture over the same timeframe (Eq. 4.6).

$$cell\ viability\ (\%) = \left(\frac{A_{sample} - A_{blank}}{A_{control} - A_{blank}}\right)\ 100\% \qquad [4.6]$$
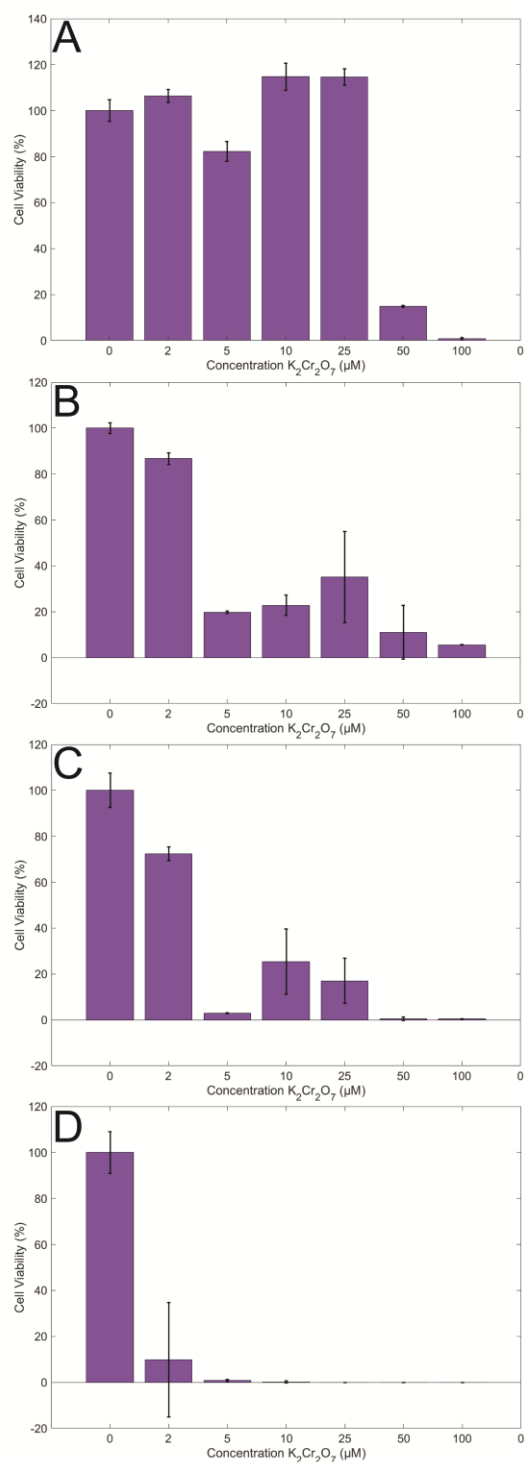
Figure 4.6 - MTT assay results on the viability of T24 cells treated with a range of concentrations of K₂Cr₂O₇ between 0 and 100 μM, for (A) 1 day, (B) 2 day, (C) 3 day, and (D) 5 day, which is represented as Mean ± Standard deviation.

MTT analysis was performed on the sample at 1, 2, 3 and 5 day incubation times. Sample averages were computed based on 6-9 replications per experiment, and compared to 18 replications of control cells. Following 1 day of incubation (Figure 4.6A), samples 2, 5, 10, and 25 µM showed a strong population viability, with minimal change from the control sample. The 50 µM sample, however, showed <15 ± 1% viability, while 100 µM exhibited near 0% surviving population.

Following two days of incubation (Figure 4.6B), the 2 µM sample population density dropped to 87 ± 3%. The 5, 10 and 25 µM sample population density, however, dropped substantially to 20 ± 0.6%, 23 ± 4% and 35 ± 20%, respectively. After 3 days incubation with $K_2Cr_2O_7$ (Figure 4.6C), 2 µM had dropped to 72 ± 3%, while 5, 10 and 25 µM had dropped to 3 ± 0.3%, 25 ± 14% and 17 ± 10%, respectively. By day 5, nearly all cells were dead in all studied concentrations, with viabilities below 10% (Figure 4.6D).

Strong cell viability was observed after 1 day of incubation, illustrating that the initial decrease in membrane permeability observed by SECM as well as the following increase did not hinder the health of the cell population. Between 1 and 2 days, a massive cell die-off was observed in all while the 2 µM sample underwent a minor decrease in viability. This transition corresponded to all three studied concentrations entering the high permeability range exceeding 200 µm/s, and maintaining a high permeability. These low dosages of $K_2Cr_2O_7$ did not immediately cause a decrease in population density, though effects of their toxicity can be observed in their membrane permeability. The membrane permeability measured with SECM demonstrated the effects on cell physiology, in these concentration and incubation time conditions. Once enough cumulative damage occurred over the duration of exposure, cellular death was finally triggered in the T24 cell. Unlike the SECM experimentation, MTT viability includes all cells within the population. This results in a much more drastic response to the $K_2Cr_2O_7$ stressor, while subpopulations of the sample that remain viable are still capable of being analyzed via SECM. As a result, a small surviving culture was able to be maintained up to 3 days for 10 µM, and 5 days for 2 and 5 µM.

4.4 Conclusions

Through the use of SECM analysis, the membrane response of T24 cells incubated with low doses of $K_2Cr_2O_7$ over an extended duration of study was successfully carried out. SECM provided a powerful non-invasive technique for monitoring single live cells without disrupting the homeostatic conditions of these cells. The changes in membrane permeability response were quantified through the comparison of experimental PACs with theoretically generated ones through finite element analysis simulations.

All three Cr (VI) concentrations (2, 5 and 10 µM) yielded a similar response curve shape over the study period. The response time of the resulting curve, however, was displaced to different times according to the concentration used to perform the incubation. Initially cells treated with all concentrations after 1 h of study showed little deviation from control (untreated) cells, which had a membrane permeability of 81 ± 17 µm/s. Following this a decrease in membrane permeability was observed in all concentrations, with the 2 µM treated cells taking 6 h of incubation to reach their minimum observed membrane permeability. The 5 and 10 µM treated cells reached their minimum observed permeability following 3 h of incubation. All samples had a steady rise in membrane permeability following this. The 2 µM and 5 µM cell samples reached their maximum cell permeability (~1000 µm/s) and plateaued around this value after 2 days of incubation. This trend continued for 5 days of incubation, after which SECM analysis was no longer possible for this sample due to significant population decrease. The higher concentration 10 µM treated sample however, reached a similar maximum after 24 h of incubation, and proceeded to slowly drop to a final value of 260 ± 53 µm/s after 3 days of incubation.

MTT studies were performed, providing complimentary analysis of overall viability of the cell populations under study. All three concentrations analyzed by SECM (2, 5 and 10 µM), as well as a higher concentration sample at 25 µM showed strong resistance to the external $K_2Cr_2O_7$ stressor after 1 day of incubation. Higher concentration studies performed at 50 and 100 µM, however, showed significant decrease in cell viability at ≤15%. Following 2 days of incubation, the higher concentrations which showed strong

viability in day 1 (5, 10, 25 µM) showed a significant decrease in viability down to ≤35%. The 2 µM sample showed a small drop in viability to 87 ± 3%. An overall decrease in cell viability was observed after 3 days of incubation. By the 5 day incubation time, all samples exhibited a cell viability ≤10%.

The MTT cell viability assay confirmed a relationship between cellular death and long duration $K_2Cr_2O_7$ exposure. This current study indicates SECM to be useful in exploring the cell membrane response to various stimuli such as concentrations and exposure times. This bioanalytical method is by no means limited to T24 cells and can be applied to other biological systems, such as cells or tissues.

4.5　References

1. O'Brien, T. J.; Ceryak, S.; Patierno, S. R., Complexities of Chromium Carcinogenesis: Role of Cellular Response, Repair and Recovery Mechanisms. *Mutat. Res.* **2003,** *533* (1-2), 3-36.
2. Mohmand, J.; Eqani, S. A.; Fasola, M.; Alamdar, A.; Mustafa, I.; Ali, N.; Liu, L.; Peng, S.; Shen, H., Human Exposure to Toxic Metals Via Contaminated Dust: Bio-Accumulation Trends and Their Potential Risk Estimation. *Chemosphere* **2015,** *132*, 142-51.
3. Chen, T.; Zhou, Z.; Xu, S.; Wang, H.; Lu, W., Adsorption Behavior Comparison of Trivalent and Hexavalent Chromium on Biochar Derived from Municipal Sludge. *Bioresour. Technol.* **2015,** *190*, 388-94.
4. Bagchi, D.; Bagchi, M.; Stohs, S. J., Chromium (Vi)-Induced Oxidative Stress, Apoptotic Cell Death and Modulation of P53 Tumor Suppressor Gene. *Mol. Cell. Biochem.* **2001,** *222* (1-2), 149-58.
5. Catelas, I.; Petit, A.; Vali, H.; Fragiskatos, C.; Meilleur, R.; Zukor, D. J.; Antoniou, J.; Huk, O. L., Quantitative Analysis of Macrophage Apoptosis Vs. Necrosis Induced by Cobalt and Chromium Ions in Vitro. *Biomaterials* **2005,** *26* (15), 2441-53.
6. Fang, Z.; Zhao, M.; Zhen, H.; Chen, L.; Shi, P.; Huang, Z., Genotoxicity of Tri- and Hexavalent Chromium Compounds in Vivo and Their Modes of Action on DNA Damage in Vitro. *PLoS One* **2014,** *9* (8), e103194.
7. Kovacik, J.; Babula, P.; Hedbavny, J.; Krystofova, O.; Provaznik, I., Physiology and Methodology of Chromium Toxicity Using Alga Scenedesmus Quadricauda as Model Object. *Chemosphere* **2015,** *120*, 23-30.
8. Wang, X. F.; Xing, M. L.; Shen, Y.; Zhu, X.; Xu, L. H., Oral Administration of Cr(Vi) Induced Oxidative Stress, DNA Damage and Apoptotic Cell Death in Mice. *Toxicol.* **2006,** *228* (1), 16-23.
9. Wang, Y.; Su, H.; Gu, Y.; Song, X.; Zhao, J., Carcinogenicity of Chromium and Chemoprevention: A Brief Update. *Onco. Targets Ther.* **2017,** *10*, 4065-4079.

10. Biological Data Relevant to the Evaluation of Carcinogenic Risk to Humans. http://monographs.iarc.fr/ENG/Monographs/vol49/mono49-6C.pdf (accessed 2017/09/26).

11. Hartwig, A., Metal Interaction with Redox Regulation: An Integrating Concept in Metal Carcinogenesis? *Free Radic. Biol. Med.* **2013,** *55*, 63-72.

12. Venter, C.; Oberholzer, H. M.; Cummings, F. R.; Bester, M. J., Effects of Metals Cadmium and Chromium Alone and in Combination on the Liver and Kidney Tissue of Male Spraque-Dawley Rats: An Ultrastructural and Electron-Energy-Loss Spectroscopy Investigation. *Microsc. Res. Tech.* **2017,** *80* (8), 878-888.

13. Kalahasthi, R. B.; Rao, R. H.; Murthy, R. B.; Kumar, M. K., Effect of Chromium(Vi) on the Status of Plasma Lipid Peroxidation and Erythrocyte Antioxidant Enzymes in Chromium Plating Workers. *Chem. Biol. Interact.* **2006,** *164* (3), 192-9.

14. Cordeiro, R. M., Reactive Oxygen Species at Phospholipid Bilayers: Distribution, Mobility and Permeation. *Biochim. Biophys. Acta* **2014,** *1838* (1 Pt B), 438-44.

15. Wong-Ekkabut, J.; Xu, Z.; Triampo, W.; Tang, I. M.; Tieleman, D. P.; Monticelli, L., Effect of Lipid Peroxidation on the Properties of Lipid Bilayers: A Molecular Dynamics Study. *Biophys. J.* **2007,** *93* (12), 4225-36.

16. Petersen, R.; Thomsen, J. F.; Jorgensen, N. K.; Mikkelsen, S., Half Life of Chromium in Serum and Urine in a Former Plasma Cutter of Stainless Steel. *Occup. Environ. Med.* **2000,** *57* (2), 140-2.

17. Setyaningsih, Y.; Husodo, A. H.; Astuti, I., Detection of Urinary 8-Hydroxydeoxyguanosine (8-Ohdg) Levels as a Biomarker of Oxidative DNA Damage among Home Industry Workers Exposed to Chromium. *Procedia Environ. Sci.* **2015,** *23*, 290-296.

18. Bard, A. J.; Denuault, G.; Lee, C.; Mandler, D.; Wipf, D. O., Scanning Electrochemical Microscopy - a New Technique for the Characterization and Modification of Surfaces. *Acc. Chem. Res.* **2002,** *23* (11), 357-363.

19. Bard, A. J.; Fan, F. R. F.; Kwak, J.; Lev, O., Scanning Electrochemical Microscopy. Introduction and Principles. *Anal. Chem.* **2002,** *61* (2), 132-138.

20. Polcari, D.; Dauphin-Ducharme, P.; Mauzeroll, J., Scanning Electrochemical Microscopy: A Comprehensive Review of Experimental Parameters from 1989 to 2015. *Chem. Rev.* **2016,** *116* (22), 13234-13278.

21. Ding, Z.; Quinn, B. M.; Bard, A. J., Kinetics of Heterogeneous Electron Transfer at Liquid/Liquid Interfaces as Studied by Secm. *J. Phys. Chem. B* **2001,** *105* (27), 6367-6374.

22. Nowierski, C.; Noël, J. J.; Shoesmith, D. W.; Ding, Z., Correlating Surface Microstructures with Reactivity on Commercially Pure Zirconium Using Scanning Electrochemical Microscopy and Scanning Electron Microscopy. *Electrochem. Commun.* **2009,** *11* (6), 1234-1236.

23. Yin, Y.; Niu, L.; Lu, M.; Guo, W.; Chen, S., In Situ Characterization of Localized Corrosion of Stainless Steel by Scanning Electrochemical Microscope. *Appl. Surf. Sci.* **2009,** *255* (22), 9193-9199.

24. Tang, J.; Zheng, J.-J.; Yu, Y.-T.; Chen, l.; Zhang, N.; Tian, Z., Selective Etching of Zno Films on an Ito Substrate Using a Scanning Electrochemical Microscope. *Electrochim. Acta* **2012,** *83*, 247-252.

25. Eifert, A.; Mizaikoff, B.; Kranz, C., Advanced Fabrication Process for Combined Atomic Force-Scanning Electrochemical Microscopy (Afm-Secm) Probes. *Micron* **2015,** *68*, 27-35.

26. Bard, A. J.; Li, X.; Zhan, W., Chemically Imaging Living Cells by Scanning Electrochemical Microscopy. *Biosens. Bioelectron.* **2006,** *22* (4), 461-72.

27. Zhao, X.; Diakowski, P. M.; Ding, Z., Deconvoluting Topography and Spatial Physiological Activity of Live Macrophage Cells by Scanning Electrochemical Microscopy in Constant-Distance Mode. *Anal. Chem.* **2010,** *82* (20), 8371-3.

28. Huang, C.; Liu, C.; Loo, J.; Stakenborg, T.; Lagae, L., Single Cell Viability Observation in Cell Dielectrophoretic Trapping on a Microchip. *Appl. Phys. Lett.* **2014,** *104* (1), 013703.

29. Koley, D.; Bard, A. J., Inhibition of the Mrp1-Mediated Transport of the Menadione-Glutathione Conjugate (Thiodione) in Hela Cells as Studied by Secm. *Proc. Nat. Acad. Sci. U.S.A.* **2012,** *109* (29), 11522-7.

30. Kim, J.; Izadyar, A.; Shen, M.; Ishimatsu, R.; Amemiya, S., Ion Permeability of the Nuclear Pore Complex and Ion-Induced Macromolecular Permeation as Studied by Scanning Electrochemical and Fluorescence Microscopy. *Anal. Chem.* **2014,** *86* (4), 2090-8.

31. Bergner, S.; Wegener, J.; Matysik, F.-M., Monitoring Passive Transport of Redox Mediators across a Confluent Cell Monolayer with Single-Cell Resolution by Means of Scanning Electrochemical Microscopy. *Anal. Methods* **2012,** *4* (3), 623-629.

32. Kuss, S.; Cornut, R.; Beaulieu, I.; Mezour, M. A.; Annabi, B.; Mauzeroll, J., Assessing Multidrug Resistance Protein 1-Mediated Function in Cancer Cell Multidrug Resistance by Scanning Electrochemical Microscopy and Flow Cytometry. *Bioelectrochemistry* **2011,** *82* (1), 29-37.

33. Kuss, S.; Polcari, D.; Geissler, M.; Brassard, D.; Mauzeroll, J., Assessment of Multidrug Resistance on Cell Coculture Patterns Using Scanning Electrochemical Microscopy. *Proc. Nat. Acad. Sci. U.S.A.* **2013,** *110* (23), 9249-54.

34. Zhao, X.; Zhang, M.; Long, Y.; Ding, Z., Redox Reactions of Reactive Oxygen Species in Aqueous Solutions as the Probe for Scanning Electrochemical Microscopy of Single Live T24 Cells. *Can. J. Chem.* **2010,** *88* (6), 569-576.

35. Zhang, M. M.; Long, Y. T.; Ding, Z., Cisplatin Effects on Evolution of Reactive Oxygen Species from Single Human Bladder Cancer Cells Investigated by Scanning Electrochemical Microscopy. *J. Inorg. Biochem.* **2012,** *108*, 115-22.

36. Zhao, X.; Lam, S.; Jass, J.; Ding, Z., Scanning Electrochemical Microscopy of Single Human Urinary Bladder Cells Using Reactive Oxygen Species as Probe of Inflammatory Response. *Electrochem. Commun.* **2010,** *12* (6), 773-776.

37. Zhao, X.; Petersen, N. O.; Ding, Z., Comparison Study of Live Cells by Atomic Force Microscopy, Confocal Microscopy, and Scanning Electrochemical Microscopy. *Can. J. Chem.* **2007,** *85* (3), 175-183.

38.   Zhan, D.; Li, X.; Nepomnyashchii, A. B.; Alpuche-Aviles, M. A.; Fan, F.-R. F.; Bard, A. J., Characterization of Ag+ Toxicity on Living Fibroblast Cells by the Ferrocenemethanol and Oxygen Response with the Scanning Electrochemical Microscope. *J. Electroanal. Chem.* **2013,** *688*, 61-68.

39.   Li, X.; Bard, A. J., Scanning Electrochemical Microscopy of Hela Cells – Effects of Ferrocene Methanol and Silver Ion. *J. Electroanal. Chem.* **2009,** *628* (1-2), 35-42.

40.   Sun, P.; Laforge, F. O.; Abeyweera, T. P.; Rotenberg, S. A.; Carpino, J.; Mirkin, M. V., Nanoelectrochemistry of Mammalian Cells. *Proc. Nat. Acad. Sci. U.S.A.* **2008,** *105* (2), 443-8.

41.   Cai, C.; Liu, B.; Mirkin, M. V.; Frank, H. A.; Rusling, J. F., Scanning Electrochemical Microscopy of Living Cells. 3.Rhodobactersphaeroides. *Anal. Chem.* **2002,** *74* (1), 114-119.

42.   Feng, W.; Rotenberg, S. A.; Mirkin, M. V., Scanning Electrochemical Microscopy of Living Cells. 5. Imaging of Fields of Normal and Metastatic Human Breast Cells. *Anal. Chem.* **2003,** *75* (16), 4148-54.

43.   Liu, B.; Cheng, W.; Rotenberg, S. A.; Mirkin, M. V., Scanning Electrochemical Microscopy of Living Cells. *J. Electroanal. Chem.* **2001,** *500* (1-2), 590-597.

44.   Liu, B.; Rotenberg, S. A.; Mirkin, M. V., Scanning Electrochemical Microscopy of Living Cells: Different Redox Activities of Nonmetastatic and Metastatic Human Breast Cells. *Proc. Nat. Acad. Sci. U.S.A.* **2000,** *97* (18), 9855-60.

45.   Li, M. S. M.; Filice, F. P.; Henderson, J. D.; Ding, Z., Probing Cd2+-Stressed Live Cell Membrane Permeability with Various Redox Mediators in Scanning Electrochemical Microscopy. *J. Phys. Chem. C* **2016,** *120* (11), 6094-6103.

46.   Li, M. S. M.; Filice, F. P.; Ding, Z., Determining Live Cell Topography by Scanning Electrochemical Microscopy. *J. Electroanal. Chem.* **2016,** *779*, 176-186.

47.   Henderson, J. D.; Filice, F. P.; Li, M. S. M.; Ding, Z., Tracking Live-Cell Response to Hexavalent Chromium Toxicity by Using Scanning Electrochemical Microscopy. *ChemElectroChem* **2017,** *4* (4), 856-863.

48.   Mosmann, T., Rapid Colorimetric Assay for Cellular Growth and Survival: Application to Proliferation and Cytotoxicity Assays. *J. Immunol. Methods* **1983,** *65* (1-2), 55-63.

49.   Filice, F. P.; Li, M. S.; Henderson, J. D.; Ding, Z., Mapping Cd(2)(+)-Induced Membrane Permeability Changes of Single Live Cells by Means of Scanning Electrochemical Microscopy. *Anal. Chim. Acta* **2016,** *908*, 85-94.

50.   Kuss, S.; Trinh, D.; Danis, L.; Mauzeroll, J., High-Speed Scanning Electrochemical Microscopy Method for Substrate Kinetic Determination: Method and Theory. *Anal. Chem.* **2015,** *87* (16), 8096-101.

51.   Guo, J.; Amemiya, S., Permeability of the Nuclear Envelope at Isolated Xenopus Oocyte Nuclei Studied by Scanning Electrochemical Microscopy. *Anal. Chem.* **2005,** *77* (7), 2147-56.

52.   Miao, W.; Ding, Z.; Bard, A. J., Solution Viscosity Effects on the Heterogeneous Electron Transfer Kinetics of Ferrocenemethanol in Dimethyl Sulfoxide−Water Mixtures. *J. Phys. Chem. B* **2002,** *106* (6), 1392-1398.

53.   Soleimani, A.; Moustafa, M. M. A. R.; Borecki, A.; Gillies, E. R., A Comparison of Covalent and Noncovalent Strategies for Paclitaxel Release Using Poly(Ester Amide) Graft Copolymer Micelles. *Can. J. Chem.* **2015,** *93* (4), 399-405.

Chapter 5

5 Trivalent Chromium-Induced Live Cell Membrane Permeability Disruption Revealed by Scanning Electrochemical Microscopy

Cr(III) is often regarded as a trace essential micronutrient that can be found in many dietary supplements due to its participation in blood glucose regulation. However, increased levels of exposure have been linked to adverse health effects in living organisms. Herein, scanning electrochemical microscopy (SECM) was used to detect variation in membrane permeability of single cells (T24) resulting from exposure to a trivalent Cr-salt, $CrCl_3$. By employing the electrochemical mediators, ferrocenemethanol (FcMeOH) and ferrocenecarboxylic acid ($FcCOO^-$), initially semi-permeable and impermeable respectively, complementary information was obtained. 3D COMSOL finite element analysis simulations were successfully used to quantify permeability coefficients of each mediator by matching experimental and simulated results. Dependent on the concentration of Cr(III) administered, three regions of membrane response were detected. Following exposure to low concentrations (up to 500 µM Cr(III)), permeability coefficients were comparable to that of control cells 80 µm/s for FcMeOH and 0 µm/s for $FcCOO^-$. This was confirmed for both mediators. As incubation concentrations were increased, the ability of FcMeOH to permeate the membrane decreased to a minimum of 17 µm/s at 7,500 µM Cr(III), while $FcCOO^-$ remained impermeable. At the highest examined concentrations, both mediators were found to demonstrate increased membrane permeability. MTT cell viability studies were also conducted on Cr(III)-treated T24 cells

to correlate the SECM findings to the toxicity effects of the metal. The viability experiments revealed a similar concentration-dependent trend as the SECM cell membrane permeability study.

5.1   Introduction

Many heavy metals, such as cadmium and chromium (VI), have toxic properties that can lead to detrimental effects in living cells and organisms.[1] By contrast, other metals such as zinc, iron and calcium, have been incorporated into biological systems and are required for healthy growth and development of an organism. These trace essential heavy metals are necessary in small (trace) quantities but can be toxic at higher concentrations.[2] The role of the metal in the body can also be dependent on its oxidation state. For example, chromium (III) is regarded as a trace essential micronutrient that is often found in many dietary supplements to promote cellular homeostasis.[3-4] However, high concentration Cr (III) exposure can lead to toxicity effects.[5-7] Chromium (VI), the other common oxidation state of chromium, is known to induce oxidative stress, cytotoxicity, and carcinogenicity regardless of its concentration.[5-6, 8-14]

The primary sources of trace essential elements to living organisms are through dietary consumption. In the case of Cr (III), it is commonly added as a supplement to animal feed and water.[15] Studies have shown Cr (III) participates in blood glucose regulation and insulin signaling in the body. Specifically, the role of low-molecular-weight chromium-binding-substance (LMWCr) is required to maintain the active conformation of the insulin receptor.[3-4]

Elevated levels of Cr(III) have been associated with heightened production of reactive oxygen species (ROS).[1, 12, 15-19] In some cases Cr(III) has been shown to yield higher ROS levels than the toxic Cr(VI) oxidation state.[10] The mechanism of Cr(III) toxicity is believed to involve not only elevated levels of ROS, but also the direct interaction of Cr(III) with DNA. The resultant DNA-adducts lead to genomic instability.[5] However, Cr (III) does not easily cross the cell membrane and is commonly brought into the cell by active means such as pinocytosis, reducing its toxic effects.[20-21]

Cr bioaccumulates primarily in the kidneys, liver and lungs of mammals, potentially leading to adverse health effects in these tissues as concentrations increase.[12, 22-24] Monitoring the levels of Cr exposure, commonly through urine content, has determined a substantial half-life of ~10 years in the body.[22, 24] Due to its ability to cause genetic damage and its ability to bioaccumulate in the urinary tract, my current study focuses on human bladder cancer (T24) cells as a model system to investigate the effects of Cr toxicity on membrane homeostasis.

Previous studies focusing on the effects of Cr toxicity in cellular processes have relied heavily on conventional fluorescence microscopy techniques, where special precautions are required in order to avoid light-induced ROS production, which can lead to cellular damage.[25-26] In addition, these fluorescent techniques are often destructive and samples are discarded following measurement.

One alternative technique that can be used is scanning electrochemical microscopy (SECM) since it is a non-destructive, non-invasive technique. SECM has been greatly developed by the Bard lab since 1989.[27-29] SECM can be used to monitor the electrochemical behavior of a sample, based on the generation/regeneration of the mediating species at a working electrode, commonly an ultramicroelectrode (UME). This technique has been utilized for a vast number of applications including but not limited to kinetic studies,[30] surface and interface studies,[31-32] microstructure fabrication,[33-34] as well as the mentioned biological applications such as cellular imaging,[35-36] membrane transport,[37-41] multidrug resistance,[42-43] cellular ROS and reactive nitrogen species (RNS), [36, 44-48] metabolic interactions[18] and cellular redox processes.[49-55] In its applications to live cell studies, the non-invasive nature of SECM allows monitoring of dynamic cellular processes, leaving biological samples unaltered provided the appropriate non-toxic mediator is selected. SECM can be used for the rapid quantification of single live cell topography and surface reactivity, as well as intracellular examination of biological processes.

These dynamic cellular processes can be monitored through the changes in faradic current as a UME approaches the cell from above. At small probe–to-cell distances, the

membrane permeability can affect the tip current. As the electrode is approached to the cell membrane, the availability of mediator from bulk electrolyte solution becomes hindered. This hindered diffusion causes a decrease in current termed as negative feedback. However, if the mediator is permeable to the cellular membrane it may cross the membrane and reach the UME tip. This has an effect of weakening the negative feedback that would be observed when compared to an impermeable membrane of the same geometry. The resultant feedback is commonly report as probe approach curves (PAC) which plot the normalized current (y-axis) against the normalized probe-to-cell distance (x-axis).

Here, the SECM depth scan imaging mode was used to investigate the membrane responses of Cr (III)-treated T24 cells. This mode moves the UME in a 2D x-z plane above the cell, generating a 2D current map that allows the acquisition of hundreds of PACs from a single scan. 3D COMSOL finite element analysis simulations were utilized to generate theoretical depth scan images and to allow quantification of membrane permeability coefficients to the redox mediators.

5.2 Experimental

5.2.1   Materials

Ferrocenemethanol (FcCH$_2$OH, 97%), ferrocenecarboxylic acid (FcCOOH, 97%), potassium chloride (KCl, 99%), and chromium chloride hexahydrate (CrCl$_3$·6H$_2$O, 99%) were purchased from Sigma-Aldrich (Mississauga, ON). Mediator solutions containing 0.9 mM FcCH$_2$OH with 0.1 M KCl were regularly prepared in deionized water (18.2 MΩ•cm MilliQ water, Millipore, Etobicoke, ON). The FcCH$_2$OH solution was diluted to half concentration with 1× phosphate buffered saline (PBS) when used experimentally. FcCOOH stock solution of 0.5 mM was prepared in PBS. At pH 7.4, FcCOOH dissociates to FcCOO$^-$ in solution. Stock solutions of 0.5 M CrCl$_3$ were prepared in autoclaved deionized water and syringe-filtered through sterile 0.2 μm Supor® Membranes (PALL Life Sciences, Mississauga, ON). 3-(4,5-dimethylthiazol-2-yl)-2,5-diphenyltetrazolium bromide (MTT) was acquired from R&D Systems Inc. (Minneapolis,

MN) in the TACS® MTT Cell Proliferation Assay Kit. Spectroscopic grade dimethyl sulfoxide (DMSO) was used to dissolve the formazan crystals (Caledon Laboratory Ltd, Georgetown, ON).

5.2.2   Cell Culture

Human urinary bladder cancer cells (T24 cells (HTB-4™)) (ATCC, Manassas, VA, USA) were grown and maintained in McCoy's 5a medium (ATCC) containing 10% Fetal Bovine Serum at 37°C with 5% CO_2. Experimental data was acquired using cells within a narrow passage window (45-48) to provide consistency among data sets.

Cell samples used for SECM experimentation were grown on uncoated 50 mm glass bottom Petri dishes (P50G-0-30-F, MatTek Corporation, Ashland, MA, USA). An hour prior to analysis, $CrCl_3$ was injected directly into the growth medium at the desired concentrations and incubated for 1 hr. Immediately before examination, the medium was removed and Cr (III)-treated T24 cells were washed thoroughly with sterile $1\times$ PBS, before the addition of the mediator solution used for SECM analysis ($FcCH_2OH$ or $FcCOO^-$).

5.2.3   Cell Viability

The effects of $CrCl_3$ on cellular viability were assessed using the MTT cell proliferation assay.[56-57] Briefly, 2×10^4 cells/well were seeded onto Corning Scientific Costar™ 96-well polystyrol flat bottom plates. After 24 hr, the growth medium was aspirated and replaced with new growth medium containing $CrCl_3$. Sodium dodecyl sulfate (0.05, 0.10, 0.15, or 0.20 mg/mL) was used as a positive control for the assay.

After incubation for 1 hr, the growth medium was carefully aspirated and replaced with 100 µL of fresh growth medium (absent of phenol red) and 10 µL of the MTT reagent. After 6 hrs, the MTT solution was carefully aspirated and the formazan crystals were dissolved with 50 µL of spectroscopic grade DMSO. The absorbance (Abs) at 540 nm was read by a M1000 PRO plate reader (Tecan Switzerland) following 1 s of shaking at 2

mm amp and 654 rpm. To remove the background medium effects, empty (blank) wells were also treated according to the MTT protocol.

5.2.4   SECM Instrumentation and Procedure

Detailed description of the SECM instrumentation and experimental procedures can be found in Chapter 2 section 2.2.5.[58] Briefly, SECM experiments were carried out using a modified Alpha-SNOM (WITec, Ulm, Germany). The Alpha-SNOM set-up included a custom UME mount and a variable temperature Petri dish mount (Bioscience Tools, San Diego, California, USA). The inverted objective lens (50×, N.A. 0.55, W.D. 10.1 mm, Nikon, Japan) located below the sample was used in the positioning and optical imaging of both the UME and cell samples. The UMEs were fabricated in-house following a previously developed methodology.[37, 46, 59] Throughout this study, the UME consisted of a 10 µm Pt wire which was sheathed in insulating glass, with the ratio of glass to Pt diameter (RG) of approximately 3. Electrochemical instrumentation consisted of a CH Instruments Electrochemical Analyzer (CHI800B, CH Instruments, Austin, TX) with a CHI200 Picoamp Booster. A Ag/AgCl electrode was used as a combined counter and reference electrode. The CHI800B output channel was connected to the WITec Alpha-SNOM data acquisition channel providing position specific electrochemical information.

Before each experiment, cyclic voltammetry (CV) was used to test for steady-state performance of the UME probe and electrochemical mediator. Identified through CV, the UME was biased at a probe potential of 0.3 V for $FcCH_2OH$ and 0.4 V for $FcCOO^-$ for their respective steady state oxidative currents (while in bulk solution). SECM analysis of all cell samples were performed at a maximum UME tip speed of 21.4 µm/s to limit the effects of forced convection and maintain steady state current.[60]

Following incubation, a Petri dish containing the $CrCl_3$-treated cells was secured to the heated stage of the Alpha-SNOM. The samples were maintained at 37.0 ± 0.2 ˚C to mimic physiological conditions for the cell line. Analysis of live cell samples was conducted over a maximum duration of 60 min. After location of a cell, the UME was then positioned near the cell of interest, followed by imaging of the cell using the depth

scan imaging mode. This allowed for real time probe-to-cell distance information, reducing the probability of collisions. Manipulation of depth scan parameters, such as scan width, depth, image resolution, and integration time, was performed through the WITec software.

5.2.5   SECM Model Simulation

Theoretical PAC data was obtained using a COMSOL Multiphysics (v5.2) model as published elsewhere.[37, 58, 61-63] A full 3D model with a symmetry plane through the center of the UME and cell was constructed to mimic the experimental set-up (Figure 5.1). Dimensions of electrode (platinum radius of 5 µm and an RG of 3) were used to create the model of the UME. Cell dimensions were surveyed optically (86 cells) to determine the average T24 cell size (semi-ellipsoidal). The cell long axis has a diameter of 26.33±0.62 µm and the shorter axis diameter was determined to be 18.23±0.39 µm. The cell height was determined previously using SECM to be 8.7±3.3 µm.[63] A semi-ellipsoid with radii y=13.5 µm, x=9.0 µm, and z=8.0 µm was defined as a cell analogue in the simulation model. Two independent domains were identified for the bulk solution (C_B) and the cell's interior (C_C). The concentrations of these domains were specified to match the initial conditions (C_B = 0.45 mM $FcCH_2OH$ or C_B = 0.50 mM $FcCOO^-$; C_C = 0 M $FcCH_2OH$ or $FcCOO^-$). The flux across the membrane boundary is dependent on a permeability coefficient (P) and the concentration gradient, as indicated by equations 5.1 and 5.2.

$$f_{in} = P(C_B - C_C) \quad [5.1]$$

$$f_{out} = P(C_C - C_B) \quad [5.2]$$

The diffusion coefficients for $FcCH_2OH$ and $FcCOO^-$ in both domains were set to 7.6×10^{-10} m^2/s and 5.7×10^{-10} m^2/s, respectively.[61, 64-65] The simulation was performed in 2 stages. The first stage allowed the two domains to reach equilibrium (over 10 min), which provided an initial concentration distribution for the UME approach. In the second stage, the electrode position was parameterized over its full experimental range of motion towards the cell.
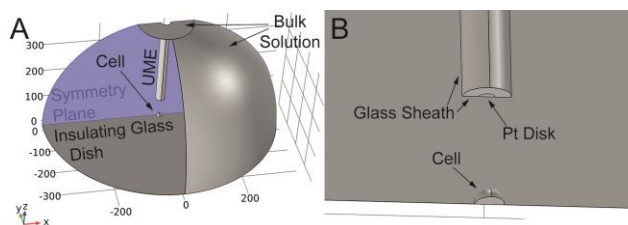
Figure 5.1 - (A) 3D model of the SECM approach to an isolated cell with key features, boundaries, and domains labeled. (B) Zoomed in and labelled view of the model geometry displayed in A, focusing on the electrode tip in close proximity to the cell membrane.

In this study, the electrode position was moved in both the x and z axes, as a set of nested parametric sweeps. This allowed the full simulation of depth scans over the cell. The theoretical depth scans can be treated as a 2D matrix of electrochemical current values with UME tip position. 1D PACs and horizontal sweeps can be extracted from the 2D matrix. This allowed fitting of the experimental PACs or horizontal sweeps. The membrane permeability coefficients were parametrically simulated, ranging between 0 – 1000 µm/s. Nesting the UME position inside of the permeability parameterization generated a set of depth scans at these desired permeability coefficients (Figure 5.2). Please note, the permeability was assumed to be homogeneous across the entire cell membrane as previously found with T24 cells challenged by Cd (II).[58] This point will be further verified in section 5.3.1. A membrane permeability coefficient of 0 µm/s produces the same depth scan profile as an ideally insulating surface (no flux) of the same geometry (Figure 5.2A). Low permeability coefficients restrict the transport of the electrochemical mediator, causing reduced current in close proximity to the cell surface (Figure 5.2B). With an increase in the permeability coefficient, less negative feedback is observed which leads to a higher electrochemical current profile (Figure 5.2C-G). A highly permeable cell membrane (Figure 5.2H) shows little electrochemical response from the cell as the mediator is able to move freely in and out of the cell towards the UME tip.
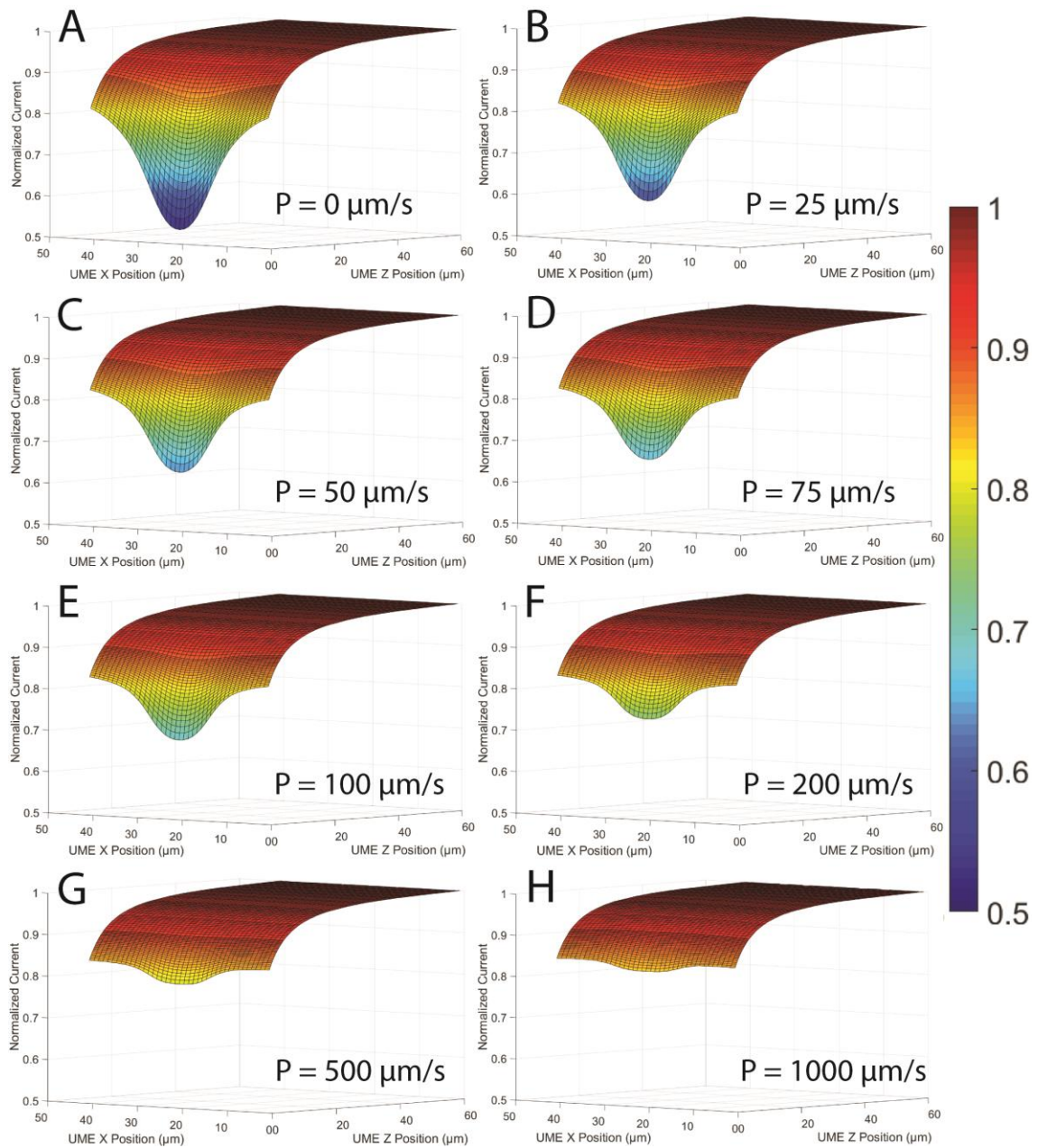
Figure 5.2 - Simulated depth scans over a single cell with membrane permeability coefficients defined as (A) 0 µm/s, (B) 25 µm/s, (C) 50 µm/s, (D) 75 µm/s, (E) 100 µm/s, (F) 200 µm/s (G) 500 µm/s and (H) 1000 µm/s.

5.3   Results and Discussion

5.3.1   Off-Axis Characterization of Cell Membrane Permeability

SECM depth scanning moves the UME in the x-z plane of solution over a single live cell. This generates a 2D electrochemical map of the region of space over the cell. Cross sections can be taken of theoretical (Figure 5.2) and experimental (Figure 5.3A) depth scans to produce more conventional PACs. Depth scan images are comprised of hundreds of PACs at different locations over the cell surface. To analyze experimental PACs taken at positions displaced from the cell center requires full 3D simulations, as the symmetry axis required for the more common 2D axially symmetric method cannot be maintained.[58, 63] The experimental PACs extracted at these locations can be overlaid on the theoretical ones to obtain quantitative characterization of membrane permeability (Figure 5.3B-D). Figure 5.3A illustrates the membrane permeability map of a T24 cell after 1 hr incubation with 250 µM Cr (III). PACs over the cell surface were extracted from the depth scan images at 3 locations represented by the red, green and blue planes. These curves were overlaid onto theoretical PACs simulated at the same physical UME positions. With a 10 µm diameter Pt UME, the membrane permeability to $FcCH_2OH$ across the whole cell surface was determined to be uniform at 75 µm/s.
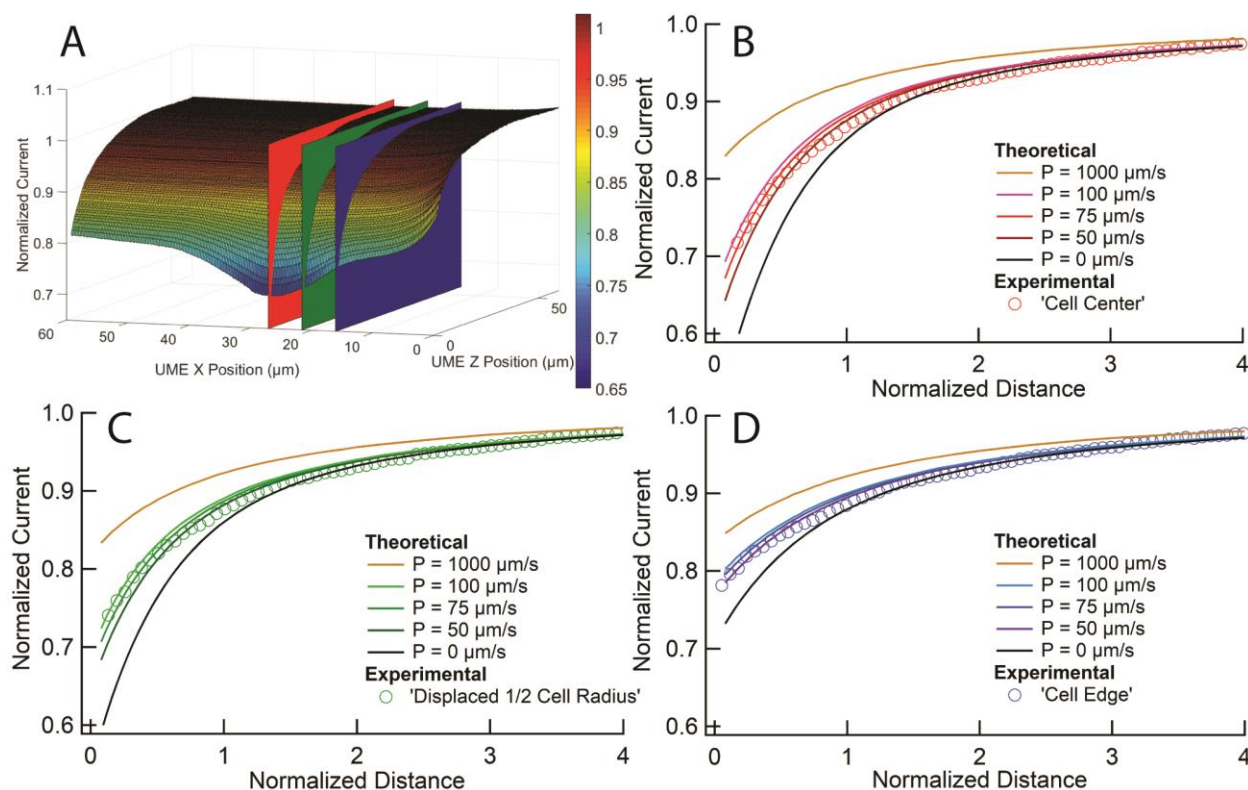
Figure 5.3 - (A) Experimental depth scan with PAC cross sections extracted along colored planes. Depth scan was acquired after 1 hr incubation of cell sample with 250 μM of CrCl$_3$. Overlap of experimental and theoretical PACs corresponding to extraction planes seen in A, at (B) the cell center, (C) ½ the cell radius from the center, and (D) the cell edge.

5.3.2   Quantification of Change in Permeability to FcCH$_2$OH Electrochemical Mediator

The electrochemical mediator FcCH$_2$OH is partially permeable to T24 cell membranes under untreated (control) conditions. The changes in membrane permeability can provide insights into the biological effects induced by exposure to external stressors.[40, 43, 65] Experimental PACs to the untreated T24 cells had an average membrane permeability coefficient (P) of 80 ± 6 μm/s.
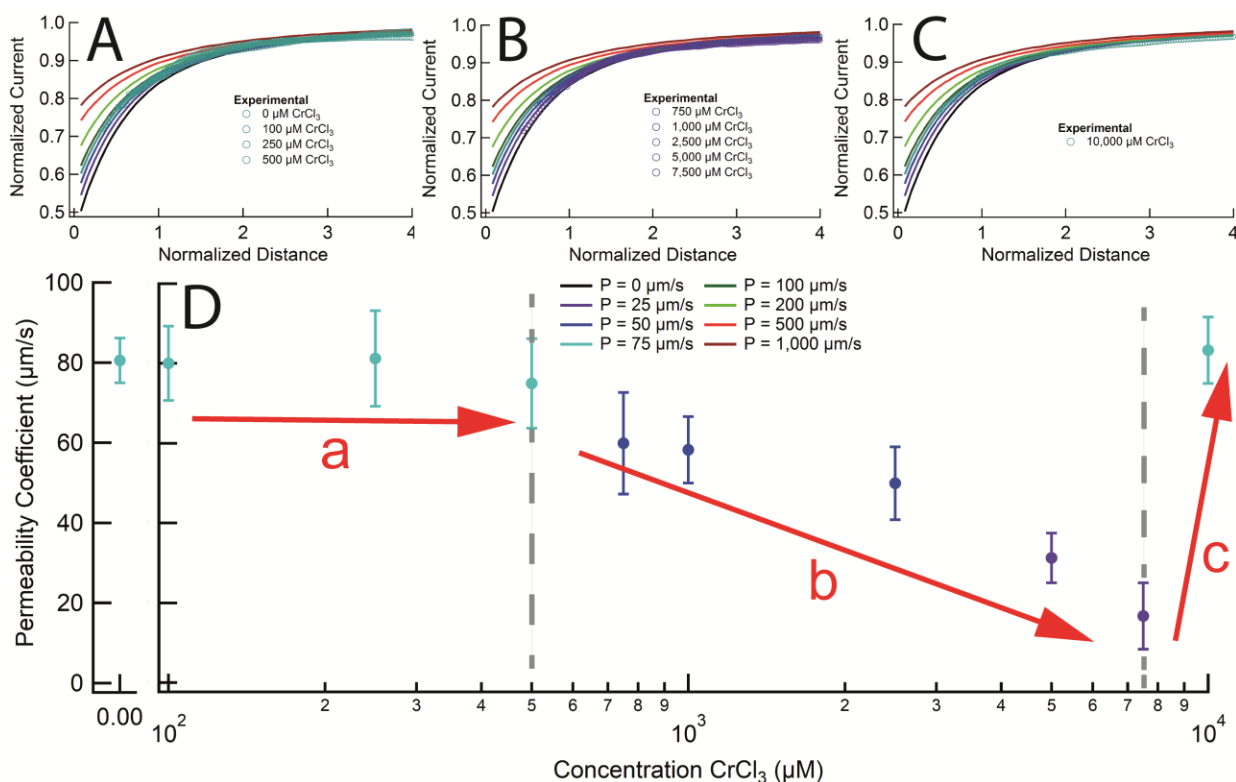
Figure 5.4 - Overlap of experimental and theoretical PACs for quantification of cell membrane permeability coefficients with FcCH₂OH electrochemical mediator. Incubation with various concentrations CrCl₃ displays regions of (A) stable, (B) decreasing, and (C) increasing membrane permeability. A graphical representation of the statistical membrane permeability change illustrating the three regions of (a) stable, (b) decreasing, and (c) increasing permeability.

After 1 hr of Cr (III) treatment between 0-500 µM, the membrane permeability and morphology of the T24 cells remained unaffected relative to the control sample (approximately 80 µm/s) (Figure 5.4A). This membrane stability region is a result of the essential role of intracellular Cr (III). At these concentrations, it appears T24 cells are capable of utilizing the additional Cr (III) for internal chemical processes, or coping with these levels of Cr(III).

After exposure to 750–7,500 µM Cr (III), a decreasing trend in permeability becomes evident (Figure 5.4B). The initial decrease observed in the 750 µM samples corresponded

to a permeability coefficient of 60 ± 13 μm/s. This was followed by a decrease in P values to 58 ± 8 μm/s and 50 ± 9 μm/s after exposure to 1,000, and 2,500 μM Cr (III), respectively. Even more significant P decreases occurred with incubation concentrations of 5,000 and 7,500 μM, showing average P values of 31 ± 6 μm/s and 17 ± 8 μm/s, respectively. This decrease may be attributed to the overwhelming of anti-oxidant defense systems since Cr (III) toxicity can lead to increased ROS generation, followed by lipid peroxidation.[5] Lipid peroxidation is known to affect changes in the bilayer thickness and membrane fluidity[66] and is a likely mechanism by which membrane characteristics are altered.

After exposure to 10,000 μM Cr (III), relaxation in P occured, returning to 83 ± 8 μm/s (Figure 5.4C). This relaxation resulted in the membrane permeability coefficient that is similar to the control samples (80 ± 6 µm/s). At this concentration, Cr (III) likely surpassed the trace essential requirements and becomes toxic. The resulting ROS production overwhelms the cellular defense systems, such as superoxide dismutase, catalase, and glutathione peroxidase, leading to oxidative damage and increased cell membrane damage.

Note that a data set of N>4 cells was obtained for each Cr (III) incubation concentration (example curves are shown in Figure 5.4A-C) and was used to determine the average ± standard error membrane permeability coefficients, which is summarized in Figure 5.4D. Three distinct regions of membrane response were observed when FcCH$_2$OH served as the SECM mediator. First, a relatively stable region was observed for incubation concentrations below 50 μM (region a). Incubations of 50–500 μM Cr (III) resulted in the loss of membrane stability and a region of decreasing permeability coefficient was observed (region b). Beyond 500 μM incubation concentrations (750, 1000 μM) caused the permeability coefficient to return to a permeability coefficient similar to control status (region c).

5.3.3 Cell Membrane Permeability to FcCOO⁻ Electrochemical Mediator
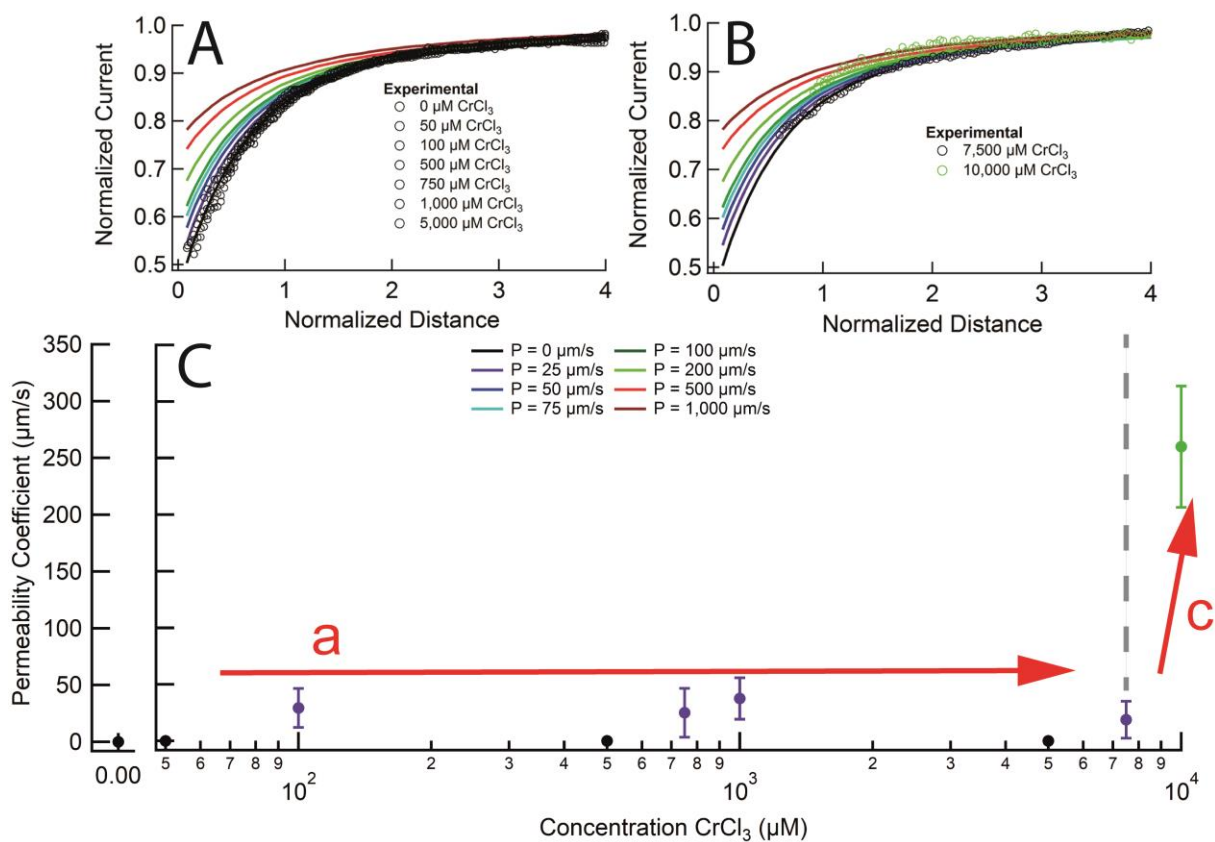
Figure 5.5 - Overlap of experimental and theoretical PACs with FcCOOH as a mediator, displaying regions of (A) stable, and (B) increasing membrane permeability following CrCl₃ incubation. A graphical representation of the membrane permeability change is also provided, showing the (a) stable, and (c) increasing permeability.

Under control conditions, SECM revealed the membrane permeability coefficient to FcCOO⁻ was 0 µm/s (membrane impermeable). This was expected due to the charged nature of the mediator at pH 7.4. The membrane permeability remained relatively stable around 0 µm/s after Cr (III) treatments less than 7,500 µM (50-5000 µM, Figure 5.5A). Minor increases were observed after 100, 750 and 1000 µM treatments, showing average $\pm$ standard error membrane permeability coefficients of 29 ± 17 µm/s, 25 ± 21 µm/s and 37 ± 18 µm/s, respectively. Due to the more hydrophilic and charged nature of the

FcCOO$^-$ mediator, it is unable to cross the hydrophobic interior of the phospholipid bilayer (cell membrane). As a result, FcCOO$^-$ is largely impermeable to the cell membrane under normal (control) conditions.[65] These results were in agreement with the SECM results previously described, as FcCH$_2$OH is partially permeable in nature, the decrease in membrane permeability trend was observable using FcCH$_2$OH but not observable using FcCOO$^-$. FcCOO$^-$, however, allows for more accurate imaging of cell topography since it is largely independent of membrane permeability under control conditions. The use of impermeable redox mediators when performing SECM on biological samples can indicate significant disruption in normal cell membrane performance.[62, 65] Therefore, the use of FcCOO$^-$ as the SECM mediator can provide good indication of when Cr (III) no longer behaves as a trace essential metal, but rather as a toxin.

After T24 cells were treated with 7,500–10,000 μM Cr (III), an increasing trend in permeability to FcCOO$^-$ was observed (Figure 5.5B), which was similar to the trend determined with FcCH$_2$OH (Figure 5.4D). When incubated with 7,500 μM Cr (III), the membrane permeability coefficient increased to 19 ± 16 μm/s. The highest concentration sample (10,000 μM Cr (III)) was found to have a membrane permeability coefficient of 260 ± 53 μm/s. This confirms a concentration-dependent effect of Cr (III) on membrane permeability in T24 cells. Over longer exposure to Cr (III), this may result in the selection of T24 cells with genetic mutations that offer greater resistance to Cr (III) poisoning. This permeability increase is likely attributed to the overwhelming of anti-oxidant defense systems as previously discussed. The effects of high Cr (III) concentration on the cell membrane were similar to that seen with FcCH$_2$OH mediator. This confirms significant oxidative cell membrane damage, such that polar compounds (FcCOO$^-$) are capable of entering the cell. In particular, lipid peroxidation is known to drastically change the membrane characteristics by increasing the number of polar functional group within the internal membrane region.[66-67]

The membrane permeability trend for FcCOO$^-$ agreed with the previously discussed trend for FcCH$_2$OH. Figure 5.5C shows the initial permeability coefficient to be 0 μm/s for

FcCOO$^-$. A trend of stability is observed (region a) at all concentrations occupied by regions a and b in the FcCH$_2$OH trend (Figure 4D). 7,500 µM Cr (III) appears to be the onset concentration at which T24 cells become permeable to FcCOO$^-$. The permeability to FcCOO$^-$ significantly increased following this concentration (region c), similar to that observed with FcCH$_2$OH.

Direct comparison of Figure 5.4D with Figure 5.5C also shows the apparent similarities in membrane responses following excessive CrCl$_3$ exposure. Examination of the Cr (III) concentrations at which membrane response is triggered in SECM can be used to judge relative toxicities.

5.3.4 MTT Cell Viability Study of T24 Cells Incubated with CrCl$_3$ for 1 hr

Since the membrane permeability trends were concentration-dependent, the overall health of the Cr(III)-treated T24 cells was also considered. This is important in understanding the effects of the heavy metal on cellular homeostasis. Here, cellular health was investigated by employing the MTT assay, routinely used to measure cellular viability of a bulk population of live cells (Figure 5.6). Cell viability is represented as mean ± standard error of 4 separate experiments (4-8 replications per experiment). Similar to the SECM studies, the T24 cells were exposed to various Cr (III) concentrations for 1 hr. These samples were compared to the healthy untreated cells from the same culture (Eq. 5.3).

$$cell\ viability\ (\%) = \left(\frac{A_{sample} - A_{blank}}{A_{control} - A_{blank}}\right) 100\% \qquad [5.3]$$
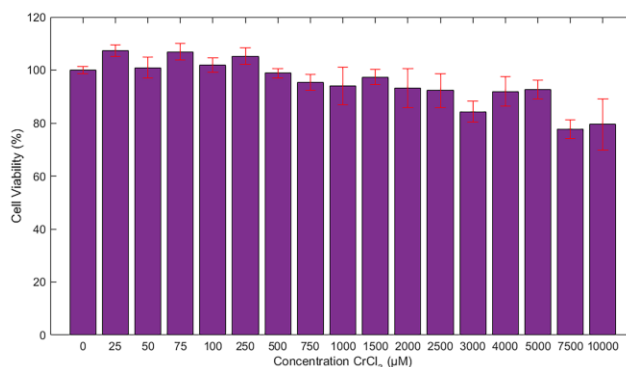
Figure 5.6 - Cell viability of T24 cells treated with a wide range of concentrations of Cr (III) for 1 hr, between 0 μM and 10,000 μM.

Cells exposed to concentrations below 500 μM showed viability with minimal deviation from the control group, approximately 100%. Exposure concentrations exceeding 500 μM, resulted in gradual decreased viability. The decrease in cell viability was found to continue with increasing exposure concentrations. This shows an increase in Cr (III) induced cellular death in T24 cells with higher Cr (III) concentrations. This observation followed the SECM studies well, as exposure to Cr (III) concentrations greater than 500 μM induced significant membrane permeability changes. The internal disruptions in cell homeostasis which lead to cell death likely contributes to the changes in the membrane that increase the membrane permeability coefficients in SECM.

5.4 Conclusion

Through the use of SECM, the membrane responses of single live Cr (III)-treated T24 cells were successfully interrogated using both FcCH$_2$OH and FcCOO$^-$ as electrochemical mediators. Full 3D simulations were computed using nested parametric programing in COMSOL Multiphysics, a finite element analysis software. These simulations were successfully carried out, generating theoretical depth scan images previously limited in 2D axial symmetry models. The simulated and experimentally acquired depth scan images allow for the extraction of electrode PACs for rapid

membrane permeability quantification. Through the comparison of experimentally and theoretically acquired PACs, changes in membrane permeability coefficients were determined. With the membrane-permeable FcCH$_2$OH, SECM revealed T24 cells exhibit a Cr (III) concentration-dependent effect on their membrane response. Incubation with low Cr concentrations showed little effect on the membrane permeability coefficients, which were similar to that of control cells. Increasing the exposure level resulted in decreased permeability coefficients. Ultimately with higher (more acute) Cr (III) exposure, the membrane permeability increased, returning to and exceeding the permeability coefficient value seen in control cells. The electrochemical mediator FcCOO$^-$, in contrast to FcCH$_2$OH, is impermeable to cell membranes. FcCOO$^-$ revealed only two concentration-dependent trends. Initially, the membrane permeability was found to remain unchanged until treated with high concentrations (more acute dosage) of Cr (III). Both FcCH$_2$OH and FcCOO- mediators exhibited strong increases in membrane permeability coefficients when subjected to similar concentrations (7500 μM CrCl$_3$ for 1 hr). These experiments show theeffectiveness of SECM in providing insights into cell membrane integrity.

5.5   References

1.   Hartwig, A., Metal Interaction with Redox Regulation: An Integrating Concept in Metal Carcinogenesis? *Free Radic. Biol. Med.* **2013,** *55*, 63-72.
2.   Dayan, A. D.; Paine, A. J., Mechanisms of Chromium Toxicity, Carcinogenicity and Allergenicity: Review of the Literature from 1985 to 2000. *Hum. Exp. Toxicol.* **2001,** *20* (9), 439-51.
3.   Cefalu, W. T.; Hu, F. B., Role of Chromium in Human Health and in Diabetes. *Diabetes Care* **2004,** *27* (11), 2741-51.
4.   Vincent, J. B., Elucidating a Biological Role for Chromium at a Molecular Level. *Acc. Chem. Res.* **2000,** *33* (7), 503-510.
5.   Balamurugan, K.; Rajaram, R.; Ramasami, T.; Narayanan, S., Chromium(Iii)-Induced Apoptosis of Lymphocytes: Death Decision by Ros and Src-Family Tyrosine Kinases. *Free Radic. Biol. Med.* **2002,** *33* (12), 1622-40.
6.   Fang, Z.; Zhao, M.; Zhen, H.; Chen, L.; Shi, P.; Huang, Z., Genotoxicity of Tri- and Hexavalent Chromium Compounds in Vivo and Their Modes of Action on DNA Damage in Vitro. *PLoS One* **2014,** *9* (8), e103194.

7.   Gikas, P.; Romanos, P., Effects of Tri-Valent (Cr(Iii)) and Hexa-Valent (Cr(Vi)) Chromium on the Growth of Activated Sludge. *J. Hazard. Mater.* **2006,** *133* (1-3), 212-7.

8.   Bagchi, D.; Bagchi, M.; Stohs, S. J., Chromium (Vi)-Induced Oxidative Stress, Apoptotic Cell Death and Modulation of P53 Tumor Suppressor Gene. *Mol. Cell. Biochem.* **2001,** *222* (1-2), 149-58.

9.   Catelas, I.; Petit, A.; Vali, H.; Fragiskatos, C.; Meilleur, R.; Zukor, D. J.; Antoniou, J.; Huk, O. L., Quantitative Analysis of Macrophage Apoptosis Vs. Necrosis Induced by Cobalt and Chromium Ions in Vitro. *Biomaterials* **2005,** *26* (15), 2441-53.

10.   Kovacik, J.; Babula, P.; Hedbavny, J.; Krystofova, O.; Provaznik, I., Physiology and Methodology of Chromium Toxicity Using Alga Scenedesmus Quadricauda as Model Object. *Chemosphere* **2015,** *120*, 23-30.

11.   O'Brien, T. J.; Ceryak, S.; Patierno, S. R., Complexities of Chromium Carcinogenesis: Role of Cellular Response, Repair and Recovery Mechanisms. *Mutat. Res.* **2003,** *533* (1-2), 3-36.

12.   Wang, X. F.; Xing, M. L.; Shen, Y.; Zhu, X.; Xu, L. H., Oral Administration of Cr(Vi) Induced Oxidative Stress, DNA Damage and Apoptotic Cell Death in Mice. *Toxicol.* **2006,** *228* (1), 16-23.

13.   Filice, F. P.; Li, M. S. M.; Wong, J. M.; Ding, Z., The Effects of Long Duration Chronic Exposure to Hexavalent Chromium on Single Live Cells Interrogated by Scanning Electrochemical Microscopy. *J. Inorg. Biochem.* **2018,** *182*, 222-229.

14.   Henderson, J. D.; Filice, F. P.; Li, M. S. M.; Ding, Z., Tracking Live-Cell Response to Hexavalent Chromium Toxicity by Using Scanning Electrochemical Microscopy. *ChemElectroChem* **2017,** *4* (4), 856-863.

15.   Liu, Y.; Liu, C.; Cheng, J.; Fan, W.; Zhang, X.; Liu, J., Growth Performance and Oxidative Damage in Kidney Induced by Oral Administration of Cr(Iii) in Chicken. *Chemosphere* **2015,** *139*, 365-71.

16.   Venter, C.; Oberholzer, H. M.; Cummings, F. R.; Bester, M. J., Effects of Metals Cadmium and Chromium Alone and in Combination on the Liver and Kidney Tissue of Male Spraque-Dawley Rats: An Ultrastructural and Electron-Energy-Loss Spectroscopy Investigation. *Microsc. Res. Tech.* **2017,** *80* (8), 878-888.

17.   Li, Y.; Hu, K.; Yu, Y.; Rotenberg, S. A.; Amatore, C.; Mirkin, M. V., Direct Electrochemical Measurements of Reactive Oxygen and Nitrogen Species in Nontransformed and Metastatic Human Breast Cells. *J. Am. Chem. Soc.* **2017,** *139* (37), 13055-13062.

18.   Joshi, V. S.; Sheet, P. S.; Cullin, N.; Kreth, J.; Koley, D., Real-Time Metabolic Interactions between Two Bacterial Species Using a Carbon-Based Ph Microsensor as a Scanning Electrochemical Microscopy Probe. *Anal. Chem.* **2017,** *89* (20), 11044-11052.

19.   Salamifar, S. E.; Lai, R. Y., Use of Combined Scanning Electrochemical and Fluorescence Microscopy for Detection of Reactive Oxygen Species in Prostate Cancer Cells. *Anal. Chem.* **2013,** *85* (20), 9417-21.

20. Suwalsky, M.; Castro, R.; Villena, F.; Sotomayor, C. P., Cr(Iii) Exerts Stronger Structural Effects Than Cr(Vi) on the Human Erythrocyte Membrane and Molecular Models. *J. Inorg. Biochem.* **2008,** *102* (4), 842-9.

21. Raja, N. S.; Sankaranarayanan, K.; Dhathathreyan, A.; Nair, B. U., Interaction of Chromium(Iii) Complexes with Model Lipid Bilayers: Implications on Cellular Uptake. *Biochim. Biophys. Acta* **2011,** *1808* (1), 332-40.

22. Petersen, R.; Thomsen, J. F.; Jorgensen, N. K.; Mikkelsen, S., Half Life of Chromium in Serum and Urine in a Former Plasma Cutter of Stainless Steel. *Occup. Environ. Med.* **2000,** *57* (2), 140-2.

23. Prescha, A.; Krzysik, M.; Zablocka-Slowinska, K.; Grajeta, H., Effects of Exposure to Dietary Chromium on Tissue Mineral Contents in Rats Fed Diets with Fiber. *Biol. Trace Elem. Res.* **2014,** *159* (1-3), 325-31.

24. Setyaningsih, Y.; Husodo, A. H.; Astuti, I., Detection of Urinary 8-Hydroxydeoxyguanosine (8-Ohdg) Levels as a Biomarker of Oxidative DNA Damage among Home Industry Workers Exposed to Chromium. *Procedia Environ. Sci.* **2015,** *23*, 290-296.

25. Wright, A.; Bubb, W. A.; Hawkins, C. L.; Davies, M. J., Singlet Oxygen–Mediated Protein Oxidation: Evidence for the Formation of Reactive Side Chain Peroxides on Tyrosine Residues. *Photochem. Photobiol.* **2002,** *76* (1), 35-46.

26. Dixit, R.; Cyr, R., Cell Damage and Reactive Oxygen Species Production Induced by Fuorescence Microscopy: Effect on Mitosis and Guidelines for Non-Invasive Fuorescence Microscopy. *Plant J.* **2003,** *36*, 280-290.

27. Bard, A. J.; Denuault, G.; Lee, C.; Mandler, D.; Wipf, D. O., Scanning Electrochemical Microscopy - a New Technique for the Characterization and Modification of Surfaces. *Acc. Chem. Res.* **2002,** *23* (11), 357-363.

28. Bard, A. J.; Fan, F. R. F.; Kwak, J.; Lev, O., Scanning Electrochemical Microscopy. Introduction and Principles. *Anal. Chem.* **2002,** *61* (2), 132-138.

29. Polcari, D.; Dauphin-Ducharme, P.; Mauzeroll, J., Scanning Electrochemical Microscopy: A Comprehensive Review of Experimental Parameters from 1989 to 2015. *Chem. Rev.* **2016,** *116* (22), 13234-13278.

30. Ding, Z.; Quinn, B. M.; Bard, A. J., Kinetics of Heterogeneous Electron Transfer at Liquid/Liquid Interfaces as Studied by Secm. *J. Phys. Chem. B* **2001,** *105* (27), 6367-6374.

31. Nowierski, C.; Noël, J. J.; Shoesmith, D. W.; Ding, Z., Correlating Surface Microstructures with Reactivity on Commercially Pure Zirconium Using Scanning Electrochemical Microscopy and Scanning Electron Microscopy. *Electrochem. Commun.* **2009,** *11* (6), 1234-1236.

32. Yin, Y.; Niu, L.; Lu, M.; Guo, W.; Chen, S., In Situ Characterization of Localized Corrosion of Stainless Steel by Scanning Electrochemical Microscope. *Appl. Surf. Sci.* **2009,** *255* (22), 9193-9199.

33. Tang, J.; Zheng, J.-J.; Yu, Y.-T.; Chen, l.; Zhang, N.; Tian, Z., Selective Etching of Zno Films on an Ito Substrate Using a Scanning Electrochemical Microscope. *Electrochim. Acta* **2012,** *83*, 247-252.

34. Eifert, A.; Mizaikoff, B.; Kranz, C., Advanced Fabrication Process for Combined Atomic Force-Scanning Electrochemical Microscopy (Afm-Secm) Probes. *Micron* **2015,** *68*, 27-35.

35. Bard, A. J.; Li, X.; Zhan, W., Chemically Imaging Living Cells by Scanning Electrochemical Microscopy. *Biosens. Bioelectron.* **2006,** *22* (4), 461-72.

36. Zhao, X.; Diakowski, P. M.; Ding, Z., Deconvoluting Topography and Spatial Physiological Activity of Live Macrophage Cells by Scanning Electrochemical Microscopy in Constant-Distance Mode. *Anal. Chem.* **2010,** *82* (20), 8371-3.

37. Li, M. S.; Filice, F. P.; Ding, Z., A Time Course Study of Cadmium Effect on Membrane Permeability of Single Human Bladder Cancer Cells Using Scanning Electrochemical Microscopy. *J. Inorg. Biochem.* **2014,** *136*, 177-83.

38. Koley, D.; Bard, A. J., Inhibition of the Mrp1-Mediated Transport of the Menadione-Glutathione Conjugate (Thiodione) in Hela Cells as Studied by Secm. *Proc. Nat. Acad. Sci. U.S.A.* **2012,** *109* (29), 11522-7.

39. Kim, J.; Izadyar, A.; Shen, M.; Ishimatsu, R.; Amemiya, S., Ion Permeability of the Nuclear Pore Complex and Ion-Induced Macromolecular Permeation as Studied by Scanning Electrochemical and Fluorescence Microscopy. *Anal. Chem.* **2014,** *86* (4), 2090-8.

40. Bergner, S.; Wegener, J.; Matysik, F.-M., Monitoring Passive Transport of Redox Mediators across a Confluent Cell Monolayer with Single-Cell Resolution by Means of Scanning Electrochemical Microscopy. *Anal. Methods* **2012,** *4* (3), 623-629.

41. Solda, A.; Valenti, G.; Marcaccio, M.; Giorgio, M.; Pelicci, P. G.; Paolucci, F.; Rapino, S., Glucose and Lactate Miniaturized Biosensors for Secm-Based High-Spatial Resolution Analysis: A Comparative Study. *ACS Sens.* **2017,** *2* (9), 1310-1318.

42. Kuss, S.; Cornut, R.; Beaulieu, I.; Mezour, M. A.; Annabi, B.; Mauzeroll, J., Assessing Multidrug Resistance Protein 1-Mediated Function in Cancer Cell Multidrug Resistance by Scanning Electrochemical Microscopy and Flow Cytometry. *Bioelectrochemistry* **2011,** *82* (1), 29-37.

43. Kuss, S.; Polcari, D.; Geissler, M.; Brassard, D.; Mauzeroll, J., Assessment of Multidrug Resistance on Cell Coculture Patterns Using Scanning Electrochemical Microscopy. *Proc. Nat. Acad. Sci. U.S.A.* **2013,** *110* (23), 9249-54.

44. Holt, K. B.; Bard, A. J., Interaction of Silver(I) Ions with the Respiratory Chain of Escherichia Coli: An Electrochemical and Scanning Electrochemical Microscopy Study of the Antimicrobial Mechanism of Micromolar Ag+. *Biochemistry* **2005,** *44* (39), 13214-23.

45. Zhao, X.; Zhang, M.; Long, Y.; Ding, Z., Redox Reactions of Reactive Oxygen Species in Aqueous Solutions as the Probe for Scanning Electrochemical Microscopy of Single Live T24 Cells. *Can. J. Chem.* **2010,** *88* (6), 569-576.

46. Zhang, M. M.; Long, Y. T.; Ding, Z., Cisplatin Effects on Evolution of Reactive Oxygen Species from Single Human Bladder Cancer Cells Investigated by Scanning Electrochemical Microscopy. *J. Inorg. Biochem.* **2012,** *108*, 115-22.

47. Zhao, X.; Lam, S.; Jass, J.; Ding, Z., Scanning Electrochemical Microscopy of Single Human Urinary Bladder Cells Using Reactive Oxygen Species as Probe of Inflammatory Response. *Electrochem. Commun.* **2010,** *12* (6), 773-776.

48. Zhao, X.; Petersen, N. O.; Ding, Z., Comparison Study of Live Cells by Atomic Force Microscopy, Confocal Microscopy, and Scanning Electrochemical Microscopy. *Can. J. Chem.* **2007,** *85* (3), 175-183.

49. Zhan, D.; Li, X.; Nepomnyashchii, A. B.; Alpuche-Aviles, M. A.; Fan, F.-R. F.; Bard, A. J., Characterization of Ag+ Toxicity on Living Fibroblast Cells by the Ferrocenemethanol and Oxygen Response with the Scanning Electrochemical Microscope. *J. Electroanal. Chem.* **2013,** *688*, 61-68.

50. Li, X.; Bard, A. J., Scanning Electrochemical Microscopy of Hela Cells – Effects of Ferrocene Methanol and Silver Ion. *J. Electroanal. Chem.* **2009,** *628* (1-2), 35-42.

51. Sun, P.; Laforge, F. O.; Abeyweera, T. P.; Rotenberg, S. A.; Carpino, J.; Mirkin, M. V., Nanoelectrochemistry of Mammalian Cells. *Proc. Nat. Acad. Sci. U.S.A.* **2008,** *105* (2), 443-8.

52. Cai, C.; Liu, B.; Mirkin, M. V.; Frank, H. A.; Rusling, J. F., Scanning Electrochemical Microscopy of Living Cells. 3.Rhodobactersphaeroides. *Anal. Chem.* **2002,** *74* (1), 114-119.

53. Feng, W.; Rotenberg, S. A.; Mirkin, M. V., Scanning Electrochemical Microscopy of Living Cells. 5. Imaging of Fields of Normal and Metastatic Human Breast Cells. *Anal. Chem.* **2003,** *75* (16), 4148-54.

54. Liu, B.; Cheng, W.; Rotenberg, S. A.; Mirkin, M. V., Scanning Electrochemical Microscopy of Living Cells. *J. Electroanal. Chem.* **2001,** *500* (1-2), 590-597.

55. Liu, B.; Rotenberg, S. A.; Mirkin, M. V., Scanning Electrochemical Microscopy of Living Cells: Different Redox Activities of Nonmetastatic and Metastatic Human Breast Cells. *Proc. Nat. Acad. Sci. U.S.A.* **2000,** *97* (18), 9855-60.

56. Mosmann, T., Rapid Colorimetric Assay for Cellular Growth and Survival: Application to Proliferation and Cytotoxicity Assays. *J. Immunol. Methods* **1983,** *65* (1-2), 55-63.

57. Soleimani, A.; Moustafa, M. M. A. R.; Borecki, A.; Gillies, E. R., A Comparison of Covalent and Noncovalent Strategies for Paclitaxel Release Using Poly(Ester Amide) Graft Copolymer Micelles. *Can. J. Chem.* **2015,** *93* (4), 399-405.

58. Filice, F. P.; Li, M. S.; Henderson, J. D.; Ding, Z., Mapping Cd(2)(+)-Induced Membrane Permeability Changes of Single Live Cells by Means of Scanning Electrochemical Microscopy. *Anal. Chim. Acta* **2016,** *908*, 85-94.

59. Henderson, J. D.; Filice, F. P.; Li, M. S. M.; Ding, Z., Tracking Live Cell Response to Cadmium (Ii) Concentrations by Scanning Electrochemical Microscopy. *J. Inorg. Biochem.* **2016,** *158*, 92-98.

60. Kuss, S.; Trinh, D.; Danis, L.; Mauzeroll, J., High-Speed Scanning Electrochemical Microscopy Method for Substrate Kinetic Determination: Method and Theory. *Anal. Chem.* **2015,** *87* (16), 8096-101.

61. Guo, J.; Amemiya, S., Permeability of the Nuclear Envelope at Isolated Xenopus Oocyte Nuclei Studied by Scanning Electrochemical Microscopy. *Anal. Chem.* **2005,** *77* (7), 2147-56.

62. Koley, D.; Bard, A. J., Triton X-100 Concentration Effects on Membrane Permeability of a Single Hela Cell by Scanning Electrochemical Microscopy (Secm). *Proc. Nat. Acad. Sci. U.S.A.* **2010,** *107* (39), 16783-7.

63. Niehorster, T.; Loschberger, A.; Gregor, I.; Kramer, B.; Rahn, H. J.; Patting, M.; Koberling, F.; Enderlein, J.; Sauer, M., Multi-Target Spectrally Resolved Fluorescence Lifetime Imaging Microscopy. *Nat. Methods* **2016,** *13* (3), 257-62.

64. Miao, W.; Ding, Z.; Bard, A. J., Solution Viscosity Effects on the Heterogeneous Electron Transfer Kinetics of Ferrocenemethanol in Dimethyl Sulfoxide–Water Mixtures. *J. Phys. Chem. B* **2002,** *106* (6), 1392-1398.

65. Li, M. S. M.; Filice, F. P.; Henderson, J. D.; Ding, Z., Probing Cd2+-Stressed Live Cell Membrane Permeability with Various Redox Mediators in Scanning Electrochemical Microscopy. *J. Phys. Chem. C* **2016,** *120* (11), 6094-6103.

66. Wong-Ekkabut, J.; Xu, Z.; Triampo, W.; Tang, I. M.; Tieleman, D. P.; Monticelli, L., Effect of Lipid Peroxidation on the Properties of Lipid Bilayers: A Molecular Dynamics Study. *Biophys. J.* **2007,** *93* (12), 4225-36.

67. Cordeiro, R. M., Reactive Oxygen Species at Phospholipid Bilayers: Distribution, Mobility and Permeation. *Biochim. Biophys. Acta* **2014,** *1838* (1 Pt B), 438-44.

Chapter 6

6   SECM Imaging and Full 3D Modelling of Asymmetric Clusters of Live Cells

Scanning Electrochemical Microscopy (SECM) has shown great strength as a bioanalytical technique for the characterization of single live cell topography, membrane permeability and extracellular reactive oxygen species. However, care must be taken to avoid the presence of adjacent cells in close proximity. Herein, we describe how these clusters of two or more cells may contribute to a combined signal. SECM is commonly coupled with simulated theoretical probe approach curves, allowing surface geometry or electrochemical reactivity to be quantified. Our novel experimental and simulation methodologies including tailored 3D SECM imaging of the live cells are reported here. These 3D modelling techniques allow the generation of 3D x-y-z cell profiles, cell surface maps at an electrode-cell separation, depth scan maps, probe approach curves to any cell spots of interest, and surface topography. The experimental quantification of cell height and topography was performed on cell clusters with an impermeable hydrophilic redox agent, ferrocenecarboxylate, for the deconvolution of these adjacent cell signals. As a proof of concept, experimental and theoretical results were compared to established model outputs. The characterization limits of commonly employed electrode sizes were assessed. Higher complex cell geometries were explored for the first time, leading to the characterization of these cell clusters with any electrode size. The above developments are versatile, and further demonstrate the strength of SECM as a bioanalytical technique for monitoring cellular homeostasis.

6.1   Introduction

Scanning electrochemical microscopy (SECM) is a powerful non-invasive analytical technique in the scanning probe microscopy family. [1-3] This technique utilizes electrochemistry at a biased ultramicroelectrode (UME, ≤25 µm in diameter) to image a region of space over a sample (or substrate) with extreme precision. Faradaic current is monitored and recorded alongside UME position, creating comprehensive maps of sample topography and surface reactivity. SECM relies on the presence of a redox species, either intrinsic to the system or added for the purposes of imaging, which is oxidized or reduced in a diffusion-controlled process yielding steady state current.

Early SECM experimentation and development accomplished by Bard et al. since 1989 laid the groundwork for it's application to a diverse range of fields. [4-5] SECM has been employed in a vast number of applications [6] including but not limited to kinetic studies, [7-8] surface and interface studies, [9-12] microstructure fabrication. [13-15] SECM has also found applications as a bioanalytical tool for cellular imaging, [16-24] membrane transport, [17, 25-33] neurotransmitter release, [34-36] multidrug resistance, [18-19, 37] ROS and RNS mapping, [24, 38-43] and cellular redox processes. [22, 44-49]

Various methods of sample imaging by SECM exist, providing one or more dimensions of probe movement. 1D analysis provides the simplest scanning method, commonly performed as probe approach curves (PACs) with the UME moving on the z-axis toward the sample, or as a horizontal line scan across the substrate at a fixed distance or current feedback (x or y axis). 2D systems of analysis can provide imaging across planes of space above a sample. The most common of these is the surface map, imaging a plane of space in the x and y direction.

In the Ding Group, a different mode of SECM has been developed, known as SECM depth scan mode.[41] Depth scanning operates in the x-z plane or y-z plane, with multiple horizontal line scans nested inside the z approach to a sample. This produces a 2D image of the current as a function of UME (x, z) or (y, z) coordinates. This imaging technique allows for the tip-to-sample distance to be more easily gauged as the experiment is being

performed, which was a limitation of conventional SECM approach methods. 2D imaging obtained in the depth scan mode have the added benefit of being composed of numerous 1D approaches at different positions. Hundreds of useable 1D PACs can be extracted from a single scan.

Imaging in 3 dimensions provides analysis of a cube of space over the sample. 3D scanning provides a map that is composed of hundreds of 2D images such as depth scans, which are in turn composed of hundreds of PACs. This yields tens of thousands of PACs in a grid over a sample of interest. A 3D map could alternatively be used to extract 2D surface maps or 1D line scans, providing numerous options for data processing in post processing. Also, similar to depth scanning, both the x and y movement is nested inside of the z directional approach with real time data reporting. This provides accurate gauging of tip-to-sample distance on approach to the sample.

Other methods of multidimensional scanning for SECM include 4D shearforce-based constant distance mode developed by Schuhmann's group. In this scanning mode, multiple constant distance images are obtained above the sample. [50] The tip-to-sample distance is controlled by the retractions of the tip based on the shearforce of the SECM probe. [50] A comprehensive 4D data set including the current feedback and shearforce of the current-tip coordinates is generated.

SECM hopping mode is another scanning method that is often performed as a 3D scan.[51] Hopping mode images the same region of space as a 3D (image stack) scan. The primary difference in these two scanning modes, is the order in which the 3 axes are scanned. In hopping mode, the electrode is positioned at the (x,y) start coordinates and a PAC is performed scanning in the z axis. The electrode approaches the sample until a predefined feedback is detected at the probe tip. The electrode is then repositioned in the xy plane and another PAC is performed. This produces a 2D grid of PACs over the sample of interest.

Quantification of physiological processes, such as membrane permeability [17, 52-53] and molecular transport of species [27] by SECM are typically assessed by overlaying

experimental PACs onto simulated theoretical curves. Simulation results can vary significantly based on the replication of experimental geometry and physical parameters in the model. As a result, the successful overlay of experimental and theoretical curves allows for the quantification of these properties. The generation of these theoretical PACs were traditionally generated as a 2D-axially symmetric simulation, using finite elemental analysis software, such as COMSOL Multiphysics or MATLAB. This simulation methodology provides simplicity of design, and fast compute times. However, the central axis of symmetry is in fact a significant limitation, restricting the characterization to only one experimental PAC (to the direct center of the sample). This limits the primary advantage of any 2D or 3D scanning method. I have developed more complex simulations to allow for the simulation of PACs at positions deviating from a cell central axis,[54] and the simulation of full 2D depth scans.[55] Modelling the experimental system in full 3D allows for the complete control of the electrode's position and model geometry with no imposed symmetry restrictions.[56-57]

The ability to model complex geometries in 3D becomes extremely useful for the analysis of live cell samples. Cell simulations regularly simplify cell geometry to single spherical domains.[17, 21] This simplification can often be made at larger electrode sizes, but complications can arise with more refined electrode tips. Care is also generally taken experimentally to avoid clusters of cells due to the possible effects of adjacent cells on tip current. This is generally done as simulating complex clusters of live cells adds additional complexity to the model. However, live cell samples rarely behave in an idealized fashion, and creating a subculture of over confluent samples for ideal cell spacing is not always possible. Herein for the first time, I will demonstrate 3D modelling of complex clusters of live cells with common UME sizes (10 μm and 4.4 μm) for SECM analysis. Simulation of single cell topography is compared to the complex model geometry to confirm the extended model design. The effects of adjacent cell proximity, when performing horizontal line scans is also explored. The limits of detection for the adjacent cell when performing a PAC approach to a cell center are emphasized with these common UME sizes, as this directly affects common methods of cell membrane permeability quantification. An experimental worst-case scenario is also explored with

extreme proximity and larger electrode size, where the simulation model is capable of providing a strong theoretical fit to the experimental results. This methodology for the theoretical quantification of samples further strengthens the SECM as a powerful bioanalytical tool for the study of single live cells.

6.2   Experimental Section

6.2.1   Materials

Ferrocenecarboxyllic acid (FcCOOH, 97%), and potassium chloride (KCl, 99%), were purchased from Sigma-Aldrich Canada (Mississauga, ON) and used without further purification. A stock solution of SECM mediator was prepared using 0.5 mM FcCOOH, dissolved in 1× phosphate buffered saline (PBS, Life Technologies, Burlington, ON).

6.2.2   Cell Preparation

Human bladder cancer cells (T24 cells (HTB-4™)) were ordered from American Type Culture Collection (ATCC, Manassas, VA, USA) and maintained according to the ATCC specified protocol. Cells were cultured in McCoy's 5a medium (ATCC) containing 10% Fetal Bovine Serum at 37°C with 5% CO_2. When preparing cells for SECM experiments, T24 cells were aliquoted directly onto sterilized glass-bottom Petri dishes (P35G-0-20-C, MatTek Corporation, Ashland, MA, USA). The cells were then incubated for a minimum of 24 hr to ensure cell adherence to the glass surface of the Petri dish. Growth medium was decanted prior to analysis via SECM, and replaced with the FcCOOH mediator solution, following thorough washing with 1× PBS.

6.2.3   SECM Instrumentation

A detailed description of the SECM instrumentation and experimental procedures can be found in Chapter 2 section 2.2.5.[54] Briefly, SECM experiments were carried out using a modified Alpha-SNOM (WITec, Ulm, Germany). The SNOM has been outfitted with a custom-fabricated UME mount in place of the upper objective lens, and a micro-incubator Petri dish mount (Bioscience Tools, San Diego, California, USA). The inverted objective lens (50×, N.A. 0.55, W.D. 10.1 mm, Nikon, Japan) was used to assist in the

positioning of the UME over live cells of interest, as well as provide optical imaging of the cells under study. High resolution UME positioning was achieved through the WITec piezoelectric positioning system. Electrochemical instrumentation consisted of a CH Instruments Electrochemical Analyzer (CHI800B, Austin, TX) and CHI200 Picoamp Booster to enhance the low current signal observed with small electrodes and dilute solutions while limiting signal noise. A simple two-electrode set-up was used with the UME as the working electrode, and a Ag/AgCl electrode as the reference/counter electrode. All potentials reported in this report are vs Ag/AgCl.

6.2.4   SECM Experimental Procedure

Before each experiment, cyclic voltammetry (CV) was used to test for steady-state performance of the UME probe and solution. The Petri dish containing the cells (30-40% confluency) was then secured to the heating stage mount maintained at 37.0 ± 0.2 ˚C. Each Petri dish was analyzed for a maximum duration of 60 min. A biased UME tip potential of 0.3 V (identified through CV) was applied to obtain steady state current with the FcCOOH electrochemical mediator. SECM analysis of all samples was performed at a maximum UME tip speed of 21.5 µm/s, to limit the effects of forced solution convection and maintain steady state current.[58] The SECM 3D imaging method was utilized on the desired cells located via the inverted microscope on the Alpha-SNOM. The 3D (image stack) method performs a constant height 2D scan of a x-y plane at the highest specified z coordinate. Following this scan, the electrode is moved down by a specified distance in the z direction and another x-y scan is performed. This is repeated until a target electrode z position is met, or the scan is manually stopped (Figure 6.1A). This allows the analysis of a 3D region of space above the sample. The 3D scanning method produces real time probe-to-cell distance information and minimizes electrode collision with the cells. Manipulation of scan parameters, such as x, y and z movement distance, scan speeds, and image resolution, was made possible through the WITec software. The resulting 3D data set is treated as a 3D matrix in MATLAB. Extractions of any 2D plane from the data set can be easily performed, producing surface maps and depth scans at any desired position over the sample (Figure 6.1B).
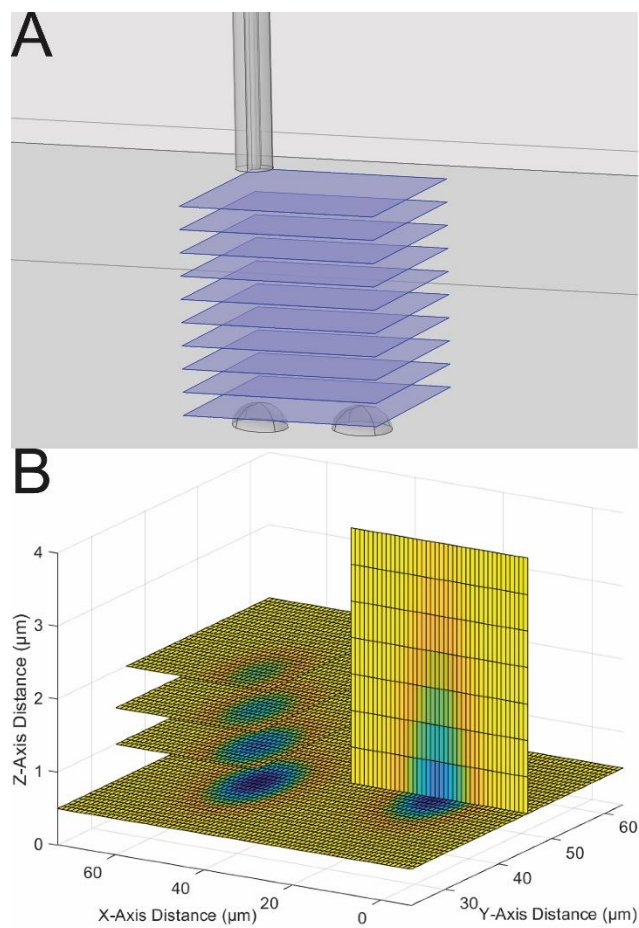
Figure 6.1 - (A) Representation of the multiple 2D surface maps that compose a single 3D SECM scan. (B) Example of multiple extractions of 2D surface maps and depth scans from 3D data set.

6.3 Simulation
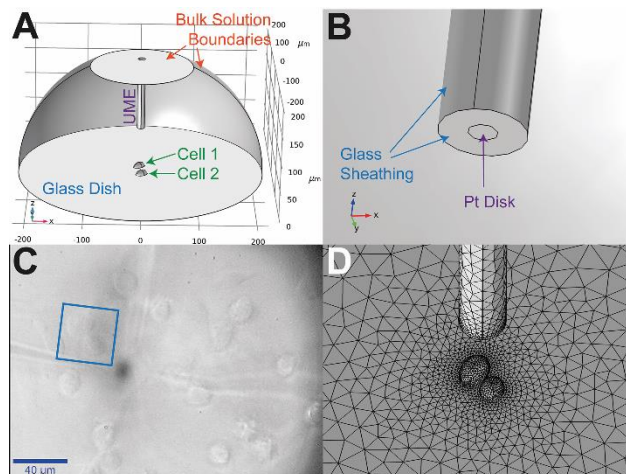
Figure 6.2 - (A) 3D model of the SECM approach to an isolated cluster of cells with key features, boundaries, and domains labeled. (B) Zoomed-in and labelled view of the electrode tip geometry. (C) Optical image of an experimental double cell with labelled UME path. (D) Meshed 3D model, focusing on the electrode tip in close proximity to the two cells imaged in C.

Theoretical SECM mapping, and all derivative scan methods (depth scan images, surface maps, PACs, etc.) were generated using COMSOL Multiphysics (v5.3, COMSOL Inc., Burlington, Massachusetts). A Full 3D model was created to simulate the same physical geometry as the SECM experiments. The electrode geometry was defined to recreate the physical characteristics of the UME utilized for the experimental analysis (10 µm or 4.4 µm Pt diameter, with a RG value of 3). The cell geometry for this 3D model was customized for each experimental sample, with dimensions derived from experimental optical and SECM depth scan images (Figure 6.2A and B). Cells were surveyed optically and measured via pixel counting. The long and short axes diameters of the cell were independently measured, as well as the distance between the cell centers, relative position, and angle of the cell long axis relative to the path of the UME as it scans (Figure 6.2C). Cells measured in included cell positions and orientation relative to each other. Cell height was measured by SECM relative to the glass Petri dish using a method described previously.[55]

The model was defined as a single solution domain, considering only the extracellular solution. This is possible owing to the selection of electrochemical mediator, FcCOOH, which is impermeable to the cell membrane under normal homeostatic conditions. The initial solution concentration at all locations in the domain was specified as $C_B = 0.5$ mM FcCOOH. The exterior solution boundaries of the model maintained this initial concentration of mediator, simulating the presence of a much larger (theoretically infinite) solution domain extending beyond the model. These bulk solution boundaries were defined as being 100× the Pt UME radius away from the cell center (500 µm away for 10 µm UME and 220 µm for 4.4 µm). The rate of the mediator transport is governed by the diffusion coefficient for the model (D), and Ficks's second law of diffusion (Eq 6.1). The diffusion coefficient for FcCOOH in the domain was set to 5.7×10^{-10} m^2/s.[59-60]

$$\frac{\partial C_B(x,y,z)}{\partial t} = D \left(\frac{\partial^2 C_B(x,y,z)}{\partial x^2} + \frac{\partial^2 C_B(x,y,z)}{\partial y^2} + \frac{\partial^2 C_B(x,y,z)}{\partial z^2} \right) [6.1]$$

A diffusion-limited one-electron oxidation reaction occurs for FcCOOH when adequate potential bias is applied to the system (0.35V vs Ag/AgCl). This was recreated in the simulation by defining a mediator concentration of zero at the biased Pt surface. The cell membrane was defined as an insulating boundary with no flux since the FcCOOH electrochemical mediator is impermeable to the cell membrane.

The COMSOL model domain was then meshed using a free tetrahedral mesh (Figure 6.2D). The meshing element size defines the simulation resolution and can influence the accuracy of the model. A minimum element size of 0.05 µm was defined, with a maximum element growth rate of 1.2, up to a maximum of 50 µm at the bulk solution boundary. The mesh was further refined at the cell membrane boundaries (0.3×) and the Pt disk of the UME (0.1×), where the concentration change was the most significant.

To simulate cell topography, a stationary phase (steady state) simulation method was utilized. The UME position relative to the cells was defined and the solution flux was simulated. The resulting concentration profile for the specified UME coordinates was saved. The UME was then repositioned, and the process was repeated. Each electrode position was simulated separately, using the parametric sweep function of COMSOL.

Parametric sweeps sequentially simulate a range of values to be investigated defined by a starting value, step size and stop condition. Multiple parametric instruction loops can be nested inside each other, allowing for the simulation of full cartesian positioning with three parameters (x, y, z). Each individual simulation maintained a full concentration map for the defined electrode position and physics conditions. The flux to the electrode surface was integrated across the Pt disk in post processing and converted to UME tip current for comparison to experimental scans.

Theoretical and experimental PACs were normalized and plotted together to allow quantification of experimental tip to sample distance. The distance was normalized to the UME critical radius used experimentally (5 μm or 2.2 μm radius). Current was normalized to bulk solution current (i_∞).

6.4   Results and Discussion

6.4.1   Double Cell Imaging with a 4.4 µm UME
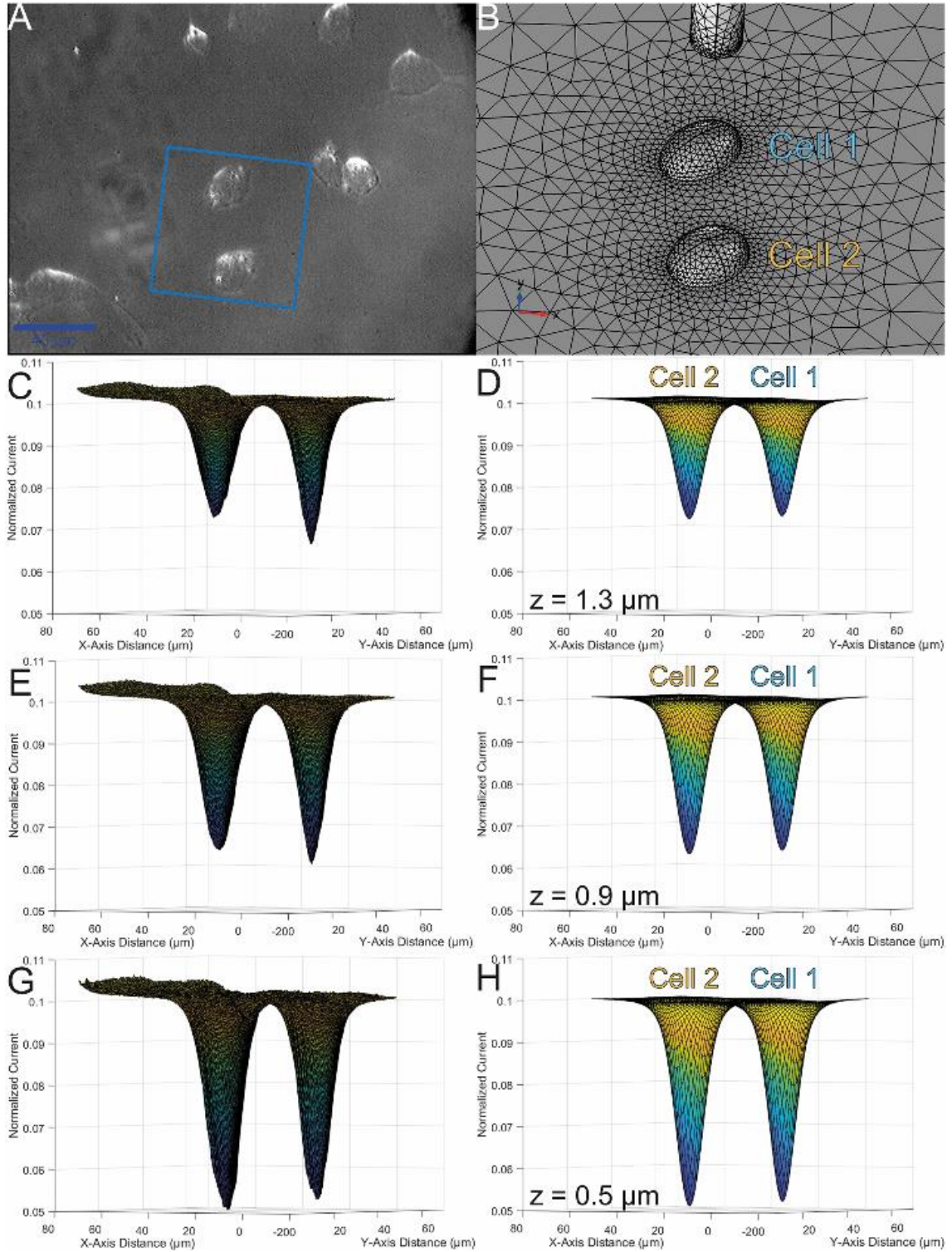
Figure 6.3 - (A) Optical image of an experimental double cell imaged with a 4.4 μm diameter UME. UME imaging area labelled in blue. (B) Meshed 3D model, of experimental double cell. (C) Experimental and (D) simulated surface maps of the double cell at tip to sample distance of 1.3 μm from the top of the cells. (E) Experimental and Simulated (F) surface maps at a tip to sample distance of 0.9 μm. (G) Experimental and (H) simulated surface maps at a tip to cell distance of 0.5 μm.

A pair of cells in close proximity to each other (41.3 μm center to center) (Figure 6.3A) was imaged using a 4.4 μm UME and modeled in 3D using COMSOL (Figure 6.3B). Cell heights were characterized by SECM and determined to vary by only 0.11 μm for the two cells. Experimental scans imaged an area of 60 μm × 60 μm yielding current maps of 256 pixel × 256 pixel. 20 different tip-to-cell distances were performed as part of the experimental scan with a 0.4 μm step distance in the z axis. Planes were extracted from this 3D image to provide 2D depth scan profiles, or surface maps of the cell samples by specifying a plane through the 3D data set in MATLAB (Figure 6.1B). Line scans were also be extracted from the 3D map, providing 1D probe approach curves (PACs) or single line scans over the samples. All of these common methods of characterization are available as part of the one 3D scan. This allows for multiple forms of characterization to be performed on the same cell sample, which can be exported in post processing. Full 3D experimental (Figure 6.3C, E, and G) and simulation (Figure 6.3D, F, and H) surface maps are displayed, providing electrochemical characterization of a region of space above the cells of interest. These represent the 3 closest experimental surface maps performed in this 3D scan. This tip to sample distance was determined to be 1.3 μm (Figure 6.3C and D), 0.9 μm (Figure 6.3E and F), and 0.5 μm (Figure 6.3G and H). This mirrors the experimental step size of 0.4 μm in the z direction. Peak size, position height and shape were found to strongly agree with the theoretically generated surface maps at multiple distances from substrate.

The complexity of the single cell being studied may necessitate additional considerations for geometry and physics. This work aims to characterize the restrictions on cell proximity that must be considered when performing simulations of this type.
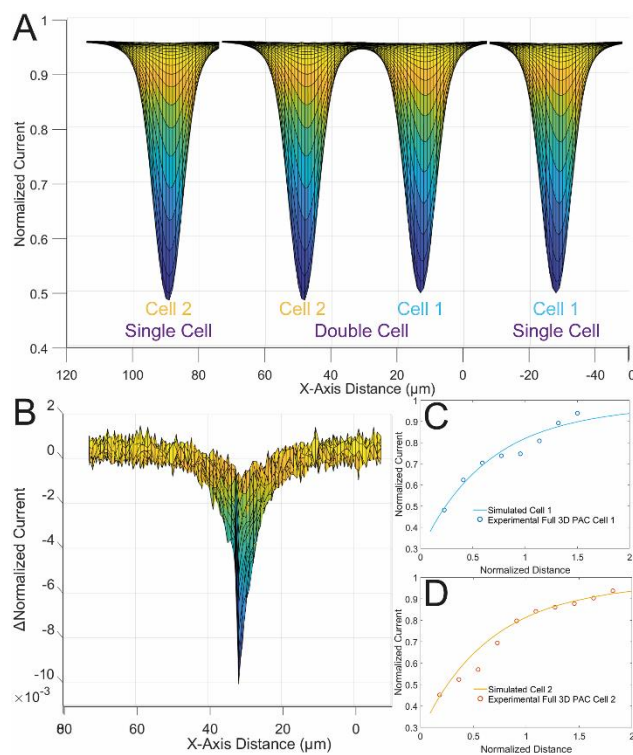
Figure 6.4 - (A) Theoretical double cell compared to individually simulated single cells of the same geometry at a tip to sample distance of 0.5 µm. (B) Difference in surface maps generated with both geometries. (C) Experimental PAC extracted from 3D image of double cell for cell 1, fitted to theoretical PAC. (D) Experimental PAC extracted from 3D image for cell 2.

The double cell system imaged in this study incorporated two cells in relative close proximity to each other, where two cells were present in the same scan. This is normally avoided experimentally due to the risk of receiving a cumulative signal from the adjacent cells. However, in this case the distance between the cells (41.3 µm center to center), and the relatively small UME tip size of 4.4 µm, allowed for negligible contribution from the adjacent cell. The theoretical map from Figure 6.3H, was re-simulated with both double cell and single cell geometry, for both cells (Figure 6.4A). This is the same theoretical system that was explored above. The difference in the surface map profile between the single cell and double cell models was calculated for all positions, with a maximum deviation of 0.01 in the normalized current of the two maps (Figure 6.4B). Deviation of

this magnitude occurs only in the region between the two cells where minor contribution from the adjacent cell is present. The majority of regions simulated had a difference of less than 0.001, including the peaks of the cell surface map. This indicates that PAC extractions were largely unaffected by the presence of the adjacent cell at this electrode size and distance. As a result, each of these cells could be simulated individually at this electrode size and cell spacing, without the need for incorporating the added complexity of the second cell. This would greatly reduce compute time without negatively affecting the resulting theoretical map or PAC.

Experimental PAC extractions were taken from the 3D scan of the double cell over each of the two cells. PACs were also extracted from the simulated 3D map for both cells and used to characterize the tip to substrate distance. The closest approach position of the UME to cell 1 had a normalized current of 0.48, which corresponds to a tip to substrate distance of 0.51 μm (Figure 6.4C). The UME had closer approach to Cell 2, yielding a normalized current of 0.45 and a tip to substrate distance of 0.40 μm (Figure 6.4D). These distances are very similar to the 0.5 μm characterization done by surface mapping observed in Figure 6.3GH. In this figure, peak intensity was very close between experimental and theoretical surface maps, with minor deviation. The individual characterization by PAC provides a more accurate measurement of this geometry. This method also allows for the characterization of the relatively minor 0.11 μm difference in cell height between the two cells. By performing the full 3D characterization, both experimentally and theoretically, the benefits of all these more targeted scans can be achieved in post processing.

6.4.2 Close Proximity Cells Imaged with a 10 µm Electrode
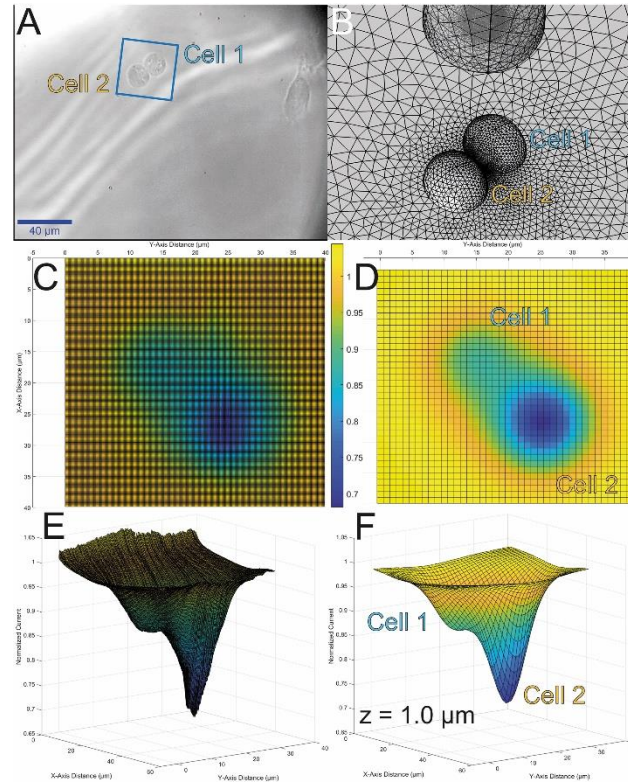
Figure 6.5 - (A) Optical micrograph of a pair of cells (14.7 µm center to center distance) to be imaged with a 10 µm UME, with scan area labelled in blue. (B) Meshed 3D model of the experimental double cells. (C) Experimental and (D) Simulated surface maps represented as a 2D xy surface map. (E) Experimental and (F) Simulated surface maps extracted from a 3D image of the double cells at a tip-to-cell distance of 1.0 µm (from the tallest cell).

The analysis of a sample utilizing a larger electrode or with cells at an extremely close proximity (14.7 µm center to center distance) is expected to have additional complexity. In many cases the cells can no longer be treated as individual cells for analysis, and more sophisticated models must be created, tailored to the specific geometry of the entire multi-cell system. This necessitates a dedicated simulation for each experimental sample, greatly increasing the computational time required. However, through the use of this

multi-cell simulation methodology, samples which were previously unusable for characterization can now be studied.

An experimental map of a pair of cells was performed incorporating both of these non-ideal conditions, with two cells in direct contact imaged by a 10 µm UME (Figure 6.5A). Experimental scans imaged an area of 40 µm × 40 µm yielding 256 pixel × 256 pixel current maps. 10 images were taken at various tip-to-cell distances. The imaging of a system that exhibits feedback overlap of adjacent cells to this degree has been previously regarded as detrimental to SECM analysis and is avoided when performing experimental analysis. The full geometry of both of these cells were measured for size and orientation, using the pixel counting methodology detailed in 6.3. The complex geometry of this experimental system was used to generate a theoretical model for the simulation of this 3D map (Figure 6.5B). A difference in cell height was observed between the two cells, with the shorter cell having a 6.75 µm height (cell 1), while the taller cell had an 8.00 µm height (cell 2). This difference in cell height was also incorporated into the model geometry.

The double cell system was imaged in 3D by SECM, and a surface map was extracted at 1.0 µm from the top of the tallest cell (cell 2). This SECM surface map was replicated theoretically and compared to the experimental map. The theoretically generated and experimentally acquired surface maps show close agreement in peak position and shape (Figure 6.5C and D). The strong feedback response of the taller cell 2, as well as the weaker feedback from the shorter cell 1, are both visible in the experimental and theoretical maps. A similar gradient of influence was observed as the UME moved away from these cells and was positioned over the glass dish adjacent to the cells. The combined profiles of the two adjacent cells matched one another in positional accuracy.

Peak intensity was also observed to show strong agreement between the experimental and theoretically acquired surface maps (Figure 6.5E and F). Through the use of this tailored theoretical model to simulate the experimental system, the complex 3D overlap in substrate influence on current feedback was simulated. This provided a method for characterizing a system which cannot be considered as separate individual cells and

analyzed using traditional practices. This provides a method of imaging and analysis for highly confluent samples, which are incapable of being re-cultured. This limitation can be imposed by the time dependence of the study, poor dispersibility of the cell line, limited quantity of the sample available, etc. Avoiding close proximity cell samples provides the ideal conditions where possible. Reducing the UME size can also provide better resolution of cell samples of this type. However, smaller UMEs require smaller tip to sample distances to resolve features and surface chemistry of the sample and can hinder the imaging of samples with significant variability in sample height. In cases where neither of these precautions can be taken, performing full 3D simulations on the experimental system tailored to the sample geometry can allow for improved sample analysis.

6.4.3   Effects of Cell Distance on Imaging

The characterization of a two cell system (41.3 µm cell spacing) with a 4.4 µm UME, where both cells are present in the same 60×60 µm scan area, detected negligible effect from the adjacent cell. The use of a larger scale electrode, and closer proximity cells (10 µm UME, 14.7 µm cell spacing), contributed to the more significant influence of an adjacent cell. This introduces increased complexity in the characterization of the cell sample. The determination of the limitations of traditional single cell modelling methods for characterization is one of the aims of this work.

Using the simulation models explored in sections 6.4.1 and 6.4.2, the cell geometry was altered to determine the limits of detection of the commonly used 4.4 µm and 10 µm electrode sizes for live cell imaging. The cell sizes were altered to reflect the statistical average of the T24 cells (96 cell samples), previously determined optically to be 18 µm $\times$ 27 µm.[32] Cell heights were set to 8 µm, as previously determined by SECM depth scan (22 cell samples).[55] The cells were oriented at the same angle and y axis position, with their short axis oriented along the x axis (Figure 6.6A). Horizonal line scans were performed at multiple tip to sample distances as cell spacing was varied. Figure 6.6 B and C show the line scans for a 4.4 µm UME at 0.5 µm, and a 10 µm UME at 1.0 µm, respectively. These distances were selected for these respective electrode sizes as they

have a similar relative tip to sample distance (normalized distance of ~0.2). At 50 µm cell spacing, neither electrode size showed significant deviation in the double cell line scan from simulations of an individual cell geometry. The curve peak heights were similarly unaffected, which is a good indicator that no deviation is expected in the PAC extraction from this data set.
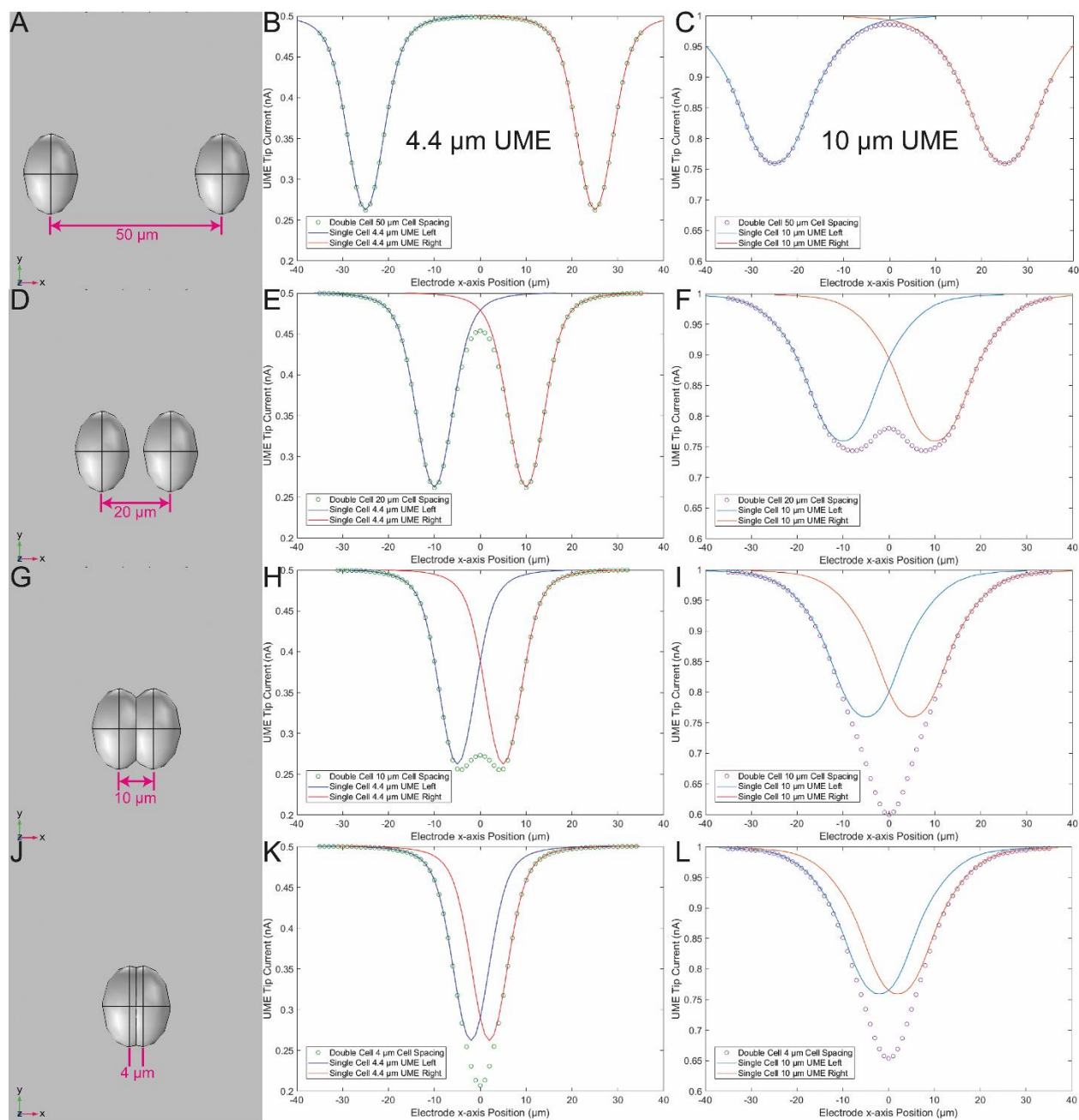
Figure 6.6 - Horizontal line scans over a set of two cells to determine SECM UME probe resolution at 0.5 μm from cell surface with a 4.4 μm UME (B,E,H,K), and 1.0 μm from the cell with a 10 μm UME (C,F,I,L; ND = ~0.2). Characterization illustrated with 50, 20, 10 and 4 μm cell spacing.

As the cells are moved within 20 µm of each other (Figure 6.6D), effects of the adjacent cell can be observed. The 4.4 µm electrode shows largely no difference in curve shape, with the exception of the region directly between the cells (Figure 6.6E). This would have an effect on surface mapping and depth scan profiles that scan across this region. However, the lack of deviation of the peak height along the bulk of the cell profiles allows for accurate PAC extraction, without the need for dedicated sample-specific modelling. The 10 µm electrode, however, shows significant deviation in curve shape at this distance, including deviation in the peak height (Figure 6.6F). At distances greater than 20 µm (simulated ≥25 µm), the peak height remained usable for PAC extraction. Therefore, for imaging with a 10 µm electrode, care should be taken to ensure the minimum spacing between cells exceeds 20 µm center to center, or the geometry and physical conditions of the full multicellular system must be considered.

A similar trend to the 10 µm electrode at 20 µm, was observed with the 4.4 µm electrode at 10 µm cell spacing. At this distance, the model geometries of the two cells were overlapping as the cell distance is less than the average cell diameter (Figure 6.6G). This geometry could be observed experimentally in cells that are adhered to each other, having recently undergone cell division. The 4.4 µm electrode feedback showed significant deviation in curve shape, and deviation in peak height at this distance (Figure 6.6H). Therefore, for imaging with a 4.4 µm electrode a minimum distance exceeding 10 µm center to center should be maintained. At this 10 µm cell spacing, the 10 µm UME is unable to distinguish the two cells from one another, providing a single combined curve (Figure 6.6I).

The simulation was continued to a cell spacing of 4 µm, where the geometry of the two cells is almost completely overlapping (Figure 6.6J). At this distance, it was no longer possible to resolve the two cells with either electrode tested (Figure 6.6KL). This cell spacing is closer than would be observed with any experimental system where two distinct cells are present. This geometry could, however, be possible with a single cell undergoing division. This illustrates the strength of 4.4 µm electrodes for imaging highly confluent live cell samples of this size.

By reducing the UME tip size further, even greater resolution of the live cell spacing would be possible. However, this also necessitates a smaller tip to substrate distance, which limits the ability to image the entire cell surface. As a result, the electrode size should be optimized for the sample size under study if obtaining surface mapping, multiple PACs, or full 3D imaging.

The full set of examined horizontal line scans at various cell spacings and tip to sample distances is visible is Figure 6.7.
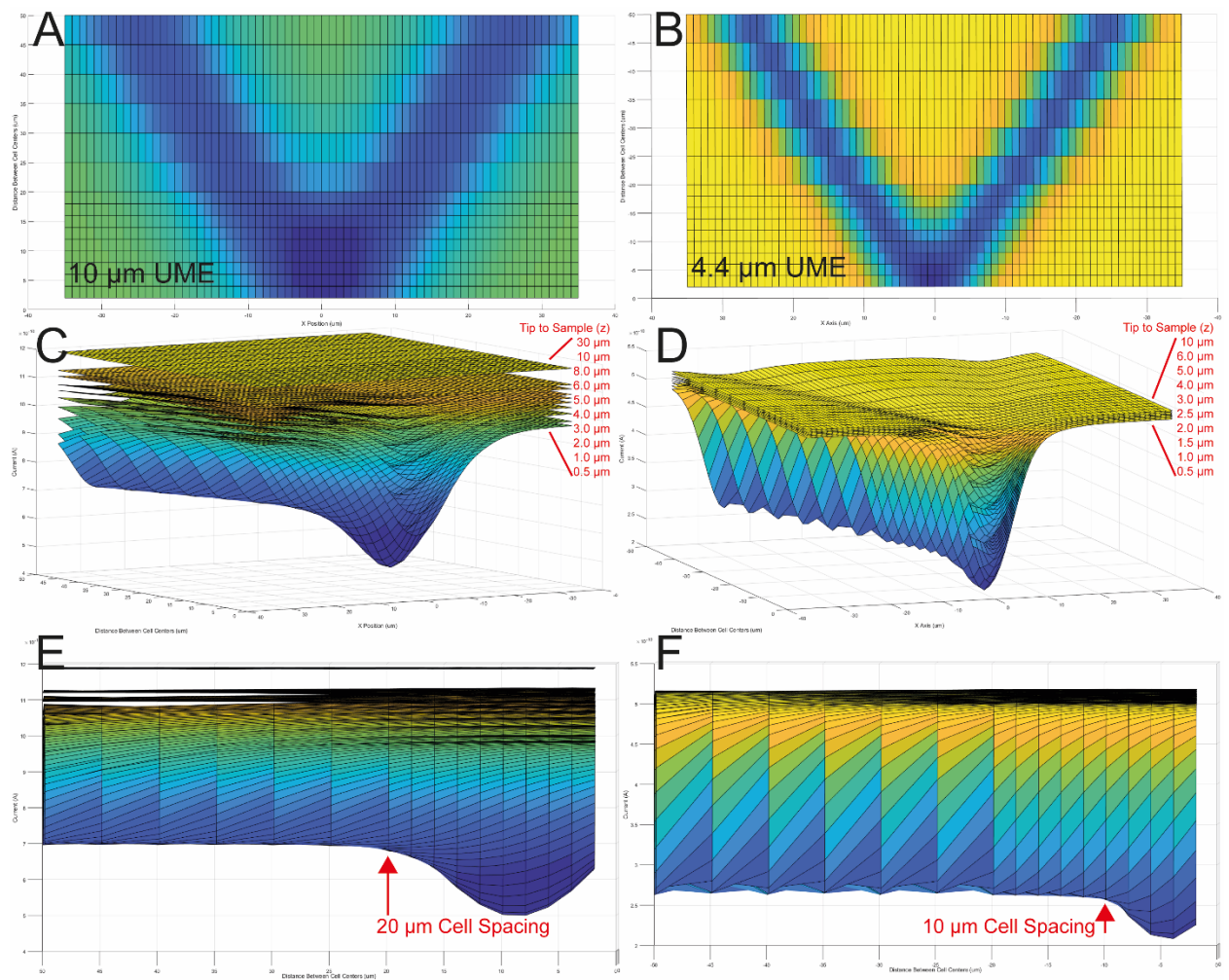
Figure 6.7 - Collection of horizontal line scans over a double cell at multiple distances to substrate using a 10 μm UME (A, C, E), and a 4.4 μm UME (B, D, F). A 2D plot of the horizontal line scans relative to cell sample spacing is provided at 0.5

μm tip to sample distance for (A) 10 μm UME and (B) 4.4 μm UME. A 3D perspective of these plots is provided for a range 10 tip to sample distances per electrode tip size (C=10 μm; D=4.4 μm). A side on image of these plots is provided, with labelling for the cell spacing distance at which major deviation from normal peak current is observed (E=10 μm; F=4.4 μm).

6.5 Conclusions

Analysis of complex systems of cells in close proximity by SECM can lead to a number of issues using traditional methods. Through the use of tailored 3D model geometries for these cell systems, experimental characterization can be performed. Cell cluster samples were modelled using two common electrode sizes for SECM imaging (10 μm and 4.4 μm). Surface maps of an experimental double cell (41.3 μm cell spacing) imaged by a 4.4 μm UME were compared to simulated maps utilizing a tailored geometry with a strong agreement in curve shape. Following this, a higher complexity experimental system was explored, incorporating two extreme proximity cells (14.7 μm cell distance) and a larger 10 μm UME. In this situation it is absolutely necessary to employ a tailored full 3D model for simulation. The simulation model was capable of providing a strong theoretical fit to the experimental results when the geometry of both cells was considered. The effects of an adjacent cell were characterized for both common UME sizes with variable cell proximity. Horizontal line scans across the two cell centers were explored to illustrate the effect on surface mapping. Limits of detection for the adjacent cell when performing a PAC approach to a cell center were also explored. It was determined that deviation from normal PAC current was observed at 20 μm spacing for 10 μm UMEs and 10 μm for 4.4 μm UMEs. This defines the limitations of traditional simulation methodology for characterizing cell samples. Cells with 20 μm or less to an adjacent cell necessitate tailored simulation geometry for 10 μm UMEs. Imaging with a 4.4 μm electrode should be performed with a cell spacing greater than 10 μm, or geometry must be tailored as well. The developed methodology for theoretical quantification of complex samples provides increased versatility in theoretical modelling of cell systems and reinforces the strength of SECM as a powerful bioanalytical tool.

6.6   References

1.   Bard, A. J.; Faulkner, L. R., *Electrochemical Methods: Fundamentals and Applications, 2nd Edition*. 2 ed.; John Wiley & Sons, Inc.: 2001, p 864.
2.   Bard, A. J.; Mirkin, M. V., *Scanning Electrochemical Microscopy*. 2 ed.; CRC Press: 2012, p 670.
3.   Zoski, C. G., Review—Advances in Scanning Electrochemical Microscopy (Secm). *J. Electrochem. Soc.* **2015,** *163* (4), H3088-H3100.
4.   Bard, A. J.; Denuault, G.; Lee, C.; Mandler, D.; Wipf, D. O., Scanning Electrochemical Microscopy - a New Technique for the Characterization and Modification of Surfaces. *Acc. Chem. Res.* **2002,** *23* (11), 357-363.
5.   Bard, A. J.; Fan, F. R. F.; Kwak, J.; Lev, O., Scanning Electrochemical Microscopy. Introduction and Principles. *Anal. Chem.* **2002,** *61* (2), 132-138.
6.   Polcari, D.; Dauphin-Ducharme, P.; Mauzeroll, J., Scanning Electrochemical Microscopy: A Comprehensive Review of Experimental Parameters from 1989 to 2015. *Chem. Rev.* **2016,** *116* (22), 13234-13278.
7.   Ding, Z.; Quinn, B. M.; Bard, A. J., Kinetics of Heterogeneous Electron Transfer at Liquid/Liquid Interfaces as Studied by Secm. *J. Phys. Chem. B* **2001,** *105* (27), 6367-6374.
8.   Wittstock, G.; Burchardt, M.; Pust, S. E.; Shen, Y.; Zhao, C., Scanning Electrochemical Microscopy for Direct Imaging of Reaction Rates. *Angew. Chem. Int. Ed. Engl.* **2007,** *46* (10), 1584-617.
9.   Nowierski, C.; Noël, J. J.; Shoesmith, D. W.; Ding, Z., Correlating Surface Microstructures with Reactivity on Commercially Pure Zirconium Using Scanning Electrochemical Microscopy and Scanning Electron Microscopy. *Electrochem. Commun.* **2009,** *11* (6), 1234-1236.
10. Yin, Y.; Niu, L.; Lu, M.; Guo, W.; Chen, S., In Situ Characterization of Localized Corrosion of Stainless Steel by Scanning Electrochemical Microscope. *Appl. Surf. Sci.* **2009,** *255* (22), 9193-9199.
11. Combellas, C.; Fuchs, A.; Kanoufi, F., Scanning Electrochemical Microscopy with a Band Microelectrode: Theory and Application. *Anal. Chem.* **2004,** *76* (13), 3612-8.
12. Schorr, N. B.; Jiang, A. G.; Rodriguez-Lopez, J., Probing Graphene Interfacial Reactivity Via Simultaneous and Colocalized Raman-Scanning Electrochemical Microscopy Imaging and Interrogation. *Anal. Chem.* **2018,** *90* (13), 7848-7854.
13. Tang, J.; Zheng, J.-J.; Yu, Y.-T.; Chen, l.; Zhang, N.; Tian, Z., Selective Etching of Zno Films on an Ito Substrate Using a Scanning Electrochemical Microscope. *Electrochim. Acta* **2012,** *83*, 247-252.
14. Eifert, A.; Mizaikoff, B.; Kranz, C., Advanced Fabrication Process for Combined Atomic Force-Scanning Electrochemical Microscopy (Afm-Secm) Probes. *Micron* **2015,** *68*, 27-35.
15. Han, L.; Zhao, X.; Hu, Z.; Zhang, J.; Cao, Y.; Yan, Y.; Tian, Z.-Q.; Tian, Z.-W.; Zhan, D., Tip Current/Positioning Close-Loop Mode of Scanning Electrochemical

Microscopy for Electrochemical Micromachining. *Electrochem. Commun.* **2017,** *82*, 117-120.

16.   Amemiya, S.; Guo, J.; Xiong, H.; Gross, D. A., Biological Applications of Scanning Electrochemical Microscopy: Chemical Imaging of Single Living Cells and Beyond. *Anal. Bioanal. Chem.* **2006,** *386* (3), 458-71.

17.   Li, M. S.; Filice, F. P.; Ding, Z., A Time Course Study of Cadmium Effect on Membrane Permeability of Single Human Bladder Cancer Cells Using Scanning Electrochemical Microscopy. *J. Inorg. Biochem.* **2014,** *136*, 177-83.

18.   Kuss, S.; Polcari, D.; Geissler, M.; Brassard, D.; Mauzeroll, J., Assessment of Multidrug Resistance on Cell Coculture Patterns Using Scanning Electrochemical Microscopy. *Proc. Nat. Acad. Sci. U.S.A.* **2013,** *110* (23), 9249-54.

19.   Kuss, S.; Cornut, R.; Beaulieu, I.; Mezour, M. A.; Annabi, B.; Mauzeroll, J., Assessing Multidrug Resistance Protein 1-Mediated Function in Cancer Cell Multidrug Resistance by Scanning Electrochemical Microscopy and Flow Cytometry. *Bioelectrochemistry* **2011,** *82* (1), 29-37.

20.   Beaulieu, I.; Kuss, S.; Mauzeroll, J.; Geissler, M., Biological Scanning Electrochemical Microscopy and Its Application to Live Cell Studies. *Anal. Chem.* **2011,** *83* (5), 1485-92.

21.   Koley, D.; Bard, A. J., Triton X-100 Concentration Effects on Membrane Permeability of a Single Hela Cell by Scanning Electrochemical Microscopy (Secm). *Proc. Nat. Acad. Sci. U.S.A.* **2010,** *107* (39), 16783-7.

22.   Liu, B.; Rotenberg, S. A.; Mirkin, M. V., Scanning Electrochemical Microscopy of Living Cells: Different Redox Activities of Nonmetastatic and Metastatic Human Breast Cells. *Proc. Nat. Acad. Sci. U.S.A.* **2000,** *97* (18), 9855-60.

23.   Bard, A. J.; Li, X.; Zhan, W., Chemically Imaging Living Cells by Scanning Electrochemical Microscopy. *Biosens. Bioelectron.* **2006,** *22* (4), 461-72.

24.   Zhao, X.; Diakowski, P. M.; Ding, Z., Deconvoluting Topography and Spatial Physiological Activity of Live Macrophage Cells by Scanning Electrochemical Microscopy in Constant-Distance Mode. *Anal. Chem.* **2010,** *82* (20), 8371-3.

25.   Nioradze, N.; Kim, J.; Amemiya, S., Quasi-Steady-State Voltammetry of Rapid Electron Transfer Reactions at the Macroscopic Substrate of the Scanning Electrochemical Microscope. *Anal. Chem.* **2011,** *83* (3), 828-35.

26.   Cannan, S.; Cervera, J.; Steliaros, R. J.; Bitziou, E.; Whitworth, A. L.; Unwin, P. R., Scanning Electrochemical Microscopy (Secm) Studies of Catalytic Ec' Processes: Theory and Experiment for Feedback, Generation/Collection and Imaging Measurements. *Phys. Chem. Chem. Phys.* **2011,** *13* (12), 5403-12.

27.   Matrab, T.; Hauquier, F.; Combellas, C.; Kanoufi, F., Scanning Electrochemical [Corrected] Microscopy Investigation of Molecular Transport [Corrected]within Polymer Brushes. *Chemphyschem* **2010,** *11* (3), 670-82.

28.   Koley, D.; Bard, A. J., Inhibition of the Mrp1-Mediated Transport of the Menadione-Glutathione Conjugate (Thiodione) in Hela Cells as Studied by Secm. *Proc. Nat. Acad. Sci. U.S.A.* **2012,** *109* (29), 11522-7.

29.   Kim, J.; Izadyar, A.; Shen, M.; Ishimatsu, R.; Amemiya, S., Ion Permeability of the Nuclear Pore Complex and Ion-Induced Macromolecular Permeation as

Studied by Scanning Electrochemical and Fluorescence Microscopy. *Anal. Chem.* **2014,** *86* (4), 2090-8.

30.   Bergner, S.; Wegener, J.; Matysik, F. M., Simultaneous Imaging and Chemical Attack of a Single Living Cell within a Confluent Cell Monolayer by Means of Scanning Electrochemical Microscopy. *Anal. Chem.* **2011,** *83* (1), 169-74.

31.   Kim, J.; Izadyar, A.; Nioradze, N.; Amemiya, S., Nanoscale Mechanism of Molecular Transport through the Nuclear Pore Complex as Studied by Scanning Electrochemical Microscopy. *J. Am. Chem. Soc.* **2013,** *135* (6), 2321-9.

32.   Filice, F. P.; Li, M. S. M.; Wong, J. M.; Ding, Z., The Effects of Long Duration Chronic Exposure to Hexavalent Chromium on Single Live Cells Interrogated by Scanning Electrochemical Microscopy. *J. Inorg. Biochem.* **2018,** *182*, 222-229.

33.   Page, A.; Kang, M.; Armitstead, A.; Perry, D.; Unwin, P. R., Quantitative Visualization of Molecular Delivery and Uptake at Living Cells with Self-Referencing Scanning Ion Conductance Microscopy-Scanning Electrochemical Microscopy. *Anal. Chem.* **2017,** *89* (5), 3021-3028.

34.   Liebetrau, J. M.; Miller, H. M.; Baur, J. E.; Takacs, S. A.; Anupunpisit, V.; Garris, P. A.; Wipf, D. O., Scanning Electrochemical Microscopy of Model Neurons: Imaging and Real-Time Detection of Morphological Changes. *Anal. Chem.* **2003,** *75* (3), 563-571.

35.   Kurulugama, R. T.; Wipf, D. O.; Takacs, S. A.; Pongmayteegul, S.; Garris, P. A.; Baur, J. E., Scanning Electrochemical Microscopy of Model Neurons: Constant Distance Imaging. *Anal. Chem.* **2005,** *77* (4), 1111-7.

36.   Iwai, N. T.; Kramaric, M.; Crabbe, D.; Wei, Y.; Chen, R.; Shen, M., Gaba Detection with Nano-Ities Pipet Electrode: A New Mechanism, Water/Dce-Octanoic Acid Interface. *Anal. Chem.* **2018,** *90* (5), 3067-3072.

37.   Polcari, D.; Hernandez-Castro, J. A.; Li, K.; Geissler, M.; Mauzeroll, J., Determination of the Relationship between Expression and Functional Activity of Multidrug Resistance-Associated Protein 1 Using Scanning Electrochemical Microscopy. *Anal. Chem.* **2017,** *89* (17), 8988-8994.

38.   Zhu, R.; Macfie, S. M.; Ding, Z., Cadmium-Induced Plant Stress Investigated by Scanning Electrochemical Microscopy. *J. Exp. Bot.* **2005,** *56* (421), 2831-8.

39.   Wang, Y.; Noel, J. M.; Velmurugan, J.; Nogala, W.; Mirkin, M. V.; Lu, C.; Guille Collignon, M.; Lemaitre, F.; Amatore, C., Nanoelectrodes for Determination of Reactive Oxygen and Nitrogen Species inside Murine Macrophages. *Proc. Nat. Acad. Sci. U.S.A.* **2012,** *109* (29), 11534-9.

40.   Zhao, X.; Petersen, N. O.; Ding, Z., Comparison Study of Live Cells by Atomic Force Microscopy, Confocal Microscopy, and Scanning Electrochemical Microscopy. *Can. J. Chem.* **2007,** *85* (3), 175-183.

41.   Zhang, M. M.; Long, Y. T.; Ding, Z., Cisplatin Effects on Evolution of Reactive Oxygen Species from Single Human Bladder Cancer Cells Investigated by Scanning Electrochemical Microscopy. *J. Inorg. Biochem.* **2012,** *108*, 115-22.

42. Zhao, X.; Zhang, M.; Long, Y.; Ding, Z., Redox Reactions of Reactive Oxygen Species in Aqueous Solutions as the Probe for Scanning Electrochemical Microscopy of Single Live T24 Cells. *Can. J. Chem.* **2010,** *88* (6), 569-576.

43. Zhao, X.; Lam, S.; Jass, J.; Ding, Z., Scanning Electrochemical Microscopy of Single Human Urinary Bladder Cells Using Reactive Oxygen Species as Probe of Inflammatory Response. *Electrochem. Commun.* **2010,** *12* (6), 773-776.

44. Zhan, D.; Li, X.; Nepomnyashchii, A. B.; Alpuche-Aviles, M. A.; Fan, F.-R. F.; Bard, A. J., Characterization of Ag+ Toxicity on Living Fibroblast Cells by the Ferrocenemethanol and Oxygen Response with the Scanning Electrochemical Microscope. *J. Electroanal. Chem.* **2013,** *688*, 61-68.

45. Li, X.; Bard, A. J., Scanning Electrochemical Microscopy of Hela Cells – Effects of Ferrocene Methanol and Silver Ion. *J. Electroanal. Chem.* **2009,** *628* (1-2), 35-42.

46. Sun, P.; Laforge, F. O.; Abeyweera, T. P.; Rotenberg, S. A.; Carpino, J.; Mirkin, M. V., Nanoelectrochemistry of Mammalian Cells. *Proc. Nat. Acad. Sci. U.S.A.* **2008,** *105* (2), 443-8.

47. Cai, C.; Liu, B.; Mirkin, M. V.; Frank, H. A.; Rusling, J. F., Scanning Electrochemical Microscopy of Living Cells. 3.Rhodobactersphaeroides. *Anal. Chem.* **2002,** *74* (1), 114-119.

48. Feng, W.; Rotenberg, S. A.; Mirkin, M. V., Scanning Electrochemical Microscopy of Living Cells. 5. Imaging of Fields of Normal and Metastatic Human Breast Cells. *Anal. Chem.* **2003,** *75* (16), 4148-54.

49. Liu, B.; Cheng, W.; Rotenberg, S. A.; Mirkin, M. V., Scanning Electrochemical Microscopy of Living Cells. *J. Electroanal. Chem.* **2001,** *500* (1-2), 590-597.

50. Nebel, M.; Eckhard, K.; Erichsen, T.; Schulte, A.; Schuhmann, W., 4d Shearforce-Based Constant-Distance Mode Scanning Electrochemical Microscopy. *Anal. Chem.* **2010,** *82* (18), 7842-8.

51. Lazenby, R. A.; McKelvey, K.; Unwin, P. R., Hopping Intermittent Contact-Scanning Electrochemical Microscopy (Hic-Secm): Visualizing Interfacial Reactions and Fluxes from Surfaces to Bulk Solution. *Anal. Chem.* **2013,** *85* (5), 2937-44.

52. Yasukawa, T.; Uchida, I.; Matsue, T., Permeation of Redox Species through a Cell Membrane of a Single, Living Algal Protoplast Studied by Microamperometry. *BBA - Biomembranes* **1998,** *1369* (1), 152-158.

53. Zhang, M. N.; Ding, Z.; Long, Y. T., Sensing Cisplatin-Induced Permeation of Single Live Human Bladder Cancer Cells by Scanning Electrochemical Microscopy. *Analyst* **2015,** *140* (17), 6054-60.

54. Filice, F. P.; Li, M. S.; Henderson, J. D.; Ding, Z., Mapping Cd(2)(+)-Induced Membrane Permeability Changes of Single Live Cells by Means of Scanning Electrochemical Microscopy. *Anal. Chim. Acta* **2016,** *908*, 85-94.

55. Li, M. S. M.; Filice, F. P.; Ding, Z., Determining Live Cell Topography by Scanning Electrochemical Microscopy. *J. Electroanal. Chem.* **2016,** *779*, 176-186.

56.   Sklyar, O.; Wittstock, G., Numerical Simulations of Complex Nonsymmetrical 3d Systems for Scanning Electrochemical Microscopy Using the Boundary Element Method. *J. Phys. Chem. B* **2002,** *106* (30), 7499-7508.

57.   Filice, F. P.; Li, M. S. M.; Henderson, J. D.; Ding, Z., Three-Dimensional Electrochemical Functionality of an Interdigitated Array Electrode by Scanning Electrochemical Microscopy. *J. Phys. Chem. C* **2015,** *119* (37), 21473-21482.

58.   Kuss, S.; Trinh, D.; Danis, L.; Mauzeroll, J., High-Speed Scanning Electrochemical Microscopy Method for Substrate Kinetic Determination: Method and Theory. *Anal. Chem.* **2015,** *87* (16), 8096-101.

59.   Rossier, J. S.; Vollet, C.; Carnal, A.; Lagger, G.; Gobry, V.; Girault, H. H.; Michel, P.; Reymond, F., Plasma Etched Polymer Microelectrochemical Systems. *Lab Chip* **2002,** *2* (3), 145-50.

60.   Li, M. S. M.; Filice, F. P.; Henderson, J. D.; Ding, Z., Probing Cd2+-Stressed Live Cell Membrane Permeability with Various Redox Mediators in Scanning Electrochemical Microscopy. *J. Phys. Chem. C* **2016,** *120* (11), 6094-6103.

Chapter 7

7   Simulation-Assisted Nanoscale Imaging of Single Live Cells with Scanning Electrochemical Microscopy

Nanoelectrodes have become an area of significant interest in recent years, which provide a number of advantages for imaging with scanning electrochemical microscopy (SECM). Since the resolution of SECM imaging is directly dependent on the size of the electrode probe, the reduced surface area of nanoelectrodes allows for the imaging of smaller sample features, or more localized electrochemical reactivity. Nanoelectrodes with a radius of 130 nm were employed to image the surface of single live cells. The use of nanoscale imaging, however, introduced additional complexity into the simulation modeling of the cell surface geometry and electrochemical reactivity. The creation of tailored simulation models accounting for these specific physical conditions was utilized to overcome the additional challenges to the characterization of the electrochemical system. Methodologies for the experimental mapping and creation of 3D simulation models of single live cells have been well developed, which are presented herein. These developments include characterization of cell surface topography, tip-to-cell distance, as well as cell membrane permeability quantification. The advanced quantification of the complex nanoscale imaging of single live cells assisted by theoretical simulations provides increased versatility to SECM as an already powerful bioanalytical tool.

7.1   Introduction

Nanoelectrodes provide a number of advantages in scanning electrochemical microscopy (SECM). The resolution of an SECM image is directly dependent on the size of the electrode probe surface. The reduced surface area of a nanoelectrode allows for the

imaging of smaller sample features, or more localized electrochemical surface reactivity. As a result, nanoelectrode imaging has become an area of significant interest in recent years.[1-2]

The small size of nanoelectrodes introduces more difficulties in fabrication than the larger, more common ultramicroelectrode (UMEs, µm scale) probes. However various fabrication methods have been developed including laser pulling [3-6], chemical vapour deposition,[7-8] pyrolytic deposition of carbon inside of nanopipettes,[9] and focus-ion-beam milling[10-11] techniques. These different methods hold their own advantages and disadvantages. In this report, laser-pulled electrodes were utilized, with 130 nm tip radius, to image single live cells.

SECM is a member of the scanning probe microscopy family.[12-14] SECM provides precise positioning of an ultramicroelectrode (UME, $\leq$25 µm diameter electrode disk) or nanoelectrode probe (nm scale). Faradaic current from an electrochemical redox reaction is monitored relative to electrode position. This allows for the mapping of surface topography and electrochemical reactivity of the sample under study. SECM scans are often coupled with finite element method (FEM) simulations to provide additional quantification of sample features.[15]

SECM imaging methods have been in development since 1989,[16-17] promoting a diverse range of applications for the techniques to be examined.[18] SECM has since been applied to kinetic studies,[19-20] surface and interface studies,[21-23] microstructure fabrication.[24-26] SECM has also found applications as a bioanalytical tool for cellular imaging,[27-36] membrane transport,[28, 37-44] neurotransmitter release,[45-46] multidrug resistance,[29-30, 47] ROS and RNS mapping,[35, 48-54] and cellular redox processes.[33, 55-60]

SECM imaging with smaller probes provides insight into more fine detail of the sample surface, including both topographical information and electrochemical reactivity.[61] This, however, introduces additional complexity into the modelling of these systems for further characterization by finite element analysis simulation. Tailored simulation models often need to be created to account for the specific geometry or reactivity of the sample when

imaged with nanoscale probes. Herein a methodology for the creation of advanced 3D simulation models for imaging single live cells will be presented. This methodology includes characterization of surface topography, tip-to-sample distance, as well as cell membrane permeability quantification in nanoscale.

7.2 Experimental Section

7.2.1 Materials

Ferrocenemethanol (FcCH$_2$OH, 97%) and hexaamineruthenium(III) chloride (Ru(NH$_3$)$_6$·Cl$_3$, 98%) were acquired from Sigma-Aldrich (Mississauga, ON). A Stock solution of SECM mediator was prepared using 0.9 mM FcCH$_2$OH and 10 mM Ru(NH$_3$)$_6^{3+}$ dissolved in 1× phosphate buffered saline (PBS, Life Technologies, Burlington, ON).

7.2.2 Cell Preparation

Human bladder cancer cells (T24 cells (HTB-4™)) were purchased from American Type Culture Collection (ATCC, Manassas, VA, USA) and maintained according to the ATCC specified protocol. Cells were cultured in McCoy's 5a medium (ATCC) containing 10% Fetal Bovine Serum and incubated at 37°C with 5% CO$_2$. When preparing cell samples for SECM experiments, T24 cells were cultured in sterile (γ-irradiated) glass bottom Petri dishes (P35G-0-20-C, MatTek Corporation, Ashland, MA, USA). Cells were incubated for a minimum of 24 hr, ensuring cell adherence to the glass surface of the Petri dish. The growth medium was decanted prior to analysis via SECM, and thoroughly washed with 1× PBS. Medium was replaced with the electrochemical mediator solution.

7.2.3 Electrode Fabrication

A Sutter Instruments P-2000 laser micropipette puller (Sutter Instrument, Novato, CA) was used to manufacture SECM nanoelectrodes in-house. The electrode fabrication procedure follows a modified version of the Mauzeroll group's .[3, 6, 62-63] Briefly, a 25 µm Pt wire (Goodfellow Metals, Cambridge, UK) was inserted into the center of a quartz glass capillary tube (o.d.: 1.00 mm, i.d.: 0.50 mm, length: 10.00 cm, Sutter Instrument).

The capillary and Pt wire are sealed and pulled in the center, yielding two electrodes. Two stages of heating were performed using different single line heat settings. For both of these steps the linear carriages were locked in place to ensure no movement. The interior of the quartz capillary was evacuated of air for these steps as well, using a custom-designed vacuum line which affixes to both ends of the capillary. First, a partial quartz seal is performed using a line setting of Heat: 580, Filament: 003, Velocity: 140, Delay: 060, Pull: 000. Following this, the complete seal of the quartz around the Pt wire was performed using the settings Heat: 580, Filament: 002, Velocity: 140, Delay: 060, Pull: 000.[5, 11]

Following the successful heat sealing of the quartz around the 25 µm Pt wire, the linear carriages were unlocked, and a final pull step was performed with setting of Heat: 780, Filament: 002, Velocity: 060, Delay: 140, Pull: 200. Pt NEs were checked optically for obvious Pt wire breakages inside the glass and tested by cyclic voltammetry (CV). Internal connections were extended and reinforced using conductive silver epoxy (Epo-Tek H20E, Billerica, MA). The Pt tips were wet polished to a flat surface using a homemade polishing wheel, with alumina-coated polishing pads (0.05 µm, Buehler, Whitby, ON).

7.2.4   SECM Instrumentation

A detailed description of the SECM instrumentation and experimental procedures can be found in Chapter 2 section 2.2.5.[64] Briefly, SECM experiments were carried out using the piezoelectric positioning system of a modified Alpha-SNOM (WITec, Ulm, Germany). A custom-milled UME mount allows for the mounting of electrodes in place of an upper objective lens. A micro-incubator Petri dish mount (Bioscience Tools, San Diego, California, USA) was secured onto the scanning stage to maintain homeostatic temperatures for cell samples. An inverted objective lens (50×, N.A. 0.55, W.D. 10.1 mm, Nikon, Japan) was used to acquire optical images and position the UME relative to the live cells of interest.

Electrochemical analysis was performed using a CH Instruments Electrochemical Analyzer (CHI800B, Austin, TX) with a CHI200 Picoamp Booster for low current high sensitivity analysis. Low current operation is common in SECM experimentation due to the use of small electrodes and dilute solutions. A simple two-electrode system was used, with an UME working electrode and a Ag/AgCl reference/counter electrode. All potentials are reported relative to the Ag/AgCl reference.

7.2.5   SECM Experimental Procedure

Steady-state performance of the UME probe and solution were verified by cyclic voltammograms (CVs) at the beginning of each experiment. Cells were cultured to a confluency of 30-40% in glass bottom Petri dishes. The Petri dish was secured to the temperature-controlled stage mount, and maintained at 37.0 ± 0.2 ˚C. Each Petri dish was analyzed for a maximum duration of 60 min. A biased UME tip potential of 0.3 V (identified through CVs) was applied to obtain steady state oxidation of $FcCH_2OH$, or a potential of -0.35V was applied to induce the steady state reduction of $Ru(NH_3)_6^{3+}$. A cell was selected optically using the inverted objective lens, and the nanoelectrode was brought in close proximity to it using the Alpha-SNOM positioning system. SECM analysis of all samples was performed at a maximum UME tip speed of 21.5 µm/s, to limit the effects of forced solution convection and maintain steady state current.[65] The nanoelectrode was slowly approached toward the cell using the SECM depth scanning method, and was carefully monitored to avoid an electrode crash. Once feedback from the cell surface could be observed, the scan was then stopped and the nanoelectrode manually positioned to the closest z position achievable within the limits of the positioning system and electrode glass sheath. Experimental surface maps were then acquired using both $FcCH_2OH$ and $Ru(NH_3)_6^{3+}$ electrochemical mediators in rapid succession. Care was taken to ensure that less than 10 min passes between the two experimental scans.

7.3 Simulation
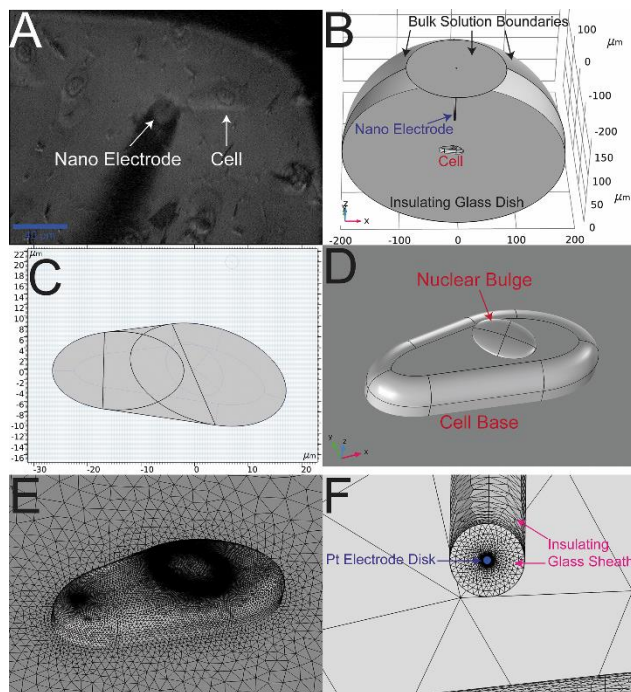
Figure 7.1 - (A) Labelled optical image of single live cell, with nanoelectrode shadow visible. (B) 3D model of the SECM approach to single live cell with key features, boundaries, and domains labeled. (C) 2D work plane of cell base geometry based on optical pixel measurements and SECM feedback. (D) Optimized 3D cell geometry for SECM imaging simulation. (E) Meshed cell geometry. (F) Labelled mesh of nanoelectrode tip.

Theoretical SECM surface mapping was generated using COMSOL Multiphysics (v5.3, COMSOL Inc., Burlington, Massachusetts). A full 3D model was constructed based on the physical dimensions of the SECM system under study (Figure 7.1B). Optical transmission images were taken of the single live cells experimentally imaged by SECM (Figure 7.1A). Pixel counting was utilized on the optical images to accurately measure the dimensions of the cell base, as well as the position, orientation and size of the nuclear bulge. The cell base was replicated using simple shapes on a 2D work plane in COMSOL (Figure 7.1C). A binary union was performed to merge all objects on the workplane, and internal boundaries were removed. The work plane was extruded up to a height of 7 µm,

and an ellipsoid was positioned in place of the nucleus with a height of 1 µm. This set the total cell height at the average cell height for T24 cells, previously characterized to be 8 µm.[66] This ratio of cell base height to nuclear bulge height was parametrized and optimized based on experimental SECM scans (section 4.1). The edges of the cell base were filleted to create a more tapered profile for the cell at its edges. The cell base and nuclear bulge were merged, and all interior boundaries were removed (Figure 7.1D).

The electrode geometry was defined as a flat Pt disk with a radius of 130 nm, and an RG of 10. This recreated the physical characteristics of the UME utilized for the experimental analysis. The bulk solution boundaries at the edges of the model were well defined as being 200 µm away from the cell center.

The model was defined as a two-domain system, composed of the solution domain and the cell interior. The solution domain initially contained 0.9 mM $FcCH_2OH$ and 10 mM $Ru(NH_3)_6^{3+}$, mirroring the experimental solution concentrations. The exterior bulk solution boundaries of the model were defined to regenerate this initial concentration of both mediators, simulating the presence of a theoretically infinite solution domain extending beyond the model. The cell interior has an initial concentration of 0 mM for both mediators. The transport of this mediator in both domains is governed by Ficks's second law of diffusion (Eq. 7.1).

$$\frac{\partial C_B(x,y,z)}{\partial t} = D \left(\frac{\partial^2 C_B(x,y,z)}{\partial x^2} + \frac{\partial^2 C_B(x,y,z)}{\partial y^2} + \frac{\partial^2 C_B(x,y,z)}{\partial z^2} \right) \text{ [7.1]}$$

where the diffusion coefficient (D) for $Ru(NH_3)_6^{3+}$ is 6.7×10^{-10} m^2/s, and the diffusion coefficient for $FcCH_2OH$ is 7.6×10^{-10} m^2/s.[67-71] The UME Pt tip was set to generate a concentration of 0 mM for both $Ru(NH_3)_6^{3+}$ and $FcCH_2OH$. The inclusion of both electrochemical mediators, and their physical parameters allowed for the simultaneous simulation of both SECM scans with identical geometry and electrode positions. Including both scans into the same model eliminated the need to maintain two versions of the same model, or constantly change parameters and rerun simulations with the different mediator conditions in the same model.

The cell membrane boundaries are defined as flux boundaries, allowing for species transport across the membrane (Eqs. 7.2 and 7.3).

$$f_{in} = P(C_B - C_C) \quad [7.2]$$

$$f_{out} = P(C_C - C_B) \quad [7.3]$$

The flux across the membrane boundary is dependent on a permeability coefficient (P) and the concentration gradient across the membrane boundary. In the case of the two electrochemical mediators, only the $FcCH_2OH$ is normally permeable to the membrane while $Ru(NH_3)_6{}^{3+}$ is impermeable. As a result there was no need to simulate the transport of $Ru(NH_3)_6{}^{3+}$ across the membrane. This eliminated the need to maintain intracellular concentrations of $Ru(NH_3)_6{}^{3+}$ and the accompanying flux boundary conditions. Optimizations such as this reduced model complexity, which lead to a corresponding reduction in memory utilization and compute time.

The COMSOL model contained a significant variation in object scale, with 4 full orders of magnitude difference in element size between the nanoelectrode tip and the bulk solution boundary. The solution domain has a diameter of 400 µm, while the electrode tip has a radius of 130 nm, causing a difference in scale of over three orders of magnitude. This necessitated significant fluctuation in meshing element size, with an extremely fine mesh at the electrode tip and a coarser mesh nearer the bulk solution boundaries. A free tetrahedral mesh was used to accomplish this. A minimum element size of 0.05 µm was defined, with a maximum element growth rate of 1.2, up to a maximum of 50 µm at the bulk solution boundary. Mesh scaling factors were manually applied to specific boundaries of interest, where significant variation in concentration commonly occurs. At these boundaries, the mesh was further refined from the free tetrahedral profile. The cell membrane was defined to have a mesh 0.3× the mesh defined by the free mesh element parameters (Figure 7.1E). While the nanoelectrode tip was refined even finer to 0.1× the free mesh parameters, yielding an element size as small as 5 nm (Figure 7.1F).

Electrode positioning was defined as a set of parametric values in this model. As well, the membrane permeability coefficient for $FcCH_2OH$ was also parameterized. Parametric

sweeps allowed for the sequential analysis of hundreds of individual simulations with varying parameters. The electrode x and y positioning were defined as a set of nested parametric sweeps, facilitating the mapping of a 2D surface over the cell. The electrode z position and membrane permeability can also be added as additional nested sweeps. However, these parameters were often specified manually in separate save files and distributed among multiple PC workstations for faster compute.

Following computation of the concentration maps, the mediator flux was integrated across the nanoelectrode surface, and converted to UME tip current for comparison to experimental scans. Theoretical and experimental current feedback was normalized to bulk solution current (i_∞).

7.4   Results and Discussion

7.4.1   Nanoscale Scanning Electrochemical Microscopy
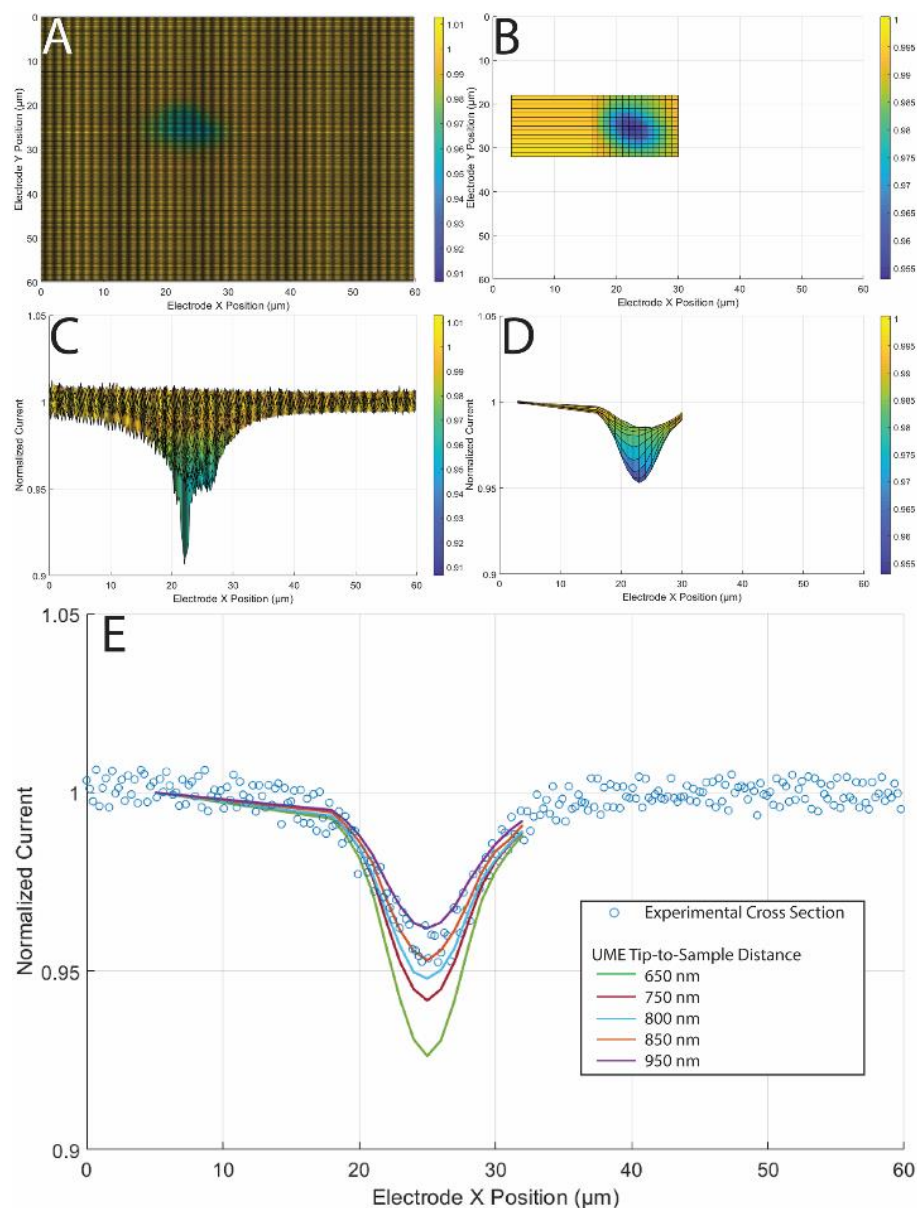
Figure 7.2 - (A) Experimental surface map of a single live cell imaged with a 130 nm radius UME and Ru(NH$_3$)$_6^{3+}$ as the mediator. (B) Simulated surface map of the cell (C) Experimental surface map viewed as 3D relief from the side. (D) Simulated surface map viewed from side. (E) Extracted experimental line scan across center of cell overlaid onto various tip to cell distances.

A surface map of a single live cell was imaged using a 130 nm radius laser-pulled electrode, and the membrane impermeable mediator $Ru(NH_3)_6^{3+}$ (Figure 7.2A). This mediator was selected for its impermeability, as it ensures that the resulting feedback is exclusively due to sample topography with no membrane permeability to consider. The surface map was performed at constant height above the cell. Comparing the resulting signal to the optical image of the cell (Figure 7.1A), it becomes evident that at the tip-to-cell distance of the surface map, only the nuclear bulge showed strong electrochemical feedback.

A full 3D simulation model was constructed based on the optical image of the cell and the electrochemical surface map. Using the geometry of the cell base, the nuclear dimensions, and their relative positions and angles, a 3D analogue of the cell surface was created. Using this model to simulate the surface map showed strong positional accuracy and size of the electrochemical response (Figure 7.2B). Observing the same experimental scan as a 3D relief, illustrates the surface shape, and peak intensity of the response generated by the proximity to the adjacent cell (Figure 7.2C). Viewing the theoretical map in the same fashion illustrates a strong agreement between the experimental and theoretical map (Figure 7.2D).

To perform this fitting, the relative heights of the nuclear bulge to cell base had to be parameterized. The cell height was fixed at 8 µm, as was previously characterized to be the average for a T24 cell.[66] The extrusion height from the base and the height of the half ellipsoid used as the nuclear bulge were specified in the model to sum to 8 µm. Fitting of an experimental horizontal sweep was performed with primary consideration for peak height of the current response and peak width. It was determined that a base height of 7 µm and a nuclear bulge height of 1 µm, yielded the strongest agreement for curve shape (Figure 7.3).
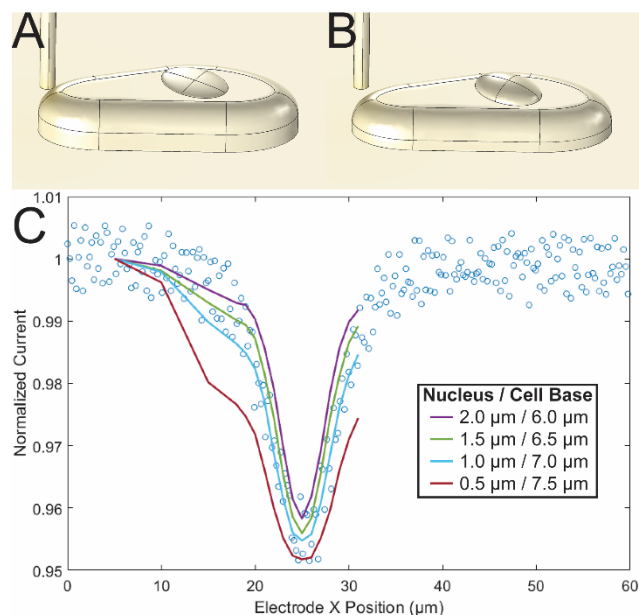
Figure 7.3– (A) Example geometry of a cell model with 7.5 µm base and 0.5 µm nuclear bulge. (B) Example geometry of a cell model with 6.0 µm base and 2.0 µm nuclear bulge. (C) Overlay of experimental horizontal sweep with $Ru(NH_3)_6^{3+}$ mediator onto theoretically generated horizontal sweeps simulated with various base/nuclear bulge heights.

Characterization of the tip to substrate distance was performed by parameterizing the electrode z axis. Multiple horizontal sweeps were performed across the center of the nuclear bulge at varying electrode heights. The resulting theoretical plots were overlaid onto a horizontal sweep extraction from the surface map across the center of the electrochemical response (Figure 7.2E). The resulting peak intensity from the experimental data shows a strong agreement with a tip-to-cell distance of 850 nm.

Nanoelectrodes provide a number of advantages for SECM imaging, but they also significantly increase the experimental difficulty. SECM image resolution is directly dependent on the size of the scanning probe. Smaller probes allow for the imaging of smaller surfaces features or clear delineation of regions with varying electrochemical reactivity. Electrodes produce a cumulative signal of all reactions occurring across their entire surface area at a given time. The extremely small surface of a nanoelectrode allows

for a much smaller spot size for imaging. However, the smaller probe size of a nanoelectrode necessitates closer positioning to the sample. This makes it difficult to avoid an electrode crash when imaging samples of varying height, sample tilt, or with moving surfaces. The lower surface area also yields smaller current response, making the signal more susceptible to electrical noise.

7.4.2　　Cell Membrane Permeability Characterization
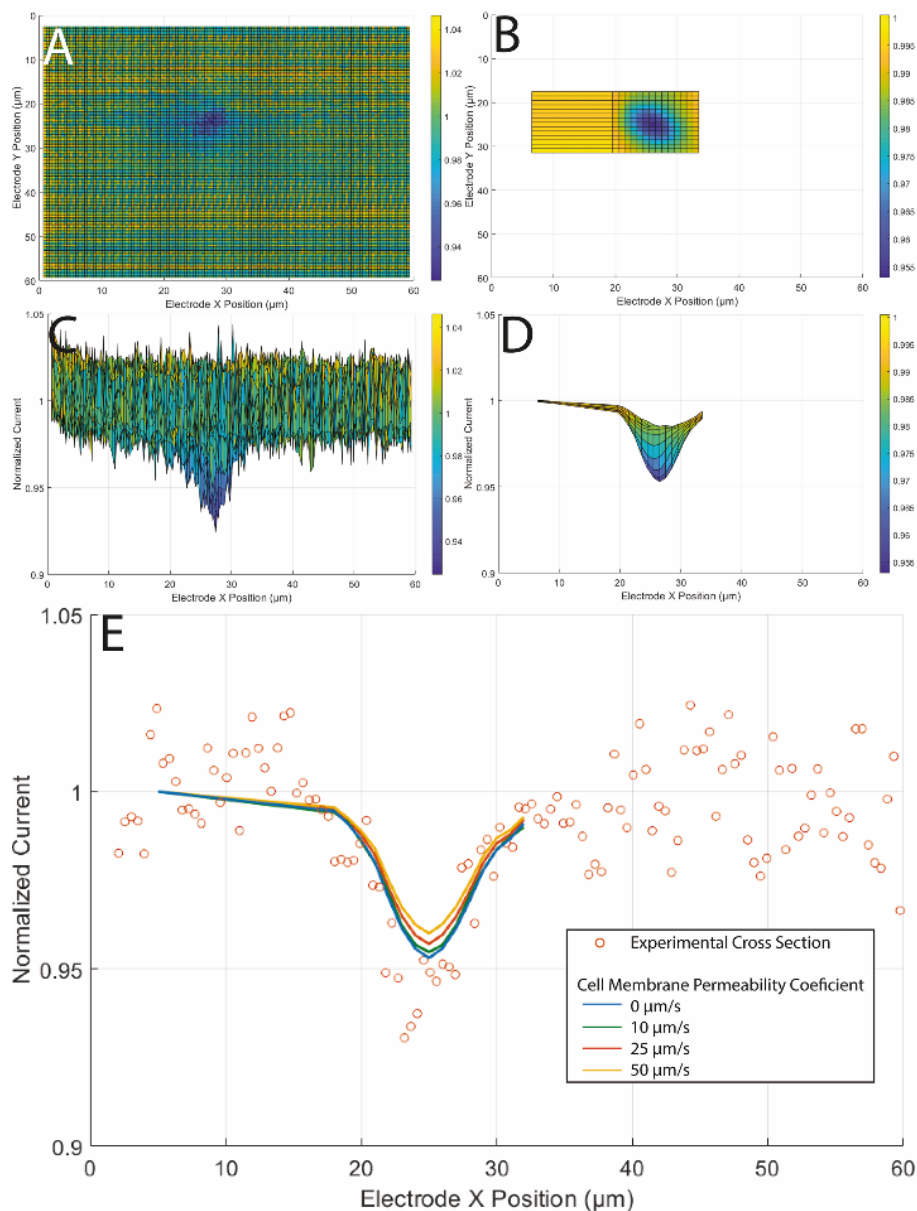
Figure 7.4 - (A) Experimental surface map of single live cell with 260 nm UME with FcCH₂OH mediator. (B) Simulated surface map of the cell (C) Experimental surface map viewed as 3D relief from the side. (D) Simulated surface map viewed from side. (E) Extracted experimental line scan across center of cell overlaid onto various tip to cell distances.

The use of the $Ru(NH_3)_6^{3+}$ mediator made it possible to accurately measure the cell surface topography, as well as provide an accurate tip-to-cell distance (section 7.4.1). This allowed the optimization of a detailed cell analogue for theoretical simulation. This optimized model geometry can be applied to more complex systems, utilizing the same cell and electrode system.

The electrochemical mediator $FcCH_2OH$ is partially permeable to the cell membrane. It is hydrophilic enough that it dissolves in the water-based systems of the cell interior and extracellular fluid. $FcCH_2OH$ is also oleophilic enough to cross the hydrophobic interior of the cell phospholipid membrane. However, it is not so oleophilic that it will accumulate between the lipid layers of the membrane. A surface map was taken of the same single live cell discussed in 7.4.1 using $FcCH_2OH$ as an electrochemical mediator (Figure 7.4A). Less than 10 min had elapsed between the start of the $Ru(NH_3)_6^{3+}$ imaging and the $FcCH_2OH$ scan, ensuring no drastic change in cell membrane shape. A lower signal to noise was observed for the $FcCH_2OH$ scans due to the greatly reduced current feedback (10^{-12} A) from the lower dissolved concentration of the $FcCH_2OH$ mediator. A curve smoothing algorithm was applied in MATLAB to reduce the more extreme signal noise for the $FcCH_2OH$ scan.

The optimized geometry and tip-to-cell distance from the $Ru(NH_3)_6^{3+}$ scan was utilized to model this system. However, the cell interior domain and flux across the cell membrane were also considered for the $FcCH_2OH$ simulation. A simulated surface map, matching the experimental scan was generated (Figure 7.4B). This surface map showed strong agreement in the degree of the electrochemical response, as well as the positional accuracy of the response.

The experimental surface map was also viewed as a 3D relief map (Figure 7.4C). This allows the peak intensity of the curve, as well as the curve shape to be more easily compared. The theoretical surface map was also plotted in this fashion (Figure 7.4D). Comparing the peak width shows strong agreement between the experimental and theoretical scan; however, the peak height becomes difficult to characterize due to the increased signal noise. Multiple horizontal line scans were simulated across the center of

the nucleus with varying membrane permeability coefficients (Figure 7.4E). An experimental horizontal sweep extraction was taken from the surface map and overlaid onto of these curves. The experimental membrane permeability agreed most strongly with the simulations for extremely low membrane permeability. Significant fitting error exists for all permeabilities below 10 μm/s. The strongest agreement between theoretical and experimental curves was found with the theoretical simulation of $P = 0$ μm/s (insulating conditions). However, due to the potential fitting error associated with this permeability range, the experimental fit corresponds more accurately to ≤10 μm/s.

7.5 Conclusions

Laser-pulled quartz sheathed electrodes were applied to the imaging of single live cells. The electrode utilized was a 130 nm radius Pt disk electrode, which was manually polished flat for SECM imaging. A cell was imaged using the membrane impermeable $Ru(NH_3)_6^{3+}$ mediator to accurately characterize cell topography. This SECM scan was used in correspondence with optical imaging to optimize cell geometry for simulation of this experimental system. The electrode tip-to-cell distance was also characterized using this electrochemical scan. This optimized simulation geometry was then carried forward to simulate the greater complexity of the cell membrane permeability. Using $FcCH_2OH$ as an electrochemical mediator, the same cell was imaged by the same electrode at the same probe distance (<10 mins between scans). Simulations of this system incorporating membrane permeability were performed with various membrane permeability coefficients. It was determined that the cell imaged agreed most strongly with a membrane permeability coefficient of ≤10 μm/s, indicating little to no flux across the membrane at the time of imaging. The development of this simulation methodology allows for tailored simulations of single live cells. These tailored models provide characterization for cell topography, as well as electrochemical characteristics such as membrane permeability. The developed methodology for theoretical quantification of complex samples provides increased versatility in theoretical modelling of cell systems and reinforces the strength of SECM as a powerful bioanalytical tool.

7.6 References

1. Kai, T.; Zoski, C. G.; Bard, A. J., Scanning Electrochemical Microscopy at the Nanometer Level. *Chem. Commun. (Camb.)* **2018,** *54* (16), 1934-1947.
2. Kranz, C., Recent Advancements in Nanoelectrodes and Nanopipettes Used in Combined Scanning Electrochemical Microscopy Techniques. *Analyst* **2014,** *139* (2), 336-52.
3. Mezour, M. A.; Morin, M.; Mauzeroll, J., Fabrication and Characterization of Laser Pulled Platinum Microelectrodes with Controlled Geometry. *Anal. Chem.* **2011,** *83* (6), 2378-82.
4. Danis, L.; Gateman, S. M.; Snowden, M. E.; Halalay, I. C.; Howe, J. Y.; Mauzeroll, J., Anodic Stripping Voltammetry at Nanoelectrodes: Trapping of Mn 2+ by Crown Ethers. *Electrochim. Acta* **2015,** *162*, 169-175.
5. Li, M. S. M.; Filice, F. P.; Ding, Z., Scanning Electrochemical Microscopy Imaging with Laser-Pulled Probes. *J. Electroanal. Chem.* **2016,** *781*, 126-135.
6. Katemann, B. B.; Schuhmann, W., Fabrication and Characterization of Needle-Type. *Electroanalysis* **2002,** *14* (1), 22-28.
7. Kim, B. M.; Murray, T.; Bau, H. H., The Fabrication of Integrated Carbon Pipes with Sub-Micron Diameters. *Nanotechnology* **2005,** *16* (8), 1317-1320.
8. Rees, H. R.; Anderson, S. E.; Privman, E.; Bau, H. H.; Venton, B. J., Carbon Nanopipette Electrodes for Dopamine Detection in Drosophila. *Anal. Chem.* **2015,** *87* (7), 3849-55.
9. Actis, P.; Tokar, S.; Clausmeyer, J.; Babakinejad, B.; Mikhaleva, S.; Cornut, R.; Takahashi, Y.; Lopez Cordoba, A.; Novak, P.; Shevchuck, A. I.; Dougan, J. A.; Kazarian, S. G.; Gorelkin, P. V.; Erofeev, A. S.; Yaminsky, I. V.; Unwin, P. R.; Schuhmann, W.; Klenerman, D.; Rusakov, D. A.; Sviderskaya, E. V.; Korchev, Y. E., Electrochemical Nanoprobes for Single-Cell Analysis. *ACS Nano* **2014,** *8* (1), 875-84.
10. Chen, R.; Hu, K.; Yu, Y.; Mirkin, M. V.; Amemiya, S., Focused-Ion-Beam-Milled Carbon Nanoelectrodes for Scanning Electrochemical Microscopy. *J. Electrochem. Soc.* **2016,** *163* (4), H3032-H3037.
11. Li, M. S. M.; Filice, F. P.; Ding, Z., Submicron Probes for Scanning Electrochemical Microscopy. *Can. J. Chem.* **2018,** *96* (3), 328-335.
12. Bard, A. J.; Faulkner, L. R., *Electrochemical Methods: Fundamentals and Applications, 2nd Edition*. 2 ed.; John Wiley & Sons, Inc.: 2001, p 864.
13. Bard, A. J.; Mirkin, M. V., *Scanning Electrochemical Microscopy*. 2 ed.; CRC Press: 2012, p 670.
14. Zoski, C. G., Review—Advances in Scanning Electrochemical Microscopy (Secm). *J. Electrochem. Soc.* **2015,** *163* (4), H3088-H3100.
15. Grime, J. M.; Edwards, M. A.; Rudd, N. C.; Unwin, P. R., Quantitative Visualization of Passive Transport across Bilayer Lipid Membranes. *Proc. Nat. Acad. Sci. U.S.A.* **2008,** *105* (38), 14277-82.
16. Bard, A. J.; Denuault, G.; Lee, C.; Mandler, D.; Wipf, D. O., Scanning Electrochemical Microscopy - a New Technique for the Characterization and Modification of Surfaces. *Acc. Chem. Res.* **2002,** *23* (11), 357-363.

17. Bard, A. J.; Fan, F. R. F.; Kwak, J.; Lev, O., Scanning Electrochemical Microscopy. Introduction and Principles. *Anal. Chem.* **2002,** *61* (2), 132-138.
18. Polcari, D.; Dauphin-Ducharme, P.; Mauzeroll, J., Scanning Electrochemical Microscopy: A Comprehensive Review of Experimental Parameters from 1989 to 2015. *Chem. Rev.* **2016,** *116* (22), 13234-13278.
19. Ding, Z.; Quinn, B. M.; Bard, A. J., Kinetics of Heterogeneous Electron Transfer at Liquid/Liquid Interfaces as Studied by Secm. *J. Phys. Chem. B* **2001,** *105* (27), 6367-6374.
20. Wittstock, G.; Burchardt, M.; Pust, S. E.; Shen, Y.; Zhao, C., Scanning Electrochemical Microscopy for Direct Imaging of Reaction Rates. *Angew. Chem. Int. Ed. Engl.* **2007,** *46* (10), 1584-617.
21. Nowierski, C.; Noël, J. J.; Shoesmith, D. W.; Ding, Z., Correlating Surface Microstructures with Reactivity on Commercially Pure Zirconium Using Scanning Electrochemical Microscopy and Scanning Electron Microscopy. *Electrochem. Commun.* **2009,** *11* (6), 1234-1236.
22. Yin, Y.; Niu, L.; Lu, M.; Guo, W.; Chen, S., In Situ Characterization of Localized Corrosion of Stainless Steel by Scanning Electrochemical Microscope. *Appl. Surf. Sci.* **2009,** *255* (22), 9193-9199.
23. Combellas, C.; Fuchs, A.; Kanoufi, F., Scanning Electrochemical Microscopy with a Band Microelectrode: Theory and Application. *Anal. Chem.* **2004,** *76* (13), 3612-8.
24. Tang, J.; Zheng, J.-J.; Yu, Y.-T.; Chen, l.; Zhang, N.; Tian, Z., Selective Etching of Zno Films on an Ito Substrate Using a Scanning Electrochemical Microscope. *Electrochim. Acta* **2012,** *83*, 247-252.
25. Eifert, A.; Mizaikoff, B.; Kranz, C., Advanced Fabrication Process for Combined Atomic Force-Scanning Electrochemical Microscopy (Afm-Secm) Probes. *Micron* **2015,** *68*, 27-35.
26. Han, L.; Zhao, X.; Hu, Z.; Zhang, J.; Cao, Y.; Yan, Y.; Tian, Z.-Q.; Tian, Z.-W.; Zhan, D., Tip Current/Positioning Close-Loop Mode of Scanning Electrochemical Microscopy for Electrochemical Micromachining. *Electrochem. Commun.* **2017,** *82*, 117-120.
27. Amemiya, S.; Guo, J.; Xiong, H.; Gross, D. A., Biological Applications of Scanning Electrochemical Microscopy: Chemical Imaging of Single Living Cells and Beyond. *Anal. Bioanal. Chem.* **2006,** *386* (3), 458-71.
28. Li, M. S.; Filice, F. P.; Ding, Z., A Time Course Study of Cadmium Effect on Membrane Permeability of Single Human Bladder Cancer Cells Using Scanning Electrochemical Microscopy. *J. Inorg. Biochem.* **2014,** *136*, 177-83.
29. Kuss, S.; Polcari, D.; Geissler, M.; Brassard, D.; Mauzeroll, J., Assessment of Multidrug Resistance on Cell Coculture Patterns Using Scanning Electrochemical Microscopy. *Proc. Nat. Acad. Sci. U.S.A.* **2013,** *110* (23), 9249-54.
30. Kuss, S.; Cornut, R.; Beaulieu, I.; Mezour, M. A.; Annabi, B.; Mauzeroll, J., Assessing Multidrug Resistance Protein 1-Mediated Function in Cancer Cell Multidrug Resistance by Scanning Electrochemical Microscopy and Flow Cytometry. *Bioelectrochemistry* **2011,** *82* (1), 29-37.

31.	Beaulieu, I.; Kuss, S.; Mauzeroll, J.; Geissler, M., Biological Scanning Electrochemical Microscopy and Its Application to Live Cell Studies. *Anal. Chem.* **2011,** *83* (5), 1485-92.

32.	Koley, D.; Bard, A. J., Triton X-100 Concentration Effects on Membrane Permeability of a Single Hela Cell by Scanning Electrochemical Microscopy (Secm). *Proc. Nat. Acad. Sci. U.S.A.* **2010,** *107* (39), 16783-7.

33.	Liu, B.; Rotenberg, S. A.; Mirkin, M. V., Scanning Electrochemical Microscopy of Living Cells: Different Redox Activities of Nonmetastatic and Metastatic Human Breast Cells. *Proc. Nat. Acad. Sci. U.S.A.* **2000,** *97* (18), 9855-60.

34.	Bard, A. J.; Li, X.; Zhan, W., Chemically Imaging Living Cells by Scanning Electrochemical Microscopy. *Biosens. Bioelectron.* **2006,** *22* (4), 461-72.

35.	Zhao, X.; Diakowski, P. M.; Ding, Z., Deconvoluting Topography and Spatial Physiological Activity of Live Macrophage Cells by Scanning Electrochemical Microscopy in Constant-Distance Mode. *Anal. Chem.* **2010,** *82* (20), 8371-3.

36.	Chen, Z.; Xie, S.; Shen, L.; Du, Y.; He, S.; Li, Q.; Liang, Z.; Meng, X.; Li, B.; Xu, X.; Ma, H.; Huang, Y.; Shao, Y., Investigation of the Interactions between Silver Nanoparticles and Hela Cells by Scanning Electrochemical Microscopy. *Analyst* **2008,** *133* (9), 1221-8.

37.	Nioradze, N.; Kim, J.; Amemiya, S., Quasi-Steady-State Voltammetry of Rapid Electron Transfer Reactions at the Macroscopic Substrate of the Scanning Electrochemical Microscope. *Anal. Chem.* **2011,** *83* (3), 828-35.

38.	Cannan, S.; Cervera, J.; Steliaros, R. J.; Bitziou, E.; Whitworth, A. L.; Unwin, P. R., Scanning Electrochemical Microscopy (Secm) Studies of Catalytic Ec' Processes: Theory and Experiment for Feedback, Generation/Collection and Imaging Measurements. *Phys. Chem. Chem. Phys.* **2011,** *13* (12), 5403-12.

39.	Matrab, T.; Hauquier, F.; Combellas, C.; Kanoufi, F., Scanning Electrochemical [Corrected] Microscopy Investigation of Molecular Transport [Corrected]within Polymer Brushes. *Chemphyschem* **2010,** *11* (3), 670-82.

40.	Koley, D.; Bard, A. J., Inhibition of the Mrp1-Mediated Transport of the Menadione-Glutathione Conjugate (Thiodione) in Hela Cells as Studied by Secm. *Proc. Nat. Acad. Sci. U.S.A.* **2012,** *109* (29), 11522-7.

41.	Kim, J.; Izadyar, A.; Shen, M.; Ishimatsu, R.; Amemiya, S., Ion Permeability of the Nuclear Pore Complex and Ion-Induced Macromolecular Permeation as Studied by Scanning Electrochemical and Fluorescence Microscopy. *Anal. Chem.* **2014,** *86* (4), 2090-8.

42.	Bergner, S.; Wegener, J.; Matysik, F. M., Simultaneous Imaging and Chemical Attack of a Single Living Cell within a Confluent Cell Monolayer by Means of Scanning Electrochemical Microscopy. *Anal. Chem.* **2011,** *83* (1), 169-74.

43.	Kim, J.; Izadyar, A.; Nioradze, N.; Amemiya, S., Nanoscale Mechanism of Molecular Transport through the Nuclear Pore Complex as Studied by Scanning Electrochemical Microscopy. *J. Am. Chem. Soc.* **2013,** *135* (6), 2321-9.

44.	Filice, F. P.; Li, M. S. M.; Wong, J. M.; Ding, Z., The Effects of Long Duration Chronic Exposure to Hexavalent Chromium on Single Live Cells Interrogated

by Scanning Electrochemical Microscopy. *J. Inorg. Biochem.* **2018,** *182*, 222-229.

45. Liebetrau, J. M.; Miller, H. M.; Baur, J. E.; Takacs, S. A.; Anupunpisit, V.; Garris, P. A.; Wipf, D. O., Scanning Electrochemical Microscopy of Model Neurons: Imaging and Real-Time Detection of Morphological Changes. *Anal. Chem.* **2003,** *75* (3), 563-571.

46. Kurulugama, R. T.; Wipf, D. O.; Takacs, S. A.; Pongmayteegul, S.; Garris, P. A.; Baur, J. E., Scanning Electrochemical Microscopy of Model Neurons: Constant Distance Imaging. *Anal. Chem.* **2005,** *77* (4), 1111-7.

47. Polcari, D.; Hernandez-Castro, J. A.; Li, K.; Geissler, M.; Mauzeroll, J., Determination of the Relationship between Expression and Functional Activity of Multidrug Resistance-Associated Protein 1 Using Scanning Electrochemical Microscopy. *Anal. Chem.* **2017,** *89* (17), 8988-8994.

48. Zhu, R.; Macfie, S. M.; Ding, Z., Cadmium-Induced Plant Stress Investigated by Scanning Electrochemical Microscopy. *J. Exp. Bot.* **2005,** *56* (421), 2831-8.

49. Wang, Y.; Noel, J. M.; Velmurugan, J.; Nogala, W.; Mirkin, M. V.; Lu, C.; Guille Collignon, M.; Lemaitre, F.; Amatore, C., Nanoelectrodes for Determination of Reactive Oxygen and Nitrogen Species inside Murine Macrophages. *Proc. Nat. Acad. Sci. U.S.A.* **2012,** *109* (29), 11534-9.

50. Zhao, X.; Petersen, N. O.; Ding, Z., Comparison Study of Live Cells by Atomic Force Microscopy, Confocal Microscopy, and Scanning Electrochemical Microscopy. *Can. J. Chem.* **2007,** *85* (3), 175-183.

51. Zhang, M. M.; Long, Y. T.; Ding, Z., Cisplatin Effects on Evolution of Reactive Oxygen Species from Single Human Bladder Cancer Cells Investigated by Scanning Electrochemical Microscopy. *J. Inorg. Biochem.* **2012,** *108*, 115-22.

52. Zhao, X.; Zhang, M.; Long, Y.; Ding, Z., Redox Reactions of Reactive Oxygen Species in Aqueous Solutions as the Probe for Scanning Electrochemical Microscopy of Single Live T24 Cells. *Can. J. Chem.* **2010,** *88* (6), 569-576.

53. Zhao, X.; Lam, S.; Jass, J.; Ding, Z., Scanning Electrochemical Microscopy of Single Human Urinary Bladder Cells Using Reactive Oxygen Species as Probe of Inflammatory Response. *Electrochem. Commun.* **2010,** *12* (6), 773-776.

54. Salamifar, S. E.; Lai, R. Y., Use of Combined Scanning Electrochemical and Fluorescence Microscopy for Detection of Reactive Oxygen Species in Prostate Cancer Cells. *Anal. Chem.* **2013,** *85* (20), 9417-21.

55. Zhan, D.; Li, X.; Nepomnyashchii, A. B.; Alpuche-Aviles, M. A.; Fan, F.-R. F.; Bard, A. J., Characterization of Ag+ Toxicity on Living Fibroblast Cells by the Ferrocenemethanol and Oxygen Response with the Scanning Electrochemical Microscope. *J. Electroanal. Chem.* **2013,** *688*, 61-68.

56. Li, X.; Bard, A. J., Scanning Electrochemical Microscopy of Hela Cells – Effects of Ferrocene Methanol and Silver Ion. *J. Electroanal. Chem.* **2009,** *628* (1-2), 35-42.

57. Sun, P.; Laforge, F. O.; Abeyweera, T. P.; Rotenberg, S. A.; Carpino, J.; Mirkin, M. V., Nanoelectrochemistry of Mammalian Cells. *Proc. Nat. Acad. Sci. U.S.A.* **2008,** *105* (2), 443-8.

58. Cai, C.; Liu, B.; Mirkin, M. V.; Frank, H. A.; Rusling, J. F., Scanning Electrochemical Microscopy of Living Cells. 3.Rhodobactersphaeroides. *Anal. Chem.* **2002,** *74* (1), 114-119.

59. Feng, W.; Rotenberg, S. A.; Mirkin, M. V., Scanning Electrochemical Microscopy of Living Cells. 5. Imaging of Fields of Normal and Metastatic Human Breast Cells. *Anal. Chem.* **2003,** *75* (16), 4148-54.

60. Liu, B.; Cheng, W.; Rotenberg, S. A.; Mirkin, M. V., Scanning Electrochemical Microscopy of Living Cells. *J. Electroanal. Chem.* **2001,** *500* (1-2), 590-597.

61. Ying, Y. L.; Ding, Z.; Zhan, D.; Long, Y. T., Advanced Electroanalytical Chemistry at Nanoelectrodes. *Chem. Sci.* **2017,** *8* (5), 3338-3348.

62. Danis, L.; Snowden, M. E.; Tefashe, U. M.; Heinemann, C. N.; Mauzeroll, J., Development of Nano-Disc Electrodes for Application as Shear Force Sensitive Electrochemical Probes. *Electrochim. Acta* **2014,** *136*, 121-129.

63. Danis, L.; Polcari, D.; Kwan, A.; Gateman, S. M.; Mauzeroll, J., Fabrication of Carbon, Gold, Platinum, Silver, and Mercury Ultramicroelectrodes with Controlled Geometry. *Anal. Chem.* **2015,** *87* (5), 2565-9.

64. Filice, F. P.; Li, M. S.; Henderson, J. D.; Ding, Z., Mapping Cd(2)(+)-Induced Membrane Permeability Changes of Single Live Cells by Means of Scanning Electrochemical Microscopy. *Anal. Chim. Acta* **2016,** *908*, 85-94.

65. Kuss, S.; Trinh, D.; Danis, L.; Mauzeroll, J., High-Speed Scanning Electrochemical Microscopy Method for Substrate Kinetic Determination: Method and Theory. *Anal. Chem.* **2015,** *87* (16), 8096-101.

66. Li, M. S. M.; Filice, F. P.; Ding, Z., Determining Live Cell Topography by Scanning Electrochemical Microscopy. *J. Electroanal. Chem.* **2016,** *779*, 176-186.

67. Rossier, J. S.; Vollet, C.; Carnal, A.; Lagger, G.; Gobry, V.; Girault, H. H.; Michel, P.; Reymond, F., Plasma Etched Polymer Microelectrochemical Systems. *Lab Chip* **2002,** *2* (3), 145-50.

68. Cermak, N.; Olcum, S.; Delgado, F. F.; Wasserman, S. C.; Payer, K. R.; M, A. M.; Knudsen, S. M.; Kimmerling, R. J.; Stevens, M. M.; Kikuchi, Y.; Sandikci, A.; Ogawa, M.; Agache, V.; Baleras, F.; Weinstock, D. M.; Manalis, S. R., High-Throughput Measurement of Single-Cell Growth Rates Using Serial Microfluidic Mass Sensor Arrays. *Nat. Biotechnol.* **2016,** *34* (10), 1052-1059.

69. Guo, J.; Amemiya, S., Permeability of the Nuclear Envelope at Isolated Xenopus Oocyte Nuclei Studied by Scanning Electrochemical Microscopy. *Anal. Chem.* **2005,** *77* (7), 2147-56.

70. Miao, W.; Ding, Z.; Bard, A. J., Solution Viscosity Effects on the Heterogeneous Electron Transfer Kinetics of Ferrocenemethanol in Dimethyl Sulfoxide−Water Mixtures. *J. Phys. Chem. B* **2002,** *106* (6), 1392-1398.

71. Mauzeroll, J.; Hueske, E. A.; Bard, A. J., Scanning Electrochemical Microscopy. 48. Hg/Pt Hemispherical Ultramicroelectrodes: Fabrication and Characterization. *Anal. Chem.* **2003,** *75* (15), 3880-9.

8   Concluding Remarks and Future Work

8.1   Concluding Remarks

As described in this dissertation, scanning electrochemical microscopy (SECM) is a powerful electroanalytical tool for the analysis of single live cell samples. This research has focused on the non-invasive quantification of single live T24 human bladder cancer cell membrane permeability. Various SECM mapping techniques (depth scan, surface mapping, 3D image stacks, etc.) were employed to image the live cells throughout this dissertation. However, previously developed simulation models restricted the usable data for membrane quantification to a single PAC over the center of a symmetric cell. To counter this restriction, SECM imaging was coupled to 3D FEM simulations which were the first of their kind. These more advanced 3D models allowed for features such as full sample mapping to match the different SECM scanning modes employed. They also allowed the replication of complex sample geometries, and the simulation of multiple mediators simultaneously, for the quantification of sample traits not previously possible. This investigation has been performed under stimuli of toxic (Cd and Cr(VI)) and trace essential (Cr(III)) metals at various concentrations and incubation times. These results were compared to cell viability to examine the possible relationship between induced cell membrane permeability and a reduction in population density. Examination of semi-permeable and impermeable electrochemical mediators, along with these viability studies showed trends in cell response to the external stressor. SECM membrane permeability characterization of single live cells was also examined using nanoscale electrodes. This nanoscale imaging necessitated a complex tailored model geometry with significant variation in meshing element size to appropriately quantify cell topography and

membrane permeability. The development of these tailored models will allow for highly localized examination of membrane permeability of single live cells.

Chapters 2, 3, and 4 examined the effects of metal toxicity (Cd and Cr(VI)) on cell membrane permeability, and compared the resulting trend to cell viability experiments. Chapter 5 examined the trace essential metal Cr (III) in low to excess concentrations. Toxic metals serve no essential biological role, but many can displace essential metals in metalloproteins and key cellular processes. This can cause a deformation of the protein structure or a change in reaction rates for the highly balanced systems that exist in living organisms. Toxic metals can also be a source of excessive reactive oxygen and reactive nitrogen species, leading to oxidative damage in cells. Their introduction into the environment of living organisms can lead to lifelong health complications, such as disease, cancers and death. If present in high enough concentrations the heavy metals can lead to the overwhelming of the antioxidant defense systems, which can induce lipid peroxidation of the cell membrane. Lipid peroxidation can affect membrane fluidity followed by membrane integrity loss, resulting the increased permeation of chemical agents. SECM provides an excellent method of characterizing the location specific membrane permeability of single live cell membranes. As a result, it is employed in the investigation in the biological response of single live cells to heavy metal toxicity.

Firstly, the effects of Cd^{2+} on single live T24 cell membrane permeability were investigated in Chapter 2 by means of SECM. The membrane permeability of FcMeOH was determined to be uniform across the T24 cell surface with the 5 µm radius electrode used. Increasing Cd^{2+} concentration, however, decreased the cell membrane permeability for the concentration range examined. Permeability dropped from 75 µm/s to 50 µm/s for the 50 µM incubation and drop as low as 25 µm/s for 100 µM.

In Chapter 3, SECM was utilized to examine the membrane response of T24 cells following exposure to toxic dichromate (Cr (VI)). Two electrochemical mediators were examined: the membrane permeable $FcCH_2OH$ and the membrane impermeable $FcCOO^-$. With $FcCH_2OH$ as the SECM mediator, Cr (VI) exposure induced three distinct concentration dependant membrane permeability regions. Low concentrations of Cr (VI)

(0-50 µM) produced relatively stable membrane permeability coefficients, remaining consistent with untreated control T24 cells. Exceeding low level exposure (50-500 µM), a decrease in membrane permeability was observed. A minimum of 25 µm/s was observed upon incubation with 500 µM of Cr (VI). Higher exposure (500-1000 µM), yielded an increase in permeability coefficient. Performing the same membrane permeability characterization with the impermeable FcCOO$^-$ mediator, SECM yielded some interesting but different results. FcCOO$^-$ is initially impermeable to the cell membrane. However, it became permeable to the cell membrane following the same incubation concentrations (>500 µM Cr (VI)) that induced an increase in cell membrane permeability for FcCH$_2$OH. This indicates significant membrane integrity loss, as the charged FcCOO$^-$ species is able to permeate the hydrophobic cell membrane. The study in this chapter was also coupled with a MTT cell viability assay. The cell viability was affected by the various concentrations of Cr (VI) in a similar trend to that of the membrane permeability response with FcCH$_2$OH as the SECM mediator.

Cr (VI) induced cell stress with lower concentrations was examined for longer durations in Chapter 4. Chapter 3 focused on more acute exposure to Cr (VI), whereas Chapter 4 payed more attention to chronic exposure. Three Cr (VI) concentrations (2, 5 and 10 µM) were examined, which yielded similar response curve shapes over the study period. The concentration-dependant variation in response time was observed with more rapid response at higher concentrations. Initial low incubation times showed little deviation from control (untreated) cells. Extending the incubation times, however, yielded a decrease in membrane permeability for all concentrations. All cell samples reached their minimum observed membrane permeability within 3 to 6 hr of incubation, with minima as low as 14 µm/s. All samples had a steady rise in membrane permeability following this. The 2 µM and 5 µM cell samples reached their maximum cell permeability (~1000 µm/s) and plateaued after 2 days of incubation. SECM analysis was no longer possible for this sample after 5 days of incubation due to significant population decrease. The higher concentration 10 µM sample, however, reached a similar maximum after 24 hr of incubation, and proceeded to slowly drop over time. Significant population decrease for this sample was observed after 3 days. MTT viability studies were performed, providing

complimentary analysis of overall health and wellness of the cell populations under study. Strong resistance to the external $K_2Cr_2O_7$ stressor for the studied concentrations was observed after 1 day of incubation. Following 2 days of incubation, the 2 µM sample showed a small drop in viability, with all higher concentrations dropping strongly to ≤35%. By 3 days an overall decrease in cell viability was observed.

In Chapter 5, the membrane response of single live cells to the trace essential heavy metal Cr (III) was successfully interrogated using both $FcCH_2OH$ and $FcCOO^-$ as SECM mediators. Full 3D FEM simulations were computed to allow for the quantification of cell membrane permeability by SECM. Using the 3D model of the cell system, full SECM depth scans were simulated. The simulated and experimentally acquired depth scan images allow for the extraction of electrode PACs at any location across the cell, for rapid membrane permeability quantification. With the membrane permeable $FcCH_2OH$, incubation with low Cr (III) concentrations (≤500 µM) showed little effect on the membrane permeability coefficients in comparison to untreated control cells. Increasing the exposure level resulted in decreased permeability coefficients, with a minimum of 17 ± 8 µm/s observed at 7500 µM $CrCl_3$. With higher Cr (III) exposure, the membrane permeability increased. The $FcCOO^-$ mediator was initially impermeable, but similarly exhibited strong increases in membrane permeability when subjected to 7500 µM $CrCl_3$ for 1 hr. This study was also coupled with a MTT cell viability test, which showed a gradual decrease in cell viability when cells were incubated with 500 µM or greater.

The simulation model created for Chapter 2 was designed to quantify the effects of Cd^{2+} on single live T24 cell membrane permeability using a SECM probe. This model was the first of its kind, coupling membrane permeability simulation with a full 3D FEM geometry. This allowed for the simulation of an SECM probe approach curve (PAC) at any location desired over the cell surface. This was a significant improvement over the previous 2D axially symmetric models which were the standard in the field. The 2D axial geometry limited the model design to symmetric samples, with PAC generation directly over the cell center. While PACs could be extracted from experimentally acquired depth scans at numerous locations over the cell, the existing models were incapable of using the

vast majority of that sample data for quantification of membrane permeability and other traits. The improved 3D model allowed for location specific simulations to quantify membrane permeability coefficients across the cell surface. Cells were incubated with different concentrations of Cd^{2+}, and the resulting membrane permeability change was quantified. The membrane permeability of $FcCH_2OH$ was determined to be uniform across the T24 cell surface with the 5 µm radius electrode used. Increasing Cd^{2+} concentration however was found to decrease the cell membrane permeability for the concentration range examined. Permeability was observed to drop from 75 µm/s to 50 µm/s for the 50 µM incubation and drop as low as 25 µm/s for 100 µM. In Chapters 3, 4 and 5, this model design was improved upon to include more accurate cell geometry, as well as numerous optimizations for reducing resource requirements and compute time. These improvements to the system resource demand allowed for the simulation not just of line scans, but full depth scans or surface maps in Chapter 5.

In Chapter 6, the analysis of complex systems of cell clusters in close proximity was carried out by means of SECM image stack 3D scanning mode with 10 µm and 4.4 µm diameter UMEs. Tailored 3D model geometries were created to allow for the simulation of these cell maps. Experimental surface maps of a pair of double cells with a cell spacing of 41.3 µm were obtained using a 4.4 µm UME and compared to simulated images. A strong agreement in curve shapes was reached. Following this, a higher complexity experimental system incorporating two extreme proximity cells (14.7 µm cell distance) was explored with a 10 µm UME. The simulation with a tailored full 3D model was capable of providing a strong theoretical fit to the experimental results when the geometry of both cells was considered. The effects of a pair of adjacent cells with variable cell proximity were further characterized for both common UME sizes. It was determined that deviation from normal PAC current was observed at <20 µm spacing for 10 µm UMEs and <10 µm for 4.4 µm UMEs. This defines the probe size dependant limits of cell proximity for SECM characterization, where the effects of the adjacent cell can be ignored.

Lastly, Chapter 7 describes the nanoscale SECM imaging of a single live cell, with a laser pulled quartz sheathed electrode having a 130 nm radius Pt disk. A single live cell was imaged using the membrane impermeable $Ru(NH_3)_6^{3+}$ mediator to accurately characterize cell topography, and electrode tip-to-cell distance. A tailored 3D model of the single live cell was created to replicate topographical scans experimentally. Using $FcCH_2OH$ as an electrochemical mediator, the same cell was imaged with <10 mins between two surface map scans. Simulations of this system incorporating membrane permeability were performed with various membrane permeability coefficients. It was determined that the cell imaged agreed most strongly with a membrane permeability coefficient ≤ 10 μm/s, indicating little to no flux across the membrane at the time of imaging. The development of this simulation methodology in this study allows for tailored simulations of single live cells. These tailored models are able to provide rich information on cell topography, as well as membrane permeability, and be easily expanded to include additional functionality such as extracellular ROS concentrations. The developed methodology for experimental and theoretical quantification of complex cells is versatile and reinforces the strength of SECM as a powerful bioanalytical tool.

8.2   Future Work

Recent advances in single live cell analysis using SECM has shown great promise for characterization of cellular physiology and pathology. The trend toward coupling SECM with other strong bioanalytical tools provides intersting options for the simultaneous aquisition of data from multiple techniques on the same cell. Well-documented electrode fabrication techniques allow for greater availability of specialized probes. SECM has demonstrated strength in its ability to detect extracellular and intracellular ROS and RNS as a label free analytical technique, leading to the quantification of these compunds and their correlation to oxidative damage. SECM is versatile analytical tool for the detection of localized membrane transport. Bulk transport across a large region of the cell membrane can be performed, or mapping of variation in membrane transport can be carried out with small scale electrodes. Analysis can also be performed over specific cell features such as ion channels to quantify the rate of species flux in and out of the cell.

This has provided an exceptional tool for the analysis of membrane permeability change induced by heavy metal stress. FEM simulations of the SECM analysis of single live cells have also become more advanced as computing power has become more available and lower cost. Highly demanding full 3D simulation models are now capable of running on consumer available gaming or workstation grade PC hardware. Increased CPU core count provides faster computation, and the availability of memory and storage space make larger more complex models viable. These allow for the creation of tailored geometry, simultaneous simulation of multiple electrochemical species, and the incorperation of additional physical calulations into the simulation. In recent years, there has been an increased prevalence of SECM studies involving nanoscale imaging. This small scale technique shall provide exellent bioanalytical tools for the electrochemical imaging of intracellular processes, localized membrane permeability, membrane embedded protiens, and small scale cellular structures.

The Pt core laser-pulled nanoelectrodes examined in this dissertation provided excellent response in the location-specific characterization of a single cell membrane. The RG of the electrode utilized for this study was, however, quite high. Higher RG values make an electrode more suceptable to smaple tilt, and variation in surface height of the sample. Optimization of the laser-pulled method has been explored in the Ding Lab, yielding extremely small nanoelectrodes (25 nm diameter Pt disk); however, the large RG remains. Optimization for smaller RG electrodes is an area of ongoing study in the Ding lab. The fabrication of nanoelectrodes with other conductive materials (Au, Ag, C, PtIr, etc.) may allow for smaller tip diameters and smaller RG. The most notable alternative conductor is pyrolytically deposited carbon nanoelectrodes,which have been developed and well documented by other labs.[1-2] These electrodes favor the fabrication of extremely small nanoelectrodes with tiny RG values, without necessitating FIB milling of the glass sheath. This fabrication methodology will be pursued and optimized for use with the Ding Lab's experimental apparatus. Improved spatial resolution of smaller electrode disks and RG values allow for the highly localized study of electrochemical change in cells when exposed to heavy metal stress. Nanoscale imaging of membranes may provide insight into regions of more pronounced change, surrounding ion channels, membrane

embedded proteins, or detect structurals deformations and pore formation. The small tip geometry from the reduced RG of these nanoelectrodes has also been shown to provide exceptional characterization of intracellular electrochemistry, while causing minimal damage to the cell under study.[3] This will allow for the characterization of intracellular ROS, as well as the probing of the nuclear envelope permeability. Combination SECM probes are also an area of significant interest. Optimization of a Pt and Ir combination probe would allow for the simultaneous aquisition of SECM surface topography and reactivity (Pt) and the location specific quantification of solution pH (Ir).

Simulations of SECM imaging of single live cells have been an area of active development in the Ding lab. Asymmetric tailored geometry simulations developed were in this dissertation. The modelling of cell clusters as well as complex surface geometry was pursued, and shown to provide strong theoretical agreement to experimental imaging. This simulation methodology will be further developed to include additional features for the modelling of the cell system. Through the inclusion of surface reaction kinetics into the physics tree of the FEM model, both steady state and time dependant models will be generated. These reaction boundaries can be applied to entire surfaces, or localized hot spots on the model geometry. This method of characterization will be employed in quantifying the kinetics of biological processes at specific points of interest on the cell membrane. Nanoscale detection of cell ROS and RNS will be added to the simulation model allowing for the quantification of hot spots across the cell membrane.

In addition, the integration of SECM into other analytical techniques such as fluorescence microscopy and Raman microspectroscopy can provide numerous advantages.[4-5] This provides strong complementary techniques for the simultaneous aquisition electrochemical and spctroscopic data. Through the fabrication of optical fiber SNOM probes, with a CVD ring electrode (SECM-SNOM), the localized imaging using both techniques can be performed.[6-7] Using this methodology the mapping of the distribution of specific proteins or receptors across the membrane may be possible. SECM is a highly versatile bioanalytical technique, offering a noninvasive characterization method with high spatial and temporal resolution.

8.3 References

1. McKelvey, K.; Nadappuram, B. P.; Actis, P.; Takahashi, Y.; Korchev, Y. E.; Matsue, T.; Robinson, C.; Unwin, P. R., Fabrication, Characterization, and Functionalization of Dual Carbon Electrodes as Probes for Scanning Electrochemical Microscopy (Secm). *Anal. Chem.* **2013,** *85* (15), 7519-26.

2. Takahashi, Y.; Shevchuk, A. I.; Novak, P.; Zhang, Y.; Ebejer, N.; Macpherson, J. V.; Unwin, P. R.; Pollard, A. J.; Roy, D.; Clifford, C. A.; Shiku, H.; Matsue, T.; Klenerman, D.; Korchev, Y. E., Multifunctional Nanoprobes for Nanoscale Chemical Imaging and Localized Chemical Delivery at Surfaces and Interfaces. *Angew. Chem. Int. Ed. Engl.* **2011,** *50* (41), 9638-42.

3. Li, Y.; Hu, K.; Yu, Y.; Rotenberg, S. A.; Amatore, C.; Mirkin, M. V., Direct Electrochemical Measurements of Reactive Oxygen and Nitrogen Species in Nontransformed and Metastatic Human Breast Cells. *J. Am. Chem. Soc.* **2017,** *139* (37), 13055-13062.

4. Salamifar, S. E.; Lai, R. Y., Use of Combined Scanning Electrochemical and Fluorescence Microscopy for Detection of Reactive Oxygen Species in Prostate Cancer Cells. *Anal. Chem.* **2013,** *85* (20), 9417-21.

5. Schorr, N. B.; Jiang, A. G.; Rodriguez-Lopez, J., Probing Graphene Interfacial Reactivity Via Simultaneous and Colocalized Raman-Scanning Electrochemical Microscopy Imaging and Interrogation. *Anal. Chem.* **2018,** *90* (13), 7848-7854.

6. Lee, Y.; Ding, Z. F.; Bard, A. J., Combined Scanning Electrochemical/Optical Microscopy with Shear Force and Current Feedback. *Anal. Chem.* **2002,** *74* (15), 3634-3643.

7. Lee, Y.; Bard, A. J., Fabrication and Characterization of Probes for Combined Scanning Electrochemical/Optical Microscopy Experiments. *Anal. Chem.* **2002,** *74* (15), 3626-3633.

Appendices

Appendix A: Copyright

Copyright Clearance Center   RightsLink®

Home   Create Account   Help   ✉

ACS Publications
Most Trusted. Most Cited. Most Read.

Title: 3D Printed and Microcontrolled: The One Hundred Dollars Scanning Electrochemical Microscope

Author: Gabriel N. Meloni

Publication: Analytical Chemistry

Publisher: American Chemical Society

Date: Sep 1, 2017

Copyright © 2017, American Chemical Society

LOGIN

If you're a copyright.com user, you can login to RightsLink using your copyright.com credentials.

Already a RightsLink user or want to learn more?

PERMISSION/LICENSE IS GRANTED FOR YOUR ORDER AT NO CHARGE

This type of permission/license, instead of the standard Terms & Conditions, is sent to you because no fee is being charged for your order. Please note the following:

- Permission is granted for your request in both print and electronic formats, and translations.
- If figures and/or tables were requested, they may be adapted or used in part.
- Please print this page for your records and send a copy of it to your publisher/graduate school.
- Appropriate credit for the requested material should be given as follows: "Reprinted (adapted) with permission from (COMPLETE REFERENCE CITATION). Copyright (YEAR) American Chemical Society." Insert appropriate information in place of the capitalized words.
- One-time permission is granted only for the use specified in your request. No additional uses are granted (such as derivative works or other editions). For any other uses, please submit a new request.

If credit is given to another source for the material you requested, permission must be obtained from that source.

BACK   CLOSE WINDOW

Copyright Clearance Center

RightsLink®

Home | Account Info | Help

ACS Publications
Most Trusted. Most Cited. Most Read.

Title:	Direct Electrochemical Measurements of Reactive Oxygen and Nitrogen Species in Nontransformed and Metastatic Human Breast Cells
Author:	Yun Li, Keke Hu, Yun Yu, et al
Publication:	Journal of the American Chemical Society
Publisher:	American Chemical Society
Date:	Sep 1, 2017

Copyright © 2017, American Chemical Society

Logged in as:
Fraser Filice
Account #:
3001316954

LOGOUT

PERMISSION/LICENSE IS GRANTED FOR YOUR ORDER AT NO CHARGE

This type of permission/license, instead of the standard Terms & Conditions, is sent to you because no fee is being charged for your order. Please note the following:

- Permission is granted for your request in both print and electronic formats, and translations.
- If figures and/or tables were requested, they may be adapted or used in part.
- Please print this page for your records and send a copy of it to your publisher/graduate school.
- Appropriate credit for the requested material should be given as follows: "Reprinted (adapted) with permission from (COMPLETE REFERENCE CITATION). Copyright (YEAR) American Chemical Society." Insert appropriate information in place of the capitalized words.
- One-time permission is granted only for the use specified in your request. No additional uses are granted (such as derivative works or other editions). For any other uses, please submit a new request.

If credit is given to another source for the material you requested, permission must be obtained from that source.

BACK | CLOSE WINDOW

Copyright Clearance Center

RightsLink®

Home   Create Account   Help

ACS Publications
Most Trusted. Most Cited. Most Read.

Title: Probing Cd2 -Stressed Live Cell Membrane Permeability with Various Redox Mediators in Scanning Electrochemical Microscopy

Author: Michelle S. M. Li, Fraser P. Filice, Jeffrey D. Henderson, et al

Publication: The Journal of Physical Chemistry C

Publisher: American Chemical Society

Date: Mar 1, 2016

Copyright © 2016, American Chemical Society

LOGIN

If you're a copyright.com user, you can login to RightsLink using your copyright.com credentials.

Already a **RightsLink user** or want to learn more?

PERMISSION/LICENSE IS GRANTED FOR YOUR ORDER AT NO CHARGE

This type of permission/license, instead of the standard Terms & Conditions, is sent to you because no fee is being charged for your order. Please note the following:

- Permission is granted for your request in both print and electronic formats, and translations.
- If figures and/or tables were requested, they may be adapted or used in part.
- Please print this page for your records and send a copy of it to your publisher/graduate school.
- Appropriate credit for the requested material should be given as follows: "Reprinted (adapted) with permission from (COMPLETE REFERENCE CITATION). Copyright (YEAR) American Chemical Society." Insert appropriate information in place of the capitalized words.
- One-time permission is granted only for the use specified in your request. No additional uses are granted (such as derivative works or other editions). For any other uses, please submit a new request.

If credit is given to another source for the material you requested, permission must be obtained from that source.

BACK   CLOSE WINDOW

Copyright Clearance Center

RightsLink®

Home | Create Account | Help

ACS Publications
Most Trusted. Most Cited. Most Read.

Title: Fixation and Permeabilization Approaches for Scanning Electrochemical Microscopy of Living Cells

Author: Alexandra Bondarenko, Tzu-En Lin, Petar Stupar, et al

Publication: Analytical Chemistry

Publisher: American Chemical Society

Date: Dec 1, 2016

Copyright © 2016, American Chemical Society

LOGIN

If you're a copyright.com user, you can login to RightsLink using your copyright.com credentials.

Already a RightsLink user or want to learn more?

PERMISSION/LICENSE IS GRANTED FOR YOUR ORDER AT NO CHARGE

This type of permission/license, instead of the standard Terms & Conditions, is sent to you because no fee is being charged for your order. Please note the following:

- Permission is granted for your request in both print and electronic formats, and translations.
- If figures and/or tables were requested, they may be adapted or used in part.
- Please print this page for your records and send a copy of it to your publisher/graduate school.
- Appropriate credit for the requested material should be given as follows: "Reprinted (adapted) with permission from (COMPLETE REFERENCE CITATION). Copyright (YEAR) American Chemical Society." Insert appropriate information in place of the capitalized words.
- One-time permission is granted only for the use specified in your request. No additional uses are granted (such as derivative works or other editions). For any other uses, please submit a new request.

If credit is given to another source for the material you requested, permission must be obtained from that source.

BACK | CLOSE WINDOW

Copyright Clearance Center

RightsLink®

Home | Account Info | Help

ACS Publications
Most Trusted. Most Cited. Most Read.

Title: Determination of the Relationship between Expression and Functional Activity of Multidrug Resistance-Associated Protein 1 using Scanning Electrochemical Microscopy

Author: David Polcari, Javier Alejandro Hernández-Castro, Kebin Li, et al

Publication: Analytical Chemistry

Publisher: American Chemical Society

Date: Sep 1, 2017

Copyright © 2017, American Chemical Society

Logged in as:
Fraser Filice
Account #:
3001316954

LOGOUT

PERMISSION/LICENSE IS GRANTED FOR YOUR ORDER AT NO CHARGE

This type of permission/license, instead of the standard Terms & Conditions, is sent to you because no fee is being charged for your order. Please note the following:

- Permission is granted for your request in both print and electronic formats, and translations.
- If figures and/or tables were requested, they may be adapted or used in part.
- Please print this page for your records and send a copy of it to your publisher/graduate school.
- Appropriate credit for the requested material should be given as follows: "Reprinted (adapted) with permission from (COMPLETE REFERENCE CITATION). Copyright (YEAR) American Chemical Society." Insert appropriate information in place of the capitalized words.
- One-time permission is granted only for the use specified in your request. No additional uses are granted (such as derivative works or other editions). For any other uses, please submit a new request.

If credit is given to another source for the material you requested, permission must be obtained from that source.

BACK | CLOSE WINDOW

Copyright Clearance Center

Note: Copyright.com supplies permissions but not the copyrighted content itself.

1	2	3
PAYMENT	REVIEW	**CONFIRMATION**

Step 3: Order Confirmation

Thank you for your order! A confirmation for your order will be sent to your account email address. If you have questions about your order, you can call us 24 hrs/day, M-F at +1.855.239.3415 Toll Free, or write to us at info@copyright.com. This is not an invoice.

Confirmation Number: 11751738
Order Date: 09/26/2018

If you paid by credit card, your order will be finalized and your card will be charged within 24 hours. If you choose to be invoiced, you can change or cancel your order until the invoice is generated.

Payment Information

Fraser Filice
ffilice@uwo.ca
+1 (519) 381-7848
Payment Method: n/a

Order Details

Physical chemistry chemical physics

Order detail ID:	71573697	**Permission Status:**	✅ **Granted**
Order License Id:	4436651490554		
ISSN:	1463-9084	**Permission type:**	Republish or display content
Publication Type:	e-Journal	**Type of use:**	Thesis/Dissertation
Volume:			
Issue:		**Requestor type**	Academic institution
Start page:			
Publisher:	ROYAL SOCIETY OF CHEMISTRY	**Format**	Electronic
Author/Editor:	Royal Society of Chemistry (Great Britain)		
		Portion	image/photo
		Number of images/photos requested	1
		The requesting person/organization	Fraser Filice
		Title or numeric reference of the portion(s)	Figure 3
		Title of the article or chapter the portion is from	N/A
		Editor of portion(s)	N/A

9/26/2018   Copyright Clearance Center

Author of portion(s)	N/A
Volume of serial or monograph	N/A
Page range of portion	26731
Publication date of portion	October 2017
Rights for	Main product
Duration of use	Life of current edition
Creation of copies for the disabled	no
With minor editing privileges	no
For distribution to	Worldwide
In the following language(s)	Original language of publication
With incidental promotional use	no
Lifetime unit quantity of new product	Up to 499
Title	COUPLING SCANNING ELECTROCHEMICAL MICROSCOPY AND 3D MODELLING TO PROBE MEMBRANE PERMEABILITY OF HUMAN BLADDER CANCER (T24) CELLS
Instructor name	n/a
Institution name	n/a
Expected presentation date	Sep 2018

Note: This item will be invoiced or charged separately through CCC's **RightsLink** service. More info $ 0.00

This is not an invoice.

Total order items: 1   **Order Total: 0.00 USD**

Confirmation Number: 11751738

Special Rightsholder Terms & Conditions

The following terms & conditions apply to the specific publication under which they are listed

---

Physical chemistry chemical physics
Permission type: Republish or display content
Type of use: Thesis/Dissertation

TERMS AND CONDITIONS

The following terms are individual to this publisher:

None

Other Terms and Conditions:

STANDARD TERMS AND CONDITIONS

1. Description of Service; Defined Terms. This Republication License enables the User to obtain licenses for republication of one or more copyrighted works as described in detail on the relevant Order Confirmation (the "Work(s)"). Copyright Clearance Center, Inc. ("CCC") grants licenses through the Service on behalf of the rightsholder identified on the Order Confirmation (the "Rightsholder"). "Republication", as used herein, generally means the inclusion of a Work, in whole or in part, in a new work or works, also as described on the Order Confirmation. "User", as used herein, means the person or entity making such republication.

2. The terms set forth in the relevant Order Confirmation, and any terms set by the Rightsholder with respect to a particular Work, govern the terms of use of Works in connection with the Service. By using the Service, the person transacting for a republication license on behalf of the User represents and warrants that he/she/it (a) has been duly authorized by the User to accept, and hereby does accept, all such terms and conditions on behalf of User, and (b) shall inform User of all such terms and conditions. In the event such person is a "freelancer" or other third party independent of User and CCC, such party shall be deemed jointly a "User" for purposes of these terms and conditions. In any event, User shall be deemed to have accepted and agreed to all such terms and conditions if User republishes the Work in any fashion.

3. **Scope of License; Limitations and Obligations.**

3.1 All Works and all rights therein, including copyright rights, remain the sole and exclusive property of the Rightsholder. The license created by the exchange of an Order Confirmation (and/or any invoice) and payment by User of the full amount set forth on that document includes only those rights expressly set forth in the Order Confirmation and in these terms and conditions, and conveys no other rights in the Work(s) to User. All rights not expressly granted are hereby reserved.

3.2 General Payment Terms: You may pay by credit card or through an account with us payable at the end of the month. If you and we agree that you may establish a standing account with CCC, then the following terms apply: Remit Payment to: Copyright Clearance Center, 29118 Network Place, Chicago, IL 60673-1291. Payments Due: Invoices are payable upon their delivery to you (or upon our notice to you that they are available to you for downloading). After 30 days, outstanding amounts will be subject to a service charge of 1-1/2% per month or, if less, the maximum rate allowed by applicable law. Unless otherwise specifically set forth in the Order Confirmation or in a separate written agreement signed by CCC, invoices are due and payable on "net 30" terms. While User may exercise the rights licensed immediately upon issuance of the Order Confirmation, the license is automatically revoked and is null and void, as if it had never been issued, if complete payment for the license is not received on a timely basis either from User directly or through a payment agent, such as a credit card company.

3.3 Unless otherwise provided in the Order Confirmation, any grant of rights to User (i) is "one-time" (including the editions and product family specified in the license), (ii) is non-exclusive and non-transferable and (iii) is subject to any and all limitations and restrictions (such as, but not limited to, limitations on duration of use or circulation) included in the Order Confirmation or invoice and/or in these terms and conditions. Upon completion of the licensed use, User shall either secure a new permission for further use of the Work(s) or immediately cease any new use of the Work(s) and shall render inaccessible (such as by deleting or by removing or severing links or other locators) any further copies of the Work (except for copies printed on paper in accordance with this license and still in User's stock at the end of such period).

3.4 In the event that the material for which a republication license is sought includes third party materials (such as photographs, illustrations, graphs, inserts and similar materials) which are identified in such material as having been used by permission, User is responsible for identifying, and seeking separate licenses (under this Service or otherwise) for, any of such third party materials; without a separate license, such third party materials may not be used.

3.5 Use of proper copyright notice for a Work is required as a condition of any license granted under the Service. Unless otherwise provided in the Order Confirmation, a proper copyright notice will read substantially as follows: "Republished with permission of [Rightsholder's name], from [Work's title, author, volume, edition number and year of copyright]; permission conveyed through Copyright Clearance Center, Inc. " Such notice must be provided in a reasonably legible font size and must be placed either immediately adjacent to the Work as used (for example, as part of a by-line or footnote

but not as a separate electronic link) or in the place where substantially all other credits or notices for the new work containing the republished Work are located. Failure to include the required notice results in loss to the Rightsholder and CCC, and the User shall be liable to pay liquidated damages for each such failure equal to twice the use fee specified in the Order Confirmation, in addition to the use fee itself and any other fees and charges specified.

3.6 User may only make alterations to the Work if and as expressly set forth in the Order Confirmation. No Work may be used in any way that is defamatory, violates the rights of third parties (including such third parties' rights of copyright, privacy, publicity, or other tangible or intangible property), or is otherwise illegal, sexually explicit or obscene. In addition, User may not conjoin a Work with any other material that may result in damage to the reputation of the Rightsholder. User agrees to inform CCC if it becomes aware of any infringement of any rights in a Work and to cooperate with any reasonable request of CCC or the Rightsholder in connection therewith.

4. Indemnity. User hereby indemnifies and agrees to defend the Rightsholder and CCC, and their respective employees and directors, against all claims, liability, damages, costs and expenses, including legal fees and expenses, arising out of any use of a Work beyond the scope of the rights granted herein, or any use of a Work which has been altered in any unauthorized way by User, including claims of defamation or infringement of rights of copyright, publicity, privacy or other tangible or intangible property.

5. Limitation of Liability. UNDER NO CIRCUMSTANCES WILL CCC OR THE RIGHTSHOLDER BE LIABLE FOR ANY DIRECT, INDIRECT, CONSEQUENTIAL OR INCIDENTAL DAMAGES (INCLUDING WITHOUT LIMITATION DAMAGES FOR LOSS OF BUSINESS PROFITS OR INFORMATION, OR FOR BUSINESS INTERRUPTION) ARISING OUT OF THE USE OR INABILITY TO USE A WORK, EVEN IF ONE OF THEM HAS BEEN ADVISED OF THE POSSIBILITY OF SUCH DAMAGES. In any event, the total liability of the Rightsholder and CCC (including their respective employees and directors) shall not exceed the total amount actually paid by User for this license. User assumes full liability for the actions and omissions of its principals, employees, agents, affiliates, successors and assigns.

6. Limited Warranties. THE WORK(S) AND RIGHT(S) ARE PROVIDED "AS IS". CCC HAS THE RIGHT TO GRANT TO USER THE RIGHTS GRANTED IN THE ORDER CONFIRMATION DOCUMENT. CCC AND THE RIGHTSHOLDER DISCLAIM ALL OTHER WARRANTIES RELATING TO THE WORK(S) AND RIGHT(S), EITHER EXPRESS OR IMPLIED, INCLUDING WITHOUT LIMITATION IMPLIED WARRANTIES OF MERCHANTABILITY OR FITNESS FOR A PARTICULAR PURPOSE. ADDITIONAL RIGHTS MAY BE REQUIRED TO USE ILLUSTRATIONS, GRAPHS, PHOTOGRAPHS, ABSTRACTS, INSERTS OR OTHER PORTIONS OF THE WORK (AS OPPOSED TO THE ENTIRE WORK) IN A MANNER CONTEMPLATED BY USER; USER UNDERSTANDS AND AGREES THAT NEITHER CCC NOR THE RIGHTSHOLDER MAY HAVE SUCH ADDITIONAL RIGHTS TO GRANT.

7. Effect of Breach. Any failure by User to pay any amount when due, or any use by User of a Work beyond the scope of the license set forth in the Order Confirmation and/or these terms and conditions, shall be a material breach of the license created by the Order Confirmation and these terms and conditions. Any breach not cured within 30 days of written notice thereof shall result in immediate termination of such license without further notice. Any unauthorized (but licensable) use of a Work that is terminated immediately upon notice thereof may be liquidated by payment of the Rightsholder's ordinary license price therefor; any unauthorized (and unlicensable) use that is not terminated immediately for any reason (including, for example, because materials containing the Work cannot reasonably be recalled) will be subject to all remedies available at law or in equity, but in no event to a payment of less than three times the Rightsholder's ordinary license price for the most closely analogous licensable use plus Rightsholder's and/or CCC's costs and expenses incurred in collecting such payment.

8. **Miscellaneous.**

8.1 User acknowledges that CCC may, from time to time, make changes or additions to the Service or to these terms and conditions, and CCC reserves the right to send notice to the User by electronic mail or otherwise for the purposes of notifying User of such changes or additions; provided that any such changes or additions shall not apply to permissions already secured and paid for.

8.2 Use of User-related information collected through the Service is governed by CCC's privacy policy, available online here: http://www.copyright.com/content/cc3/en/tools/footer/privacypolicy.html.

8.3 The licensing transaction described in the Order Confirmation is personal to User. Therefore, User may not assign or transfer to any other person (whether a natural person or an organization of any kind) the license created by the Order Confirmation and these terms and conditions or any rights granted hereunder; provided, however, that User may assign such license in its entirety on written notice to CCC in the event of a transfer of all or substantially all of User's rights in the new material which includes the Work(s) licensed under this Service.

8.4 No amendment or waiver of any terms is binding unless set forth in writing and signed by the parties. The Rightsholder and CCC hereby object to any terms contained in any writing prepared by the User or its principals, employees, agents or affiliates and purporting to govern or otherwise relate to the licensing transaction described in the Order Confirmation, which terms are in any way inconsistent with any terms set forth in the Order Confirmation and/or in these terms and conditions or CCC's standard operating procedures, whether such writing is prepared prior to, simultaneously with or subsequent to the Order Confirmation, and whether such writing appears on a copy of the Order Confirmation or in a separate instrument.

8.5 The licensing transaction described in the Order Confirmation document shall be governed by and construed under the law of the State of New York, USA, without regard to the principles thereof of conflicts of law. Any case, controversy, suit, action, or proceeding arising out of, in connection with, or related to such licensing transaction shall be brought, at CCC's sole discretion, in any federal or state court located in the County of New York, State of New York, USA, or in any federal or state court whose geographical jurisdiction covers the location of the Rightsholder set forth in the Order Confirmation. The parties expressly submit to the personal jurisdiction and venue of each such federal or state court.If you have any comments or questions about the Service or Copyright Clearance Center, please contact us at 978-750-8400 or send an e-mail to info@copyright.com.

v 1.1

Close

Copyright Clearance Center

RightsLink®

Home | Account Info | Help

ACS Publications
Most Trusted. Most Cited. Most Read.

Title: Single Synaptic Observation of Cholinergic Neurotransmission on Living Neurons: Concentration and Dynamics

Author: Mei Shen, Zizheng Qu, Justin DesLaurier, et al

Publication: Journal of the American Chemical Society

Publisher: American Chemical Society

Date: Jun 1, 2018

Copyright © 2018, American Chemical Society

Logged in as:
Fraser Filice
Account #:
3001316954

LOGOUT

PERMISSION/LICENSE IS GRANTED FOR YOUR ORDER AT NO CHARGE

This type of permission/license, instead of the standard Terms & Conditions, is sent to you because no fee is being charged for your order. Please note the following:

- Permission is granted for your request in both print and electronic formats, and translations.
- If figures and/or tables were requested, they may be adapted or used in part.
- Please print this page for your records and send a copy of it to your publisher/graduate school.
- Appropriate credit for the requested material should be given as follows: "Reprinted (adapted) with permission from (COMPLETE REFERENCE CITATION). Copyright (YEAR) American Chemical Society." Insert appropriate information in place of the capitalized words.
- One-time permission is granted only for the use specified in your request. No additional uses are granted (such as derivative works or other editions). For any other uses, please submit a new request.

If credit is given to another source for the material you requested, permission must be obtained from that source.

BACK | CLOSE WINDOW

Copyright Clearance Center — RightsLink®

Home | Account Info | Help

ACS Publications — Most Trusted. Most Cited. Most Read.

Title: Quantitative Visualization of Molecular Delivery and Uptake at Living Cells with Self-Referencing Scanning Ion Conductance Microscopy-Scanning Electrochemical Microscopy

Author: Ashley Page, Minkyung Kang, Alexander Armitstead, et al

Publication: Analytical Chemistry

Publisher: American Chemical Society

Date: Mar 1, 2017

Copyright © 2017, American Chemical Society

Logged in as:
Fraser Filice
Account #:
3001316954

LOGOUT

PERMISSION/LICENSE IS GRANTED FOR YOUR ORDER AT NO CHARGE

This type of permission/license, instead of the standard Terms & Conditions, is sent to you because no fee is being charged for your order. Please note the following:

- Permission is granted for your request in both print and electronic formats, and translations.
- If figures and/or tables were requested, they may be adapted or used in part.
- Please print this page for your records and send a copy of it to your publisher/graduate school.
- Appropriate credit for the requested material should be given as follows: "Reprinted (adapted) with permission from (COMPLETE REFERENCE CITATION). Copyright (YEAR) American Chemical Society." Insert appropriate information in place of the capitalized words.
- One-time permission is granted only for the use specified in your request. No additional uses are granted (such as derivative works or other editions). For any other uses, please submit a new request.

If credit is given to another source for the material you requested, permission must be obtained from that source.

BACK | CLOSE WINDOW

JOHN WILEY AND SONS LICENSE
TERMS AND CONDITIONS

Aug 02, 2018

This Agreement between Mr. Fraser Filice ("You") and John Wiley and Sons ("John Wiley and Sons") consists of your license details and the terms and conditions provided by John Wiley and Sons and Copyright Clearance Center.

License Number	4400901174129
License date	Aug 02, 2018
Licensed Content Publisher	John Wiley and Sons
Licensed Content Publication	ChemElectroChem
Licensed Content Title	Tracking Live-Cell Response to Hexavalent Chromium Toxicity by using Scanning Electrochemical Microscopy
Licensed Content Author	Jeffrey D. Henderson, Fraser P. Filice, Michelle S. M. Li, et al
Licensed Content Date	Feb 16, 2017
Licensed Content Volume	4
Licensed Content Issue	4
Licensed Content Pages	8
Type of use	Dissertation/Thesis
Requestor type	Author of this Wiley article
Format	Electronic
Portion	Full article
Will you be translating?	No
Title of your thesis / dissertation	COUPLING SCANNING ELECTROCHEMICAL MICROSCOPY AND 3D MODELLING TO PROBE MEMBRANE PERMEABILITY OF HUMAN BLADDER CANCER (T24) CELLS
Expected completion date	Sep 2018
Expected size (number of pages)	265
Requestor Location	Mr. Fraser Filice 1151 Richmond St London, ON N6A3K7 Canada Attn: Mr. Fraser Filice
Publisher Tax ID	EU826007151
Total	0.00 CAD
Terms and Conditions	

TERMS AND CONDITIONS

which a Wiley Company has exclusive publishing rights in relation to a particular work (collectively "WILEY"). By clicking "accept" in connection with completing this licensing transaction, you agree that the following terms and conditions apply to this transaction (along with the billing and payment terms and conditions established by the Copyright Clearance Center Inc., ("CCC's Billing and Payment terms and conditions"), at the time that you opened your RightsLink account (these are available at any time at http://myaccount.copyright.com).

Terms and Conditions

- The materials you have requested permission to reproduce or reuse (the "Wiley Materials") are protected by copyright.

- You are hereby granted a personal, non-exclusive, non-sub licensable (on a stand-alone basis), non-transferable, worldwide, limited license to reproduce the Wiley Materials for the purpose specified in the licensing process. This license, **and any CONTENT (PDF or image file) purchased as part of your order,** is for a one-time use only and limited to any maximum distribution number specified in the license. The first instance of republication or reuse granted by this license must be completed within two years of the date of the grant of this license (although copies prepared before the end date may be distributed thereafter). The Wiley Materials shall not be used in any other manner or for any other purpose, beyond what is granted in the license. Permission is granted subject to an appropriate acknowledgement given to the author, title of the material/book/journal and the publisher. You shall also duplicate the copyright notice that appears in the Wiley publication in your use of the Wiley Material. Permission is also granted on the understanding that nowhere in the text is a previously published source acknowledged for all or part of this Wiley Material. Any third party content is expressly excluded from this permission.

- With respect to the Wiley Materials, all rights are reserved. Except as expressly granted by the terms of the license, no part of the Wiley Materials may be copied, modified, adapted (except for minor reformatting required by the new Publication), translated, reproduced, transferred or distributed, in any form or by any means, and no derivative works may be made based on the Wiley Materials without the prior permission of the respective copyright owner.**For STM Signatory Publishers clearing permission under the terms of the STM Permissions Guidelines only, the terms of the license are extended to include subsequent editions and for editions in other languages, provided such editions are for the work as a whole in situ and does not involve the separate exploitation of the permitted figures or extracts,** You may not alter, remove or suppress in any manner any copyright, trademark or other notices displayed by the Wiley Materials. You may not license, rent, sell, loan, lease, pledge, offer as security, transfer or assign the Wiley Materials on a stand-alone basis, or any of the rights granted to you hereunder to any other person.

- The Wiley Materials and all of the intellectual property rights therein shall at all times remain the exclusive property of John Wiley & Sons Inc, the Wiley Companies, or their respective licensors, and your interest therein is only that of having possession of

and the right to reproduce the Wiley Materials pursuant to Section 2 herein during the continuance of this Agreement. You agree that you own no right, title or interest in or to the Wiley Materials or any of the intellectual property rights therein. You shall have no rights hereunder other than the license as provided for above in Section 2. No right, license or interest to any trademark, trade name, service mark or other branding ("Marks") of WILEY or its licensors is granted hereunder, and you agree that you shall not assert any such right, license or interest with respect thereto

- NEITHER WILEY NOR ITS LICENSORS MAKES ANY WARRANTY OR REPRESENTATION OF ANY KIND TO YOU OR ANY THIRD PARTY, EXPRESS, IMPLIED OR STATUTORY, WITH RESPECT TO THE MATERIALS OR THE ACCURACY OF ANY INFORMATION CONTAINED IN THE MATERIALS, INCLUDING, WITHOUT LIMITATION, ANY IMPLIED WARRANTY OF MERCHANTABILITY, ACCURACY, SATISFACTORY QUALITY, FITNESS FOR A PARTICULAR PURPOSE, USABILITY, INTEGRATION OR NON-INFRINGEMENT AND ALL SUCH WARRANTIES ARE HEREBY EXCLUDED BY WILEY AND ITS LICENSORS AND WAIVED BY YOU.

- WILEY shall have the right to terminate this Agreement immediately upon breach of this Agreement by you.

- You shall indemnify, defend and hold harmless WILEY, its Licensors and their respective directors, officers, agents and employees, from and against any actual or threatened claims, demands, causes of action or proceedings arising from any breach of this Agreement by you.

- IN NO EVENT SHALL WILEY OR ITS LICENSORS BE LIABLE TO YOU OR ANY OTHER PARTY OR ANY OTHER PERSON OR ENTITY FOR ANY SPECIAL, CONSEQUENTIAL, INCIDENTAL, INDIRECT, EXEMPLARY OR PUNITIVE DAMAGES, HOWEVER CAUSED, ARISING OUT OF OR IN CONNECTION WITH THE DOWNLOADING, PROVISIONING, VIEWING OR USE OF THE MATERIALS REGARDLESS OF THE FORM OF ACTION, WHETHER FOR BREACH OF CONTRACT, BREACH OF WARRANTY, TORT, NEGLIGENCE, INFRINGEMENT OR OTHERWISE (INCLUDING, WITHOUT LIMITATION, DAMAGES BASED ON LOSS OF PROFITS, DATA, FILES, USE, BUSINESS OPPORTUNITY OR CLAIMS OF THIRD PARTIES), AND WHETHER OR NOT THE PARTY HAS BEEN ADVISED OF THE POSSIBILITY OF SUCH DAMAGES. THIS LIMITATION SHALL APPLY NOTWITHSTANDING ANY FAILURE OF ESSENTIAL PURPOSE OF ANY LIMITED REMEDY PROVIDED HEREIN.

- Should any provision of this Agreement be held by a court of competent jurisdiction to be illegal, invalid, or unenforceable, that provision shall be deemed amended to achieve as nearly as possible the same economic effect as the original provision, and the legality, validity and enforceability of the remaining provisions of this Agreement shall not be affected or impaired thereby.

- The failure of either party to enforce any term or condition of this Agreement shall not constitute a waiver of either party's right to enforce each and every term and condition of this Agreement. No breach under this agreement shall be deemed waived or excused by either party unless such waiver or consent is in writing signed by the party granting such waiver or consent. The waiver by or consent of a party to a breach of any provision of this Agreement shall not operate or be construed as a waiver of or consent to any other or subsequent breach by such other party.

- This Agreement may not be assigned (including by operation of law or otherwise) by you without WILEY's prior written consent.

- Any fee required for this permission shall be non-refundable after thirty (30) days from receipt by the CCC.

- These terms and conditions together with CCC's Billing and Payment terms and conditions (which are incorporated herein) form the entire agreement between you and WILEY concerning this licensing transaction and (in the absence of fraud) supersedes all prior agreements and representations of the parties, oral or written. This Agreement may not be amended except in writing signed by both parties. This Agreement shall be binding upon and inure to the benefit of the parties' successors, legal representatives, and authorized assigns.

- In the event of any conflict between your obligations established by these terms and conditions and those established by CCC's Billing and Payment terms and conditions, these terms and conditions shall prevail.

- WILEY expressly reserves all rights not specifically granted in the combination of (i) the license details provided by you and accepted in the course of this licensing transaction, (ii) these terms and conditions and (iii) CCC's Billing and Payment terms and conditions.

- This Agreement will be void if the Type of Use, Format, Circulation, or Requestor Type was misrepresented during the licensing process.

- This Agreement shall be governed by and construed in accordance with the laws of the State of New York, USA, without regards to such state's conflict of law rules. Any legal action, suit or proceeding arising out of or relating to these Terms and Conditions or the breach thereof shall be instituted in a court of competent jurisdiction in New York County in the State of New York in the United States of America and each party hereby consents and submits to the personal jurisdiction of such court, waives any objection to venue in such court and consents to service of process by registered or certified mail, return receipt requested, at the last known address of such party.

WILEY OPEN ACCESS TERMS AND CONDITIONS
Wiley Publishes Open Access Articles in fully Open Access Journals and in Subscription

Curriculum Vitae

Name: First Name Last Name **Fraser Patrick Filice**

Post-secondary Education and Degrees:

The University of Western Ontario
London, Ontario, Canada
2006-2014 B.Sc.

The University of Western Ontario
London, Ontario, Canada
2014-2018 Ph.D.

Honours and Awards:

Western Graduate Research Scholarship (WGRS)
2014-2017

Province of Ontario Graduate Scholarship (OGS)
2017

Fallona Family Interdisciplinary Science OGS
2018

Province of Ontario Graduate Scholarship (OGS)
2018

Canadian Society for Chemistry (CSC) 2018 - Analytical
Division's Best Graduate Student Oral Presentation Award in the
Electrochemistry Symposium.
CSC Conference and Exhibition, Edmonton, AB.
"3D Imaging and Modelling of Live Cell Clusters with Scanning
Electrochemical Microscopy."
May 27-31, 2018

Related Work Experience

Teaching Assistant
The University of Western Ontario (Chemistry Dept.)
2014-2017

Lead Hardware Architect, RoadLAB
The University of Western Ontario (Computer Science Dept.)
2009

Publications:

[14]. **F.P. Filice**, M.S.M. Li, Z. Ding, Simulation Assisted Nanoscale Imaging of Single Live Cells with Scanning Electrochemical Microscopy, Adv. Theory Simulations (2018), DOI: 10.1002/adts.201800124

[13]. **F.P. Filice**, M.S.M. Li, J. Wong, Z. Ding, SECM Imaging and Full 3D Modelling of Asymmetric Clusters of Live Cells, (2018), *Submitted*

[12]. **F.P. Filice**, Z. Ding, Analysing Single Live Cells by Scanning Electrochemical Microscopy, (2018), DOI: 10.1039/C8AN01490F

[11]. **F.P. Filice**, J.D. Henderson, M.S.M. Li, Z. Ding, Trivalent Chromium Induced Live Cell Membrane Permeability Disruption Revealed by Scanning Electrochemical Microscopy, (2018), *Submitted*

[10]. **F.P. Filice**, M.S.M. Li, J. Wong, Z. Ding, The Effects of Long Duration Chronic Exposure to Hexavalent Chromium on Single Live Cells Interrogated by Scanning Electrochemical Microscopy, J. Inorg. Biochem., *182*, 222-229 (2018).

[9]. M.S.M. Li, **F.P. Filice**, Z. Ding, Submicron Probes for Scanning Electrochemical Microscopy, Can. J. Chem., *96*, 328-335 (2018).

[8]. J.D. Henderson, **F.P. Filice**, M.S.M. Li, Z. Ding, Tracking Live Cell Response to Hexavalent Chromium Toxicity by Scanning Electrochemical Microscopy, ChemElectroChem, *4*, 856-863 (2017).

[7]. M.S.M. Li, **F.P. Filice**, Z. Ding, Scanning Electrochemical Microscopy Imaging with Laser-pulled Probes, J. Electroanal. Chem., *781*, 126-135 (2016).

[6]. J.D. Henderson, **F.P. Filice**, M.S. Li, Z. Ding, Tracking Live Cell Response to Cadmium (II) Concentrations by Scanning Electrochemical Microscopy, J. Inorg. Biochem., *15*8, 92-8 (2016).

[5]. M.S.M. Li, **F.P. Filice**, Z. Ding, Determining Live Cell Topography by Scanning Electrochemical Microscopy, J. Electroanal. Chem., *779*, 176-186 (2016).

[4]. M.S.M. Li, **F.P. Filice**, J.D. Henderson, Z.F. Ding, Probing Cd^{2+}-Stressed Live Cell Membrane Permeability with Various Redox Mediators in Scanning Electrochemical Microscopy, J. Phys. Chem. C, *120*, 6094-6103 (2016).

[3]. **F.P. Filice**, M.S. Li, J.D. Henderson, Z. Ding, Mapping Cd^{2+}-Induced Membrane Permeability Changes of Single Live Cells by Means of Scanning Electrochemical Microscopy, Anal. Chim. Acta, *908*, 85-94 (2016).

[2]. **F.P. Filice**, M.S.M. Li, J.D. Henderson, Z.F. Ding, Three-Dimensional Electrochemical Functionality of an Interdigitated Array Electrode by Scanning Electrochemical Microscopy, J. Phys. Chem. C, *119*, 21473-21482 (2015).

[1]. M.S. Li, **F.P. Filice**, Z. Ding, A Time Course Study of Cadmium Effect on Membrane Permeability of Single Human Bladder Cancer Cells Using Scanning Electrochemical Microscopy, J. Inorg. Biochem., *136*, 177-83 (2014).

Presentations:

[9]. "Toward Nano-Scale Scanning Electrochemical Microscopy of Single Live Cells by Means of COMSOL®," **Fraser P. Filice**, Michelle S.M. Li, and Zhifeng Ding, COMSOL Conference 2018 Boston, Newton, MA, October 3-5, 2018.

[8]. "3D Imaging and Modelling of Live Cell Clusters with Scanning Electrochemical Microscopy," **Fraser P. Filice**, Michelle S.M. Li, and Zhifeng Ding, Canadian Society for Chemistry Conference and Exhibition (CSC 2018), Edmonton, AB, May 27-31, 2018.

[7]. "Full Three-Dimensional Imaging and Modelling of Complex Clusters of Live Cells by Scanning Electrochemical Microscopy*,"* **Fraser P. Filice**, Michelle S.M. Li*,* and Zhifeng Ding, Electrochemical Society Student Chapter, London, ON, December 15, 2017 (Featured on Symposium Booklet Cover).

[6]. "Chromium Induced Cell Membrane Response Quantified by Scanning Electrochemical Microscopy," **Fraser P. Filice**, Jeffrey D. Henderson, Michelle S.M. Li, and Zhifeng Ding, WITec Alpha300R Workshop, Guelph, ON, August 15, 2017.

[5]. "Live Cell Response to Dichromate Toxicity Quantified by Scanning Electrochemical Microscopy*,"* **Fraser P. Filice**, Jeffrey D. Henderson, Michelle S.M. Li, and Zhifeng Ding, Canadian Society for Chemistry Conference and Exhibition (CSC 2017), Toronto, ON, May 28-June 1, 2017.

[4]. "Tracking Live Cell Response to Hexavalent Chromium Toxicity by Scanning Electrochemical Microscopy," **Fraser P. Filice**, Jeffrey D. Henderson, Michelle S.M. Li, and Zhifeng Ding, Canadian Society for Chemistry Conference and Exhibition (CanBIC 2017), Parry Sound, ON, May 24-26, 2017.

[3]. "Cd^{2+}-Induced Membrane Permeability Changes in T24 Cells by Scanning Electrochemical Microscopy**,"** Michelle S. M. Li, **Fraser P. Filice**, Jeffrey D. Henderson, and Zhifeng Ding, Gordon Research Conference on the Cell Biology of Metals, Mount Snow West Dover, VT, July 26-31, 2015**.**

[2]. "Mapping of Single Live Cell Membrane Permeability when Exposed to Toxic Cd^{2+} by Means of Scanning Electrochemical Microscopy," **Fraser P. Filice**, Michelle S. M. Li, Jeffrey D. Henderson and Zhifeng Ding, Gordon Research Conference on the Cell Biology of Metals, Mount Snow West Dover, VT, July 26-31, 2015.

[1]. "Determining Membrane Permeability of Single Live Cells by Means of Scanning Electrochemical Microscopy and Asymmetric 3D Simulations," **Fraser P. Filice**, Michelle S. M. Li, Jeffrey D. Henderson and Zhifeng Ding, Centre for Advanced Materials and Biomaterials Research (CAMBR), London, ON, April 27, 2015.